Models of CJ deflagrations and their transition to detonations from the interaction of a detonation wave with a perforated plate

by

Wentian Wang

Thesis submitted to the
Faculty of Graduate and Postdoctoral Studies
In partial fulfillment of the requirements
For the M.A.Sc. degree in
Mechanical Engineering

Department of Mechanical Engineering
Faculty of Engineering
University of Ottawa

Abstract

The last stage of a deflagration-to-detonation transition (DDT) process involves the propagation and acceleration of a fast flame. This process is currently poorly understood. The difficulties lie in its complex structure, which is turbulent and involves multi-dimensional gasdynamic phenomena. Previous experimental studies have established these fast flames from the interaction of a detonation wave with a row of obstacles or porous plate. Two main questions remain unsolved: 1) What is the propagation speed of the fast flame obtained in these configurations and 2), Which factors dominate the occurrence of the DDT phenomenon? To answer these questions, two models have been constructed in the present work.

Firstly, a quasi-1D gasdynamic model is proposed for estimating the transmitted reaction front speed and the strength of the transmitted shock. By alternately assuming a Chapman-Jouguet (CJ) deflagration or an inert shock, the model estimated the transmitted shock speeds. The comparison with extensive experimental data for a range of hydrocarbon fast flames revealed that the burning velocity required for transition to detonation was the CJ value.

Secondly, a numerical shock-induced ignition model, which can impose mechanical fluctuations from a driven piston, was established in order to investigate the ignition and acceleration process, thereby clarifying the other question of interest. The results from the simulations indicated that the mechanical fluctuations can play an important role in triggering DDT by means of promoting the local ignition and amplification of the reaction front stemming from such ignition. It was also found that the maximum amplification effects occur with a fluctuation period between the non-fluctuated ignition delay and the time scale of chemical energy deposition. The inert simulation results show that two types of gasdynamic effects from the fluctuations were vital to the hot-spot formation. These hot spots make significant contribution to the detonation initiation.

Acknowledgements

First of all, I wish to give my great appreciation to Dr. Matei I. Radulescu, my supervisor, for introducing me to the fantastic world of compressible fluids, giving me the chance to be part of his excellent research team, continually guiding me through the difficulties, and encouraging me. His patient supervision illuminates my academmic road and hones my research skills.

I would also like to express my full gratitude to Dr. James G. McDonald, my co-supervisor, for greatly improving my skills in CFD and understanding of mathematics. This work was financially supported by a NSERC and Shell Collaborative Research and Development (CRD) grant to Dr. Radulescu. This funding is greatly acknowledged.

I need to give my special thanks to my colleague, Qiang Xiao, who spent plenty of time helping me to sharpen my thesis and enhance my writing skills.

A great thanks should be given to my research team, for offering the important help for both my academics and my life.

Dedication

This is dedicated to my father, Li Wang, to my mother, Hua Liu, to my grandfather Honglin Wang, to my grandmother, Lvduan Gao, who love me, believe in me, inspire me and have supported me every step of the way.

Table of Contents

List of Tables

List of Figures

Chapter 1

Introduction

1.1 Problem Definition

Generally speaking, there are two types of self-propagating combustion waves: deflagrations and detonations. Deflagration waves propagate at relatively low subsonic velocities with respect to the reactants ahead of them. A detonation wave is a supersonic combustion wave across which the thermodynamic states (e.g., pressure and temperature) increase sharply[22].

Deflagration to detonation transition (DDT) is a process in which a flame propagates from the subsonic regime, dominated by turbulent heat and mass diffusion, to a combustion mode in which the adiabatic compression and ignition takes over as transport mechanism. Such transitions are important in many practical applications, such as explosion safety [3, 45], pulse detonation engines [36, 2], and engine knock [47].

When a mixture ignites as a low-speed subsonic flame initially, complex geometries deform the flame and increase its surface area. Turbulence further promotes the burning velocity. The resulting increase in global rate of energy deposition leads to the flame acceleration [23, 9]. Such a flame would finally evolve to a detonation, given enough space and time. The early stages of premixed flame acceleration, such as laminar and turbulent flames, are well modeled and understood for the context of current work. The last stage of acceleration is called a fast flame and is not fully clear yet. In this stage, the flame burning velocity may become comparable with the local sound speed. Gasdynamic coupling can arise, which further intensifies the compression waves. In this regime, both turbulent transport and auto-ignition phenomena can become important. Gasdynamic evolution associated with wave motion plays an important role. Compression waves are sent forward into the unreacted mixture from the flame. Thus, the study of fast flames and their transition to detonation conditions are useful to predict the formation of a detonation.

Previous studies have suggested that the fast flame in DDT processes can be set-up using the problem of a detonation passing through a perforated plate, which gives rise to

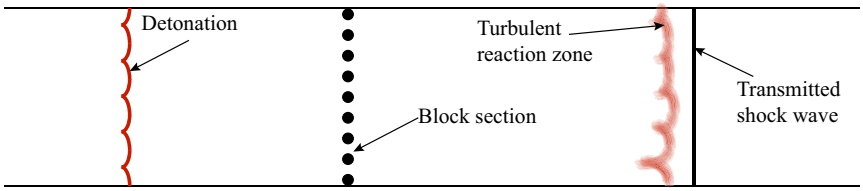

Figure 1.1: A schematic diagram showing a detonation wave passing over cylindrical obstacles and forming transmitted shock-flame complex.

a shock wave, followed by a turbulent reaction zone[6, 37]. Figure 1.1 shows a detonation wave passing over a series of obstacles and giving rise to a transmitted shock followed by a turbulent fast-flame reaction zone. The goal of the current research is to establish a model for the transmitted shock-flame complex and study how its transition to a detonation is affected by local flow perturbations giving rise to hotspots. Although the goal is to study the prosess that a transmitted shock transitioning to a detonation, the method used to obtain the transmitted shock is by passing a detonation through a set of obstacles.

1.2 Background

Early studies of the detonation-obstruction interaction problem by Chao [6] experimentally recorded the interaction between a detonation and a perforated plate. Qualitative features of the interaction were explained. Figure 1.2 (left) gives a self-luminous streak photograph of a detonation passing through a perforated plate [6]. In this figure, the plate is at the right edge of the photo. A reflected shock can be observed. This indicates that the rear part of the shock tube does not have complex gasdynamic phenomena. Chao also conducted an experiment involving a strong incident shock wave interacting with a perforated plate[6]. Fig.1.2(right) shows this experiment with the perforated plate assembled on the left edge of the photo. In this experiment one can see the generation of a strong transmitted wave penetrating to the right. A series of oblique patterns are also observed behind the transmitted shock, which means the transmitted section contains complex gasdynamic features.

Grondin and Lee recorded single photographs of detonations interacting with a perforated plate[19]. From Fig.1.3, several reflected waves and transmitted waves can be observed, e.g., see the second frame. After the interaction between the waves, the transmitted wave front became more planar. The reaction front finally gradually decoupled from the shock front, as seen in the last frame. It indicates that the reaction front could be decoupled from the leading shock when passing over the obstructions.

In some of Grondin and Lee's argon diluted experiments, the onset of detonation occurred near the perforated plate. This is a DDT process in a fast flame. Figure 1.4 shows a sequence of images showing the onset of a detonation. In the second frame, just before

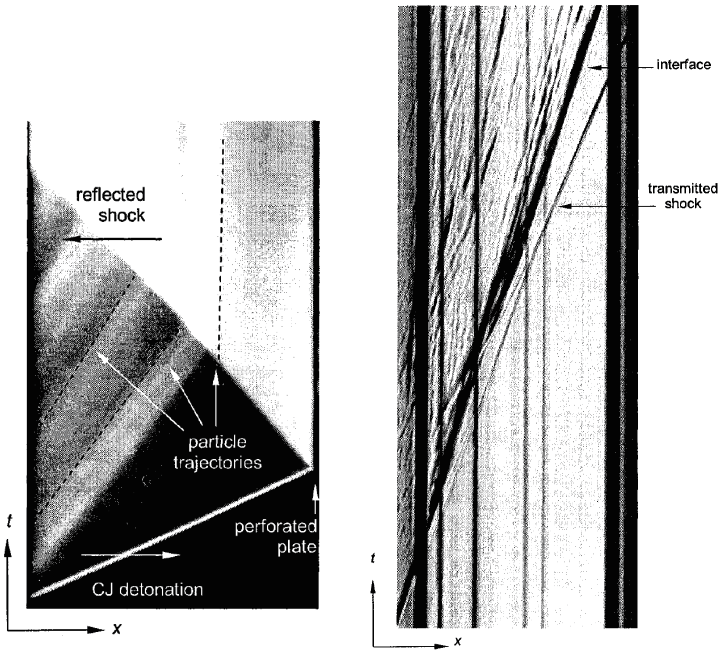

Figure 1.2: Left: a detonation interacting with a series of obstacles, before and after interaction. Right: a shock wave interacting with perforated plate, after the interaction [6].

the re-ignition, one can find the complicated structure behind the reaction front. Grondin and Lee interpreted the complicated structures as meta-stable turbulent reaction zones. They consider such turbulence as one of the key factors leading to detonation [19]. It is therefore desirable to establish a single model of fluctuations such as turbulent and others when studying the transition to detonation.

The complicated structures observed in Grondin and Lee's photographs have been more clearly resolved by Maley [26] and Saif [37] with high-speed visualization techniques. Maley used a single cylinder to substitute the blocking plate. From Fig.1.5 for a developed detonation passing over the cylindrical obstacle, the wave front was first inclined by the convergent-divergent section. Then the two wave fronts collide with each other leading to a Mach reflection. The shock front gradually becomes planar through frame 19 to 25 in Fig.1.5. A reaction front appears to decouple from the shock front at the frame 15. The Mach reflection generates a pair of triple points moving along the leading shock front. Such triple points are the loci where transverse shocks interact with the leading shock, which give rise to strong shear layers. Ignition spots were observed behind the Mach shocks from repeated triple point collisions (e.g., at frames 7, 13 and 17). Strong turbulent structures were also observed behind the triple points. This experiment reveals that the evolution of detonation-cylinder interaction problem is qualitatively the same as what has been observed in the detonation-perforated plate interaction problem.

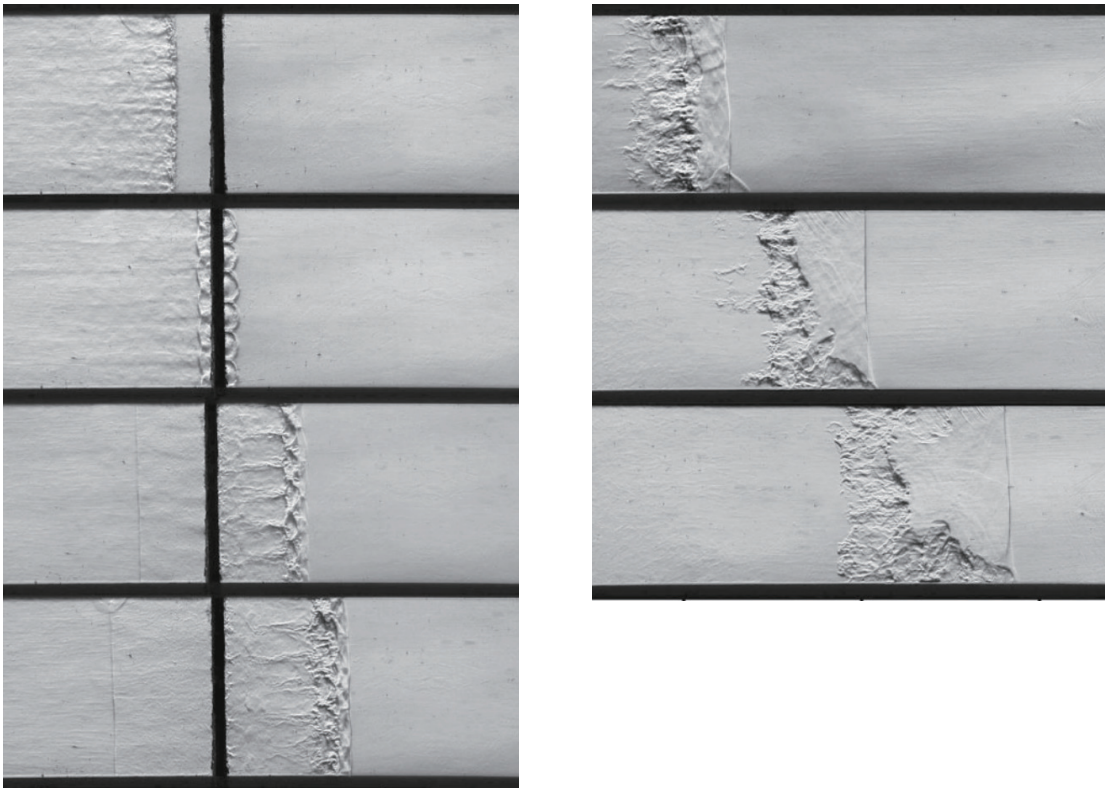

Figure 1.3: The decoupling of a flame and leading shock for C_2H_2+2.5O_2 diluted with 70%Ar [19].

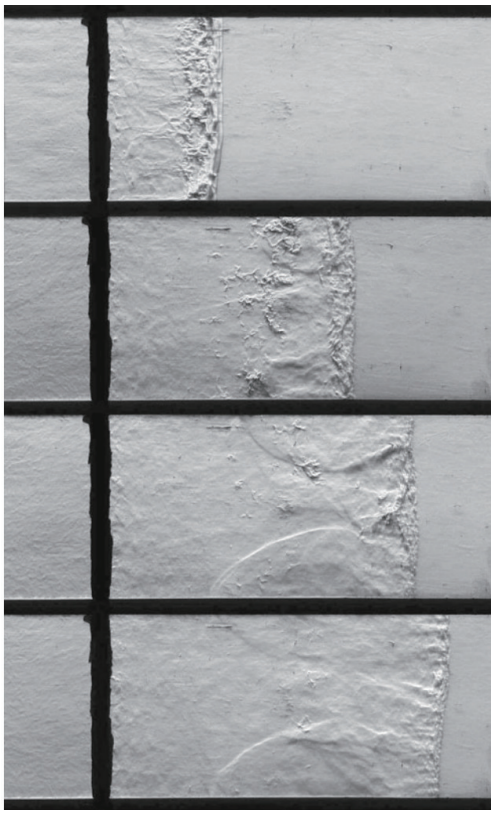

Figure 1.4: The onset detonation was found between the second and the third frame, C_2H_2+2.5O_2+70%Ar [19].

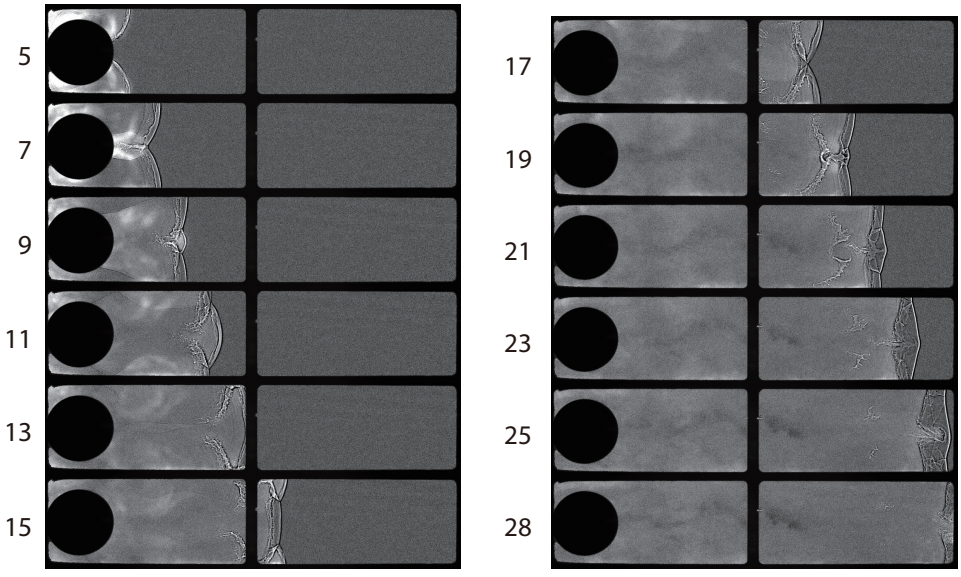

Figure 1.5: Detonation transmission as an attenuated shock-flame complex over a cylinder[26].

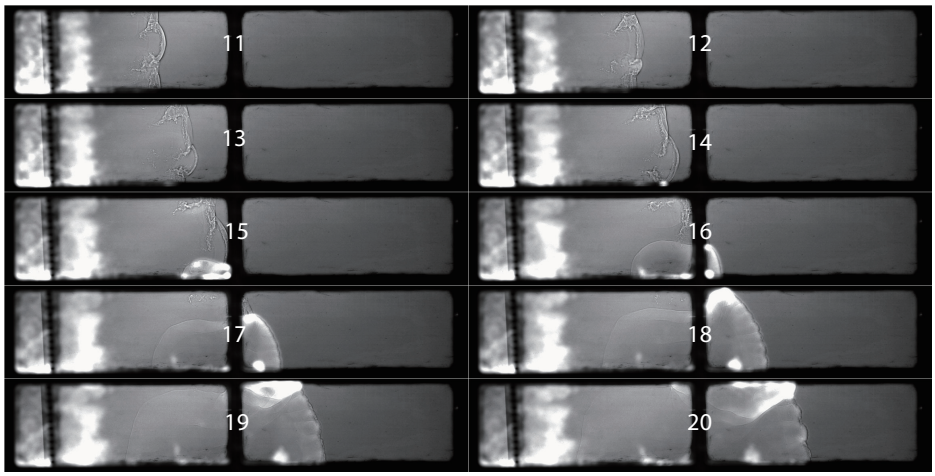

Figure 1.6: Detonation interacts with a column of ten cylinders[37].

As a continuation of Maley's study, Saif used multiple cylinders instead of one large cylinder to construct the blockage section. An example of a typical experiment is shown in Fig.1.6. After the detonation-obstruction interaction, the initial perturbations induced by the obstacle geometry gave rise to a re-organization of the leading shock to fewer triple points. An irregular reaction zone resembling the structure of the front in Maley's experiments was observed.

Detonations or deflagrations with a sonic condition behind them are called Chapman-Jouguet (CJ) detonations or CJ deflagration [22]. It has been suggested that the flame burning velocity prior to transition to a detonation reaches the Chapman-Jouguet(CJ) deflagration speed [23, 33]. This corresponds to the maximum burning velocity admissible for a steady solution [23]. Once the burning velocity exceeds the CJ deflagration, only unsteady solutions exist with strong pressure gradients. Forward facing compression waves are then in phase with the flame and amplify, eventually causing transition to detonation [34].

Furthermore, steady CJ deflagrations have also been observed in obstructed tubes for high obstructions not permitting the final transition to detonation by Chue et al. [7]. Such stable flames in this state are said to exist in the "choking regime". Figure 1.7 compares experimental "choked" flame speeds with CJ-deflagration speeds. The experiments are conducted in blocked shock tubes with blockage ratio of 0.43. The choked flame speeds have been recorded and compared with CJ speeds by Chue et al. Their experiments show good agreement with CJ-deflagration assumption, which indicates the existence of steady CJ deflagration. Valiev et al. [49] further studied DDT in narrow channels and found the last quasi-steady stage before the flame changing to the detonation seems to be a CJ deflagration. It has also been argued by Chao [6] and Radulescu [34] that the quasi-steady

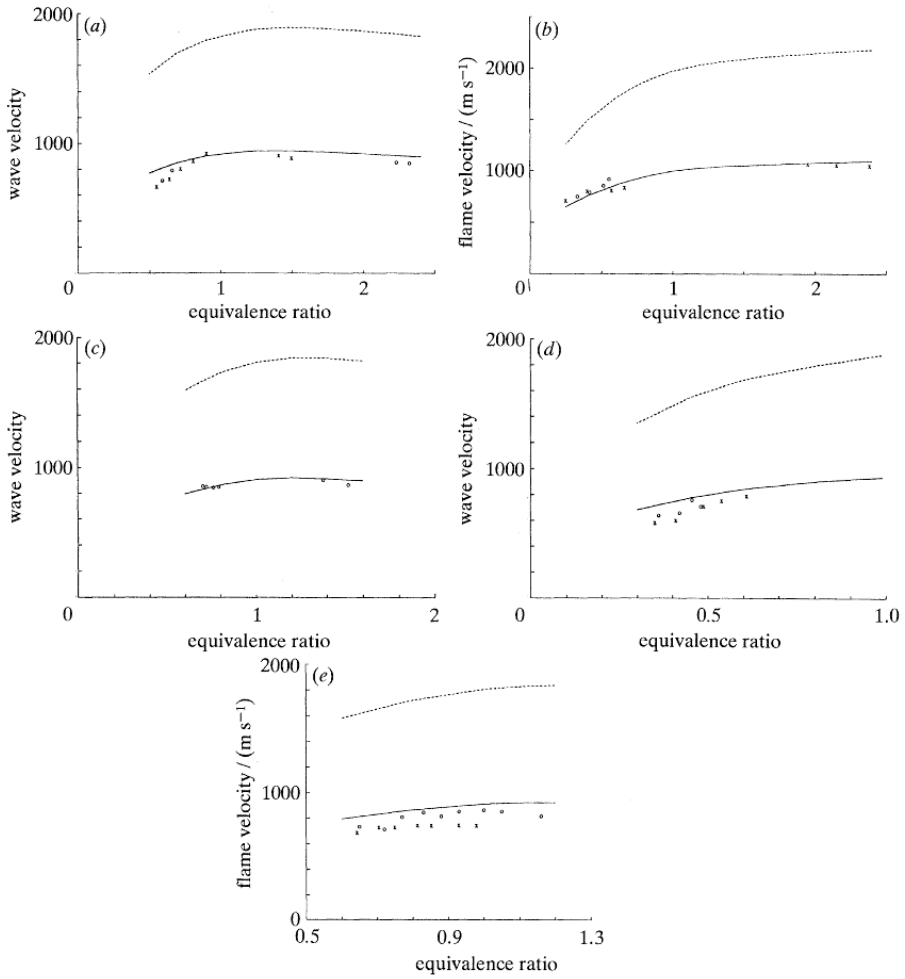

Figure 1.7: Comparison of experimental chocked flame speed with theoretical CJ deflagration and detonation speed. Circle, diameter=15 cm; cross-section, diameter=5 cm. a)Ethylene-air mixture; b)Hydrogen-air mixture; c) propane-air mixture; d) acetylene-air mixture; d)Methane-air mixture. Dash line, CJ-detonation speed; solid line, CJ-deflagration speed[7].

regimes prior to the detonation formation in the problem addressed in current work are CJ deflagrations. It appears that the CJ-deflagration stage is a critical steady speed that a flame can reach prior to transition.

In view of the indirect past observations discussed above, the following question arises: *Are the quasi-steady waves in the detonation initiation experiments of detonation-obstruction interaction problems CJ deflagrations?*. This is the first question addressed in the present thesis.

On the other hand, Maley's work revealed that the shock reflection in methane drives strong jets behind periodically formed Mach shocks. Such a process could intensify hotspot formation [27]. Very recently, Maxwell et al. [28] approached this problem numerically using large-eddy simulation(CLEM-LES) to study the quenched detonation re-initiation process. It was found that the turbulent speed fluctuations induced by gasdynamic heating from triple point collisions plays a very important role for the fast flame amplification to a detonation. Therefore, the study of the relationship between the gasdynamic fluctuations and fast flame acceleration becomes very significant.

Previous experimental studies showed that the hotspots occurred in the induction zone between the reaction front and the leading precursor shock during the re-initiation and the deflagration to detonation transition process. For example, Bhattacharjee [4] found the auto-ignition which evolved to detonation occurs at the hotspots behind the leading shock. It can be inferred that shock-induced hotspots in the fluctuating induction zone usually results in detonation initiation. This scenario could thus be simplified to shock-induced ignition in a induction zone with local fluctuations.

In spite of the very complex and 3D nature of hotspot formation in the fast flame amplification process described qualitatively above, it is of interest to introduce and study a one-dimensional model of the shock induced ignition process. The role of fluctuations will be studied by imposing perturbations of controlled wavelength and amplitude in the induction zone. A significant body of work has been devoted to this problem *without* the presence of fluctuations or with single perturbations, as reviewed below. Thus, the present thesis will build upon this existing knowledge in order to quantify the role of fluctuations in the DDT process.

Previous work has addressed the role of non-homogeneities on detonation initiation when a single hotspot was present. For example, Montgomery et al [32] numerically investigated the 1D ignition with temperature and composition gradient. Chue et al. [8] simulated the shock-induced ignition with density perturbations. The acceleration of fast flames following shock induced ignition in the absence of perturbations have been studied extensively by Sharpe and Short[39], who focused on the temperature gradient effect on shock-induced ignition. Their study analytically established a 1D asymptotic model to describe the shock-induced ignition with non-uniform temperature induction zone. Short[43] numerically investigated the formation of detonations by putting perturbations into the

initial induction zone, but did not consider the precursor shock. Bauwens[1] worked on the temperature gradient effect on shock-induced ignition analytically, but his work focused on the formation of temperature gradient which results from the chemical kinetics. Kapila's[21] research was based on the constant temperature gradient and analyzed the temperature gradient effects on the detonation formation. Other researchers [10, 11, 20, 44] also approached the analytical solution of detonation formation in different initial conditions with asymptotic methods.

Nonetheless, these works did not take the continuous mechanical wave fluctuations into consideration. The second research question of present work is to extend the 1D shock induced ignition model of Sharpe and others in order to study the relation between the acceleration of the fast flame and mechanical perturbations in the reaction zone triggered gasdynamically as a train of waves.

1.3 Scope of the Current Work

The objective of the present thesis is to clarify the process of DDT in its last stages when gasdynamics couple with the turbulent flame motion. Two research questions will be addressed:

1. Are the reaction waves observed prior to the formation of detonations Chapman-Jouguet deflagrations?

2. What is the role of gasdynamic fluctuations leading to hotspot formation of varying amplitude and frequency on the detonation transition process?

The first question will be addressed by examining more closely the vast experimental database provided by Saif [37]. A quasi-1D analytical model will be formulated for the detonation transmission process across a perforated plate, such that the wave speed can be established in terms of an arbitrary burning velocity. Comparison with the experiments of Saif for the lead front speed will thus permit to infer the turbulent burning velocity and determine whether it is close to the CJ condition.

To answer the second question, a shock-induced ignition model has been established. A numerical framework was developed, where an advancing piston in a reactive gas generates a leading shock. The piston is allowed to have fluctuations in its speed, in order to generate gasdynamic disturbances in the reaction zone. The frequency and amplitude of these disturbances can be controlled, in order to clarify their effect on the fast flame acceleration.

To better analyze the gasdynamic problem, inert simulations have also been run. The inert simulation mapped the temperature distribution inside the induction zone behind the leading shock.

The thesis is organized as follows: Chapter 2 addresses the first research question. The second research question is addressed in the remainder of the thesis. Chapter 3 provides the definition of the mathematical model solved and the numerical methods used to find the solutions. Chapter 4 provides the results of inert calculations. Chapters 5 and 6 provide the results for ignition evolution in two reactive mixtures. The presentation of these results is followed by general discussions and a summary of the contributions to knowledge provided by this work.

Chapter 2

Gas Dynamic Model for CJ Deflagrations in a Detonation Transmission Problem

2.1 Detonation Decoupling Problem

As discussed in the introduction, the detonation-obstruction interaction may result in the decoupling between the leading transmitted shock and the transmitted reaction front (e.g., Fig.1.5 and Fig.1.6). The leading shock would slow down after such interaction. A visible reaction front could be observed following the transmitted shock, but fails to sustain the transmitted shock to form a detonation. One of the research questions raised in Chapter 1 is predicting the reaction front speed relative to the gases in front of it (i.e., the burning velocity) and classify the combustion mode in this stage. Since the incoming flow is not static but accelerated by the leading shock, one needs to know the post shock state before calculating the reaction speed. An alternative view is to assume the reaction speed and calculate the transmitted shock speed. Since the shock speed can be measured accurately in the experiments, this procedure can infer the desired flame speed.

2.2 Inert Gasdynamic Model Formulation

In order to solve the reaction problem, inert gasdynamics was first studied by considering a shock wave interacting with obstacles in a shock tube. After the interaction, a reflected shock and a transmitted shock are generated. A numerical experiment was conducted to clarify the structure of the shock-cylinder interaction. A typical result is shown in Fig.2.1[34]. The results were obtained using a dedicated in-house software for compressible simulations (MG). An incident shock (not shown in the figure), initially propagated with Mach number of 6.2 and interacted with a half cylinder. The cylinder is placed at x=0 and had a diameter of 0.75 that of the channel height. The latter was used as characteristic length for non-dimensionalization. The height of the numerical experiment section is 1

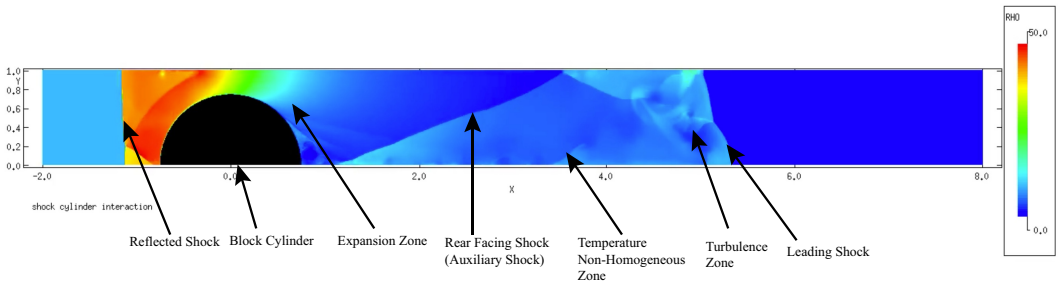

Figure 2.1: 2D simulation on shock-cylinder interaction[34], non-dimensional density plot.

(dimensionless). The figure records density distribution after an incident shock interacting with a half cylinder. One is able to observe that a reflected shock wave propagates to the left after the interaction. The pressure becomes high in the convergent area after the reflected shock. There are also some transverse shock waves following the reflecting shock. Such transverse shock waves are formed by the 2D interaction. The gas above the cylinder first converges above the upstream part of the cylinder, and then diverges above the downstream part of the cylinder. In the convergent section the flow is subsonic. If the open ratio (throat cross section area divided by total cross section area) is low enough, the gas at the throat would retain a Mach number of 1. The right divergent section will further accelerate the gas and form supersonic flow (Expansion Zone in Figure 2.1). Behind the isentropic expansion zone, there are several oblique shocks facing to the rear to re-compress the over-expanded supersonic gas. There is a transmitted shock leading the gasdynamics structures in the whole transmitted section. There is a complex turbulent zone attached to the transmitted leading shock, which separates the gas shocked by incident shock and by transmitted shock. These features are necessary to be modeled.

In order to model the interaction in quasi-1D, two assumptions have to be made: (1) the transverse effects of the gasdynamic structures could be reasonably approximated in a transverse average sense; (2) longitudinally, the series of shock waves propagating in same direction needs to be combined in one single shock wave. For the transverse shocks behind the reflected shock, their longitudinal component can be incorporated into the reflected shock. Similarly, the oblique shock system after the obstacle will be equivalently replaced by a coalesced rear-facing auxiliary shock while neglecting their transverse effects. Nevertheless, the isentropic convergent-divergent section will not be neglected in the quasi-1D model. Furthermore, the turbulence zone is not resolved but rather modeled as a jump across a contact surface. As a result, such a complicated 2D inert gasdynamic system for an incident shock passing over an obstacle can be modeled in quasi-1D by a right-propagating transmitted shock, a following contact surface, a rear-facing auxiliary shock, a convergent-divergent area, and a left-propagating reflected shock, as shown in detail in Fig.2.2.

To test the inert gasdynamic model, the 2D numerical simulation results of the previous shock-cylinder interaction were compared with the results predicted by this model with the

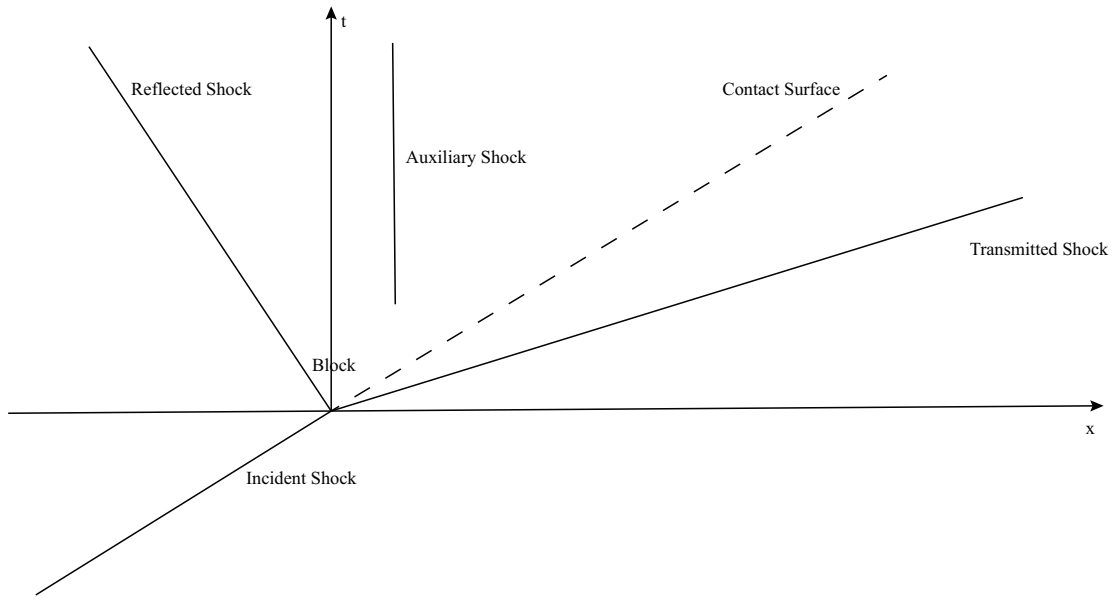

Figure 2.2: Inert model structure in x-t diagram.

same incident shock. Figure 2.3 shows the evolution of the numerically calculated Mach number of the transmitted shock along the top wall and the bottom wall compared with the predictions made with the inert gasdynamic model. The simulation is the same one as what is in Fig.2.1. It can be seen that the model predictions are in a very good agreement with the 2D numerical simulations, suggesting a good reliability of this model.

2.3 Reactive Model Formulation

Very recently, Saif experimentally conducted a systematic study on detonation waves passing across a column of cylindrical obstacles [37, 38]. Figure 2.4 shows one of his experimental results illustrating the evolution of detonation passing the obstacles. From the shadowgraph photographs, it can be seen that there is an additional reaction front behind the leading shock, which means an extra combustion wave should be added into the previously established inert gasdynamic model.

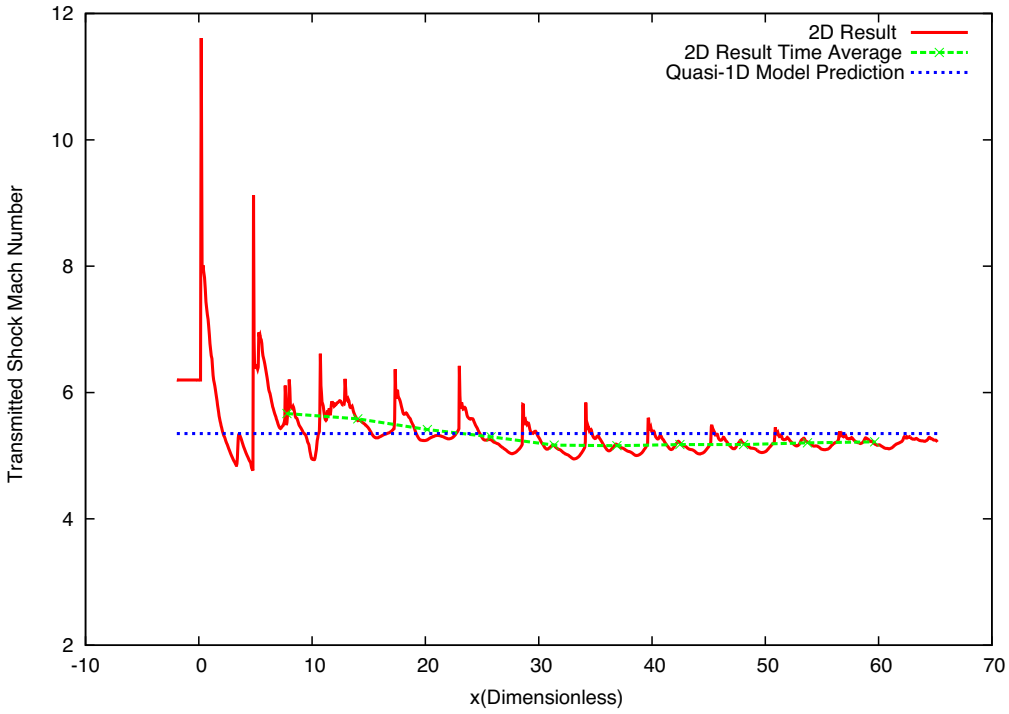

Figure 2.3: Comparison between the transmitted shock speed from model prediction and from numerical experiment[34].

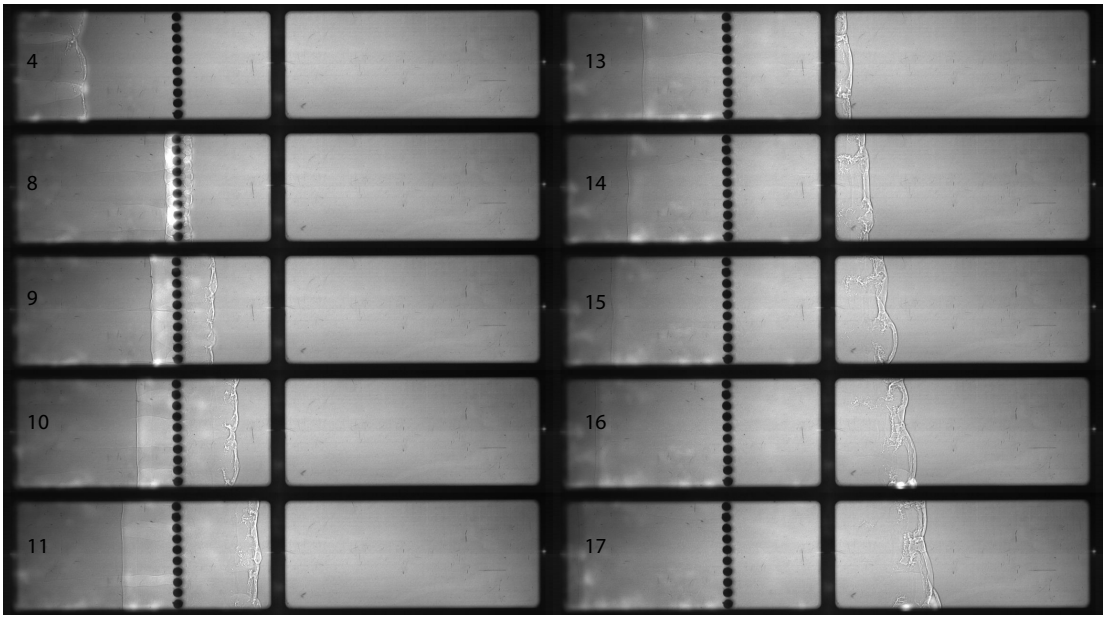

Figure 2.4: Sequence of shadow-graph frames illustrating the transmission of a detonation past a row of cylinders, giving rise to a fast flame complex; methane and oxygen mixture.[37].

Figure 2.5 demonstrates the wave system involved in the simplified quasi-1D reactive gasdynamic model. It comprises a transmitted leading shock, a combustion wave (assumed as a CJ deflagration wave), a contact surface, an auxiliary shock, a converging-diverging section, and a left-propagating reflected shock. In other words, the reactive model added a reaction front between the contact surface and the transmitted shock.

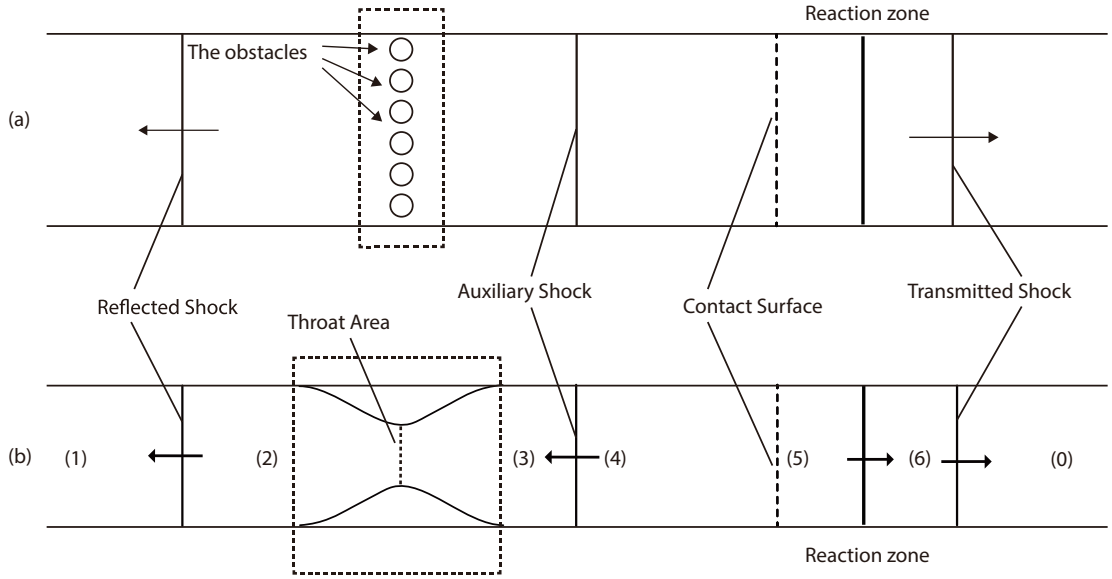

Figure 2.5: Gasdynamic system: (a) sketch of experimental setup and (b) sketch of idealized model.

Figure 2.6 shows the corresponding x-t diagram. Noteworthy is that the blockage ratio (75% and 95% in our study) is high enough to assume a choked flow at the throat of the convergent-divergent section. In Fig.2.5 (b), the state 0 is ambient state. The state 1 is the post incident detonation state with burnt gas. The flow in state 2 is subsonic and accelerates in the convergent-divergent nozzle towards supersonic in state 3. The gas in state 4 contains the reacted gas which has been re-compressed by the auxiliary shock. The gas in state 5 is reacted through the Chapman-Jouguet deflagration. The state 6 is the induction zone.

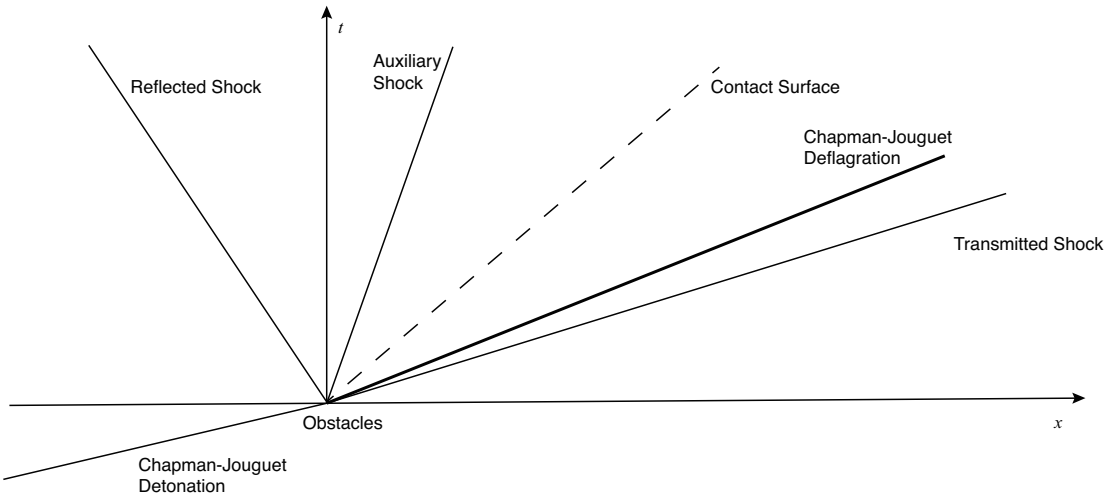

Figure 2.6: x-t diagram showing the characteristics evolving in reactive model.

2.4 Location of the Auxiliary Shock

In this model, there would be two different scenarios regarding the position of the auxiliary shock, i.e., located inside the divergent section or outside the throat area. If the auxiliary shock is weak but the flow speed at the nozzle exit is high enough, the auxiliary shock will be blown downstream, although it is a left facing shock (Figure 2.7 a). When the auxiliary shock is strong enough, the shock can be stabilized in the divergent section (Figure 2.7 b). For the moving auxiliary shock, the expansion gas is always supersonic. Nevertheless, in the fixed auxiliary shock scenario, the supersonic gas only expands partially and is compressed to the subsonic state by the auxiliary shock. In the detonation problem, the leading shock is always a strong shock, indicating that the auxiliary shock is always blown downstream. For the inert problem, when the incident shock is weak, the auxiliary shock may stabilize inside the divergent section.

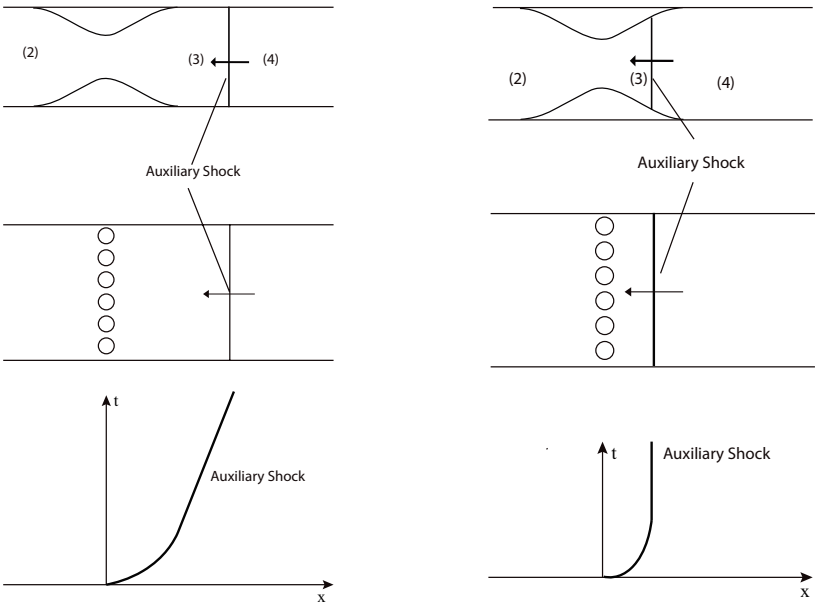

Figure 2.7: Two types of auxiliary shock:a) moving auxiliary shock and b) fixed auxiliary shock.

2.5 Governing Equations for Substructures

The reflected shock, auxiliary shock and transmitted shock are treated using the shock-condition equations:

$$\frac{u_2 - u_1}{c_1} = \frac{2M^2 - 2}{(\gamma + 1)M}, \tag{2.1}$$

$$\frac{\rho_2}{\rho_1} = \frac{(\gamma + 1)M^2}{(\gamma - 1)M^2 + 2}, \tag{2.2}$$

$$\frac{p_2}{p_1} = \frac{2\gamma(M^2 - 1)}{\gamma + 1} + 1. \tag{2.3}$$

where the subscript 1 refers to the non-shocked state. The subscript 2 represents the shocked state, which is unknown and is controlled by the shock Mach number M. Moreover, u, p, ρ and γ are particle velocity, pressure, density and isentropic expansion factor respectively.

The isentropic relations are applied for the convergent-divergent area with a sonic throat:

$$\frac{A}{A^*} = \frac{1}{M}\left[\left(\frac{2}{\gamma + 1}\right)\left(1 + \frac{\gamma - 1}{2}M^2\right)\right]^{\frac{\gamma + 1}{2(\gamma - 1)}}, \tag{2.4}$$

where A is the maximum cross section area, and A^* is throat open cross section area. It is assumed that the throat section is at sonic condition with $M^* = 1$. The states through this convergent-divergent section can be calculated as follows:

$$\frac{p_2}{p_1} = \left[\frac{1+\frac{\gamma-1}{2}M_1^2}{1+\frac{\gamma-1}{2}M_2^2}\right]^{\frac{\gamma}{\gamma-1}} \tag{2.5}$$

$$\frac{\rho_2}{\rho_1} = \left(\frac{p_2}{p_1}\right)^{\frac{1}{\gamma}} \tag{2.6}$$

$$\frac{c_2}{c_1} = \left(\frac{\rho_2}{\rho_1}\right)^{\frac{\gamma-1}{2}} \tag{2.7}$$

The reaction zone is considered to be a Chapman-Jouguet deflagration. It is modeled as a gasdynamic discontinuity with different specific heat ratios(isentropic expansion coefficient) [15, 22] for the reactants and products. Once the specific heat ratio of the product has been estimated (using CEA CJ detonation product calculation[29]), Eq. 2.8 below gives the changes in specific volume across the deflagration wave or detonation wave. The conservation laws are used to calculate the pressure and velocity changes across the deflagration or detonation waves, in terms of the specific volume change,

$$v_b = (\gamma_b - 1)\left(\frac{q}{\gamma_b p_b} + \frac{\gamma_{ub} v_{ub}}{\gamma_b(\gamma_{ub}-1)}\right) \pm (\gamma_b - 1)$$
$$\sqrt{\left(\frac{q}{p_{ub}}\right)^2 + 2\left(\frac{\gamma_{ub}}{\gamma_b(\gamma_{ub}-1)} - \frac{1}{\gamma_b^2-1}\right)\frac{q v_{ub}}{p_{ub}} + \frac{\gamma_b^2-\gamma_{ub}^2}{\gamma_b^2(\gamma_{ub}-1)^2(\gamma_b^2-1)} v_{ub}^2}. \tag{2.8}$$

In the above equation, the plus branch represents the CJ-deflagration condition and the minus branch represents the CJ-detonation condition. γ_{ub} is the isentropic expansion coefficient for reactants and γ_b for products; v_{ub} is the specific volume for reactants and v_b for products; p_{ub} is the pressure for reactants; and q is heat of reaction. The only property required for the products is the isentropic expansion coefficient γ_b. CEA (a gasdynamic equilibrium software) Chapman-Jouguet detonation calculator [29] was used to estimate such coefficient, since this coefficient would not change significantly with the small amount of thermodynamic property changes.

The post-deflagration pressure can be computed by using the reacted specific volume, v_b, which is:

$$\frac{p_b}{p_{ub}} = \frac{\frac{2q}{p_{ub}v_{ub}} + \frac{\gamma_{ub}+1}{\gamma_{ub}-1} - \frac{v_b}{v_{ub}}}{\frac{(\gamma_b+1)v_{ub}}{(\gamma_b-1)v_b} - 1}. \tag{2.9}$$

Once the two thermodynamic properties (specific volume and pressure) have been obtained, the complete thermodynamic states could be obtained using the ideal gas law.

2.6 Gas Parameters and Solution Methodology

Independent chemical equilibrium calculations were conducted with the NASA CEA program to obtain the CJ detonation speed, and the isentropic exponents in the unburnt and burnt gases. These values were assumed to be constant in the remainder of the calculation. The heat release was also extracted from the chemical equilibrium calculations by requiring that the correct CJ detonation Mach number should be predicted by the two-gamma CJ detonation model.

The solution was obtained by sequentially applying the jump conditions across each discontinuity, as shown in Fig.2.8. The state behind the reflected shock (state 2) was obtained by simultaneously requiring that the flow at the throat be chocked. State 3 was obtained from the isentropic relations in terms of state 2. It is not possible to solve states 4 to 6 directly, since the auxiliary shock strength and transmitted shock strength are unknown. Instead an iterative procedure was needed. A guess was first made for the auxiliary shock strength, which permitted obtaining the gas state at the left side of the contact surface. The strength of the transmitted shock was also guessed, in order to obtain the post shock gas state (state 6). The CJ deflagration solution provides the information for state 5. The two guessed values for the shock strengths were updated until states 4 and 5 had the same velocity and pressure. If the velocity and pressure are not matched, the bisection method was implemented with a large initial solution range, in order to find a proper auxiliary shock strength and transmitted shock strength.

2.7 Results and Discussion

2.7.1 Predicted wave speed

The model provides predictions for the transmitted leading shock wave speeds of two different assumptions: inert and CJ deflagration. The calculated results for a stoichiometric propane and oxygen at an initial pressure of 8.5 kPa are shown in Fig.2.9. The higher curve shows the predicted speed for a reactive case using the CJ deflagration assumption. The lower curve shows predicted speeds for an inert case. For both cases, the wave speeds reduce as the blockage ratio increases.

2.7.2 Comparison with Experiments

Table 2.1 shows the predicted transmitted wave speeds corresponding to the experimental conditions reported by Saif [37]. The results of experiments conducted at 75% and 90% blockage ratio with five different mixtures reported by Saif [37] have been compared with the model predictions in this table. One can see that the model only predicts a

Table 2.1: Model prediction for parameters observed in experiments by Saif [37].

Mixture	Blockage Ratio	Ambient Pressure	Transmitted wave speed CJ-Deflagration Solution	Transmitted wave speed Quenched Solution	Deflagration speed in CJ-Deflagration Solution
CH_4+$2O_2$	75%	3400Pa	1486m/s	1039m/s	328m/s
		11000Pa	1517m/s	1058m/s	334m/s
	90%	10300Pa	1118m/s	812m/s	207m/s
		15800Pa	1126m/s	817m/s	208m/s
C_3H_8+$5O_2$	75%	3400Pa	1443m/s	987m/s	272m/s
		3800Pa	1445m/s	989m/s	272m/s
	90%	4100Pa	1060m/s	758m/s	170m/s
		7600Pa	1071m/s	765m/s	171m/s
$2C_2H_6$+$7O_2$	75%	2400Pa	1449m/s	1000m/s	291m/s
		6200Pa	1474m/s	1015m/s	294m/s
	90%	6200Pa	1082m/s	778m/s	183m/s
		11000Pa	1093m/s	784m/s	184m/s
C_2H_4+$3O_2$	75%	3400Pa	1462m/s	1011m/s	306m/s
		6900Pa	1482m/s	1023m/s	309m/s
	90%	4100Pa	1079m/s	778m/s	190m/s
		9000Pa	1095m/s	788m/s	191m/s
$2C_2H_2$+$5O_2$	75%	9700Pa	1135m/s	827m/s	324m/s
		11000Pa	1138m/s	829m/s	324m/s
+21Ar	90%	11000Pa	850m/s	644m/s	200m/s
		18000Pa	856m/s	649m/s	201m/s

weak dependence of wave speed on the pressure. Figure 2.10 shows a comparison between experimental data, and lead shock speed predicted by the CJ deflagration model at a blockage ratio of 75%. The results characterize the re-initiation and failure scenarios after detonations passing the cylindrical obstacles. An exception exists for the argon diluted acetylene-oxygen mixture since no re-initiation phenomena were found in the experiments in the studied pressure range. For the re-initiation cases, i.e., at high pressures, the comparison was established between the transmitted wave speeds both from experiments and the corresponding model predictions. The bottom black horizontal line is the prediction speed from the model. One should note that the model provides only one solution for each ambient pressure cases. This is because the energy release in the self-similar model has been non-dimensionalized by the ambient $p_0 v_0$ which is only related to T_0. Since the heat release and T_0 does not change, the results do not perform any difference when change the initial pressure. It is not meaningful to compare the experimental result with quenched solution, because all the experimental cases are re-initiated.

From the comparison, it can be seen that the model predicts very well the transmitted wave speeds for the re-ignition cases. For the methane oxygen case, conclusions are more difficult because of the spread in experimental data.

On the other hand, the model under-predicts the transmitted wave speed of the quenched detonations for most of the mixtures except argon diluted acetylene oxygen. This discrepancy is due to the slow quenching process or incomplete quenching. In Saif's experiments, where detonations failed, the reaction did not stop immediately in the divergent section and needed enough time to decay to a laminar flame with negligible burning velocity [37]. The transmitted shock wave kept slowing down and still had a tendency to decay at the end of experimental test section. The experimental records were not on the fully developed gasdynamic structure in these mixtures. The transmitted wave speed in argon-diluted acetylene-oxygen mixture is much more stable, which could be considered as a fully developed quenched flow. The model predicted this case very well. One could also conclude that the diluted mixture takes less time to quench.

Figure 2.11 shows the comparison between the model and the experimental statistics on the leading shock speed for 90% blockage ratio. Different from the 75% blockage ratio case, detonation was experimentally found to quench even at the high pressure in the mixture of argon diluted acetylene oxygen. Their transmitted wave speeds can be very well predicted by the present model. While for the other mixtures, the same observation and conclusion with the case of 75% blockage ratio can be made for the 90% ratio.

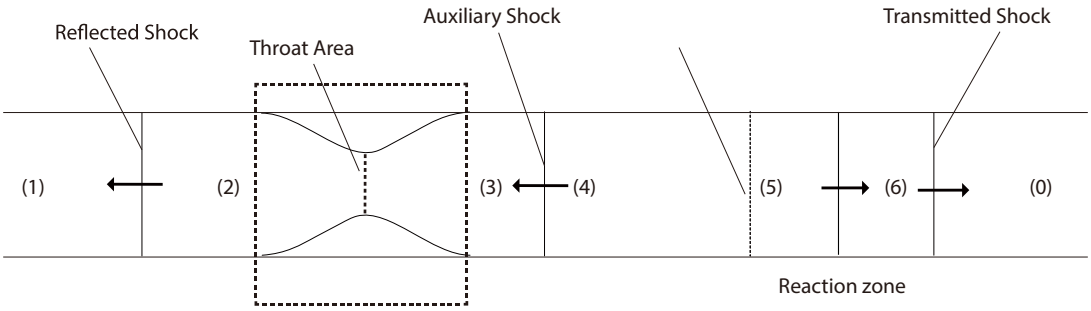

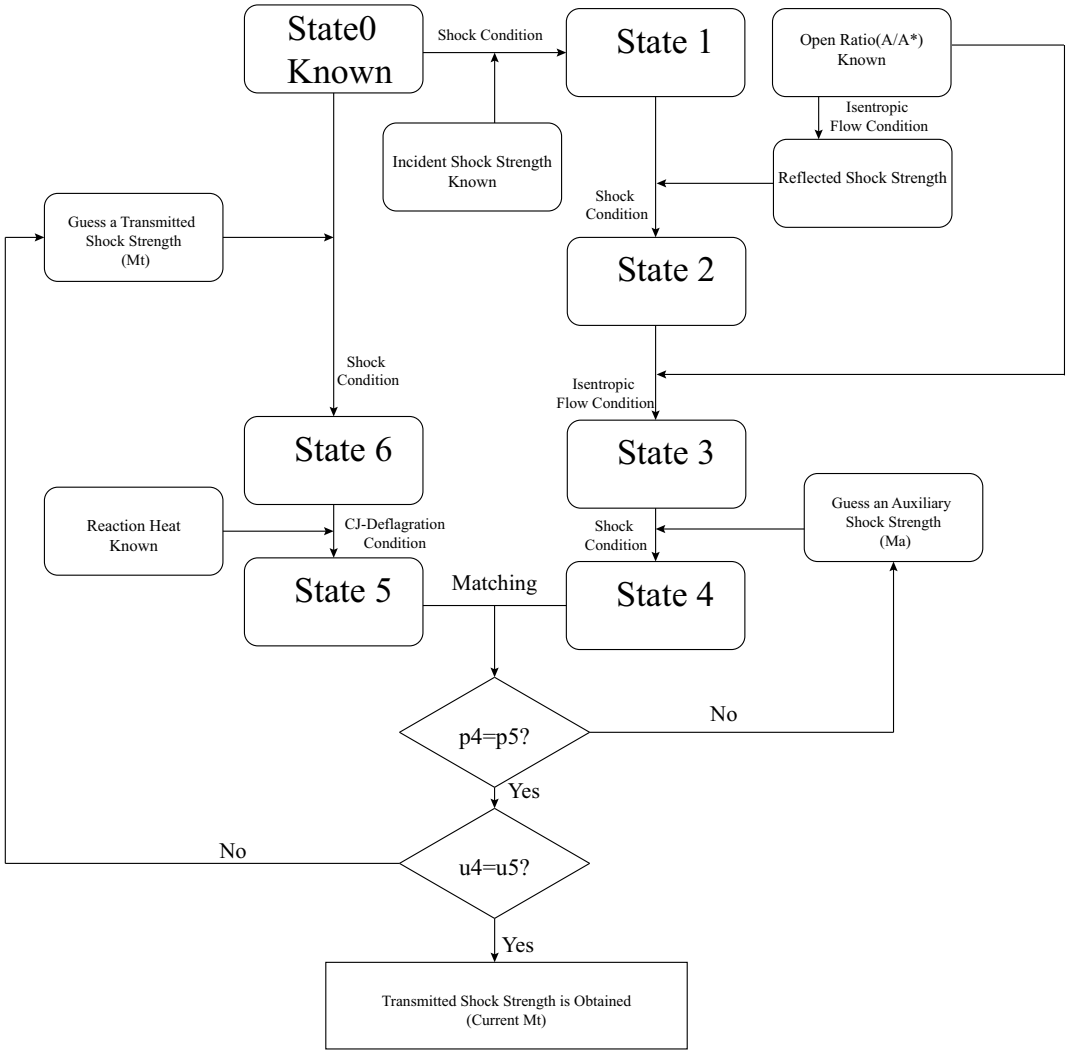

Figure 2.8: Algorithm to seek the transmitted shock strength.

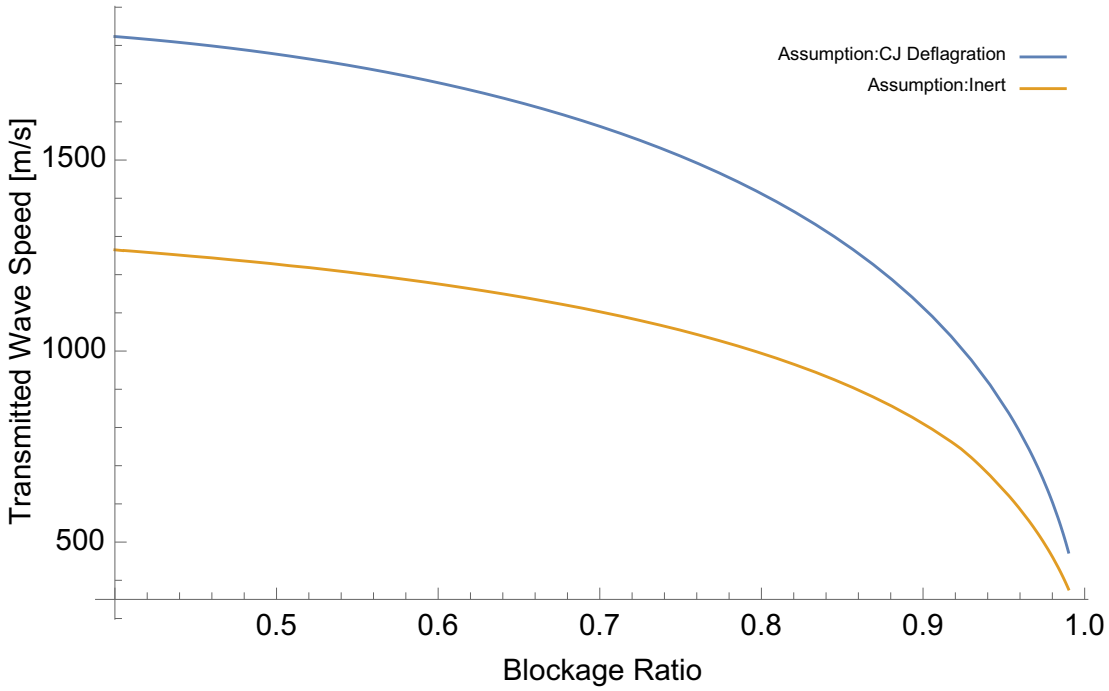

Figure 2.9: Two branches of solution, C_3H_8, 8.5 kPa.

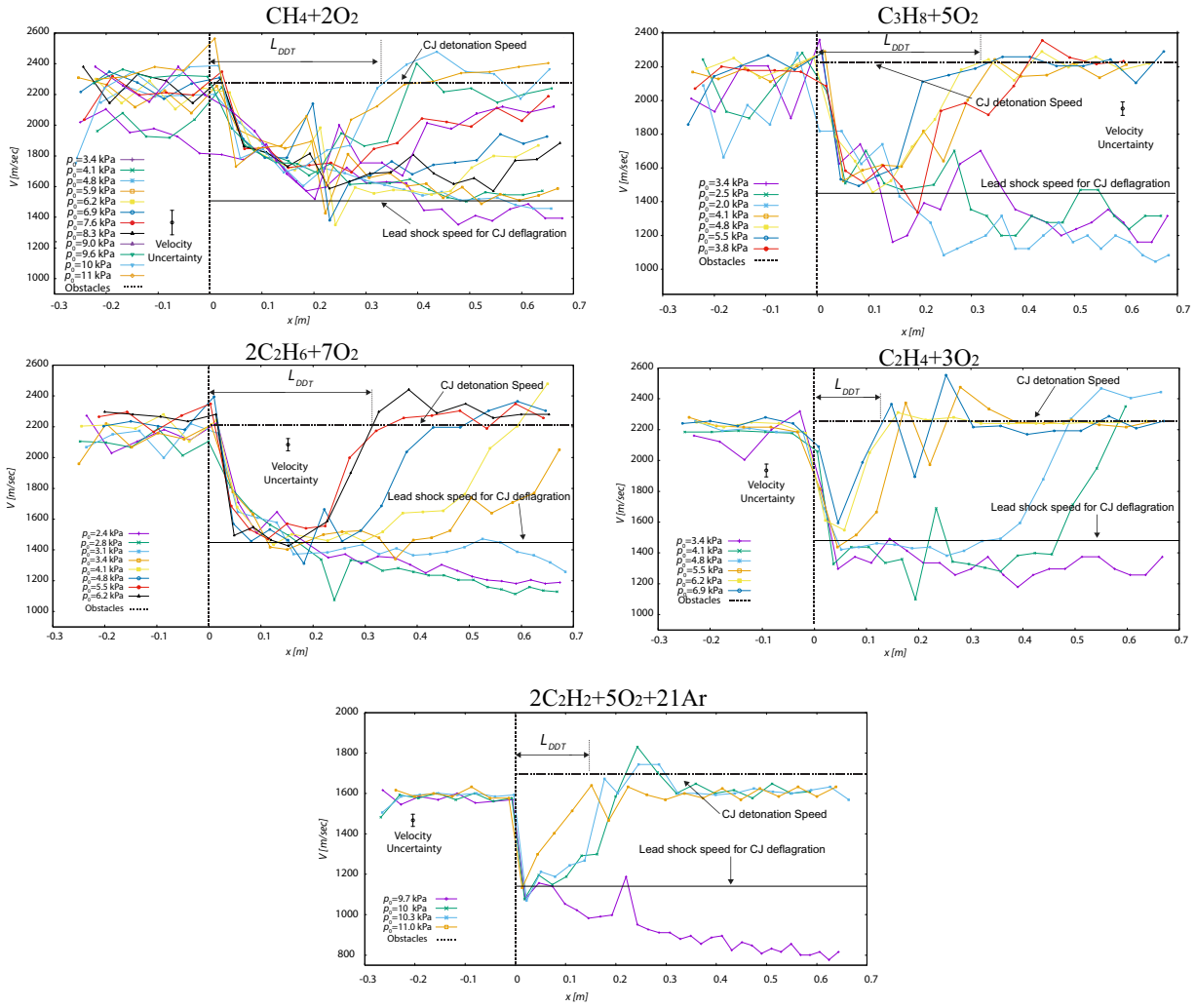

Figure 2.10: Comparison between the model prediction and experimental data at blockage ratio of 75%.

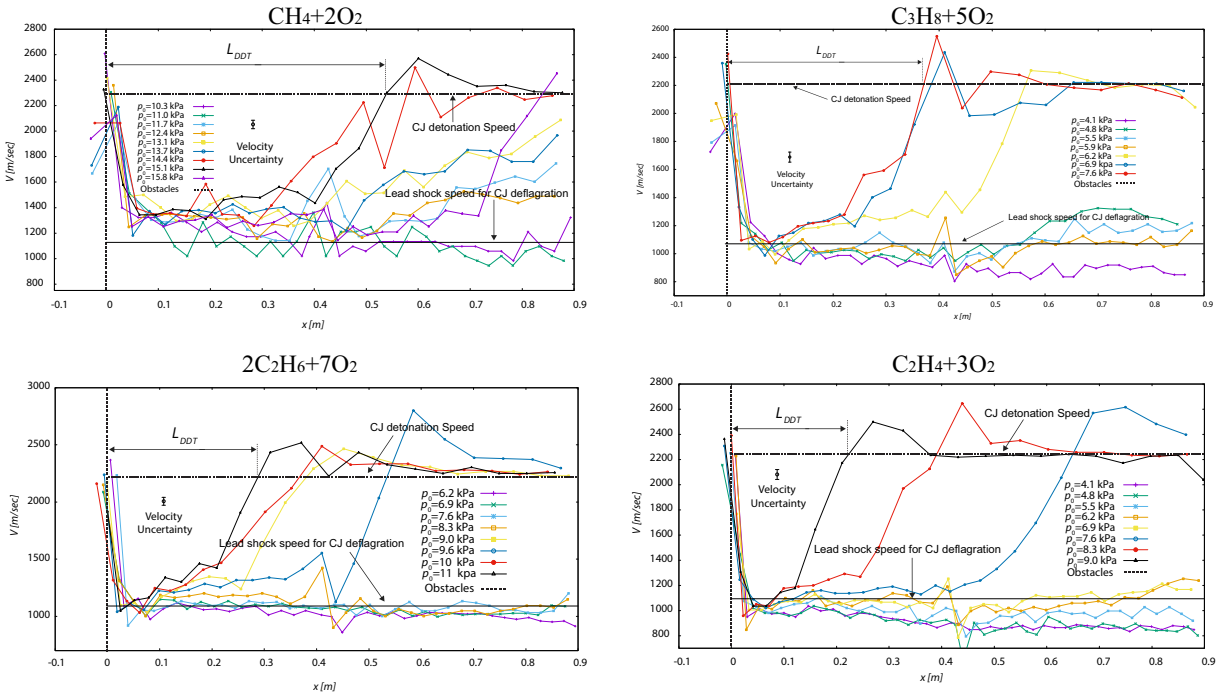

Figure 2.11: Comparison of transmitted shock speed between the model prediction and experimental data in 90% blockage ratio.

Chapter 3

1D Lagrangian Numerical Model with Detailed Chemistry for Shock Induced Ignition with Mechanical Fluctuations

3.1 Problem Definition

A sufficiently strong shock wave can directly initiate combustion waves in gases by auto-ignition. This phenomenon of shock-induced ignition has considerable significance, since it is closely related with complex detonation phenomenon. First, ignition via shock compression provides one mechanism for self-sustained detonations. Also, auto-ignition behind reflected shocks is sometimes seen in the DDT process, possibly resulting in the onset of detonations. Due to complicated phenomena (e.g., interaction of multiple reflected shocks), the influencing mechanism of this phenomenon on DDT is not yet well understood. Moreover, the quenched detonation by the perforated plate comprises a leading shock and a trailing decoupled reaction front. When the shock is strong enough, it will likely ignite the shocked gases behind, thereby leading to the re-initiation of detonation. Therefore, to examine the roles the shock-induced ignition plays in DDT or detonation re-initiation processes, this section presents a systematic study of this phenomenon with the purpose of revealing the influencing factors that could trigger detonation initiation.

The 1D numerical works of Melguizo-Gavilanes [30] and Sharpe [40, 42] have shown that the ignition can be induced by a shock, which was generated by a moving piston of a constant speed at one end of a tube. Melguizo-Gavilanes' simulation reveals that the ignition reaction front may form a secondary shock, if the energy release is sufficiently fast on induction time scales. Sharpe has developed a 2-step chain-branching kinetic model to asymptotically predict the reaction front acceleration. Nevertheless, multi-dimensional effects, such as transverse shock and turbulence, play important roles in detonation initiation process. The previous numerical approach[43][1][21], which based on the Euler description,

did not take those effects into consideration.

Dziemiska et al. studied the shock induced ignition by 2D simulations [13]. Their study focused on boundary layer effects in the shock-induced ignition. Nonetheless, Dziemiska's work lacks a quantitative relationship between such 2D effects and the DDT. The 2D simulations have too many details which are hard to quantitatively isolate. To numerically investigate such a re-initiation problem without discarding multi-dimensional factors, the present study proposes to impose mechanical fluctuations in the 1D framework to represent the effects of the multi-dimensional structures.

3.1.1 Problem Set-up

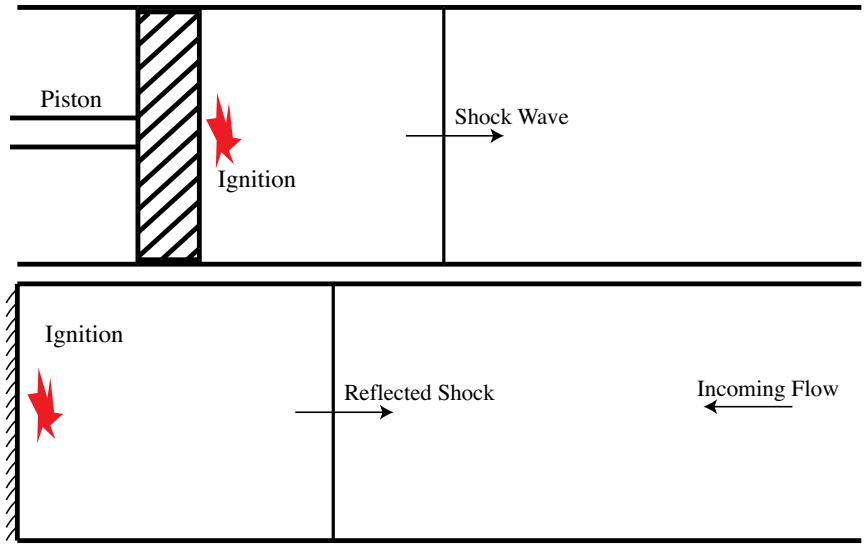

Figure 3.1: Piston driving shock induced ignition and reflected shock induced ignition.

Figure 3.1 shows two typical methods for studying 1D shocks numerically. In the bottom figure, the left end side is a fixed wall, with an initially leftward-moving flow with a constant velocity. A shock is then generated at the left wall and propagates rightwards. In the top figure, a piston moves to the right with a constant speed into a static gas. A shock wave is generated at the piston and propagates towards the right. It is easy to see that the two set-ups are the same if one considers a change of reference frame .

Most researchers use the second set-up to study the shock induced ignition problem. The advantage of this setting is that the boundary conditions are easy to handle numerically in Eulerian coordinate. Nevertheless, this thesis uses the moving-piston set-up, because a moving piston is more convenient to generate mechanical fluctuations, which are the important aspect of this study.

3.1.2 Mechanical Fluctuation Definition

The mechanical fluctuations are imposed on the left piston boundary condition. The left piston speed is modeled by a sinusoidal function of time in current study as

$$u_p = u_m + A\sin(2\pi f t), \tag{3.1}$$

where u_m is the mean speed of the piston, A is the fluctuation amplitude and f is the fluctuation frequency.

3.2 General Numerical Framework

The simulation involves compressible reactive flow. The numerical model is thus required to model both the compressible hydrodynamics and chemical kinetics. This framework is constructed in two parts, one is the frozen gasdynamics solver and the other is constant volume full chemistry kinetics solver. An operator-splitting approach is used in the numerical model. Thus, each simulation step contains one frozen gasdynamic step and one chemical step. After each sub-step, thermodynamic properties are passed between the solvers. The precise properties that are exchanged between the two solvers are density, pressure and the specific static internal energy. Since the chemical kinetics does not change the local flow speed, this property is not exchanged. The following two sections explain the specifics of how each solver is implemented.

3.3 Hydrodynamic Numerical Methodology

3.3.1 Lagrangian Scheme

Previous numerical studies on shock-induced ignition often use an Eulerian approach[30, 40, 42]. Nevertheless, it is not convenient to model the fluctuating moving piston in this framework. Instead, a Lagrangian scheme could easily control the piston speed by imposing an appropriate left boundary condition. Thus, the current work adopts the Lagrangian description for numerically investigating the shock-induced ignition phenomenon.

In this Lagrangian scheme, physical space is replaced by a Lagrangian space denoted by the independent variable, ϕ. The Lagrangian space variable ϕ is zero when $t = 0$, $x = 0$. The general relation between x and ϕ is

$$d\phi = \rho dx. \tag{3.2}$$

Thus, the initial coordinate transformation from Euler space to Lagrangian space is

$$\phi(x, 0) = \int_0^x \rho dx. \tag{3.3}$$

When $t > 0$, each mass unit retains the same ϕ value, which gives the inverse coordinate transformation as

$$x(\phi, t) = x(\phi, 0) + \int_0^t u(\phi, t)dt. \tag{3.4}$$

In the Lagrangian system, each part of the continuous gas has its fixed Lagrangian coordinates, ϕ. For the piston problem the left boundary of the whole domain is always at $\phi = 0$. The physical meaning of ϕ could be explained as the amount of gas mass between the left boundary(piston) and a given point.

3.3.2 Governing Equations

The one-dimensional governing equations for this model are three conservation laws. For mass conservation, there is no mass "flowing" in Lagrangian space, which makes the mass inside any volume of the space constant. Nonetheless, different from Eulerian treatments, the size of volumes in Lagrangian space vary with time. Mass conservation is denoted as volume-density relation:

$$\frac{\partial v}{\partial t} - \frac{\partial u}{\partial \phi} = 0. \tag{3.5}$$

Here, v is the specific volume and u is the particle velocity. Momentum conservation in Lagrangian scheme is expressed as

$$\frac{\partial u}{\partial t} + \frac{\partial p}{\partial \phi} = 0. \tag{3.6}$$

In the equation above, p is pressure. The first term represents the momentum increment of each mass unit and the second term gives the net force acting on it. The Lagrangian description of energy conservation is

$$\frac{\partial e_{tot}}{\partial t} + \frac{\partial pu}{\partial \phi} = 0. \tag{3.7}$$

In the equation above, e_{tot} is specific total energy. The only form of energy transfer in this Lagrangian setting is pressure work. The total energy consists of two parts: static internal energy, e, and flow kinetic energy, e_k. Chemical energy is constant during each hydrodynamic iteration. This constant value would be updated after each static chemical simulation. The energy that varies during the hydrodynamic update is the total energy

$$e_{tot} = e + e_k. \tag{3.8}$$

The governing equations for this model are Eq.3.5, 3.6 and 3.7.

3.3.3 Static Internal Energy and Flow Kinetic Energy

The static thermodynamic energy could have a different reference state. A reasonable way to determine the internal energy is directly using Cantera integrated internal energy

function[18] instead of the perfect gas law. This is real gas model:

$$e = \sum_{i}^{n} y_i e_i, \tag{3.9}$$

where y_i is the mass fraction of species "i", and e_i is the specific internal energy for species "i".
This method has been selected to evaluate the static internal energy. To calculate wave speeds for the hydrodynamic flux calculations, the perfect gas law is assumed. The wave speeds from the perfect gas assumption are accurate enough to ensure the stability of the upwind scheme. As this is the only time that the perfect gas law is used, it does not affect the accuracy of converged solutions.
The flow kinetic energy is

$$e_k = \frac{u^2}{2}, \tag{3.10}$$

where "u" is the flow velocity.

3.3.4 Model wave speeds and hyperbolicity

The governing equations can be expressed in the vector form as:

$$\frac{\partial U}{\partial t} + \frac{\partial F}{\partial \phi} = 0, \tag{3.11}$$

with

$$U = [v, u, e_{tot}]^T. \tag{3.12}$$

In order to approximate the wave speeds using the perfect gas relation, the flux vector is approximated as

$$F = \begin{bmatrix} -u & \dfrac{\left(e_h - \dfrac{u^2}{2}\right)(\gamma - 1)}{v} & \dfrac{\left(e_h - \dfrac{u^2}{2}\right) u(\gamma - 1)}{v} \end{bmatrix}^T. \tag{3.13}$$

The flux Jacobian matrix C becomes

$$C = \begin{vmatrix} 0 & -1 & 0 \\ -\dfrac{(\gamma - 1)\left(e_h - \dfrac{u^2}{2}\right)}{v^2} & -\dfrac{(\gamma - 1)u}{v} & \dfrac{\gamma - 1}{v} \\ -\dfrac{(\gamma - 1)\left(e_h - \dfrac{u^2}{2}\right) u}{v^2} & \dfrac{(\gamma - 1)\left(e_h - \dfrac{3u^2}{2}\right)}{v} & \dfrac{(\gamma - 1)u}{v} \end{vmatrix}. \tag{3.14}$$

The eigenvalues of matrix C are

$$\lambda_1 = 0 \tag{3.15}$$

$$\lambda_2 = -\frac{\sqrt{\gamma p v}}{v} = -\frac{c}{v} \tag{3.16}$$

$$\lambda_3 = \frac{\sqrt{\gamma p v}}{v} = \frac{c}{v} \tag{3.17}$$

where c is the wave speed in real space. Since λ_1, λ_2 and λ_3 are always real and distinct, the system is hyperbolic. Upwind finite-volume schemes are well suited for the solution of such conservation laws [24]. This is the technique chosen here. The perfect gas assumptions is only assumed to approximate wave speeds. For inter-cell fluxes, real gas pressures are used.

3.3.5 Discretization

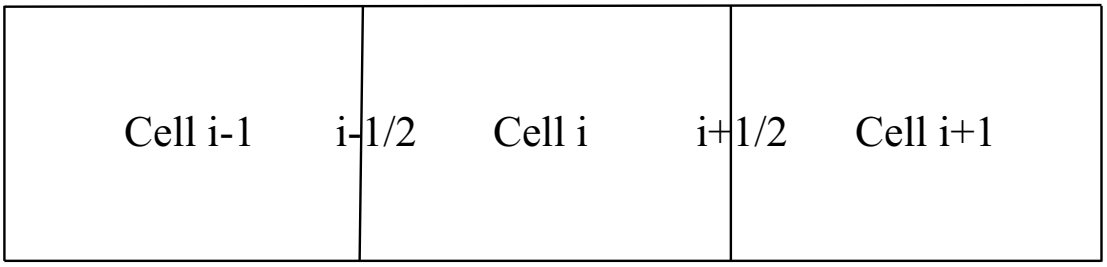

Figure 3.2: Finite volume scheme on 3 cells.

Figure 3.2 shows a portion of the spatial discretization for Eq. 3.11 using 3 cells. At a time t, each cell has an average value for solution vector of $U_{t,i-1}$,$U_{t,i}$ and $U_{t,i+1}$. Integrating equation 3.11 from $\phi_{i-1/2}$ to $\phi_{i+1/2}$ and from t to $t+\Delta t$, the following relationship is found,

$$(U_{t+\Delta t,i} - U_{t,i})\Delta\phi = (F_{t,i-1/2} - F_{t,i+1/2})\Delta t. \tag{3.18}$$

For the cell i, the properties at $t + \Delta t$ can be calculated by its properties at t:

$$U_{t+\Delta t,i} = U_{t,i} + (F_{t,i-1/2} - F_{t,i+1/2})\frac{\Delta t}{\Delta\phi}. \tag{3.19}$$

In the equation above, $\Delta\phi$ is the length of the cell i, while $F_{t,i-1/2}$ and $F_{t,i+1/2}$ represent the flux properties at the left boundary and the right boundary of cell i.

3.3.6 Flux Solver

To obtain the fluxes on the cell boundary, Godunov proposed solving a Riemann problem between the two cells[16]. Exactly solving the Riemann problem at each flux calculation is numerically expensive. Given the errors made in other aspects of a typical solver, approximate Riemann solvers are usually preferable. Roe directly linearized the Jacobian matrix and exactly solved the linearized problem [35]. Harten, Lax and van Leer proposed

an even simpler method that only requires knowledge of the fastest left and right wave speeds [14] [48] (i.e., the HLL scheme). It is the HLL solver that is chosen in the current study. The HLL flux can be expressed as

$$F_{t,i-1/2} = \frac{\lambda^l_{t,i-1/2}\lambda^r_{t,i-1/2}(U^r_{t,i-1/2} - U^l_{t,i-1/2}) + \lambda^r_{t,i-1/2}F^l_{t,i-1/2} - \lambda^l_{t,i-1/2}F^r_{t,i-1/2}}{\lambda^l_{t,i-1/2} - \lambda^r_{t,i-1/2}}. \tag{3.20}$$

The $F^l_{t,i-1/2}$ and $F^r_{t,i-1/2}$ are the flux variables computed from the conservative variables on the left and right side of the interface,

$$F^l_{t,i-1/2} = F(U^l_{t,i-1/2}),$$
$$F^r_{t,i-1/2} = F(U^r_{t,i-1/2}).$$

The λ is corresponding characteristic wave speed.
For a first-order accurate version of this scheme, where the cell average is the only representative of the solution within each cell, the conserved variables near the boundary is the same as the cell average value:

$$U^l_{t,i-1/2} = U_{t,i-1}, \tag{3.21}$$

$$U^r_{t,i-1/2} = U_{t,i}. \tag{3.22}$$

3.3.7 Second-order Spatial Accuracy

The simplest method to improve the accuracy of a simulation is increasing the resolution by increasing the numbers of cells. Nonetheless, this leads to a substantial increase in computational cost. This is partially due to the fact that the size of each time step must decrease as the resolution grows. For stability, the timestep is limited by the time it takes for a wave to traverse a cell. Usually a safety factor, known as the Courant number (CFL),which must be between 0 and 1 is used [12]. The following equation shows the method to evaluate the time step:

$$\Delta t = \frac{CFL\Delta\phi}{|\lambda|_{max}}. \tag{3.23}$$

The total simulation expense is proportional to the product between the total number of cells and total number of time steps. Equation 3.23 implies that the net number of step is proportional to the number of cells in 1D. Thus the time complexity of the 1D Lagrangian simulation is $O(N^2)$.

Another way to increase the accuracy of the solution without worsening the time-step restriction is to increase the sub-cell accuracy of the solution representation [24]. Equations 3.21 and 3.22 provide the method of evaluating the boundary properties in the firs-order scheme. Compared to a first-order approach, the present second-order scheme

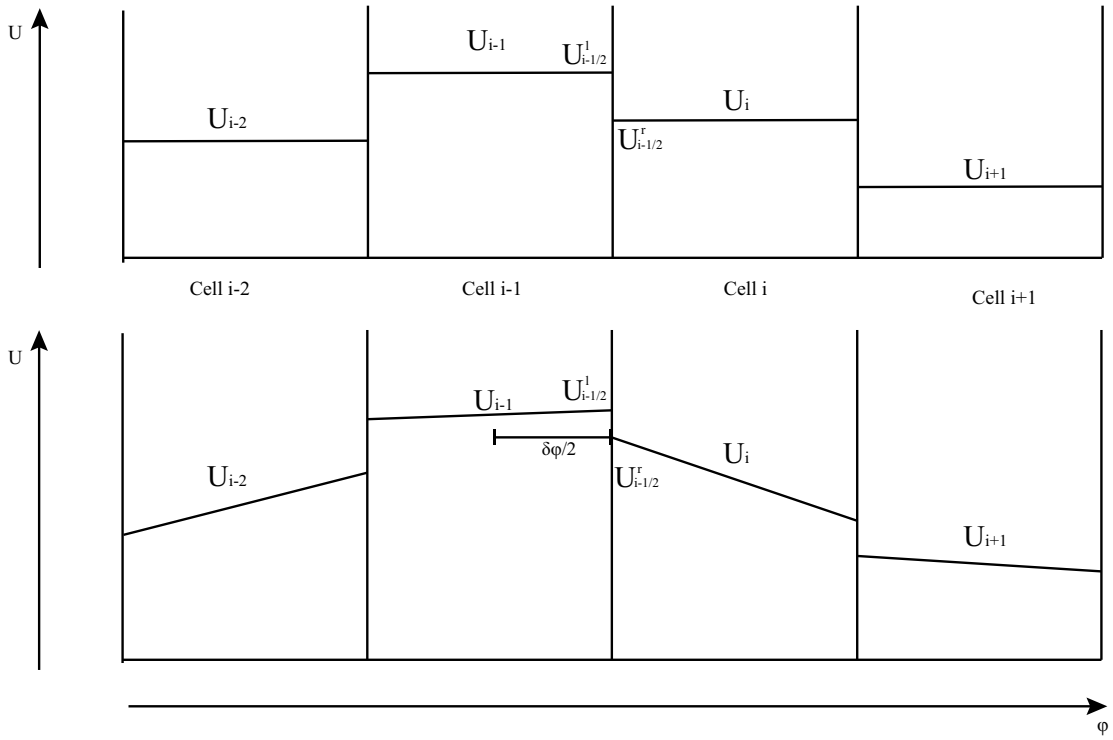

Figure 3.3: Comparison between the solution representation in the first-order spatial differencing(top) and second-order spatial differencing(bottom).

approximates the properties in a cell as a linear function of ϕ instead of a constant. This is illustrated in Fig.3.3. The expression for the solution value at the cell interface becomes

$$U^l_{t,i-1/2} = U_{t,i-1} + k_{i-1}\frac{\Delta\phi}{2}, \tag{3.24}$$

$$U^r_{t,i-1/2} = U_{t,i} - k_i\frac{\Delta\phi}{2}. \tag{3.25}$$

The second order scheme introduces a new variable k_i to describe the slope of $U-\phi$ in cell i. The central scheme evaluates the slope by using the properties on the two adjacent cells:

$$k_i = \Phi(r_i)\frac{U_{i+1} - U_{i-1}}{2\Delta\phi}. \tag{3.26}$$

Here $0 < \Phi(r_i) < 1$ is the numerical slope limiter which transitions between first order and second order. The limiter is necessary, because globally second-order schemes cannot be globally stable. This is a consequence of Godunov's theorem[17]. The first-order scheme can often over-estimate the discontinuity on the cell boundary. This overestimation generates excess numerical dissipation, which oversmears the solution and degrades accuracy. The second-order scheme reduces such over-estimations, but sometimes it may generate artificial solution extrema. These extrema lead to numerical oscillations and solution instability. To avoid the spurious oscillation on the high-order scheme, van Albada limiter has been selected for this numerical framework[50]

$$\Phi(r) = \frac{r^2 + r}{r^2 + 1}, \tag{3.27}$$

$$r_i = \frac{u_i - u_{i-1}}{u_{i+1} - u_i}. \tag{3.28}$$

The simulation is only as accurate as its weakest point. The full advantage of second-order spatial accuracy will not be seen if a first-order temporal scheme is used. Therefore, for this work a predictor-correcting scheme is used. The iteration process from t to $t+\Delta t$ is listed as following:

$$\begin{aligned}
F_{t,i+1/2} &= F(U_{t+\Delta t,i-1}, U_{t+\Delta t,i}, U_{t+\Delta t,i+1}, U_{t+\Delta t,i+2}) \\
U^{1st}_{t+\Delta t,i} &= U_{t,i} + (F_{t,i-1/2} - F_{t,i+1/2})\frac{\Delta t}{\Delta\phi} \\
F'_{t+\Delta t,i+1/2} &= F(U^{1st}_{t+\Delta t,i-1}, U^{1st}_{t+\Delta t,i}, U^{1st}_{t+\Delta t,i+1}, U^{1st}_{t+\Delta t,i+2}) \\
F_{t+\Delta t/2,i+1/2} &= \frac{F'_{t+\Delta t,i+1/2} + F_{t,i+1/2}}{2} \\
U^{2nd}_{t+\Delta t,i} &= U_{t,i} + (F_{t+\Delta t/2,i-1/2} - F_{t+\Delta t/2,i+1/2})\frac{\Delta t}{\Delta\phi},
\end{aligned}$$

where F are the flux vector and U is the conserved variable vector. The first variable subscript represents the time and the second one represents the space or cell number. The first equation above uses flux solver to evaluate the flux at t. It requires conserved

variables from four adjacent cells because the second-order spacial scheme uses three cells to reconstruct each cell, and each flux requires two adjacent reconstructed cells. The second equation provides the first-order temporal accuracy estimation at $t + \Delta t$. Similar to the first equation, the third equation evaluates the flux at $t + \Delta t$ with second-order flux solver. It requires the solution from first-order scheme. The fourth equation is the temporal reconstruction which computes the average flux between t and $t + \Delta t$. The flux result of the fourth equation is with second-order spacial-temporal accuracy. The last equation used this flux to calibrate the marching result.

3.4 Validation of the Hydrodynamic Solver

Two frozen hydrodynamic problems have been adopted to check the reliability of the hydrodynamic solver. The first case is a Riemann problem involving a weak shock and expansion fan, and the other is a strong shock wave problem. For the second problem, the shock wave is generated by a piston on the left boundary of the domain. Their detailed initial conditions are listed in Tables 3.1 and 3.2, respectively. The results calculated from the hydrodynamic solver were compared with the exact solutions obtained from exactly solving the Riemann problems.

Table 3.1: Shock-expansion test settings.

	Left Side	Right Side
Velocity	0	0
Pressurel	2	1
Density	1	0.5
γ		1.4
CFL		0.7
Final Time		0.3
Initial Discontinuity Location:x=1		x=1

Table 3.2: Strong shock test settings.

Initial Velocity	0
Initial Pressure	1.01×10^5 Pa
Initial Temperature	293K
Piston Speed	1500m/s
CFL	0.7
Final Time	0.03
Initial Discontinuity Location	No Initial Discontinuity

Figure 3.4, 3.5 and 3.6 show the comparisons of the calculated pressure, density and velocity with the corresponding exact solutions for the first problem. It is easy to see that

the calculated results are in excellent agreement with the analytical values, suggesting a good reliability of the solver.

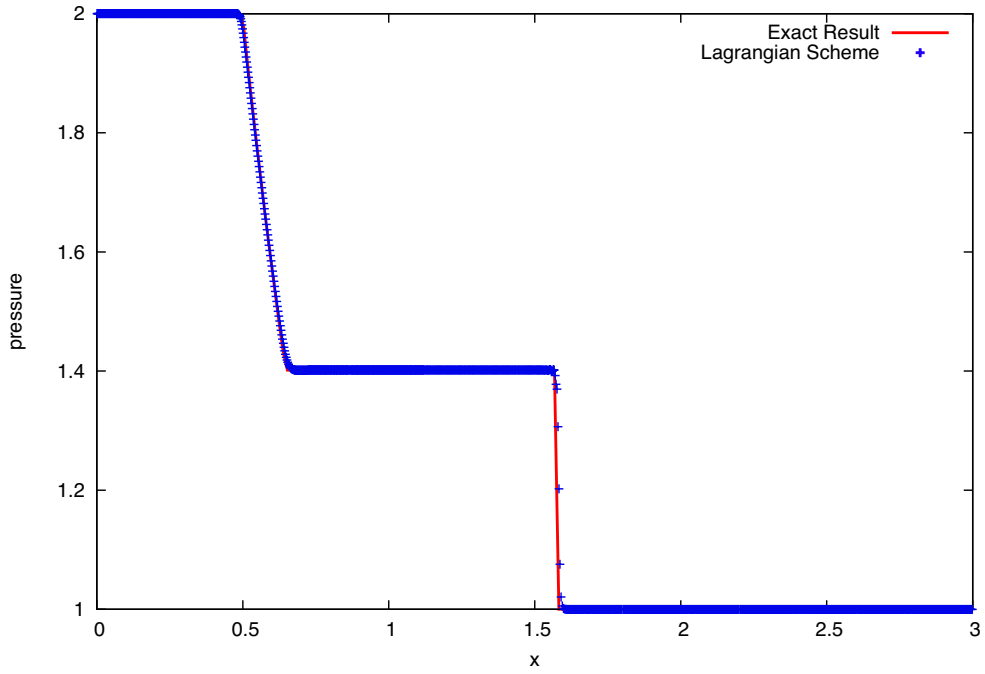

Figure 3.4: Pressure profile for shock-expansion problem.

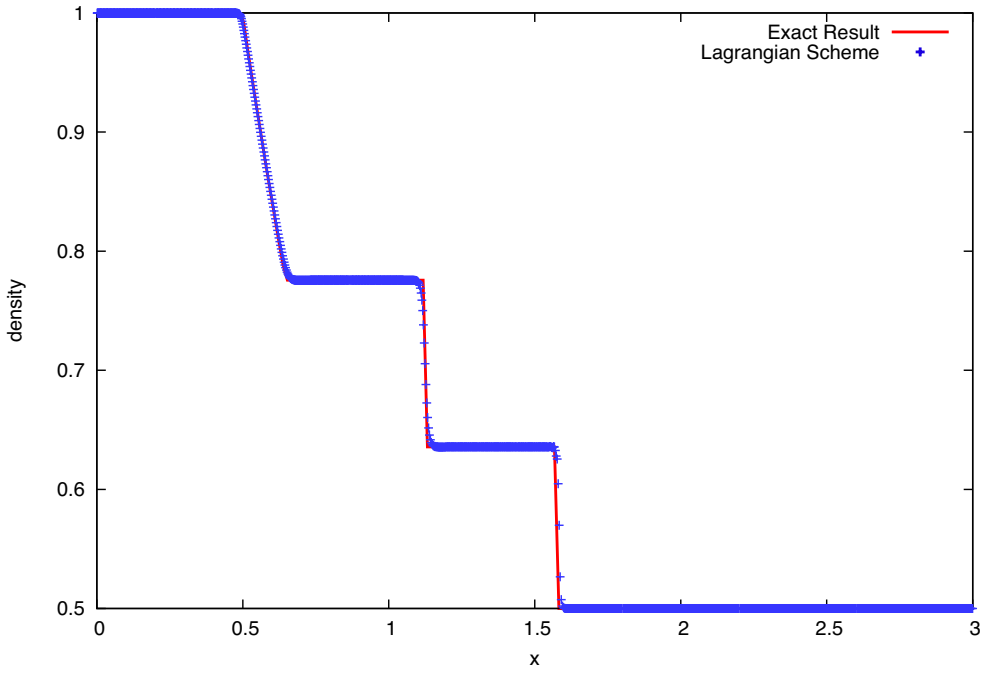

Figure 3.5: Density profile for shock-expansion problem.

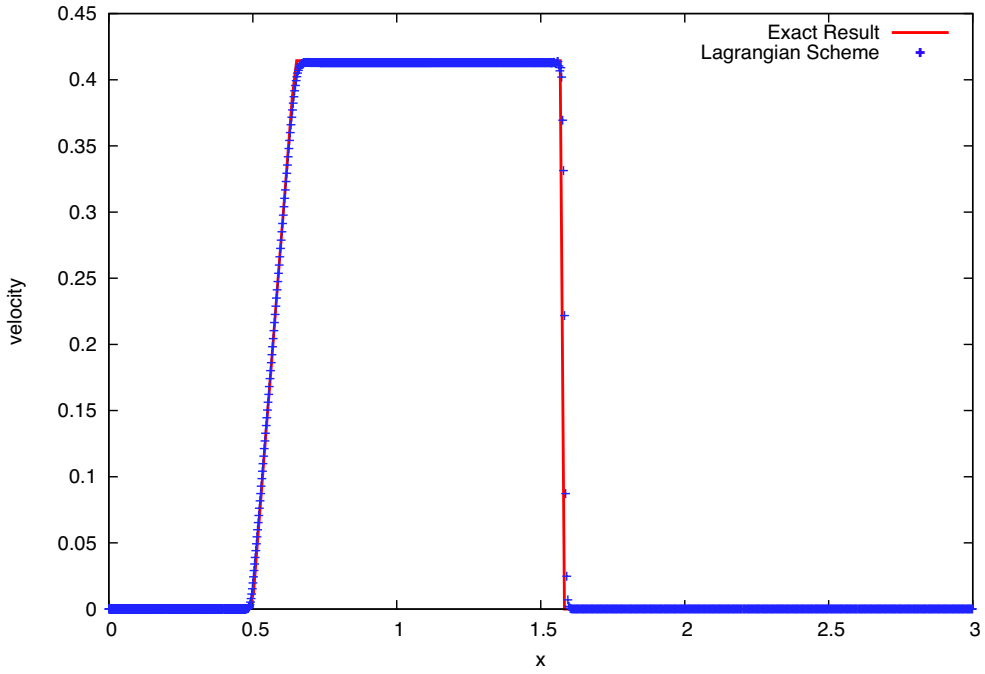

Figure 3.6: Velocity profile for shock-expansion problem.

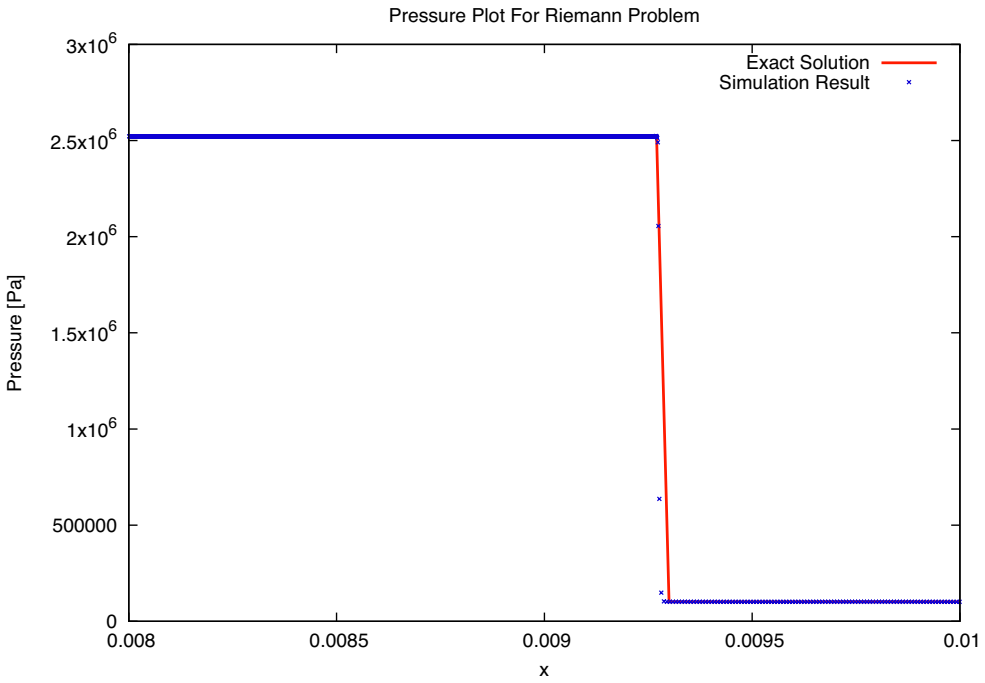

Figure 3.7: Pressure plot on strong shock test with initial condition fixed.

Figure 3.7, 3.8 and 3.9 show the compared results of the second problem. It can be seen that the strong shock is captured with excellent fidelity by the code. This further confirms the robustness and high reliability of the present hydrodynamic solver, especially for piston-driven problems. Again, such problems are the interest of this work.

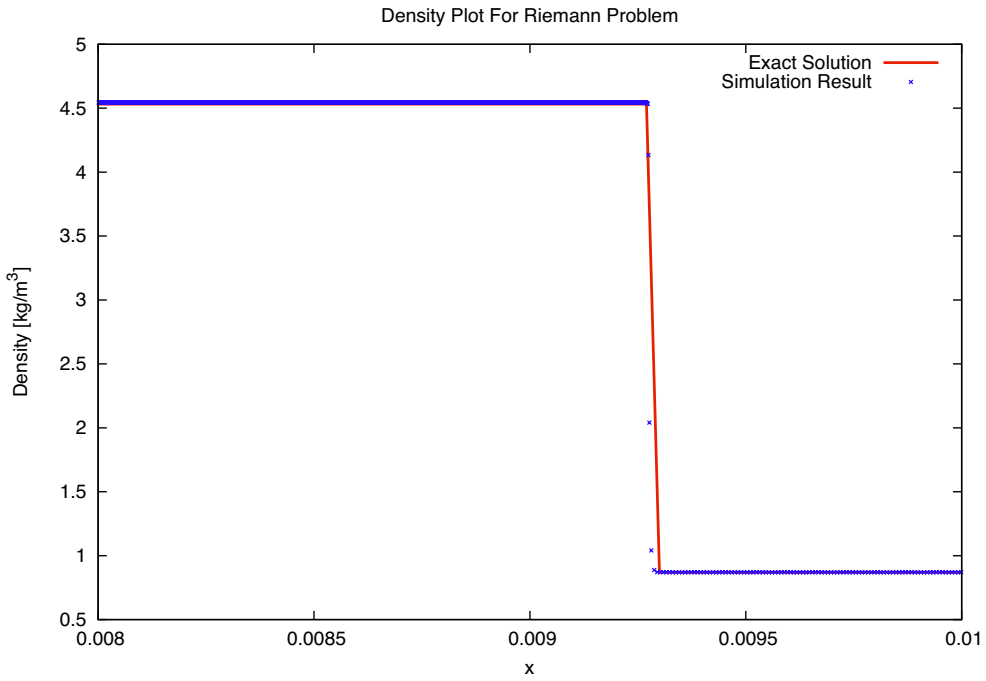

Figure 3.8: Density plot on strong shock test with initial condition fixed.

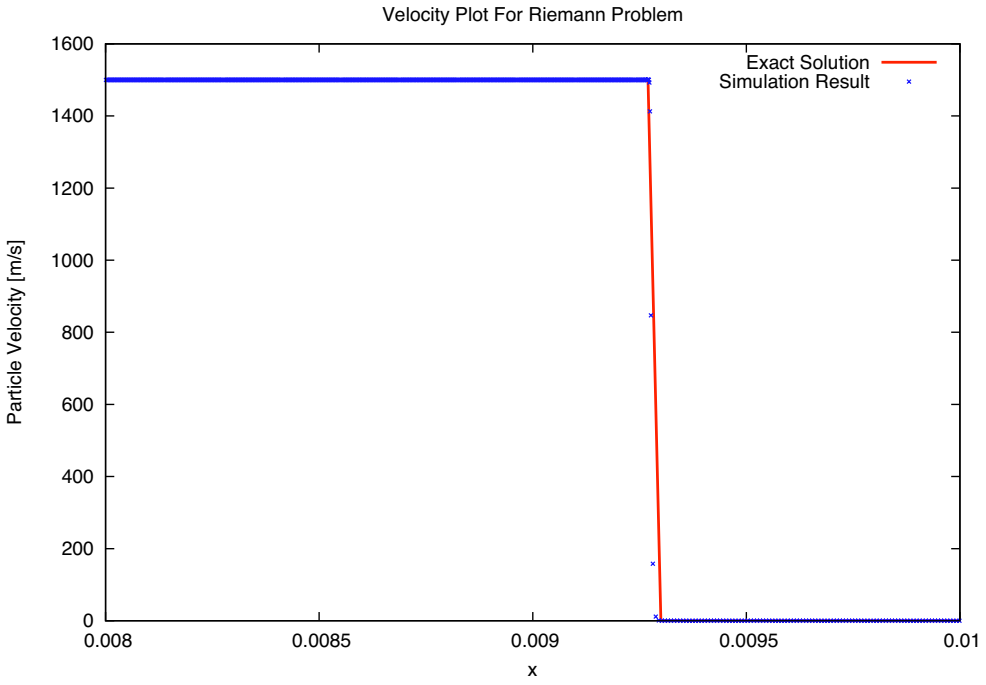

Figure 3.9: Velocity plot on strong shock test with initial condition fixed.

3.5 Chemical Kinetics and Operator Splitting Methodology

3.5.1 Full Chemical Kinetic Approach

The chemical kinetics is calculated using the Cantera computational framework, which is an open-source suite of object-oriented software tools for problems involving chemical kinetics [18]. The shorten San Diego mechanism database has been selected for operating ethylene-oxygen chemical kinetics and Li-hydrogen mechanism database has been selected for operating hydrogen-oxygen chemical kinetics [51, 52, 25]. Cantera provides a "reactor" model that solves the reactive model equations in a fixed volume. The present solution code uses one reactor for each Lagrangian cell. After the hydrodynamimc substep, the reactor advances the chemical kinetics. The chemical step obeys the following equation:

$$\frac{Dv}{Dt} = 0 \tag{3.29}$$

$$\frac{Du}{Dt} = 0 \tag{3.30}$$

$$\frac{De_{tot}}{Dt} = 0 \tag{3.31}$$

$$c_v \frac{DT}{Dt} = -v \sum_{i=1}^{n} \omega_i e_i \tag{3.32}$$

where ω_i is the mass formation rate of species "i" and e_i is the specific internal energy for species "i". c_v is the current specific heat capacity for constant volume. The chemical operator was initialized by imputing the density and the static internal energy from the hydrodynamic operation part before each advancing of chemical step. The chemical simulator does not change the conserved variables but provides the evolved pressure to flux solver. Because the total internal energy contains the chemical energy, the chemical reaction step does not change the total internal energy. The chemical species data is also updated during the chemical marching. To transform the conserved variables to primitive variables, species data is required because a real gas model is adopted. Figure 3.10 shows the flow chart of the corresponding calculation procedure.

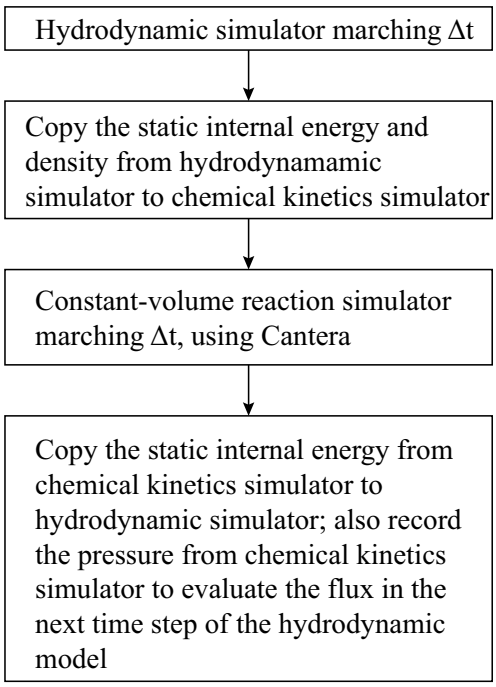

Figure 3.10: Substeps for one time step of solver.

3.6 Verification of Chemical-Hydrodynamic Numerical Solver

In order to validate the combination of chemical kinetics solver and the hydrodynamic solver, a steady ZND detonaton was simulated. The simulation was initiated with an over-driven ZND detonation in a stoichiometric mixture of hydrogen and oxygen with a piston speed of 1500 m/s. The state ahead of the shock wave is in 1.01×10^5 Pa and 293 K. For comparison, standard ZND profiles are computed by SDToolbox[5] and used as reference solutions. This reference solution is also used as the initial condition for the present numerical solution. In this verification case, the CFL number is 0.7 and the total number of cells is 2000.

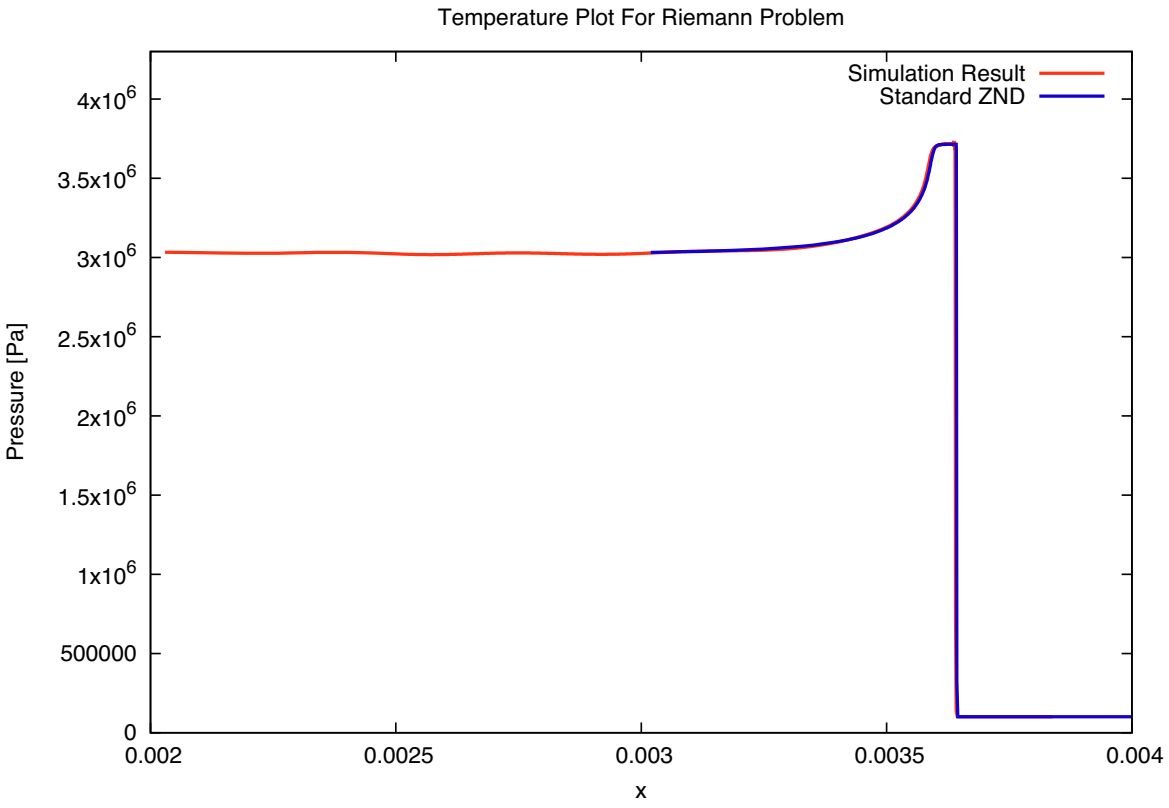

Figure 3.11: Pressure plot on ZND structure test.

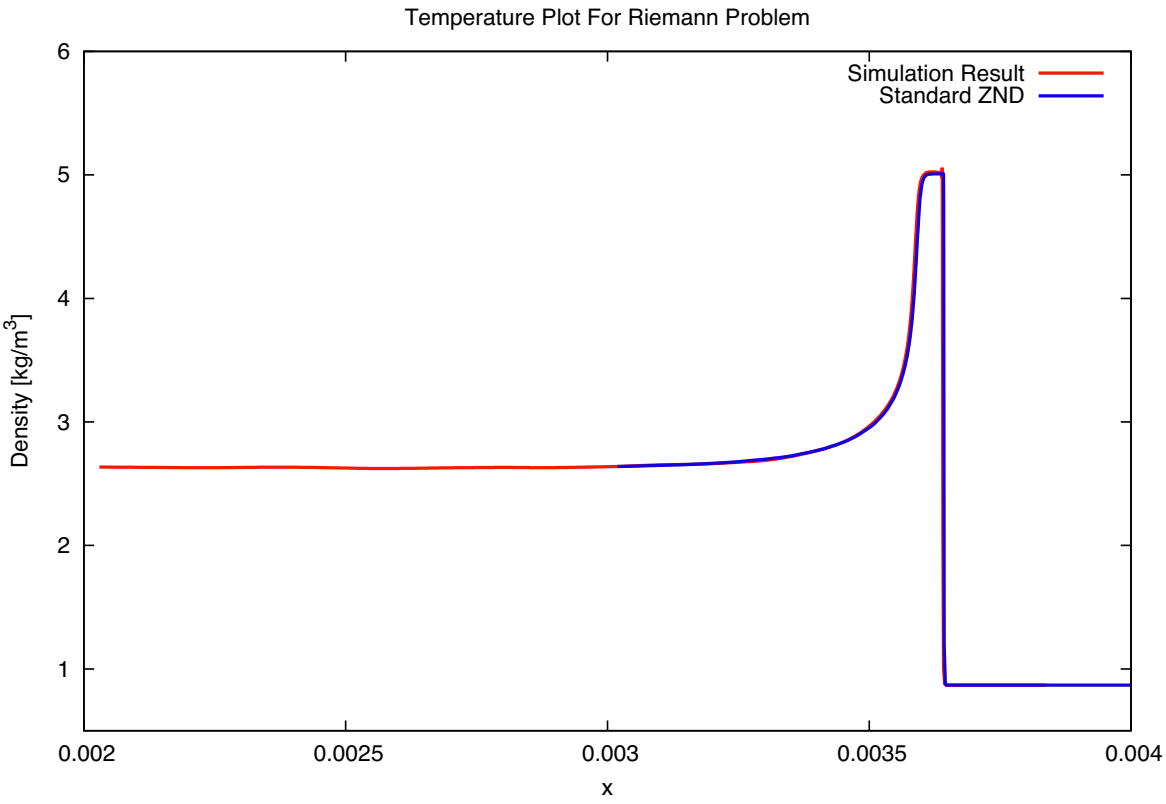

Figure 3.12: Density plot on ZND structure test.

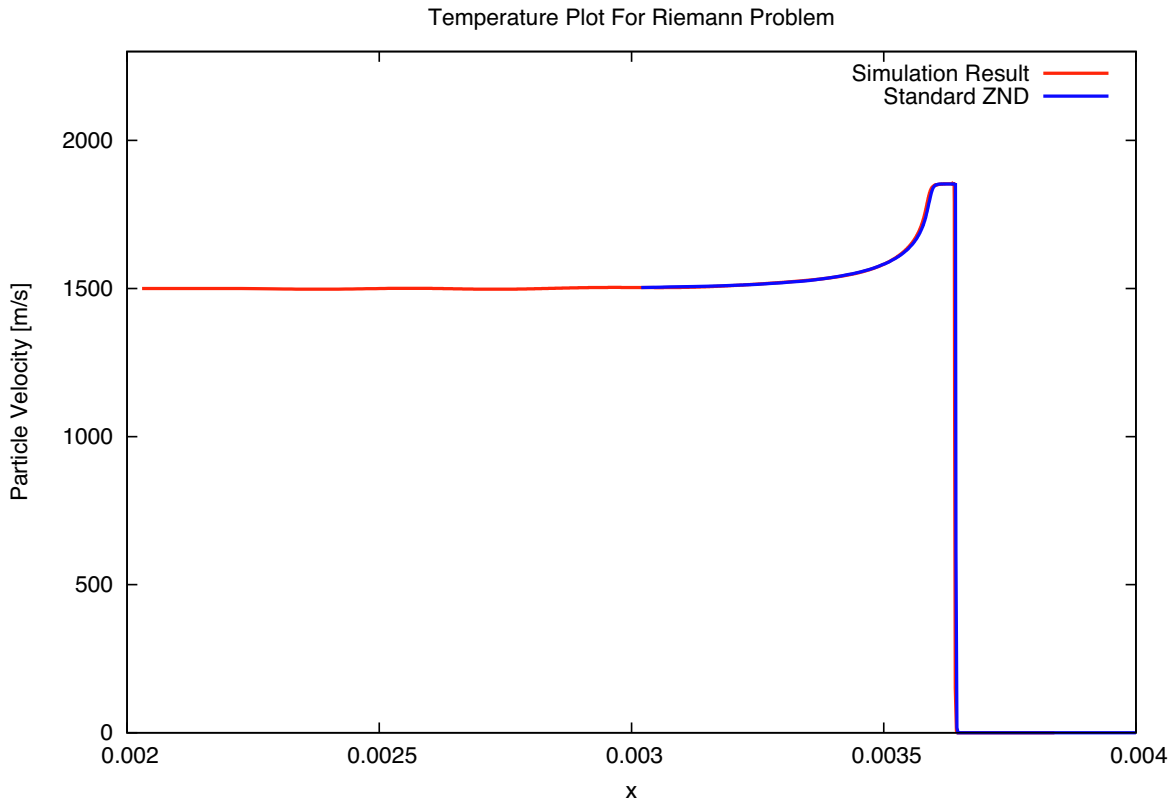

Figure 3.13: Velocity plot on ZND structure test.

Figures 3.11, 3.12 and 3.13 show the performance of the complete simulator on the ZND detonation evolution. The blue line is the reference solution. The left end of this reference solution is placed at $x = 0$ when $t = 0$ for simulation initiation. The red line is the simulation result by setting the piston speed of 1500 m/s, placing the initial condition and running the simulation for 1.35×10^{-6} s. Then, the blue curve has been moved to the right with a distance, which is the product between the detonation wave speed and simulation time. If the numerical framework is reliable, the two curves should overlap each other. The figure shows this overlapping, which means that the ZND detonation maintains the right structure and propagates with the correct speed. Thus, the reliability of the current numerical framework has been verified.

Chapter 4

Inert Numerical Studies with Fluctuating Induction Zone

4.1 Objective of Inert Numerical Study

The first study is on the fluctuating-piston problem described in Chapter 3 for the inert case in order to understand the gasdynamic effects generated by an oscillating piston. The reactive problem is treated in the following chapter.

4.2 Inert Simulation Result

Several inert simulations have been run in order to study the temperature distribution behind a fluctuated shock. The inert simulations were computed using a chemically frozen hydrogen-oxygen stoichiometric mixture, which is also one of the reactive simulation media considered later. The ambient states are fixed at T=293 K and p=5876 Pa. The incident shock strength was set to be M=3.83 so that the non-fluctuated post-shock state was controlled to T=1100 K and p=1 atm. The fluctuation amplitude were set to be 5% of the mean piston speed.

The first case imposed fluctuations with a frequency, f=453.5 kHz, and is shown in Fig.4.1. It is clear to see that the post-shock gas has been fluctuated. The sinusoidal pattern gradually transforms into an "N" shaped wave. The large fluctuation amplitude appears near the piston and the amplitude decays away from the piston. This is because of the energy dissipation, which will be discussed in a later section.

One is also able to recognize the regular fluctuation structures near the piston and complex features near the leading shock. As can be observed in the figure, the temperature pattern between the first peak and the second peak has irregular features in the blue curve.

This is due to the non-linear reflection of the Right Running Waves (RRW) generated by the piston with the leading shock, which generates entropy waves along lines of constant ϕ and weaker Left Running Waves (LRW). The coincidence between the signals at different times for fixed values of ϕ indicates that the entropy waves control the temperature distribution, as expected.

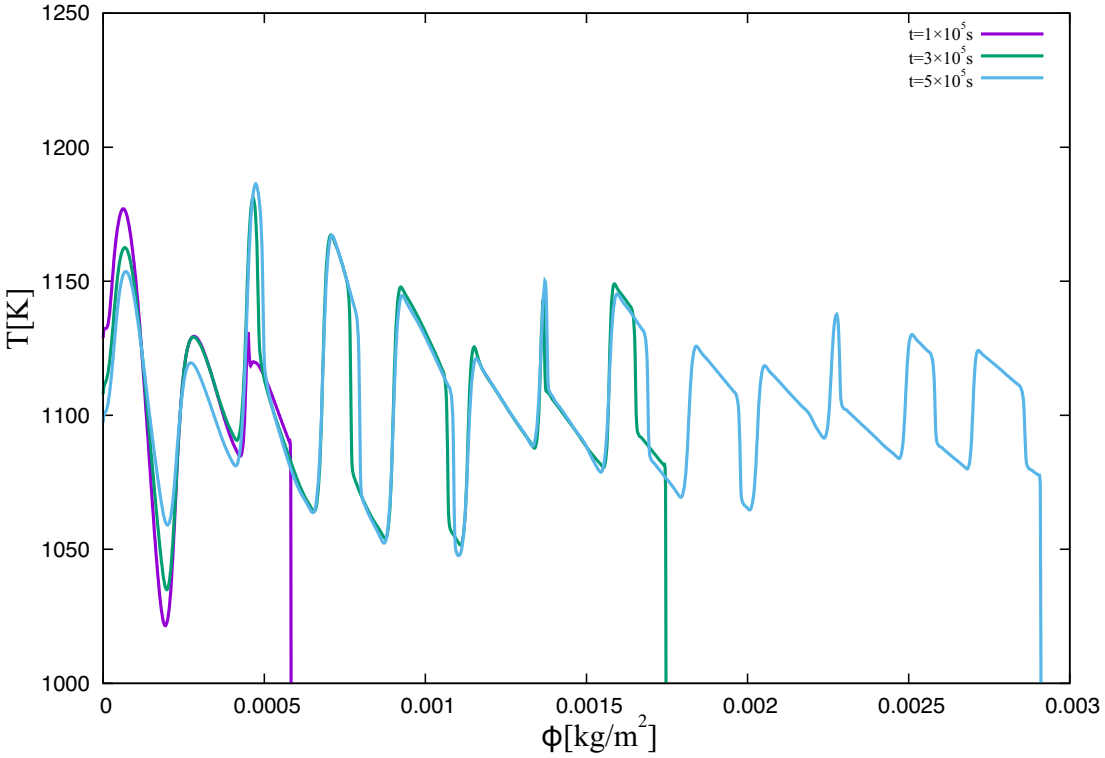

Figure 4.1: Temperature plot of fluctuating incident shock, ambient state:T=293 K; non-fluctuated shocked state: T=1100 K, p=1 atm; fluctuation: piston fluctuation speed=5% of mean speed, frequency=453.5 kHz.

For the second case, the fluctuation frequency is increased to 4535 kHz, but all other parameters are kept the same. The result is very different from previous case, as is shown in Fig.4.2. The temperature near the oscillating piston is much larger than that farther away behind the leading shock. The temperature away from the piston is much more uniform than before.

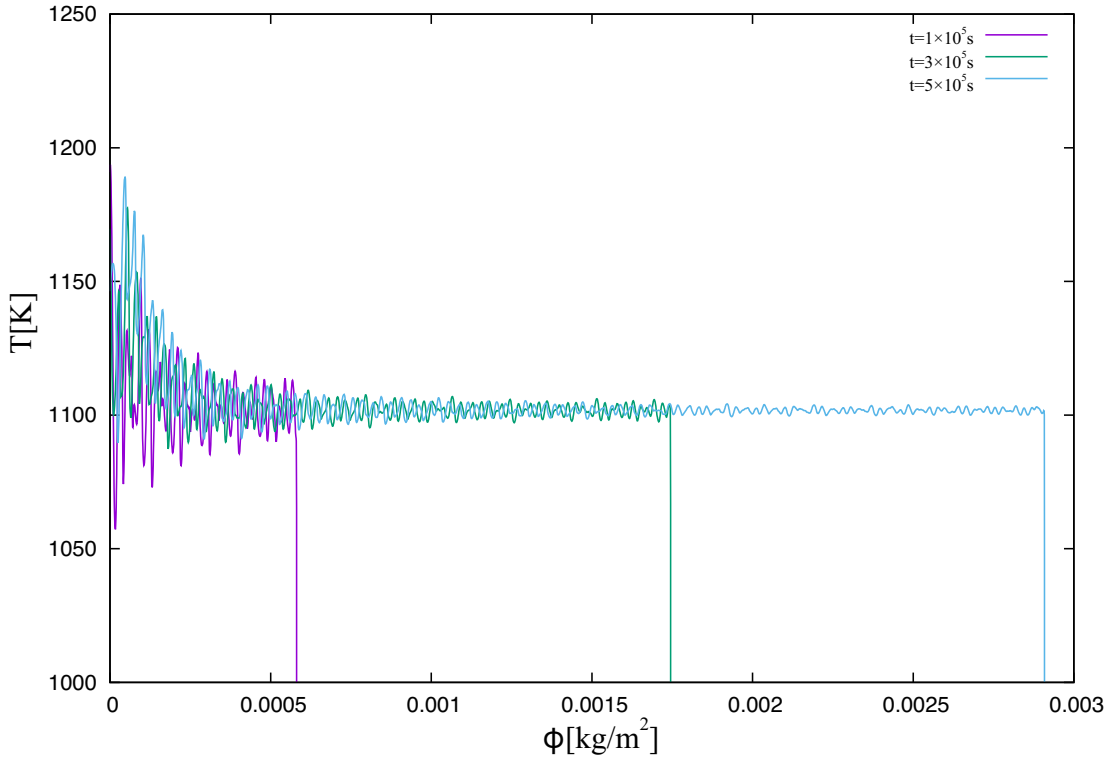

Figure 4.2: Temperature plot of fluctuating incident shock, ambient state:T=293 K; non-fluctuated shocked state: T=1100 K, p=1 atm; fluctuation: piston fluctuation speed=5% mean speed, frequency=4535 kHz.

Figure 4.3 shows a zoom-in of the x-axis from Fig.4.2 in order to clearly observe the details near the piston.

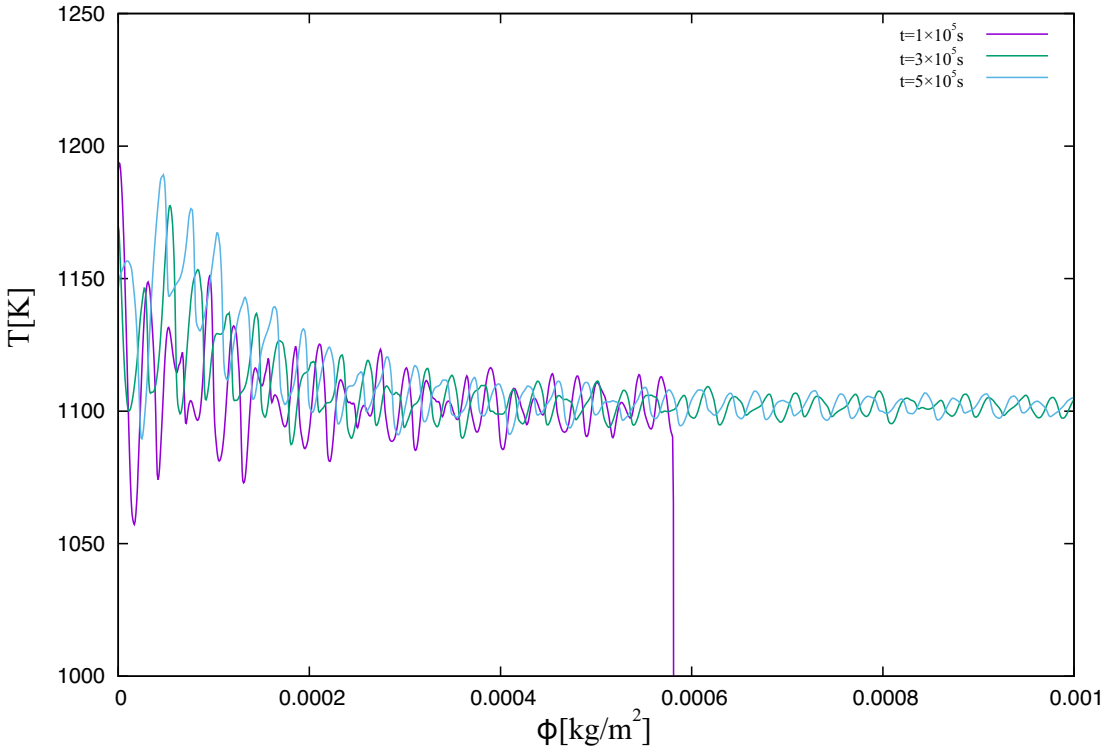

Figure 4.3: Zoomed temperature plot of fluctuating incident shock, ambient state:T=293 K; non-fluctuated shocked state: T=1100K, p=1atm; fluctuation: piston fluctuation speed=5% of mean speed, frequency=4535kHz.

As can be seen in Fig.4.3, the fluctuation amplitude decays as the distance from the piston increases. Also the heat of the gas concentrates in the area near the piston, which causes the increasing of average local temperature. This concentration is due to the shock dissipation which would be discussed in the following sections.

4.3 Local Hotspot Formation

In the oscillating-piston-driven shock problem, local hotspots form at the location where compression waves catch up with the leading shock. The increase of the mean temperature results from the irreversible heat that the leading shock over generates. Using a linear approximation of the shock equation near Mach number $M = M_0$, one can obtain this overheat temperature in the hotspots. The detailed derivation of such relationship is provided in Appendix C. The cardinal relationship is given by the following equation:

$$\Delta T_m = \left(v_0 \Theta + \frac{p_0 \Theta}{\Gamma} - \frac{T_0}{p_0} \frac{1-\gamma}{\gamma} \Theta \right) \Delta u, \tag{4.1}$$

where T_0, v_0 and p_0 are the non-shocked temperature, specific volume and pressure, respectively. The variable ΔT_m is the overheat temperature of the local gas, which represents the hotspots formation. It is zero when the leading shock does not have fluctuation. The variable Δu is the instantaneous post-shock particle velocity, which represents the fluctuating shock strength. The intermediate parameters Γ and Θ are constructed by constants and denoted as following:

$$\Gamma = -p_0\rho_0\frac{\gamma\left(\gamma+1\right)M_0^4}{\gamma+1}, \tag{4.2}$$

$$\Theta = \frac{2p_0\gamma M_0^3}{c_0\left(M^2+1\right)}. \tag{4.3}$$

All the parameters above are constant so that ΔT_m has the linear relation with Δu. The equation above explained the hotspot formation from a fluctuating leading shock wave. The hotspots form because the leading shock strength is varying. When the leading shock strength is slightly larger than its average strength, the gas which was shocked at that moment would form a hotspot. If the instantaneous shock strength was smaller than its average strength, the gas which was shocked at that moment would generate the local cool area. The size of hotspots can be reasonably described by the fluctuation wave length λ.

$$\lambda = \frac{c_0}{f\left(\frac{c_0}{u^*}-1\right)}. \tag{4.4}$$

In equation above c_0 is the post-shock sound speed and u^* represents the relative speed at which the leading shock departs from the piston. Thus the maximum gradient of the mean temperature could be approximately calculated using the maximum temperature variation divided by half wave length, as

$$\frac{\partial T}{\partial x}_{max_{hs}} = \frac{2\Delta T_m}{\lambda}. \tag{4.5}$$

4.4 Heat Dissipation

The other important gasdynamic effect is the energy dissipation from the "N"-type fluctuation waves in the gas. Although the mechanical fluctuation initially generated are sinusoidal acoustic waves, strong acoustic waves eventually steepen to "N"-type of shock waves, shown in Fig.4.4. These shock fluctuations dissipate energy to the gas and become weaker during propagation. The gas near the piston is hotter because the "N" waves near the piston are stronger and the "N" waves become weaker since they have dissipated their energy to the gas.

4.4.1 Model of a Decaying "N" Wave

In order to solve the decay rate of the "N" wave, one needs to understand the shock wave strength evolution with non-uniform post-shock condition. Figure 4.4 shows the shock

waves followed by expansion fans. The shock change equation(Eq. 4.6)[53] gives the shock wave strength change in terms of the post-shock condition [15],

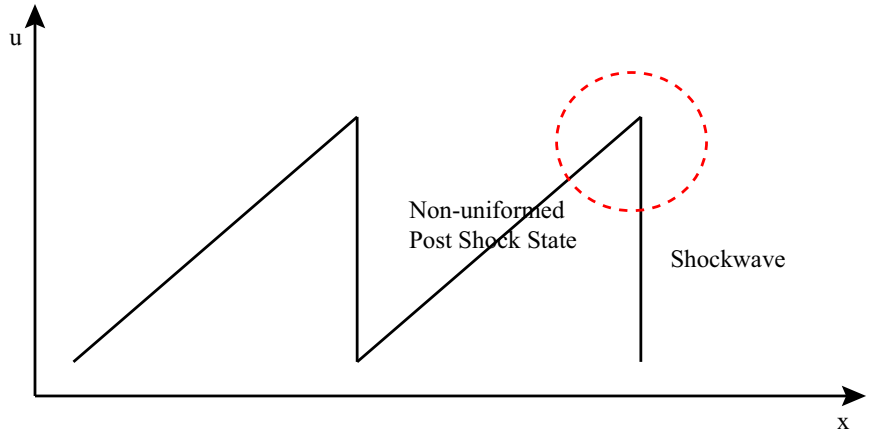

Figure 4.4: N-type shock wave.

$$\left.\frac{du}{dt}\right|_s = -\frac{\rho\left[c^2-(u-D)^2\right]}{\Theta+\rho(u-D)}\frac{\partial u}{\partial x}, \tag{4.6}$$

where Θ is the partial derivative of the post-shock pressure with respect to particle velocity, and has been expressed in Eq. 4.3. The shock change equations used the post-shock density, ρ, velocity, u, sound speed, c, shock speed, D, post-shock pressure derivative, Θ, and the post-shock velocity gradient, $\dfrac{\partial u}{\partial x}$, to predict the change of the shock strength.

4.4.2 The Decaying Rate of "N" Wave

In this problem the slope of the post-shock velocity can be expressed using its initial fluctuation wavelength as

$$\frac{\partial u}{\partial x} = \frac{u}{L}, \tag{4.7}$$

where L is the wavelength of the fluctuations, which has been assumed to be constant. Used the shock condition, the derivative of the post-shock particle velocity can be expressed using the derivative of the shock Mach number as

$$\left.\frac{du}{dt}\right|_s = \frac{2c_0\left(M^2+1\right)}{\left(\gamma+1\right)M^2}\frac{dM}{dt}. \tag{4.8}$$

Using the shock change equation, one has

$$\frac{dM}{dt} = -\frac{(M+1)^2(M-1)^2}{3M^2+1}\frac{c_0}{L}, \tag{4.9}$$

where c_0/L is fluctuation frequency. The simplified expression becomes

$$\frac{dM}{dt} = -\frac{(M+1)^2(M-1)^2}{3M^2+1} f. \tag{4.10}$$

In this thesis the simplified equation above is called "N" fluctuation wave change equation. The Mach number of an "N" fluctuating shock wave decays as a function that is only related to the Mach number itself and the fluctuation frequency. The fluctuation frequency is taken as a constant here.

Assuming the shock wave speed is constant, the "N" fluctuation wave change equation can be written as

$$\frac{dM}{dx} = -\frac{(M+1)^2(M-1)^2}{3M^2+1} f c_0. \tag{4.11}$$

4.4.3 Dissipation Rate Calculation

The irreversible heat dissipated by the fluctuating shock can be calculated by considering the entropy increase. The fluctuation cycle includes a shock wave and an isentropic expansion fan. The expansion process is reversible and all the irreversible heat stored in the gases comes from the shock waves.

Assuming the non-shocked gas has a temperature of T_0, the shock wave gives both reversible and irreversible heat to the gas. Then, the gas expands isentropically within the expansion fan. The temperature decreases during the expansion and finally reaches T_0. All the irreversible heat in this cycle can be calculated by using the entropy changes,

$$\delta q_i = T_0 \Delta s. \tag{4.12}$$

Here, T_0 could be selected as non-fluctuating post-leading shock temperature. The total entropy increasing is conserved entirely by the shock wave and given by

$$\Delta s = R \ln \left\{ z^{\frac{1}{\gamma-1}} \left[\frac{(\gamma+1)z + (\gamma-1)}{(\gamma+1) + (\gamma-1)z} \right]^{\frac{-\gamma}{\gamma-1}} \right\}, \tag{4.13}$$

where z is the pressure ratio(shocked pressure over non-shocked pressure) through the shock wave,

$$z = \frac{p_2}{p_1} = \frac{2\gamma(M^2-1)}{\gamma+1} + 1. \tag{4.14}$$

Defining that δq_i represents the irreversible heat deposited by a single fluctuating shock wave. If one needs to calculate the average storage rate of such irreversible heat, $\frac{\bar{\delta q_i}}{\delta t}$, one need to multiply simply by the frequency,

$$\frac{\bar{\delta q_i}}{\delta t} = \delta q_i f. \tag{4.15}$$

The temperature increasing within a certain particle can be calculated by time integration and using a constant-pressure heat capacity. This temperature increase only considers the heat dissipation effect,

$$T = T_0 + \frac{\delta \bar{q}_i}{\delta t} \frac{t}{c_p}. \tag{4.16}$$

The detailed derivation of "N"-wave model is presented in Appendix B.

4.5 Conclusion

There are two induction zone effects that redistribute the post-shock temperature. The first one, acoustic-shock interaction, generates the local hotspots while the other one, "N" wave dissipation, may concentrate the energy in the section which is closest to piston. Both effects have positive correlation with the fluctuation amplitude. The acoustic-shock interaction is not sensitive to the frequency. Nevertheless, the "N" wave dissipation is related to the fluctuation frequency. In the higher-frequency case, the fluctuation wave loses its energy more quickly and the majority fluctuation energy is converted to heat and is stored in the gas that is closest to the piston. The hotspots are not significant compared to the dissipation overheating. In the low frequency case, the effect of acoustic-shock interaction becomes more dominant. The global temperature pattern shows significant hotspots but not a heat concentration near the piston.

Chapter 5

Reactive Hydrogen-Oxygen Results

5.1 Objective of This Chapter

This chapter investigates the effect of the mechanical fluctuations' amplitude and frequency on ignition and detonation formation in a reactive mixture of hydrogen and oxygen. Results for ignition in a typical hydrocarbon are presented in the next chapter.

5.2 Initial Condition Settings and Numerical Settings

Hydrogen-Oxygen kinetics is one of the simplest combustion kinetics. Comparing to the kinetics of hydrocarbons, it is numerically cheap and well understood. This is the reason that the first numerical investigation is on this mixture. The initial state here is 293 K. Initial pressure was chosen such that the post-shock state in the absence of fluctuations was 1100 K and 1 atm. This choice was motivated by the abundance of experiments on reference ignition data, e.g. induction delay, for hydrogen-oxygen at 1 atm. Moreover, the post-shock temperature has been fixed at 1100 K because this temperature corresponds to the lower limit of high-temperature ignition [31] for hydrogen-oxygen ignition in 1 atm. This chapter focuses on high-temperature ignition, where the scale of induction time t_i and of reaction time t_r are close to each other. The mean speed of the piston is 1626m/s. The CFL number is set to 0.7 and the number of cells is 2000 for all the simulations in this chapter. For reference, the reaction time t_r for the chosen case is $5\mu s$. In the induction zone, the Lagrangian wave speed is $\rho c = 134.83$ kg/(m^2 s), giving the characteristic reaction zone width of $\Delta\phi = 6.74 \times 10^{-4}$ kg/m^2. This means that approximately 250 grid points captured the reaction zone.

5.3 Reference Ignition without Fluctuations

Before running the fluctuating cases, a non-fluctuated shock-induced ignition has been simulated first. The 1D Results are shown using $\phi - t$ diagrams, where ϕ is the Lagrangian

coordinate, and t is time coordinate. First the stable shock-induced ignition has been run in order to make reference as shown in Fig.5.1. In the $\phi - t$ diagram, particle paths have been fixed to the vertical lines. We analyze temperature because it can reflect both chemical reaction and hydrodynamic characteristics.

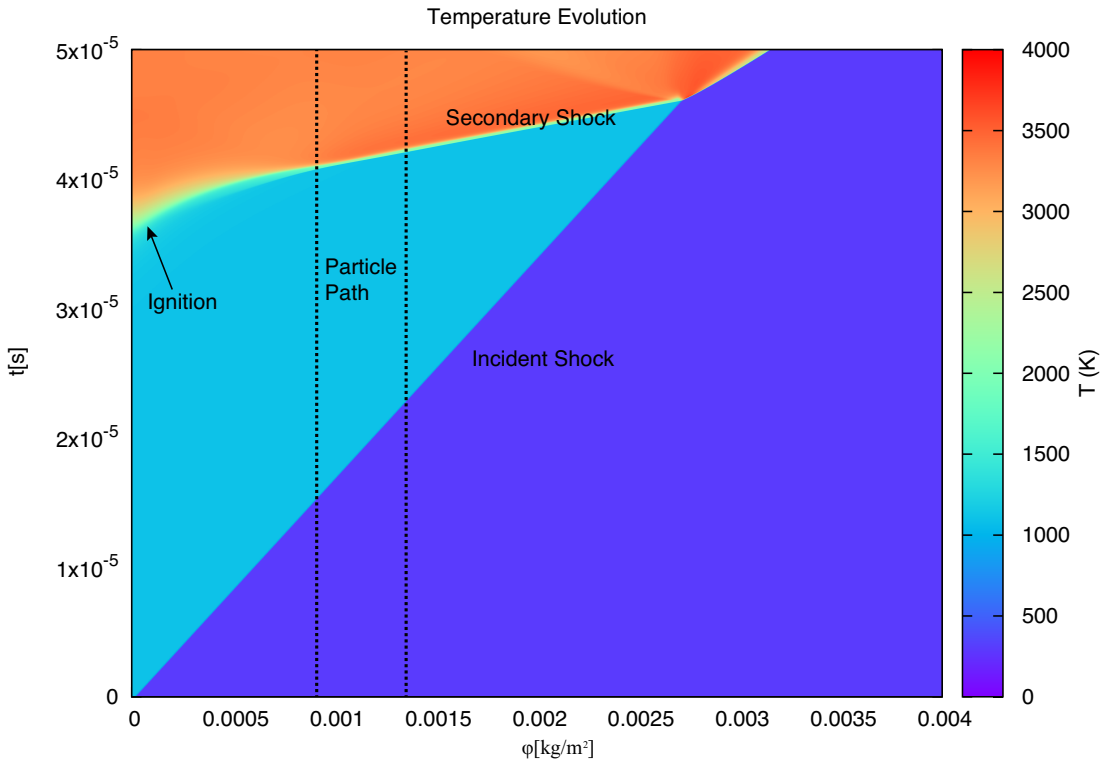

Figure 5.1: Hydrogen shock-induced ignition with post shock state in 1100K without fluctuation.

In Fig.5.1, the shock wave is formed at $t = 0$. Behind the shock, the temperature stays constant until the first ignition, which happens at $t = 35$ μs. The gas adjacent to the piston ignited first and then the reaction front expanded into the unburnt region. This expansion compressed the unburnt gas and accelerated the ignition process of downstream gas. Once the compression wave of the same family met each other, a secondary shock was formed. This shock was driven by the combustion. Once the secondary shock caught up with the incident shock, a detonation was formed and a series of expansion wave formed and propagated backwards.

5.4 Ignition with Fluctuations

The investigation of situations with piston-induced fluctuations comprises 16 simulations, which have the same ambient state. The mean speed of the piston has been chosen so that the post incident shock states are the same. In each simulation, the frequency and/or the amplitude has been changed. Four frequency levels have been selected and four fluctuation strengths have been tested on each frequency level.

From CEA calculation, the non-fluctuated hydrogen-oxygen mixture has an ignition delay of $t_i = 3.3 \times 10^{-5}$ s, which corresponds to the frequency $f_i = 30.30$ kHz. The non-fluctuating hydrogen-oxygen mixture has heat-releasing time of $t_r = 2.0 \times 10^{-6}$ s, which corresponds to the frequency $f_i = 500.0$ kHz. One frequency (4.535 kHz) smaller than the ignition delay frequency, two (45.35 kHz and 453.5 kHz) between the ignition-delay frequency and the heat-release frequency and one (4535 kHz) greater than heat-release frequency have been selected.

The fluctuation amplitude of the piston speed is fixed at 5%, 10%, 15% and 20%. These four values have been selected because amplitudes smaller than 5% may give a nearly linear response and may not qualitatively change the ignition regime. Fluctuations stronger than 20% have not been considered in this thesis because they are deemed too strong and could cause strong shocks and bring too many non-linear effect into the analysis. Temperature profile is selected as the plotted variable in this chapter, because the temperature profile reflects both gasdynamic and reaction features. The particle velocity, pressure and density profiles for each simulation can be found in Appendix D. The corresponding resolution tests are shown in Appendix F.

5.4.1 4.535 kHz Fluctuation

Figure 5.2 shows the 5% piston speed fluctuation with a frequency of 4.535 kHz. The ignition started at 3.2×10^{-4} s. Compared to the stable piston (Fig.5.1), the ignition delay does not change much(shorten by 9%). At this frequency, the fluctuating wavelength is greater than the induction zone.

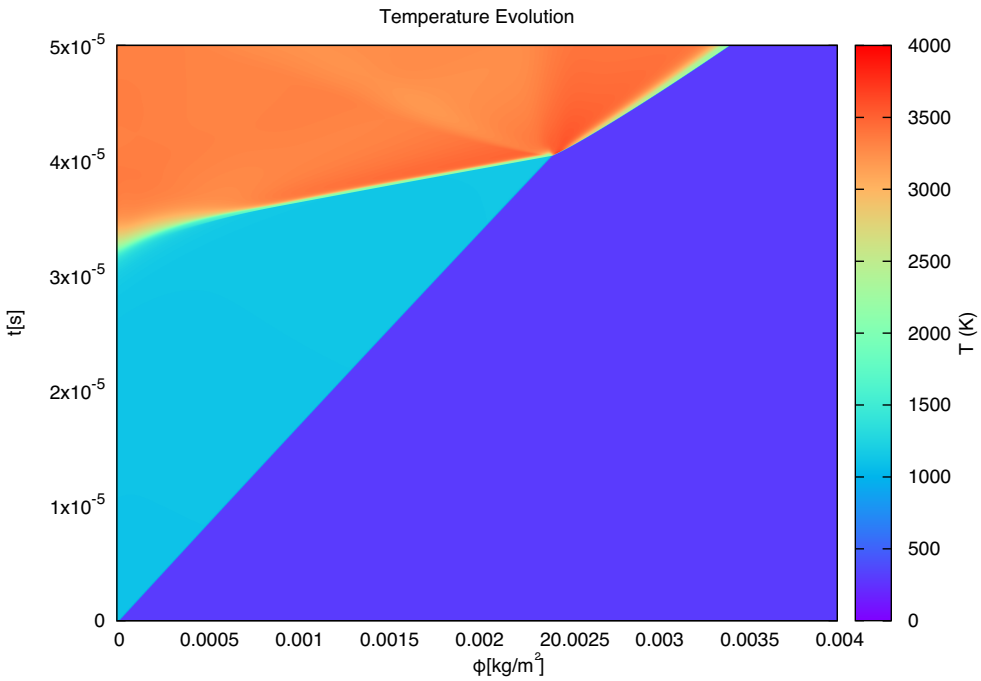

Figure 5.2: Hydrogen fluctuating shock-induced ignition with a post shock temperature of 1100 K and piston oscillation frequency of 4.535 kHz and amplitude of 5%.

Figure 5.3 provides the simulation results at 10% amplitude at the same frequency. One is able to observe that the ignition delay has been shortened slightly. The ignition patterns are the same as what one can observe for the non-fluctuated ignition case. The ignition started near the piston, the initial reaction zone is wide, which means the initial reacting gas has long exothermic period. The first ignited gas compressed the unreacted gas and formed a shock wave. The shock wave accelerated the reaction progress and the reaction zone became smaller and smaller in this acceleration process. In this simulation, the first ignition delay is 2.9×10^{-5} s and the detonation formation time is 3.6×10^{-5} s.

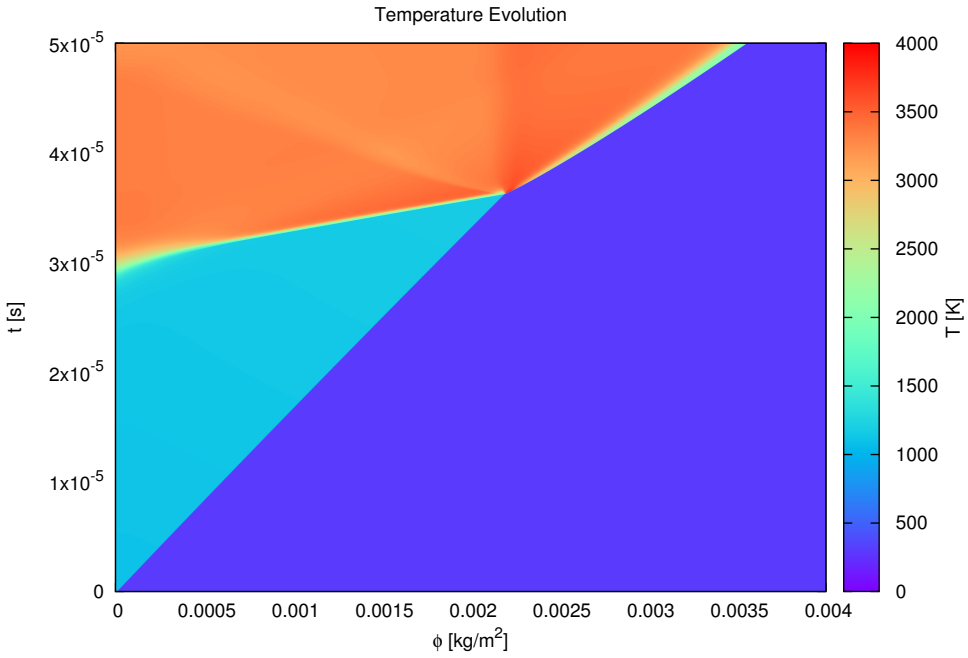

Figure 5.3: Hydrogen fluctuating shock-induced ignition with a post shock temperature of 1100 K and piston oscillation frequency of 4.535 kHz and amplitude of 10%.

When the amplitude is increased to 15%, the temperature pattern is still not drastically changed, as shown in Fig.5.4. The first ignition time has now been decreased to 2.7×10^{-5} s and the detonation formation time has been shortened to 3.3×10^{-5} s.

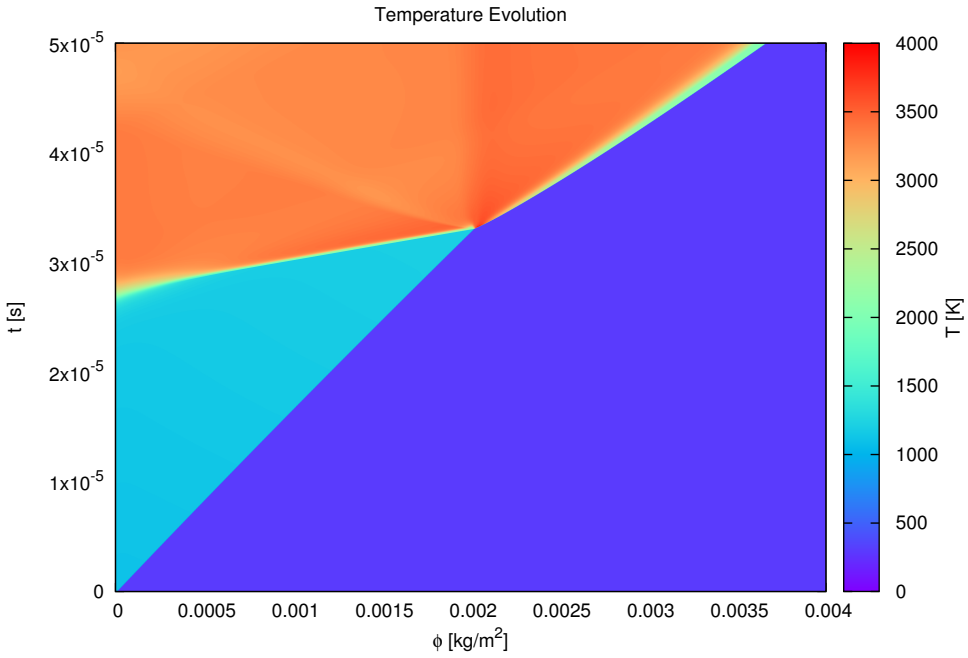

Figure 5.4: Hydrogen fluctuating shock-induced ignition in 1100K frequency=4.535 kHz and amplitude of 15%.

Similarly, in the 20% amplitude simulation, the pattern does not have substantial change, shown in Fig.5.5. The first ignition time is now 2.5×10^{-5} s and detonation formation time is 3.1×10^{-5} s.

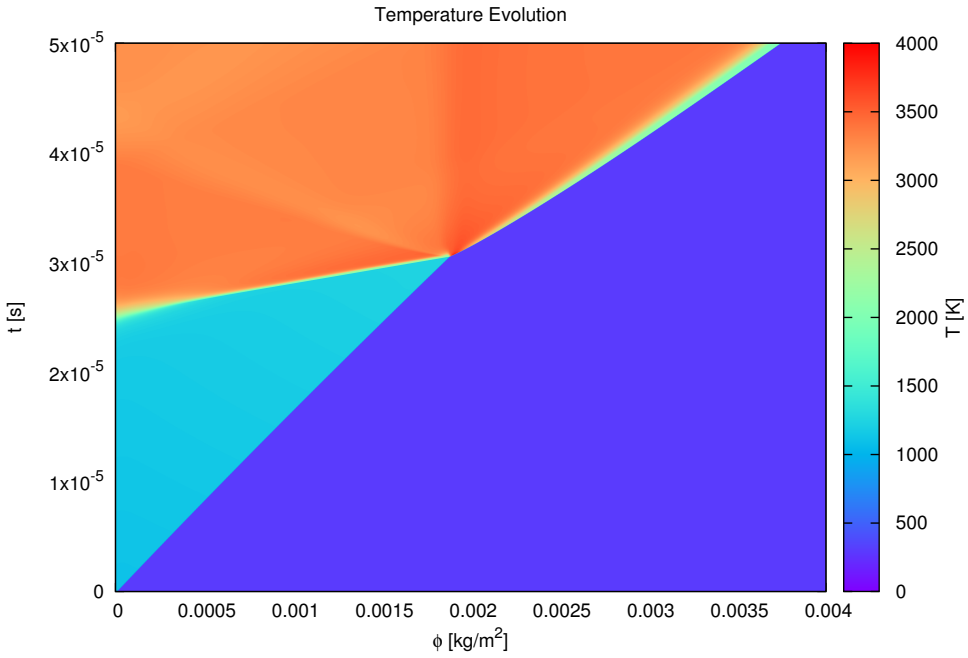

Figure 5.5: Hydrogen fluctuating shock-induced ignition with a post shock temperature of 1100 K and piston oscillation frequency of 4.535 kHz and amplitude of 20%.

In this set of simulations, the ignition patterns do not have significant difference comparing to the non-fluctuated ignition simulation. The ignition started near the piston. The initial reaction front accelerated to a constant speed and formed a secondary shock.

5.4.2 45.35 kHz Fluctuation

Figure 5.6 shows the simulation results obtained with fluctuations at a frequency of 45.35 kHz and with 5% fluctuation amplitude on the piston speed. The ignition regime has changed to hot-spot ignition. The first ignition began at $\phi = 0.0003$ kg/m^2. The ignition pattern at $\phi = 0.0003$ kg/m^2 is flat but not parallel to the incident shock wave. The ignition which initiate with a horizontal pattern stands for the simultaneous ignition, where the reaction propagates by ignition delay sequence (i.e., a fast flame). The gas around this section released heat simultaneously. This ignition released a large amount of energy and formed two strong shock waves. The first shock wave propagated forward and had been gradually intensified by the reaction. The second shock wave propagated backward and had been reflected by the piston. In this simulation, the first ignition delay is 3.3×10^{-5} s and the detonation formation time is 4.0×10^{-5} s.

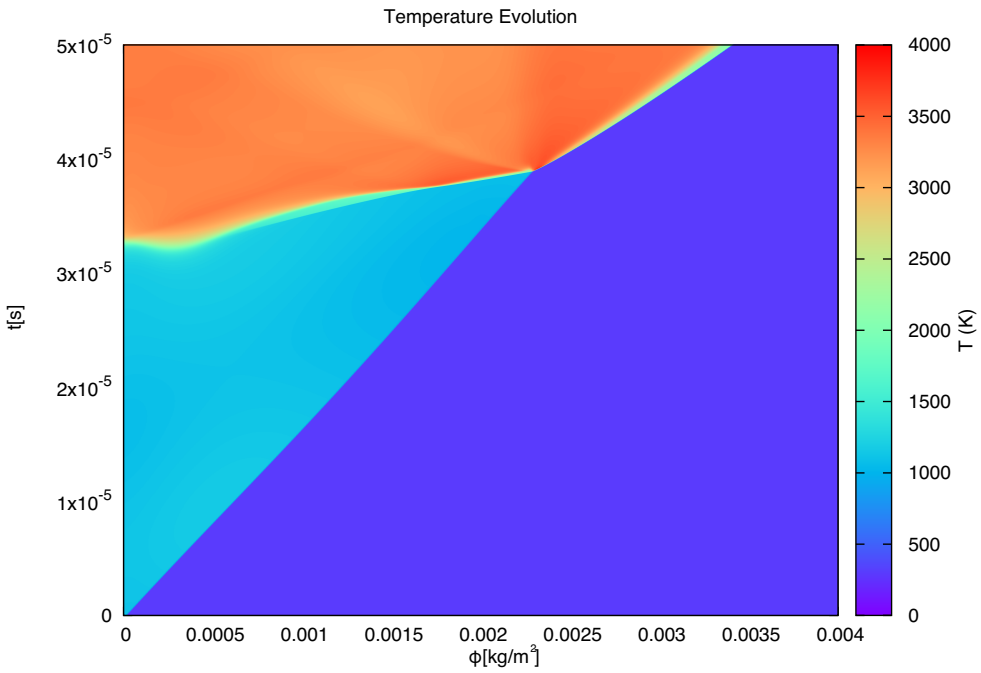

Figure 5.6: Hydrogen fluctuating shock-induced ignition with a post shock temperature of 1100 K and piston oscillation frequency of 45.35 kHz and amplitude of 5%.

Figure 5.7 shows the simulation result with 45.35 kHz and fluctuation with an amplitude of 10%. The patterns are qualitatively the same as what has been observed in Fig.5.6. Five significant shock waves formed before the detonation generated. These waves are numbered in Fig.5.7. The first shock is the incident shock. The second shock is the forward propagating shock from simultaneous ignition. The third shock is the back propagated shock from simultaneous ignition. The forth shock is the reflected shock from the third shock. The fifth shock is a strong shock driven by the reaction. It is found that the ignition formed shock (the second shock) is not in phase with the reaction. Only when the reaction driven shock V catches up with the shock II, the shock II can directly initiate the reaction. The first ignition time has been advanced to 2.7×10^{-5} s and the detonation formation time is 3.4^{-5} s.

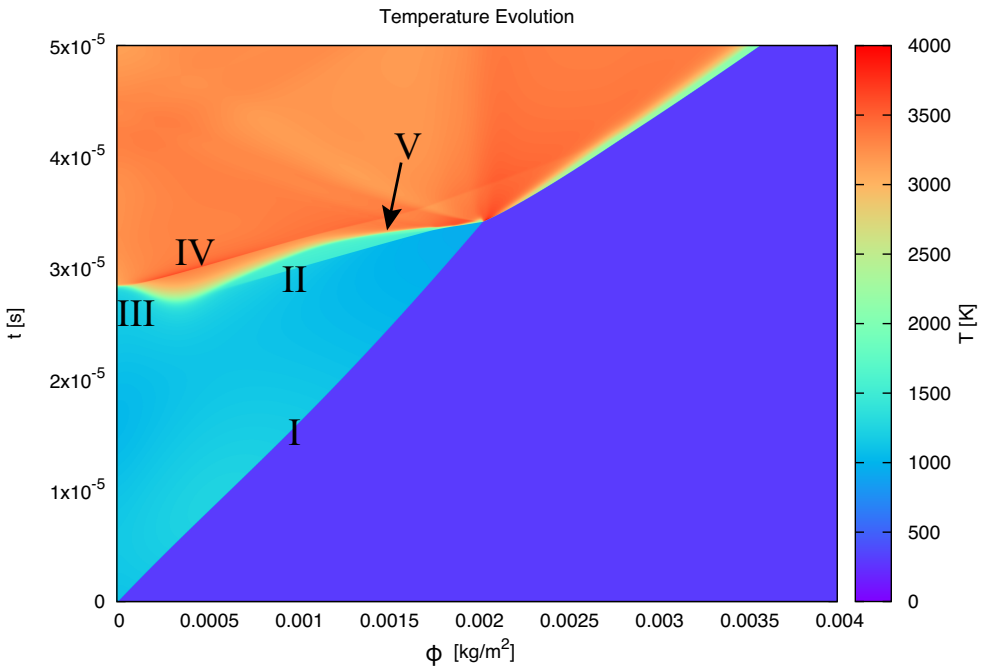

Figure 5.7: Hydrogen fluctuating shock-induced ignition with a post shock temperature of 1100 K and piston oscillation frequency of 45.35 kHz and amplitude of 10%.

Increasing the fluctuation amplitude to 15% at a frequency of 45.35 kHz, the ignition pattern becomes more complicated (Figure 5.8). After the first ignition, the reaction zone decouples with the shock II immediately. There was a new shock VI that formed by the shock IV reaction zone interaction. The shock II and shock VI both accelerated the induction process but neither drove the reaction. The reaction was still driven by the shock V. In this circumstance, the first ignition delay and detonation formation time are 2.0^{-5} s and 3.2×10^{-5} s, respectively.

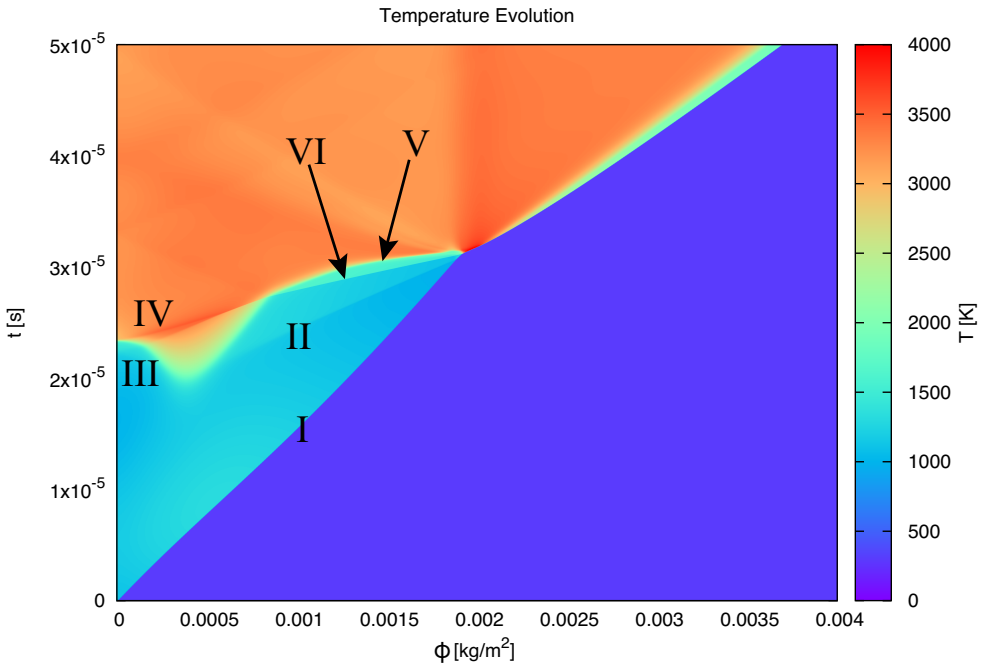

Figure 5.8: Hydrogen fluctuating shock-induced ignition with a post shock temperature of 1100 K and piston oscillation frequency of 45.35 kHz and amplitude of 15%.

In Fig.5.9, the fluctuation amplitude is increased to 20%, still with a frequency of 45.35 kHz. The first ignition delay has now been shortened to 1.3×10^{-5} s. The reaction zone decoupled from the shock II but when the shock II caught up with the shock I, a new strong shock was generated. The detonation was forming at 1.8×10^{-5} s. The detonation reaction zone fluctuated so that the thickness of the reaction zone oscillated.

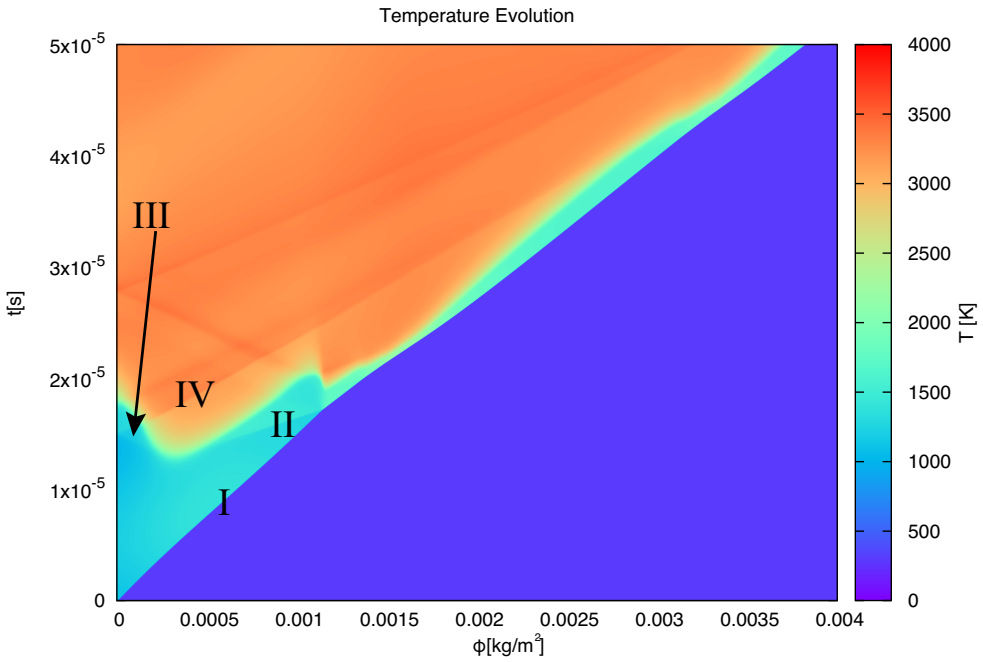

Figure 5.9: Hydrogen fluctuating shock-induced ignition with a post shock temperature of 1100 K and piston oscillation frequency of 45.35 kHz and amplitude of 20%.

5.4.3 453.5 kHz Fluctuation

When the fluctuation frequency is increased to 453.5 kHz, the ignition patterns again present a qualitatively similar group of results (Figure 5.10, 5.11, 5.12 and5.17). In these four simulations the reaction ignited in multiple hotspots. It is easy to recognize the forward-fluctuation waves and local hotspots. The first ignition started at 3.0×10^{-5} s in the 5% amplitude case, as shown in Fig.5.10. The first four ignition hotspots did not generate strong shocks. The early hot-spot ignition intensified the fluctuation wave, which homogeneously increases the induction zone temperature and makes the later hot-spot induction time shorter. When the ignition delay decreased, the hot-spots become less significant in the $\phi - t$ diagram. Nevertheless, the reaction propagated faster in the later hot-spot ignitions. Finally the ignition propagated in phase with a shock wave. Then the self driven shock caught up with the incident shock and formed a detonation.

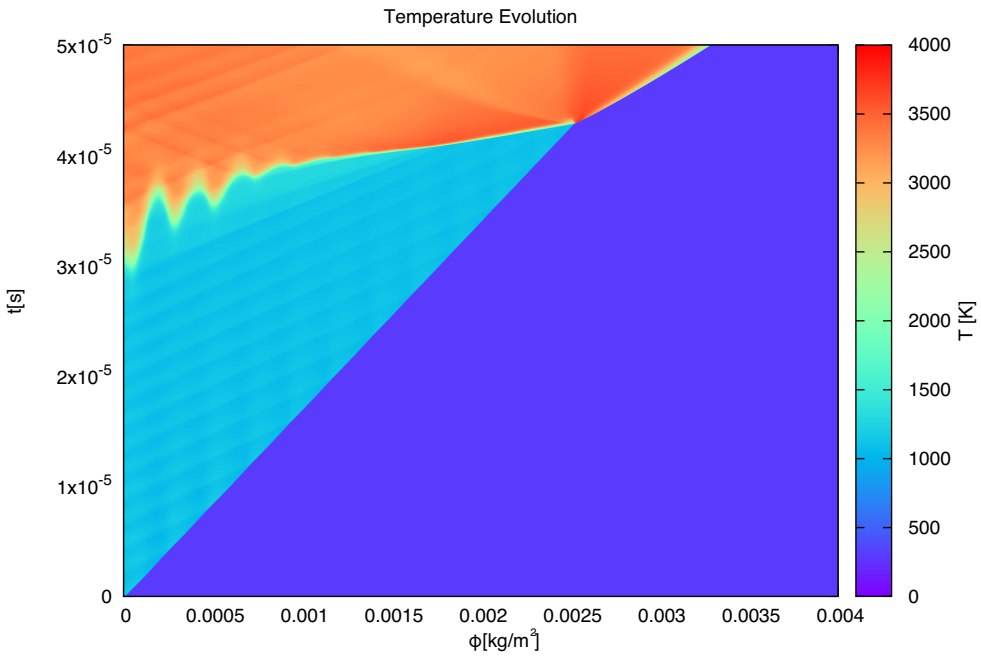

Figure 5.10: Hydrogen fluctuating shock-induced ignition with a post shock temperature of 1100 K and piston oscillation frequency of 453.5 kHz and amplitude of 5%.

The first ignition delay decreased with the fluctuation amplitude increasing. In the 10% amplitude simulation, it reaches 2.2×10^{-5} s, as shown in Fig.5.11. In this simulation, the hotspots become more significant in the $\phi - t$ diagram. Nevertheless, the acceleration of such reaction front is much slower.

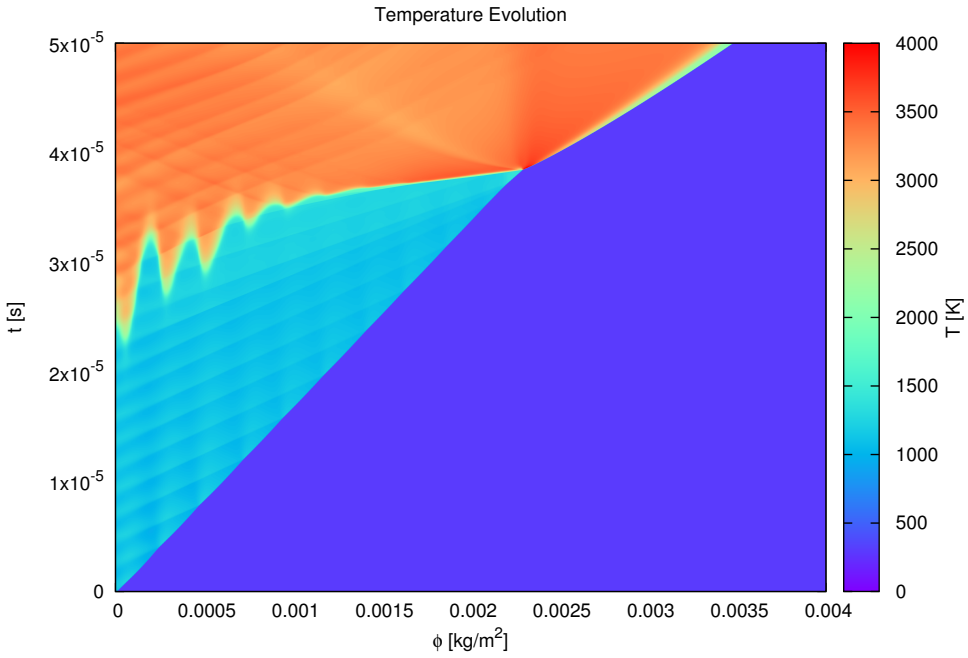

Figure 5.11: Hydrogen fluctuating shock-induced ignition with a post shock temperature of 1100 K and piston oscillation frequency of 453.5 kHz and amplitude of 10%.

In the 15% amplitude case, the patterns does not deviate significantly from what can be observed in the 10% amplitude simulation. The ignition delay decreases to 1.7×10^{-5} s, as seen in Fig.5.8, where detonation formation time is 3.2×10^{-5} s.

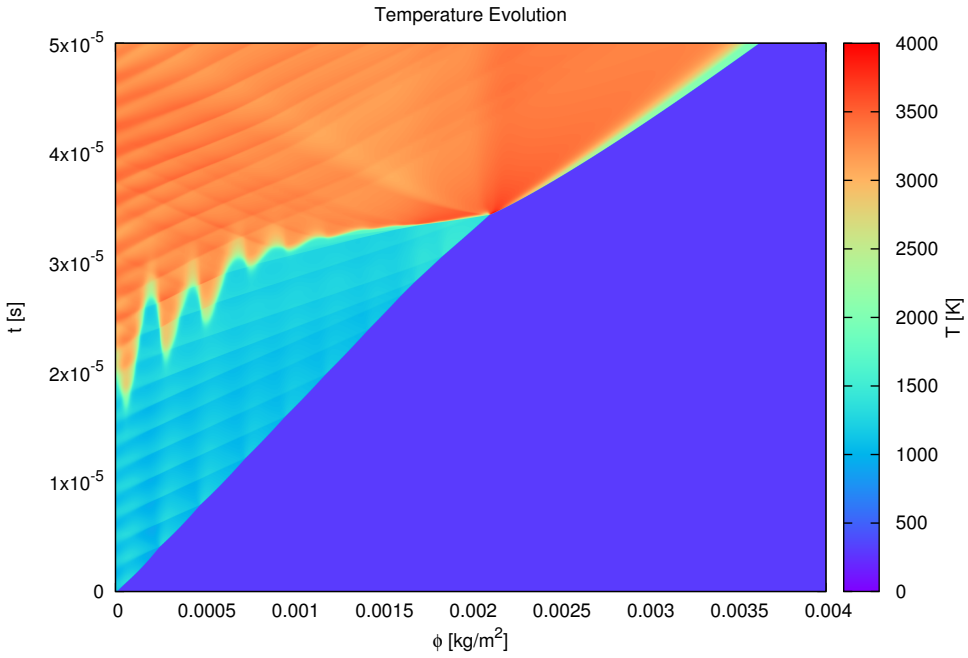

Figure 5.12: Hydrogen fluctuating shock-induced ignition with a post shock temperature of 1100 K and piston oscillation frequency of 453.5 kHz and amplitude of 15%.

In Fig.5.13, the ignition delay has finally been advanced to 1.2×10^{-5} s when the amplitude of the piston speed fluctuation is 20% . The hotspots intensified the fluctuation significantly in this simulation. The last two hotspots in Fig.5.13 were generated by intensified fluctuation waves. These two fluctuation waves were intensified by the first hotspot.

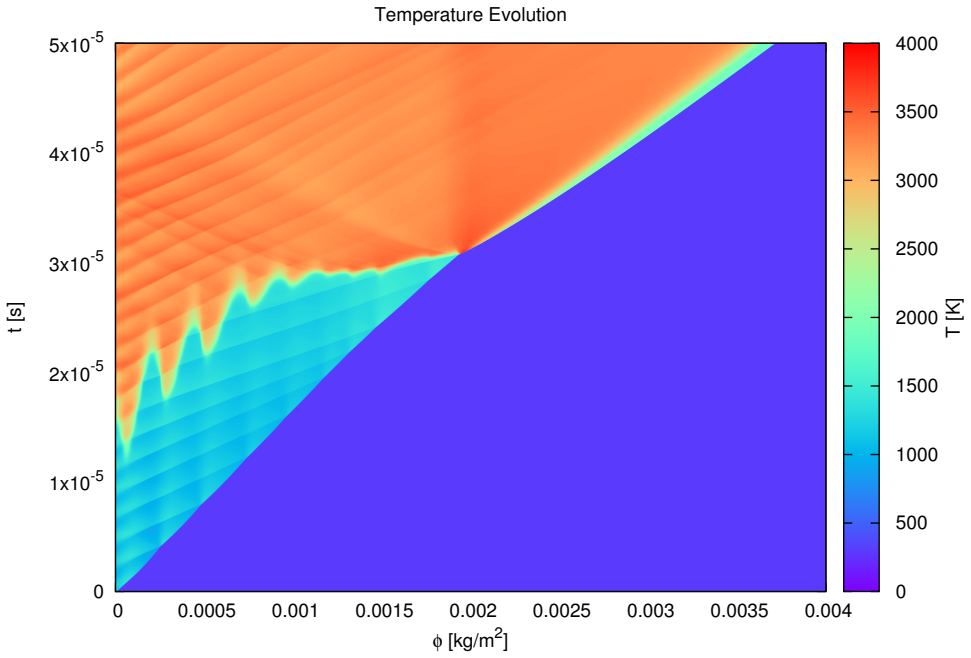

Figure 5.13: Hydrogen fluctuating shock-induced ignition with a post shock temperature of 1100 K and piston oscillation frequency of 453.5 kHz and amplitude of 20%.

5.4.4 4535 kHz Fluctuation

Increasing the fluctuation frequency to 4535 kHz, the hot-spot ignition disappears, as seen in Fig.5.14, 5.15, 5.16 and 5.17. The ignition in these cases began adjacent to the piston. The reaction initially propagated very slowly but kept accelerating. When the reaction propagated to $\phi = 0.0003$ kg/m^2, the propagation speed rapidly increased. Then, the reaction zone thickness decreased significantly. Finally, a self-driven shock wave formed. The self-driven shock wave caught up with the incident shock wave and generated a detonation. Figure 5.14 exhibits the ignition pattern for the 5% fluctuation level. The ignition delay in this figure is 2.8×10^{-5} s. Figure 5.15 shows the ignition pattern at the 10% fluctuation level. The ignition delay in this figure is 1.8×10^{-5} s. Figure 5.16 gives the ignition result for the 15% fluctuation level. The ignition delay in this figure is 1.3×10^{-5} s. Figure 5.17 provides the simulation result for the 20% fluctuation level. The ignition delay in this figure is 1.0×10^{-5} s. As can be observed, the ignition delay decreases with increasing fluctuation amplitude.

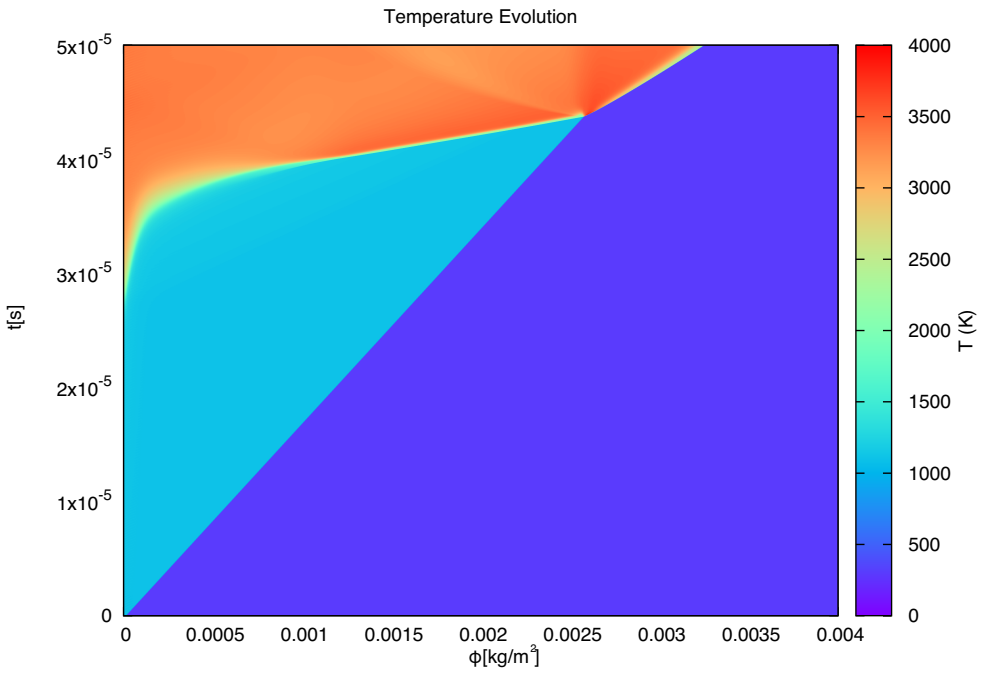

Figure 5.14: Hydrogen fluctuating shock-induced ignition with a post shock temperature of 1100 K and piston oscillation frequency of 4535 kHz and amplitude of 5%.

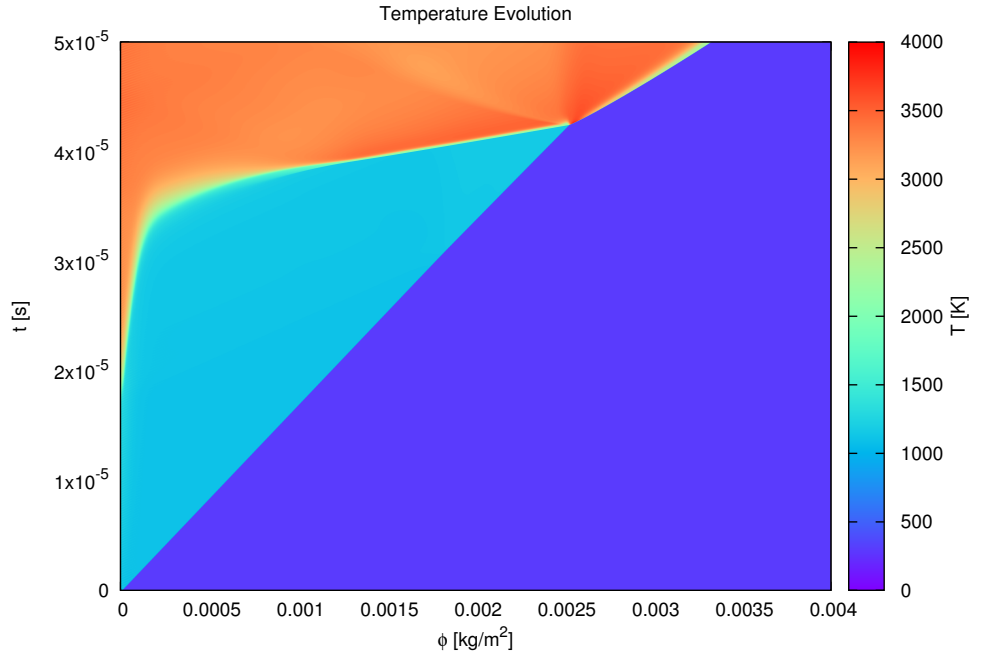

Figure 5.15: Hydrogen fluctuating shock-induced ignition with a post shock temperature of 1100 K and piston oscillation frequency of 4535 kHz and amplitude of 10%.

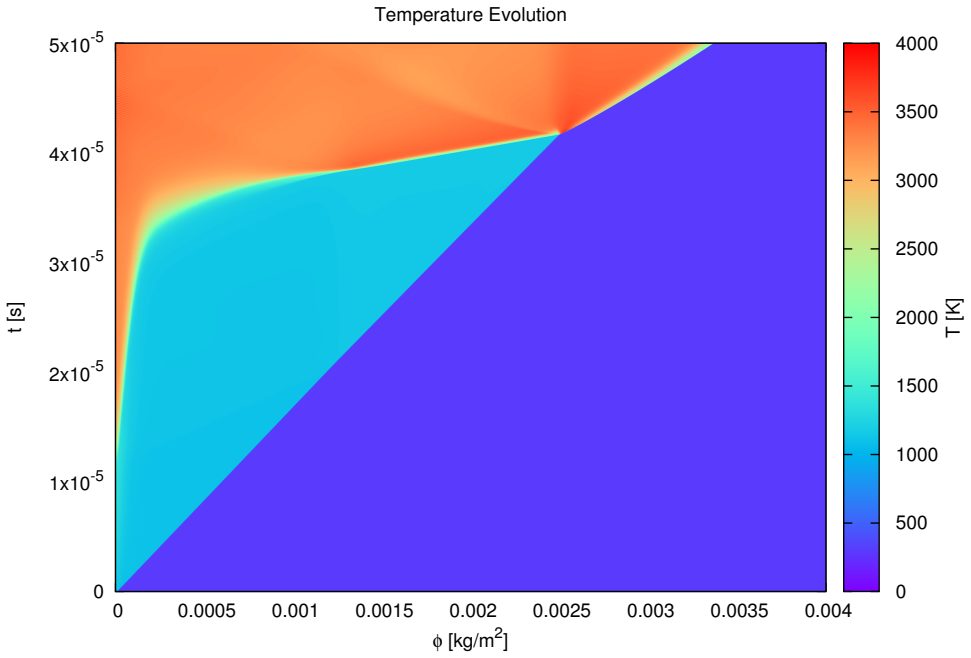

Figure 5.16: Hydrogen fluctuating shock-induced ignition with a post shock temperature of 1100 K and piston oscillation frequency of 4535 kHz and amplitude of 15%.

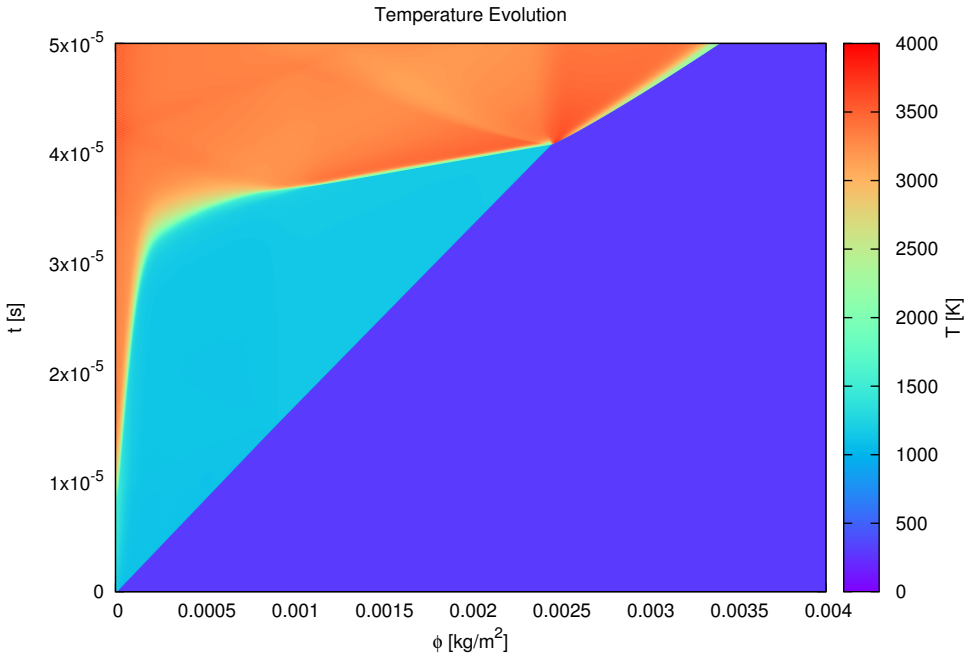

Figure 5.17: Hydrogen fluctuating shock-induced ignition with a post shock temperature of 1100 K and piston oscillation frequency of 4535 kHz and amplitude of 20%.

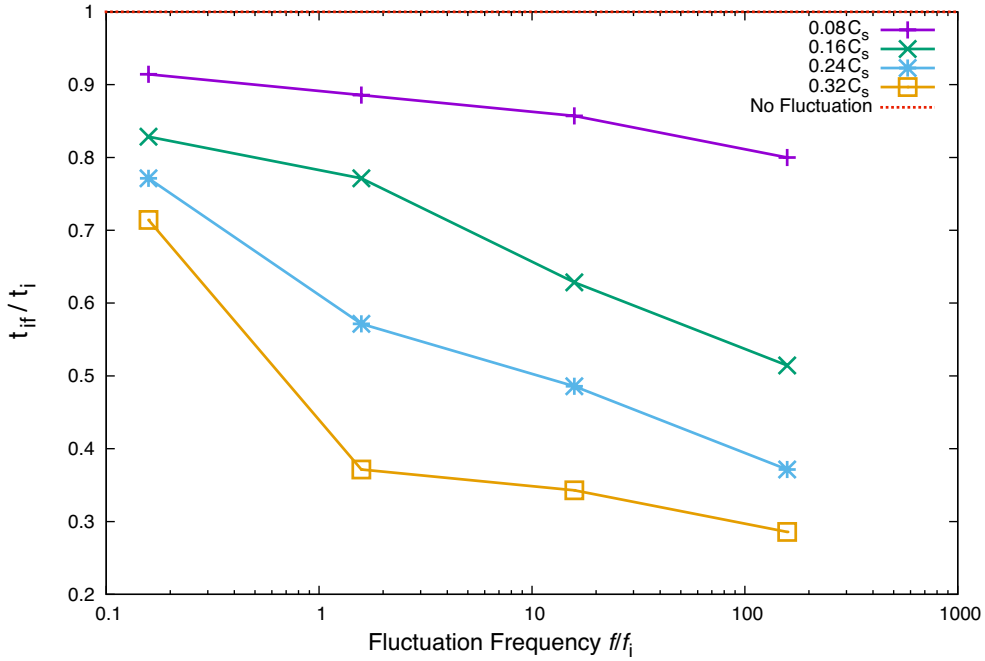

Figure 5.18: The ignition delay changes in different fluctuation circumstance.

5.5 Discussion

The amplitude-frequency study indicates that stronger fluctuations will always speed up the induction process. Figure 5.18 compares the ignition delay of the first ignited gas in each simulation. The x-axis represents the fluctuation frequency and y-axis is the fluctuated ignition delay t_{if} normalized by the non-fluctuated ignition delay, t_i. The frequency values has been non-dimensional by the inverse non-fluctuated ignition delay f_i, and the fluctuation amplitudes has been non-dimensional by the non-fluctuated post-shock sound speed C_s. By increasing the amplitude while maintaining the same frequency, the first ignition delay is shortened. The increasing of frequency also speeds the ignition process.

However, in order to form a detonation, the reaction front must accelerate and form a secondary shock. Figure 5.19 shows the time spent from the start to the point at which the reaction front catch up with the incident shock t_{df}, normalized by the non-fluctuated ignition delay t_i. In this comparison, oscillations of high amplitude promote to detonation-formation. Nonetheless, the increasing frequency does not monotonically influence the detonation formation time. For the case in which the fluctuation period is longer than the ignition delay, the detonation requires at least 3.1×10^{-5} s to form. For the larger frequency of 45.35 kHz, the deflagration to detonation transition (DDT) time is shortened (green lines). This fluctuation period is at the level between the induction time, t_i, and the main reaction time, t_r. Nevertheless, when the frequency is again increased to 453.5 kHz, the DDT time increases which is shown in blue lines. The fluctuation period is still between t_i and t_r. When the frequency is increased to 4535 kHz, the DDT time is very close to the non-fluctuating case and presents small sensitivity to the amplitude. At this frequency,

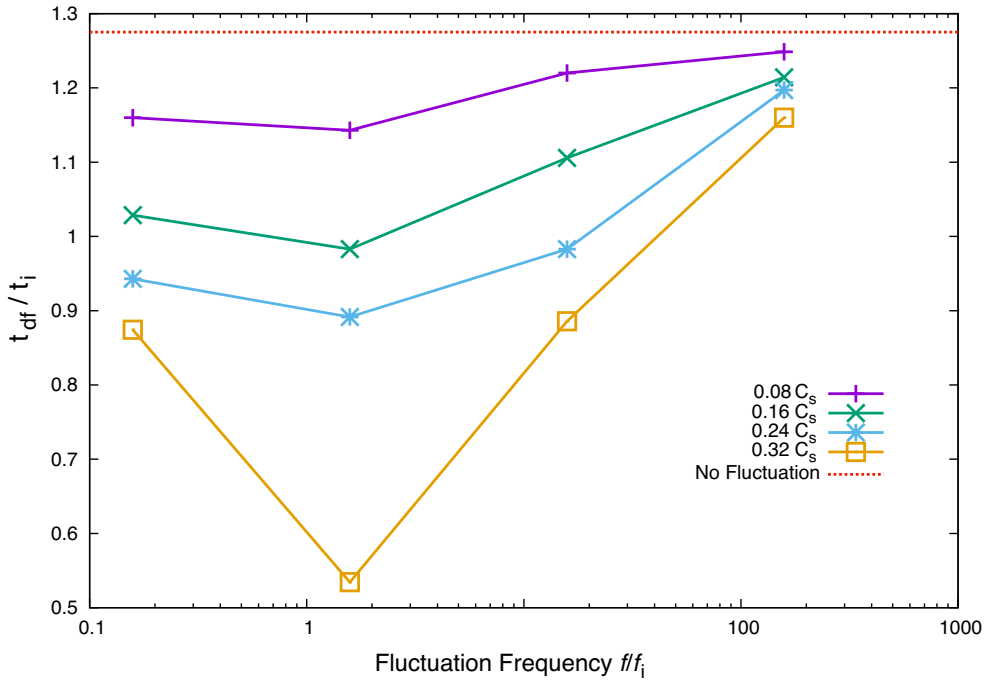

Figure 5.19: The actual time to form detonation in different fluctuation circumstance.

the DDT times are longer than all the cases for other frequencies. This is because of the dissipation phenomenon of the fluctuation. The detailed discussion of this dissipation is in Chapter 4. Comparing the Fig.4.1(453.5 kHz) and Fig.4.3(4535 kHz), the dissipation rate is significantly larger for the latter. Most of the wave energy has been transferred to heat and stored near the piston. The concentration of the energy can hardly promote the acceleration of the reaction front in this case.

Moreover, it is known that a rapid acceleration of the reaction front will occur if the reaction front speed is in phase with the acoustic waves. If the reaction sequence for a hotspot is in phase with the acoustic wave, the initial reaction front can receive the maximum amplification from the hotspot ignition. As can be observed from Fig.5.6, 5.7, 5.8 and 5.9, the ignition sequence of these hotspots are almost in phase with the acoustic waves, which provides an excellent circumstance for reaction front accelerating. It is also found the DDT times for the simulation of this frequency are the shortest, which further indicates that the hotspots that provide the ignition sequence in phase with acoustic waves accelerates DDT substantially.

Chapter 6

Reactive Ethylene-Oxygen Results

6.1 Outline

This chapter reports a series of calculations similar to those of the previous chapter, but focusing on ignition and DDT in ethylene-oxygen. We chose reference states corresponding to the experiments of Saif discussed in the Introduction and analyzed in Chapter 2.

6.2 Initial Condition Settings and Numerical Settings

The initial condition and the shock strength are selected from one of Saif's ethylene-oxygen experiments[37]. The selection of this mixture was based on the characteristics of its kinetics, which permitted numerical simulation at an affordable price. First, a short mechanism optimized for ethylene-oxygen combustion can be used in order to improve the expensive numerical cost on general hydrocarbon combustion [51, 52]. Second, reference experiment data are in 5 mixtures: CH_4+$2O_2$, C_3H_8+$5O_2$, C_2H_6+$7O_2$, C_2H_4+$3O_2$ and $2C_2H_2$+$5O_2$+21Ar. The last mixture is relatively stable and the detonation re-initiation results are relatively clear in each case, which means the fluctuation does not play an important role in this mixture comparing to the other 4 mixtures. The argon-diluted acetylene does not have enough value to investigate in current work. The mixture of C_2H_4+$3O_2$ has the minimum t_i/t_r, for which the requirement for the numerical resolution is the least prohibitive. This is the reason why the ethylene-oxygen system was selected. The initial pressure and temperature are 6200 Pa and 300K, respectively. The piston speed is set to be 1258m/s, which provides the incident shock Mach number $M = 4.50$ and corresponds to the one of the experimental conditions in Saif's work. The reason we selected the case with initial pressure of 6200 Pa is that the Saif's work shows one re-initiation experiment and one experiment without detonation re-initiation [37]. In this condition, the ignition is in low temperature ignition [31]. The CFL number is set to 0.7 and the number of cells is 5000 for all the simulations in this chapter except the case with frequency of 200 kHz and amplitude of 20%. This case used 10000 cells and the CFL number is set to 0.7. The cell number selection rule obeys that the minimum cell number

should be chosen to resolve the reaction zone. For reference, the reaction time for the chosen case is 1.0 μs. In the induction zone, the Lagrangian wave speed is $\rho c = 265.86$ kg/(m^2 s), giving the characteristic reaction zone width of $\Delta\phi = 2.65 \times 10^{-4}$ kg/m^2. This means that approximately 4 points captured the reaction zone.

6.3 Ignition without fluctuations

A numerical solution without fluctuations is shown in Fig.6.1. The first ignition was at $t = 1.42 \times 10^{-3}$ s. In this mixture, the first ignition accelerated fast and quickly formed a secondary shock. The detonation formed at $t = 1.55 \times 10^{-3}$ s. The acceleration was very short so that the reaction propagates at supersonic speed initially after the start. This is owing to the sensitivity of the mixture. In this circumstance, the relative activation energy and t_i/t_r are much higher than for hydrogen-oxygen, as discussed below.

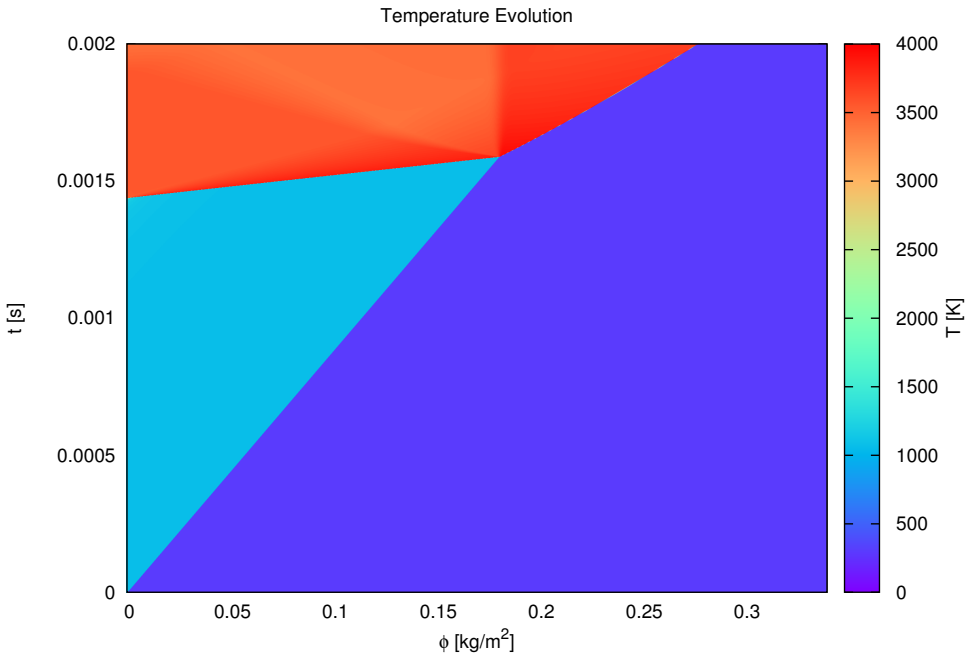

Figure 6.1: Ethylene non-fluctuated shock induced ignition.

6.4 Ignition with Fluctuations

As in the previous chapter, four frequencies and four amplitudes are selected to study the influence of fluctuations on ethylene shock-induced ignition. The four amplitudes are in 5%, 10%, 15% and 20% of the mean speed. The 4 frequencies are 0.2 kHz, 2.0 kHz, 20 kHz and 200 kHz. For ethylene, ignition delay in the non-fluctuated case is $t_i = 1.4 \times 10^{-3}$ s, which

corresponds to the frequency $f_i = 0.71$ kHz and its main reaction time is $t_r = 1.0 \times 10^{-6}$ s, which is related to a frequency $f_r = 1000$ kHz. The four chosen frequencies are all below f_r, but three of them are higher than f_i. This thesis did not conduct simulations at higher frequencies owing to the time cost of the full chemistry simulations. The complete details of the simulations presented in this chapter are shown in Appendix E and the corresponding resolution tests are in Appendix F.

6.4.1 0.2 kHz Fluctuation

The conditions of the first set of cases all use $f = 0.2$ kHz, which is below f_i. At this frequency, one can treat the fluctuation as a constant gradient of temperature in the induction zone since the wave length is greater than the length of the induction zone. Figure 6.2 shows the result for an amplitude of 5% mean speed. In this figure, one can observe that the ignition still started from piston, rather than from hotspots. The first ignition is at 1.05×10^{-3} s. After the first ignition, the reaction quickly accelerates to above the sound speed and drives a strong secondary shock.

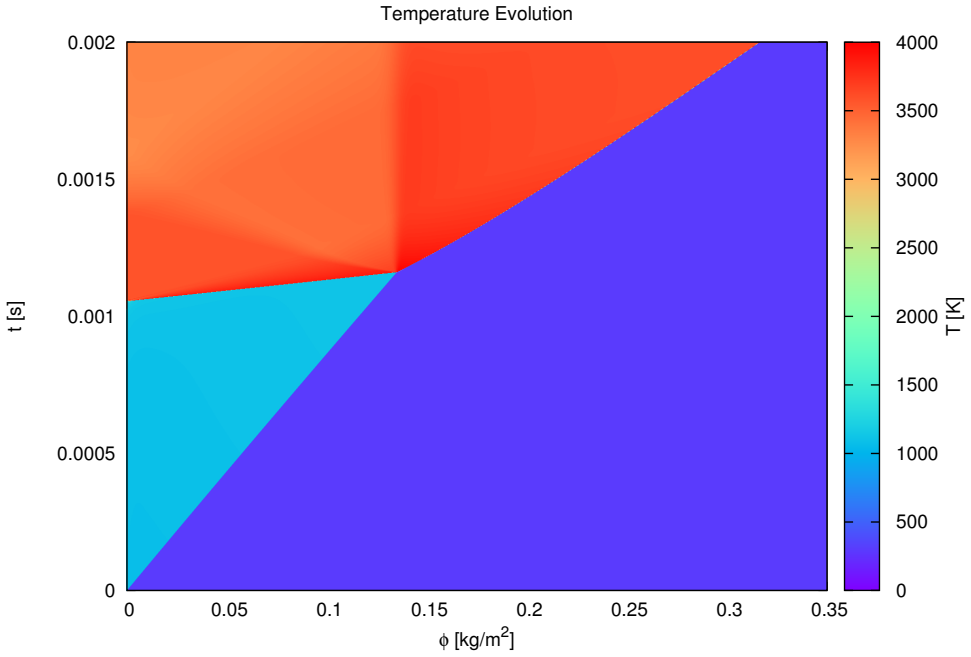

Figure 6.2: Ethylene fluctuating shock-induced ignition with incident shock Mach number of 4.5, and piston oscillation frequency of 0.2 kHz and amplitude of 5%.

Figure 6.3 shows the simulation result obtained with a 10% amplitude and disturbance at 0.2 kHz. The ignition started from the piston. Nevertheless, one is able to observe

a simultaneous ignition, where the reaction pattern becomes horizontal. The presence of simultaneous ignition means the reaction front penetrates into the front of the secondary shock wave, because the ignition sequence around this area is in the opposite phase with the shock sequence. All the gases in that area ignited together at one moment. The shock wave falls behind the reaction front. The first ignition is at 8.5×10^{-4} s and quickly drives a secondary shock. The shock then falls behind the reaction front at $\phi = 0.02$ kg/m^2. Another secondary shock is formed at $\phi = 0.03$ kg/m^2 which is coupled with the reaction front until detonation formation.

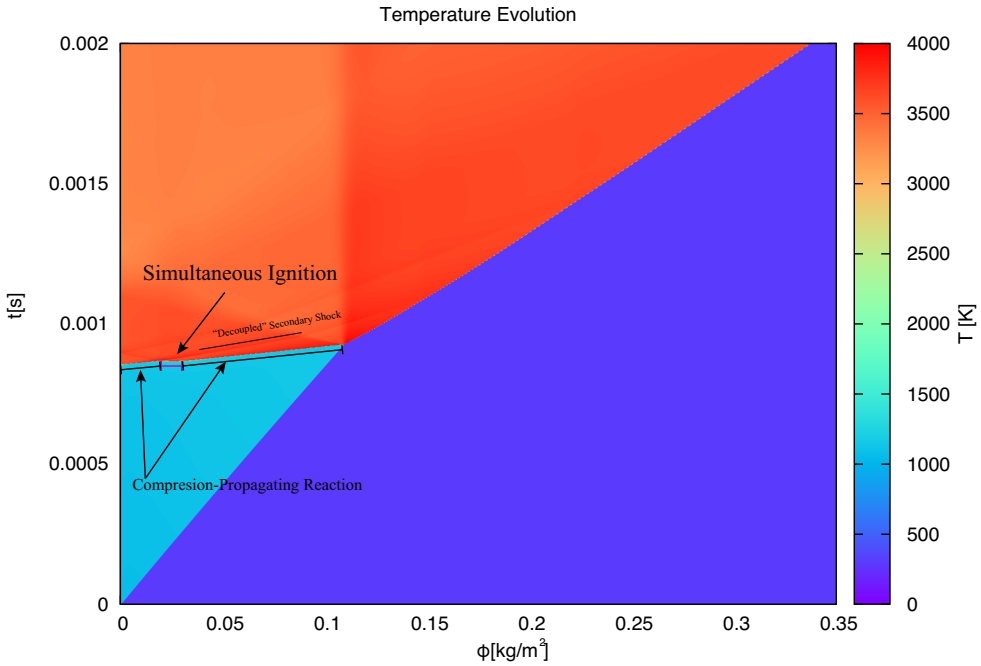

Figure 6.3: Ethylene fluctuating shock-induced ignition with incident shock Mach number of 4.5, and piston oscillation frequency of 0.2 kHz and amplitude of 10%.

Figures 6.4 and 6.5 respectively show the results at the same frequency but with amplitudes of 15% and 20%. The characteristics in these three simulations (amplitude of 10%, 15% and 20%) are the same. The ignitions started from hotspots and generated two shocks. One of the shocks propagated to the right and the other to the left. Both of them are driven by the reaction front. The first ignition is 7.5×10^{-4}s for 15% amplitude and 6.2×10^{-4} s for 20% amplitude, respectively.

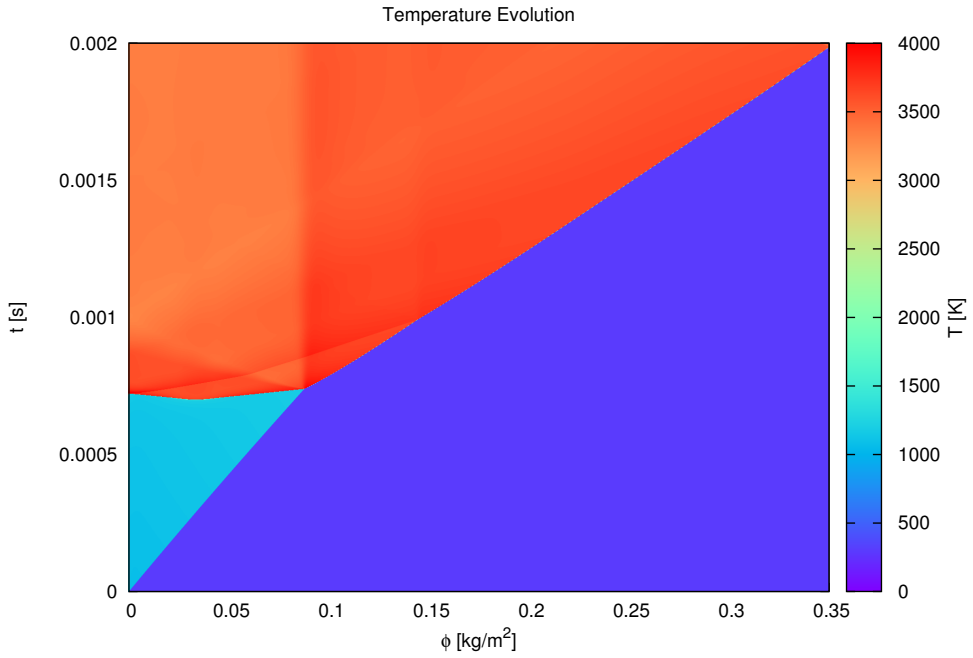

Figure 6.4: Ethylene fluctuating shock-induced ignition with incident shock Mach number of 4.5, and piston oscillation frequency of 0.2 kHz and amplitude of 15%.

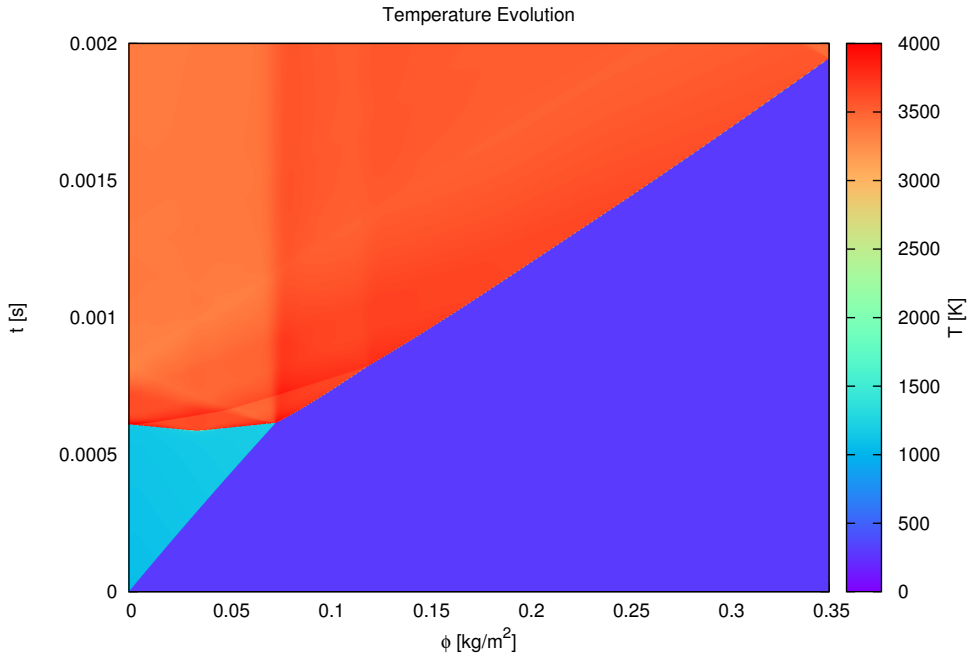

Figure 6.5: Ethylene fluctuating shock-induced ignition with incident shock Mach number of 4.5, and piston oscillation frequency of 0.2 kHz and amplitude of 20%.

6.4.2 2.0 kHz Fluctuation

The ignition patterns for a frequency of 2.0 kHz are qualitatively similar to each other, as shown in Fig 6.6, 6.7, 6.8 and 6.9. The ignitions in these four simulations all started from hotspots. The ignition quickly accelerated to above the sound speed and drove two secondary shocks, with one propagating forward and the other backward. In the 5% amplitude case, the first ignition point was at $\phi_i = 0.02$ kg/m^2 with $t_i = 7.3 \times 10^{-4}$ s.

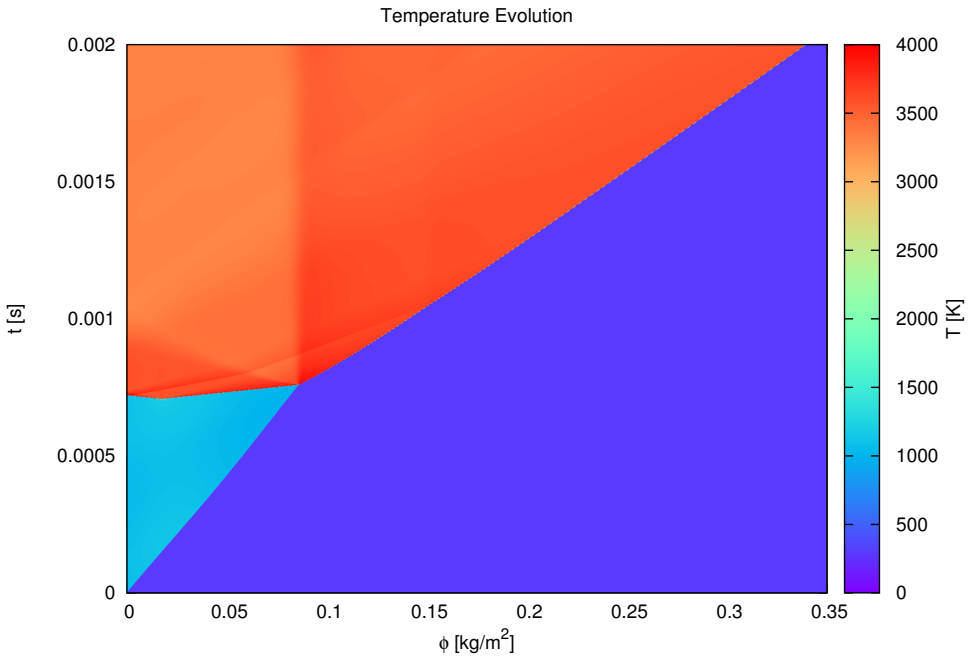

Figure 6.6: Ethylene fluctuating shock-induced ignition with incident shock Mach number of 4.5, and piston oscillation frequency of 2.0 kHz and amplitude of 5%.

When the amplitude is increased to 10% at this frequency, the first ignition delay is reduced substantially, as shown in Fig.6.7. The first ignition delay has been shortened to 2.8×10^{-4} s. Similar to simulation with a 5% amplitude, the first ignition was directly initiated with supersonic speed and propagated both forward and backward.

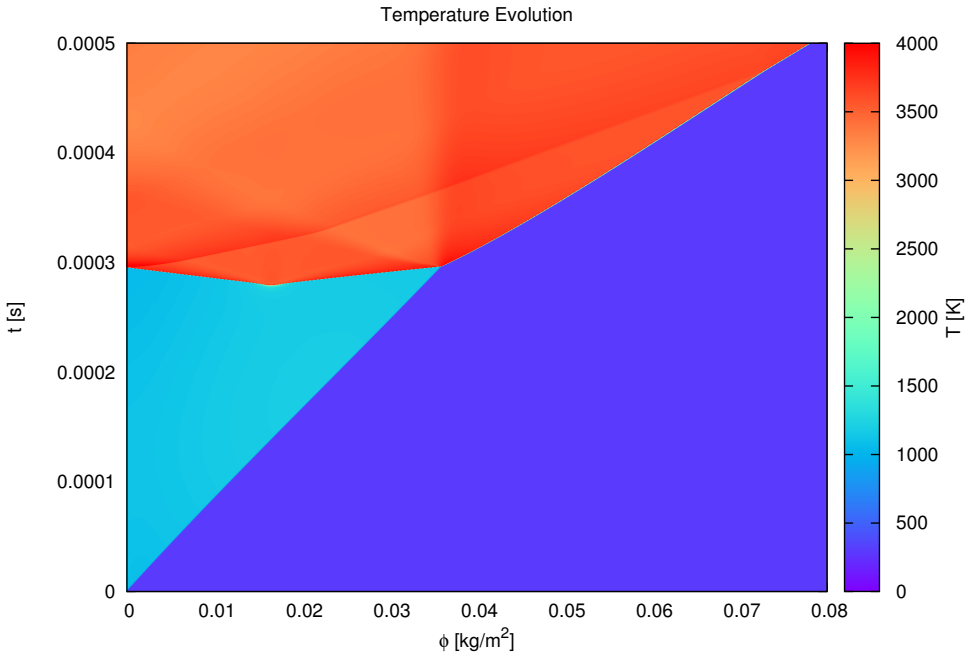

Figure 6.7: Ethylene fluctuating shock-induced ignition with incident shock Mach number of 4.5, and piston oscillation frequency of 2.0 kHz and amplitude of 10%.

Figures 6.8 and 6.9 illustrate the ignition evolution for 15% and 20% amplitude, respectively. The first ignition delays are 1.5×10^{-4} s and 1.2×10^{-4} s for the 15% and 20% amplitude cases, respectively. When the amplitude varies between 10% and 20%, the ignition delay and the detonation-formation time do not show a qualitative change, compared to the more substantial change observed when passing from 0% to 10% at this frequency.

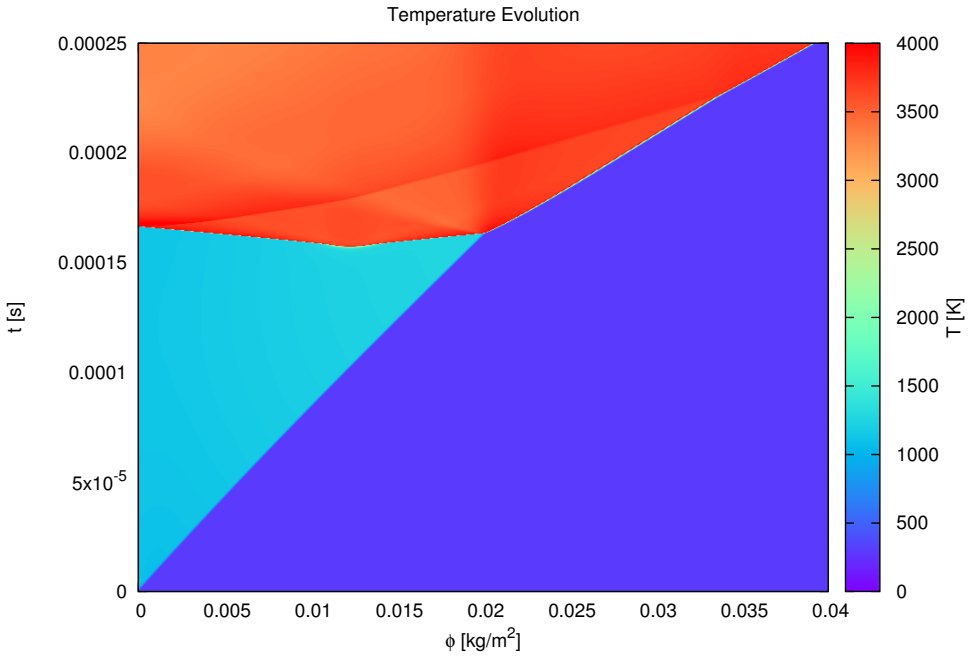

Figure 6.8: Ethylene fluctuating shock-induced ignition with incident shock Mach number of 4.5, and piston oscillation frequency of 2.0 kHz and amplitude of 15%.

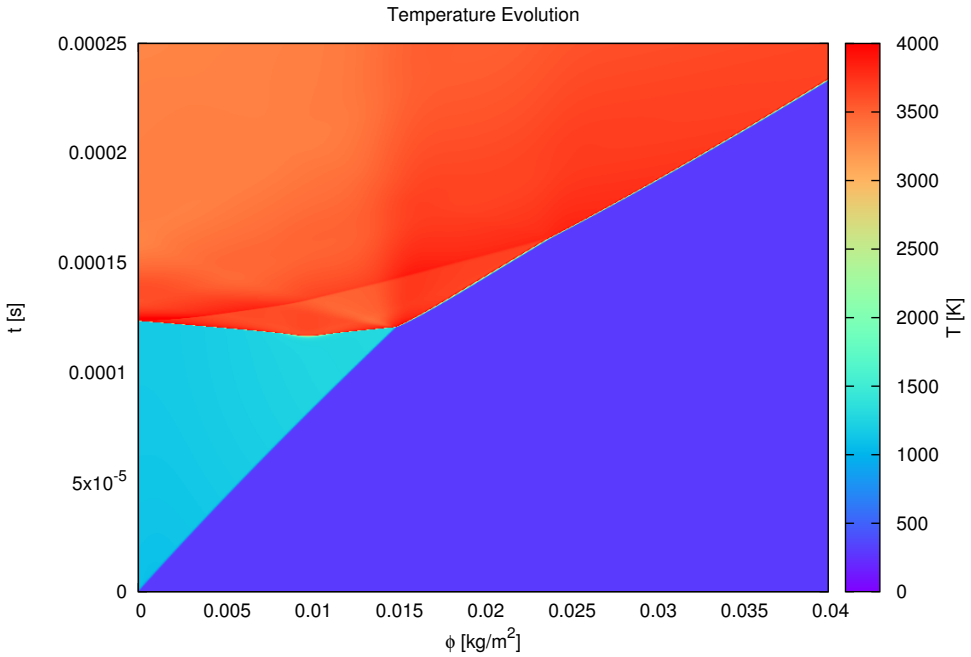

Figure 6.9: Ethylene fluctuating shock-induced ignition with incident shock Mach number of 4.5, and piston oscillation frequency of 2.0 kHz and amplitude of 20%.

6.4.3 20 kHz Fluctuation

The ignition patterns at 20 kHz frequency have different features. Figure 6.10 shows the simulation result with 5% amplitude in this frequency. One can clearly observe fluctuation wave patterns (oblique) and the individual hotspots (vertical). The ignition started at the first hotspot in $\phi_i = 0.002$ kg/m^2 and $t_i = 7.4 \times 10^{-4}$ s. The reaction took about 10^{-5} s to accelerate and form a supersonic reaction front.

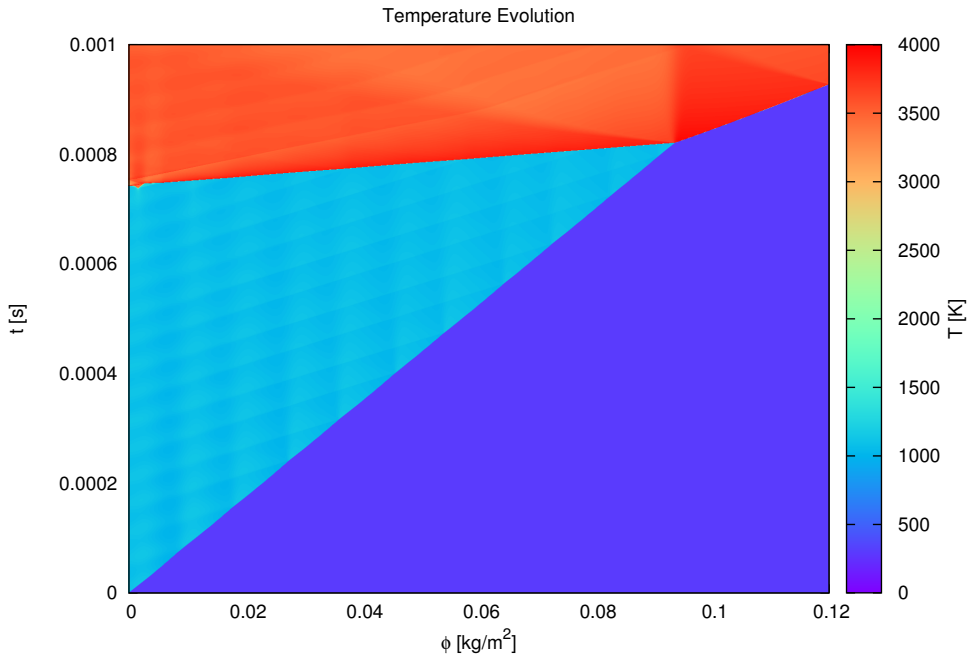

Figure 6.10: Ethylene fluctuating shock-induced ignition with incident shock Mach number of 4.5, and piston oscillation frequency of 20 kHz and amplitude of 5%.

Figure 6.11 provides the simulation result with a 10% amplitude. The result is the same as the 5% simulation, except for the shorter ignition delay and DDT time. In this figure, more details of the reaction front acceleration are shown. The two shock waves were generated from hot-spot ignition. The one propagated towards left and the other to the right. The combustion front decoupled from the two shocks on both sides. The left propagating reaction front quickly accelerated to a supersonic speed and drove another shock before reaching the piston. Such acceleration generated a compression shock wave which propagates to the right. The right propagating reaction front accelerated slower than left one, because the left gas was shocked earlier. It was not in phase with any shock wave until the compression shock wave from the left reached it.

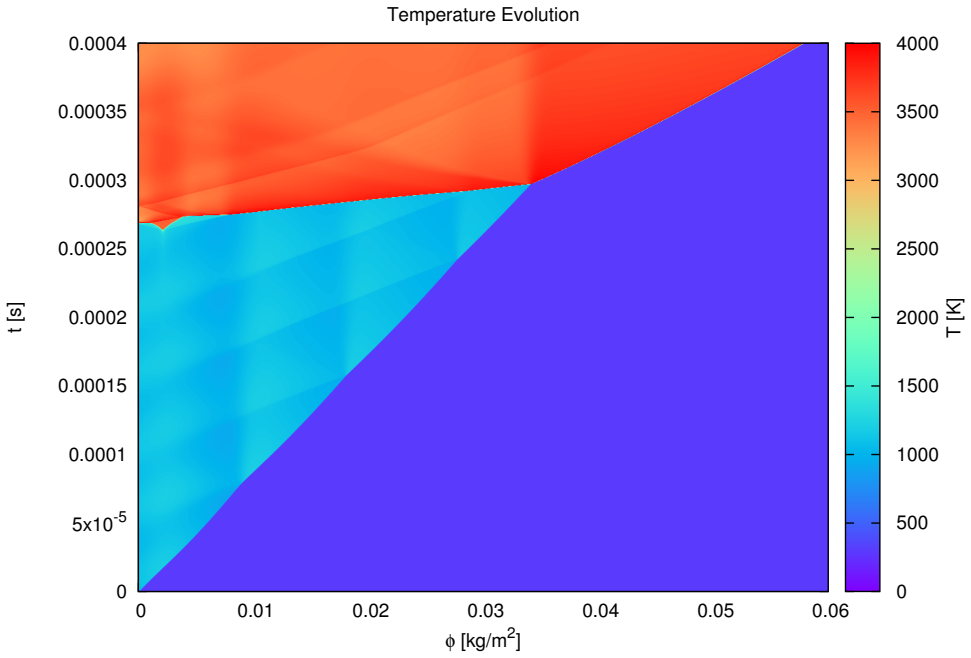

Figure 6.11: Ethylene fluctuating shock-induced ignition with incident shock Mach number of 4.5, and piston oscillation frequency of 20 kHz and amplitude of 10%.

For the 15% amplitude case, the right propagating reaction front accelerates faster than the leftward one, as shown in Fig.6.12. This is owing to the heat distribution in a hotspot, because the shock wave sequence is started at left and ended at right while the hotspots provide the shorter ignition delay at right side within this area. If the leftward propagating wave is accelerated faster, it means the shock sequence dominate the reaction sequence. Nonetheless, if the rightward propagating wave accelerated much faster than the leftward one, the heat redistribution dominates the reaction sequence. The ignition length is comparable with the fluctuation wave length.

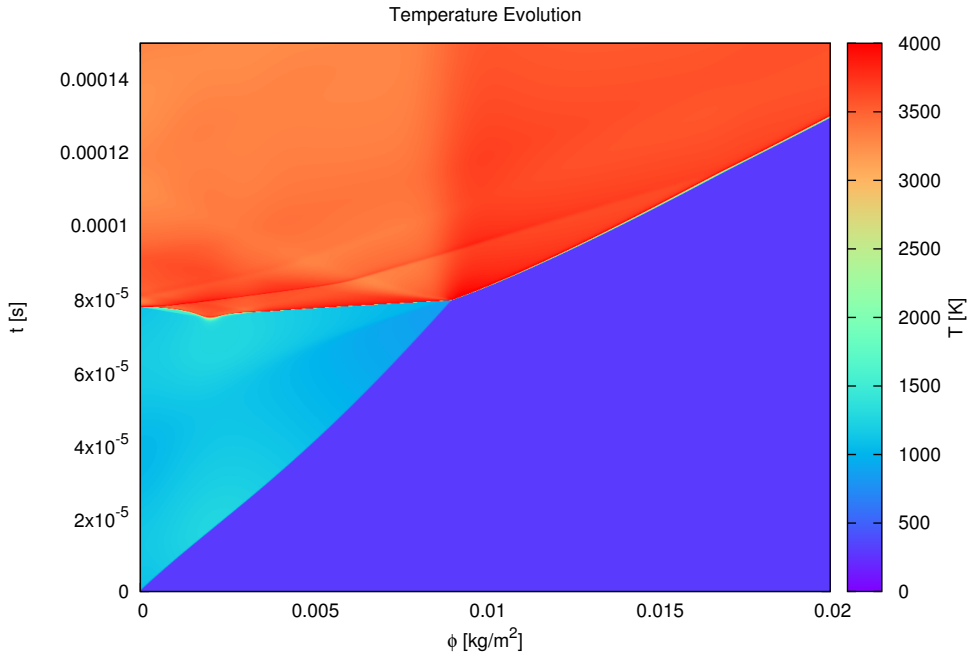

Figure 6.12: Ethylene fluctuating shock-induced ignition with incident shock Mach number of 4.5, and piston oscillation frequency of 20 kHz and amplitude of 15%.

In the 20% amplitude case, the temperature gradient plays a more important role in the reaction front acceleration, which is shown in Fig.6.13. It could be clearly seen that the current ignition delay is shorter than the oscillating period of fluctuation. The right propagating reaction front accelerated much faster than the left propagating reaction front. One could say that the temperature gradient plays more important roles than 15% case. It is because of the sequence of the reaction is controlled by the hotspots. The discussion of this mechanism has been explained in the previous paragraph.

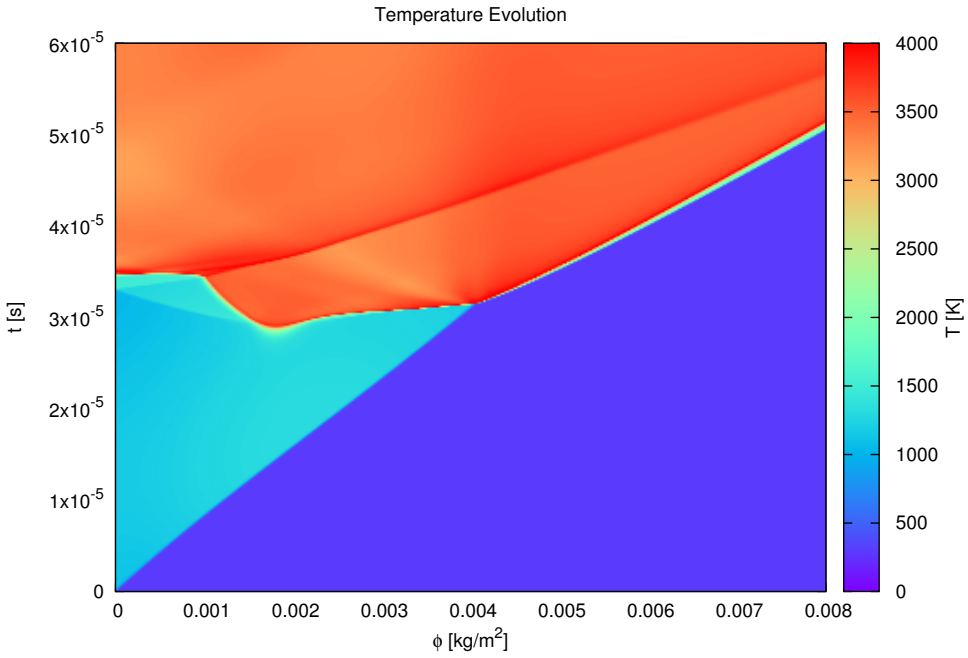

Figure 6.13: Ethylene fluctuating shock-induced ignition with incident shock Mach number of 4.5, and piston oscillation frequency of 20 kHz and amplitude of 20%.

6.4.4 200 kHz Fluctuation

At this frequency, the ignition regime is sensitive to the fluctuation amplitude. With an amplitude of 5%, the ignition started from piston and no hot-spot ignition appears, as shown in Fig.6.14. Increasing the amplitude to 10%, the hotspots appear in Fig.6.15. Such hot-spot reactions quickly accelerated and were in phase with the secondary shock. When the amplitude reaches 15% in Fig.6.16, the hot-spot ignition becomes more significant, and the reaction took longer to drive the secondary shock. The initial speed of the reaction front in this amplitude is very low. The 20% amplitude simulation gives a totally different scenario, as shown in Fig.6.17. The first hotspot ignites very quickly, but the reaction front propagated with a very slow speed. The first two hotspots both ignited very early but neither drove a secondary shock until the end of the simulation. However, the first two ignition hotspots fortified the compression fluctuation shock.

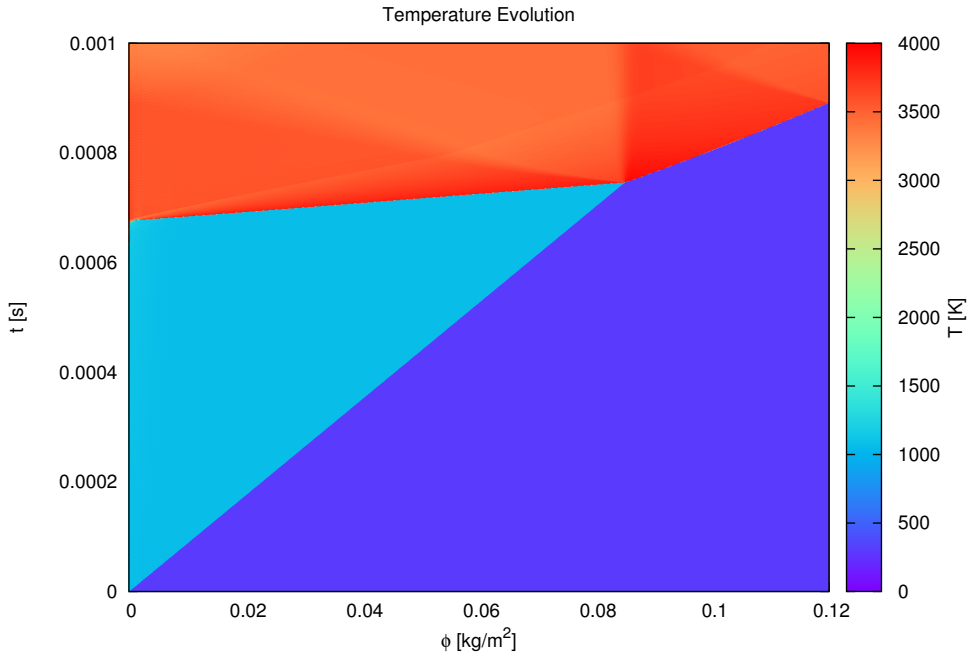

Figure 6.14: Eythane fluctuated shock-induced ignition($\bar{up}$ =1258m/s, frequency=200 kHz and amplitude of 5%.

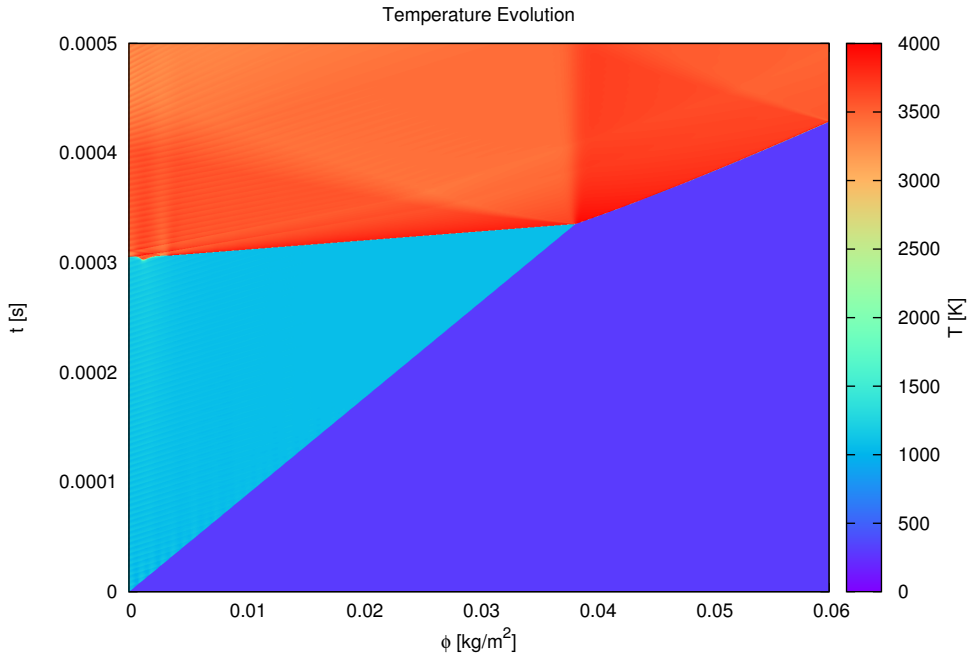

Figure 6.15: Ethylene fluctuating shock-induced ignition with incident shock Mach number of 4.5, and piston oscillation frequency of 200 kHz and amplitude of 10%.

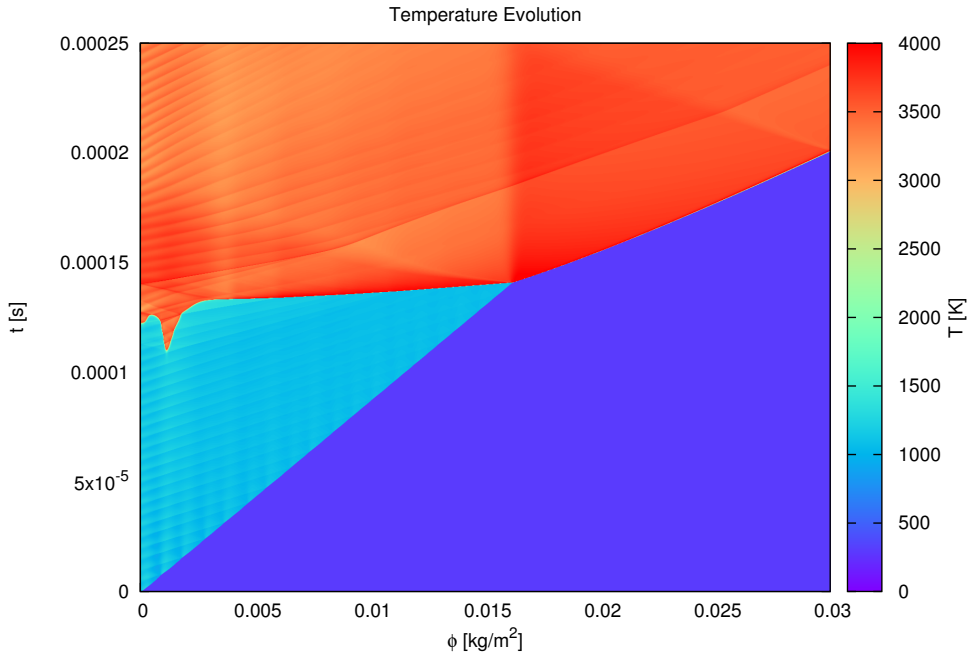

Figure 6.16: Ethylene fluctuating shock-induced ignition with incident shock Mach number of 4.5, and piston oscillation frequency of 200 kHz and amplitude of 15%.

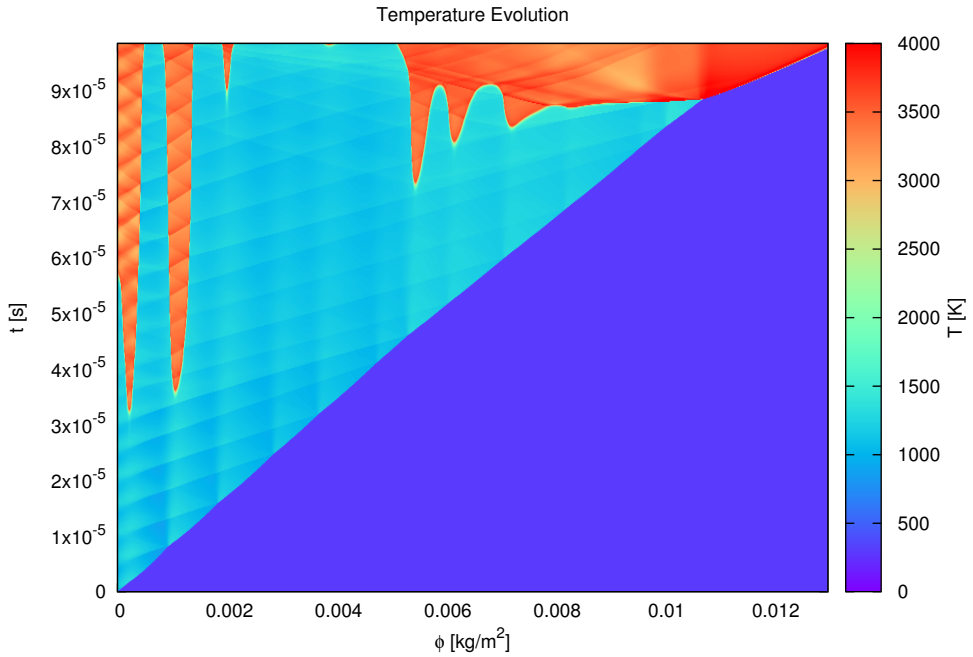

Figure 6.17: Ethylene fluctuating shock-induced ignition with incident shock Mach number of 4.5, and piston oscillation frequency of 200 kHz and amplitude of 20%.

6.5 Discussion

The effects that the fluctuations produced on detonation formation are quite different between the simulation of hydrogen and ethylene. The main reason comes from the difference in the sensitivity of the ignition delay to temperature changes, which has the form

$$t_i \sim e^{\frac{E_a}{RT}}, \tag{6.1}$$

where E_a is activation energy and R is universal gas constant, and T is the temperature in the induction zone. The sensitivity of the induction time can be expressed as:

$$\left| \frac{T}{t_i} \frac{dt_i}{dT} \right| = \frac{E_a}{RT}. \tag{6.2}$$

For the conditions of the numerical simulations, the reduced activation energy for hydrogen system is $\frac{E_a}{RT} = 8.60$, while it is 20.44 for the ethylene system. In the present work, these global activation energies are extracted from Cantera simulations at constant volume by perturbing the initial temperatures.

Note also that the ratio of induction to reaction time is also much larger in the ethylene system ($t_i/t_r = 1408.45$) than it is in the hydrogen system ($t_i/t_r = 6.60$). This explains why the acceleration of the reaction front is much larger in the ethylene system. This is fully compatible with the analytical predictions of Sharpe [41] and Tang & Radulescu [46] for shock induced ignition in a gas described by an induction-reaction two-step model.

Other general trends are noteworthy. When the effects of amplitude change are isolated, one finds that the detonation formation time monotonically decreases with increasing amplitude. Despite that, the effect of the amplitude becomes less pronounced at higher amplitudes. The curve of the detonation-formation time is monotonically decreasing, but the absolute slope gradually reduces. One could reasonably speculate that there is a saturation limit of the detonation formation time under which an increase of the fluctuation amplitude would no longer control the detonation formation time. This saturation limit may be controlled by the exothermic time.

The analysis of the frequency dependence shows that an increase in frequency does not monotonically reduce the time to detonation formation. At relatively low frequency, an increase of frequency can advance the detonation formation. Nevertheless, increasing the frequency would prevent detonation formation if the frequency is above a critical value. This value is between f_i and f_r for the two mixtures investigated. The reason for this phenomenon is that the high frequency mechanical oscillation would transform to shock waves very quickly. These oscillated shock waves would dissipate the energy to the local gas and fail to propagate over long distances, as discussed in Chapter 4. The dissipation would generate only localized hotspots, and the temperature of hotspots does not have a

significant effect on detonation development. The hotspots would ignite at an early stage, but whether such ignition would be able to develop to detonation depends on the size of hotspot. If the hotspot is too small, the ignition would not be able to accelerate to local sound speed. At moderate frequency, hotspots with a proper size will form and promote detonation formation. The very high frequency, hotspots will be generated and advance the first ignition, but the hotspots would be too small to develop to detonation. On the other hand, oscillations with extremely low frequency would not generate hotspots, because the oscillations are too slow and the detonation would have been generated before the hotspot formed.

In some high-frequency high-amplitude simulations, the detonation generation is a complicated process, as shown in Fig.6.17. First, the oscillation in the early stage generated small hotspots. These hotspots were ignited locally. Then, the ignition released a compression wave to the unburnt gas. Some parts of compression wave merged with the compression fluctuations sent from piston and intensified the fluctuation. The intensified fluctuation generated secondary hotspots when interacting with the leading shock. These secondary hotspots have different sizes since the intensified fluctuation wave have different strength. The large hotspots finally developed to detonation.

Figure 6.18 shows the first ignition delay changes for different fluctuation conditions. Different from the hydrogen high temperature ignition plot, here the y-axis is in logarithmic scale, because the ignition delay is exponential related to the temperature which has been controlled by fluctuation amplitude in the simulations. Like the hydrogen result in Fig.5.18, ignition delay decreased monotonously with increasing amplitude. As frequency changes from 0.2 kHz to 2 kHz, the induction delay is shortened significantly. Nevertheless, further increasing the frequency to 20 kHz, the ignition delay does not change in the cases with fluctuation amplitude of 5% or 10%. Such discrepancy of the ignition delay only appears in strong fluctuation amplitude case(15% and 20%). There is little difference between the $20kHz$ line and $200kHz$ line in the test amplitude range.

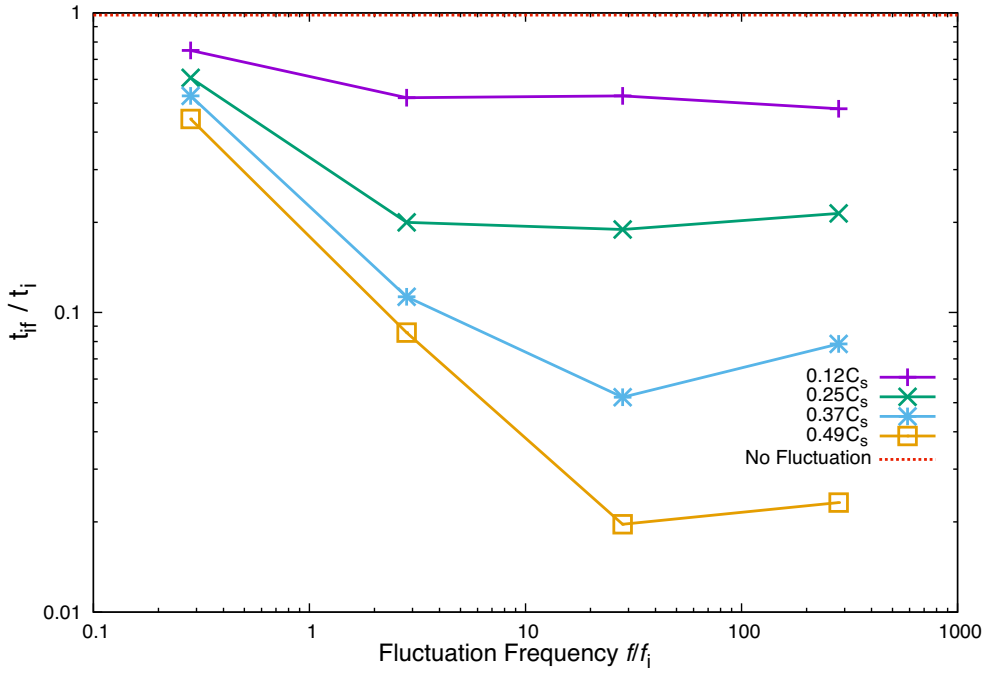

Figure 6.18: The ignition delay changes in different fluctuation circumstance.

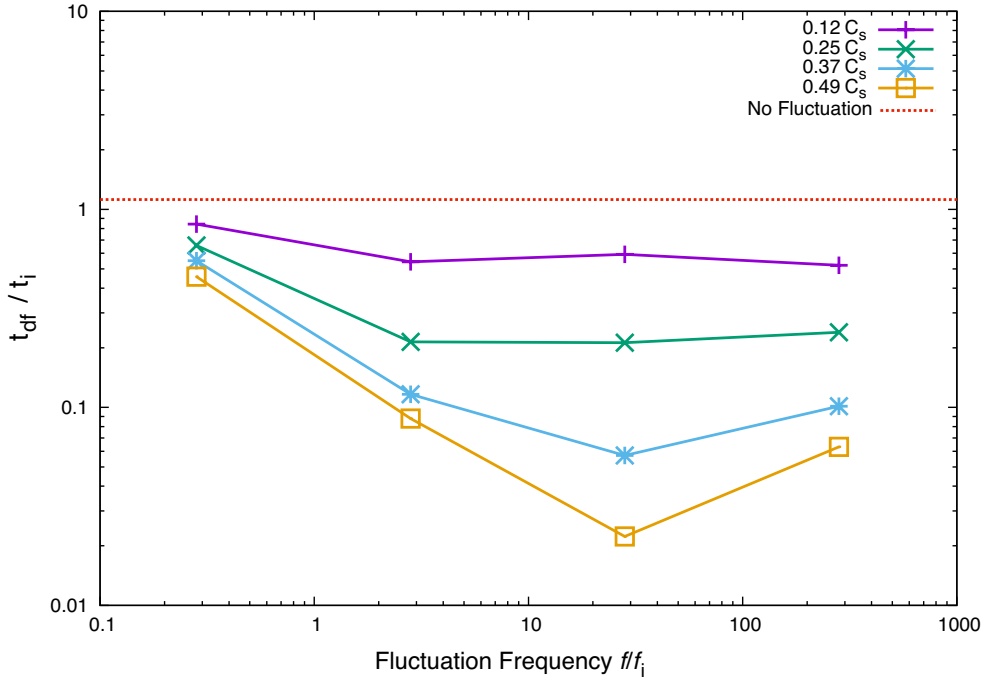

Figure 6.19: The actual time to form detonation in different fluctuation circumstance.

Figure 6.19 shows the time that the reactive secondary shock caught up with the in-

cident shock, which is the detonation formation point. It is shown that an increasing in amplitude always decreases the detonation-formation time. For the frequency, the cases oscillating at 0.2 kHz has always much longer detonation formation time than others. This is because only this frequency is below f_i. From other three lines, one can observe that this is frequency of 20 kHz the ignition delay is minimized. Either intensifying the frequency to 200 kHz or reducing it to 2 kHz delays the detonation formation.

The current work does not take the phase effect into the consideration. It can be supposed that the initial phase would have high effect if the fluctuation frequency is comparable or lower than the characteristic frequency associated with the induction process. In a relative high frequency the initial fluctuation phase is not expected to play a significant role, as many oscillation periods exist prior to ignition. One of the future work could be on this direction.

The fluctuations in the current study are in 1D. In a 3D situation, these fluctuations come from the fast flame, the transverse waves and other instabilities from upstream. Such fluctuations lead to the formation of hotspots. The hotspot ignition may accelerate to a speed which is in phase with acoustic wave, or decouple from the acoustic. If the ignition decouples from the acoustic, it will create new fluctuations, which may trigger the formation of secondary hotspot. Finally, one of the hotspot ignition is able to maintain the speed in phase with acoustic, and lead to detonation. Such hotspot ignition is complex.

Chapter 7

Conclusion

7.1 Contributions to the State of Knowledge

The main contributions to the state of knowledge of the present thesis are as follows:

1. A quasi-1D model capable of estimating the transmitted shock speed in the detonation-obstruction problem by means of solving the gasdynamic equilibrium equations and implementing appropriate combustion assumptions has been proposed. The results, based on the CJ-deflagration assumptions, have been compared with experimental data. The predicted transmitted shock speed exhibits a very good agreement with experimental data, which further proves that the fast flames are CJ deflagrations. The results of the present thesis thus suggest that a *sufficient* condition for detonation formation is that the reaction front burning velocity is close the Chapman Jouguet value.

2. A 1D shock-induced ignition model has been used to analyze the detonation-initiation time by considering the mechanical fluctuations in different conditions. The present work shows that the mechanical fluctuation could be the dominant factor in determining the DDT time scale, which explains why the DDT time scale shows significant discrepancies in some experiments which have the same initial conditions. Quantitative results and qualitative analysis have been obtained. The quantitative results shows that the fluctuations with a period between the ignition delay and exothermic time scale can shorten the DDT process significantly. An optimal fluctuation period exists between these two time scales. It is found that the presence of hotspots in the induction zone is paramount for enhancing the DDT process. Analysis and inert simulations revealed the two gasdynamic phenomena which contribute to the induction-zone hotspot formation. The first effect is fluctuation-leading-shock interaction, which forms local hotspots. The second novel phenomena discovers the "N" wave dissipation mechanism, which concentrates the wave energy close to the source of fluctuations, promoting local hot spot creation.

7.2 Future Work

An immediate future work is the expansion of cases studied to different fluctuation amplitudes and frequencies. The phase and the wave shape effect should be analyzed in further detail. More detonation-obstruction experiment with variation of obstruction size could also be obtained. The application of the current work and future work could ultimately help predicting the DDT timescale in some critical conditions where DDT is very sensitive and transition time are difficult to predict. By favoring fluctuations at certain wavelengths or filtering fluctuations at other wavelengths, one may able to control the DDT in these critical conditions.

Bibliography

[1] L. Bauwens. Ignition between a shock and a contact surface: Influence of the downstream temperature. *Proceedings of the Combustion Institute*, 28(1):653 – 661, 2000.

[2] T.V. Bazhenova and V.V. Golub. Use of gas detonation in a controlled frequency mode. *Combustion, Explosion, and Shock Waves*, 39(4):365–381, 2003.

[3] P.E.M. Berthelot and P. Vieille. Nouvelles recherches sur la propagation des phénomènes explosifs dans les gaz. *CR Acad. Sci. Paris*, 95:151–157, 1882.

[4] R.R. Bhattacharjee, S.S-M. Lau-Chapdelaine, G. Maines, L. Maley, and M.I. Radulescu. Detonation re-initiation mechanism following the mach reflection of a quenched detonation. *Proceedings of the Combustion Institute*, 34(2):1893–1901, 2013.

[5] S. Browne, J Ziegler, and J.E. Shepherd. Numerical solution methods for shock and detonation jump conditions. *Energy Conservation*, 1(w2):w2, 2004.

[6] J. Chao. *Critical deflagration waves that lead to the onset of detonation*. PhD thesis, McGill University, Montreal,QC,Canada, 2006.

[7] R.S. Chue, J.F. Clarke, and J.H.S. Lee. Chapman–Jouguet deflagrations. *Proc. R. Soc. Lond. A*, 441(1913):607–623, 1993.

[8] R.S. Chue, J.H.S. Lee, and F. Zhang. Transition from fast deflagration to detonation under the influence of periodic longitudinal perturbations. *Shock Waves*, 5(3):159–167, Oct 1995.

[9] G. Ciccarelli and S. Dorofeev. Flame acceleration and transition to detonation in ducts. *Progress in Energy and Combustion Science*, 34(4):499 – 550, 2008.

[10] J.F. Clarke. Fast flames, waves and detonation. *Progress in Energy and Combustion Science*, 15(3):241 – 271, 1989.

[11] J.F. Clarke and R.S. Cant. Non-steady gas dynamic effects in the induction domain behind a strong shock wave. Technical report, Cranfield Institute of Technology, 1982.

[12] R. Courant, K. Friedrichs, and H. Lewy. Über die partiellen differenzengleichungen der mathematischen physik. *Mathematische annalen*, 100(1):32–74, 1928.

[13] E. Dziemiska and A. Koichi Hayashi. Auto-ignition and ddt driven by shock wave boundary layer interaction in oxyhydrogen mixture. *International Journal of Hydrogen Energy*, 38(10):4185 – 4193, 2013.

[14] B. Einfeldt. On godunov-type methods for gas dynamics. *SIAM Journal on Numerical Analysis*, 25(2):294–318, 1988.

[15] W. Fickett and W.C. Davis. *Detonation: theory and experiment*. Courier Corporation, 2012.

[16] S.K. Godunov. A difference method for numerical calculation of discontinuous solutions of the equations of hydrodynamics. *Matematicheskii Sbornik*, 89(3):271–306, 1959.

[17] S.K. Godunov and V.S. Ryabenki. Theory of difference schemes-an introduction. *Amsterdam: North Holland, 1964*, 1964.

[18] D.G. Goodwin, H.K. Moffat, and R.L. Speth. Cantera: An object-oriented software toolkit for chemical kinetics, thermodynamics, and transport processes. http://www.cantera.org, 2017. Version 2.3.0.

[19] J.S. Grondin and J.H.S. Lee. Experimental observation of the onset of detonation downstream of a perforated plate. *Shock Waves*, 20(5):381–386, 2010.

[20] T.L. Jackson and A.K. Kapila. Shock-induced thermal runaway. *SIAM Journal on Applied Mathematics*, 45(1):130–137, 1985.

[21] A.K. Kapila, D.W. Schwendeman, J.J. Quirk, and T. Hawa. Mechanisms of detonation formation due to a temperature gradient. *Combustion Theory and Modelling*, 6(4):553–594, 2002.

[22] J.H.S. Lee. *The detonation phenomenon*, volume 2. Cambridge University Press Cambridge, 2008.

[23] J.H.S. Lee and I.O. Moen. The mechanisms of transition from deflagration to detonation in vapor cloud explosions. *Progress in Energy and Combustion Science*, 6(4):359 – 389, 1980.

[24] R.J. LeVeque. *Finite volume methods for hyperbolic problems*, volume 31. Cambridge university press, 2002.

[25] J. Li, Z. Zhao, A. Kazakov, and F.L. Dryer. An updated comprehensive kinetic model of hydrogen combustion. *International journal of chemical kinetics*, 36(10):566–575, 2004.

[26] L. Maley. *On shock reflections in fast flames*. PhD thesis, M. Sc Thesis, Department of Mechanical Engineering, University of Ottawa, Ottawa, ON, 2015.

[27] L. Maley, R. Bhattacharjee, S.S-M. Lau-Chapdelaine, and M.I. Radulescu. Influence of hydrodynamic instabilities on the propagation mechanism of fast flames. *Proceedings of the Combustion Institute*, 35(2):2117 – 2126, 2015.

[28] B. Maxwell, A. Pekalski, and M.I. Radulescu. Modelling of the transition of a turbulent shock-flame complex to detonation using the linear eddy model. *Combustion and Flame*, 192:340 – 357, 2018.

[29] B.J. McBride and S. Gordon. *Computer Program for Calculation of Complex Chemical Equilibrium Compositions and Applications: II.* Nationa Aeronautics and Space Administration, Office of Management , 1996.

[30] J. Melguizo-Gavilanes, N. Rezaeyan, M. Tian, and L. Bauwens. Shock-induced ignition with single step arrhenius kinetics. *International Journal of Hydrogen Energy*, 36(3):2374 – 2380, 2011. The Third Annual International Conference on Hydrogen Safety.

[31] J.W. Meyer and A.K. Oppenheim. On the shock-induced ignition of explosive gases. In *Symposium (International) on Combustion*, volume 13, pages 1153–1164. Elsevier, 1971.

[32] C.J. Montgomery, A.M. Khokhlov, and E.S. Oran. The effect of mixing irregularities on mixed-region critical length for deflagration-to-detonation transition. *Combustion and Flame*, 115(1):38 – 50, 1998.

[33] A.Y. Poludnenko, T.A. Gardiner, and E.S. Oran. Spontaneous transition of turbulent flames to detonations in unconfined media. *Physical Review Letters*, 107(5):054501, 2011.

[34] M.I. Radulescu, W. Wang, M Saif, M Levin, and A Pekalski. On Chapman Jouguet deflagrations. In *Proceedings of 25th International Colloquium on the Dynamics of Explosions and Reactive Systems*, 2015.

[35] P.L. Roe. Approximate riemann solvers, parameter vectors, and difference schemes. *Journal of computational physics*, 43(2):357–372, 1981.

[36] G.D. Roy, S.M. Frolov, A.A. Borisov, and D.W. Netzer. Pulse detonation propulsion: challenges, current status, and future perspective. *Progress in Energy and Combustion Science*, 30(6):545–672, 2004.

[37] M. Saif. Run-up distance from deflagration to detonation in fast flames. Master's thesis, University of Ottawa, April 2016.

[38] M. Saif, W. Wang, A. Pekalski, M. Levin, and M.I. Radulescu. Chapman–Jouguet deflagrations and their transition to detonation. *Proceedings of the Combustion Institute*, 36(2):2771–2779, 2017.

[39] G. J. Sharpe and M. Short. Detonation ignition from a temperature gradient for a two-step chain-branching kinetics model. *Journal of Fluid Mechanics*, 476:267292, 2003.

[40] G.J. Sharpe. Shock-induced ignition for a two-step chain-branching kinetics model. *Physics of Fluids*, 14(12):4372–4388, 2002.

[41] G.J. Sharpe. Shock-induced ignition for a two-step chain-branching kinetics model. *Physics of Fluids*, 14(12):4372–4388, 2002.

[42] G.J. Sharpe and M. Short. Shock induced ignition of thermally sensitive explosives. *IMA Journal of Applied Mathematics*, 69(5):493–520, 2004.

[43] M. Short. On the critical conditions for the initiation of a detonation in a nonuniformly perturbed reactive fluid. *SIAM Journal on Applied Mathematics*, 57(5):1242–1280, 1997.

[44] M. Short and J.W. Dold. Unsteady gasdynamic evolution of an induction domain between a contact surface and a shock wave. i: Thermal runaway. *SIAM Journal on Applied Mathematics*, 56(5):1295–1316, 1996.

[45] D.W. Stamps and M. Berman. High-temperature hydrogen combustion in reactor safety applications. *Nuclear science and engineering*, 109(1):39–48, 1991.

[46] J. Tang and M.I. Radulescu. Dynamics of shock induced ignition in ficketts model: Influence of χ. *Proceedings of the Combustion Institute*, 34(2):2035–2041, 2013.

[47] H.T. Tizard. *The Causes of Detonation in Internal-Combustion Engines*. North East Coast Institution of Engineers and Shipbuliders, 1921.

[48] E.F. Toro, M. Spruce, and W. Speares. Restoration of the contact surface in the hll-riemann solver. *Shock waves*, 4(1):25–34, 1994.

[49] D.M. Valiev, V. Bychkov, V. Akkerman, L.E. Eriksson, and C.K. Law. Quasi-steady stages in the process of premixed flame acceleration in narrow channels. *Physics of Fluids*, 25(9):096101, 2013.

[50] G.D. Van Albada, B. Van Leer, and W.W. Roberts. A comparative study of computational methods in cosmic gas dynamics. In *Upwind and High-Resolution Schemes*, pages 95–103. Springer, 1997.

[51] B. Varatharajan and F.A. Williams. Ethylene ignition and detonation chemistry, part 1: Detailed modeling and experimental comparison. *Journal of Propulsion and Power*, 18(2):344–351, 2002.

[52] B. Varatharajan and F.A. Williams. Ethylene ignition and detonation chemistry, part 2: Ignition histories and reduced mechanisms. *Journal of Propulsion and Power*, 18(2):352–362, 2002.

[53] Gerald Beresford Whitham. *Linear and nonlinear waves*, volume 42. John Wiley & Sons, 2011.

APPENDICES

Appendix A

Mathematical Derivation of CJ-Deflagration Conditions

In Chapter 2, jump conditions accross a CJ deflagration are used in the quasi-one-dimensional analysis. Relevant relations are derived in this appendix. Conservation laws and sonic relations are used to solve the Chapman-Jouguet condition and to obtain the deflagration conditions. The CJ Deflagration wave has a unique property that the particle speed behind the wave is sonic in the wave frame of reference. In this CJ frame of reference, the incoming flow has a velocity of u_z, a pressure of P_z, a density of ρ_z and an isentropic expansion coefficient of γ_z. Correspondingly, the burnt gas has velocity of u_y, pressure of P_y, density of ρ_y and an isentropic expansion coefficient of γ_y. The specific heat release is q. Across the CJ deflagration wave, mass conservation and momentum conservation gives

$$\rho_y \left(u_y - u_{\mathrm{CJ}}\right) = \rho_z \left(u_z - u_{\mathrm{CJ}}\right),$$

$$\left(\rho_y \left(u_y - u_{\mathrm{CJ}}\right)\right)^2 + P_y = \left(\rho_z \left(u_z - u_{\mathrm{CJ}}\right)\right)^2 + P_z.$$

Across the CJ deflagration wave, the Hugoniot curve gave us

$$h_y \rho_y \left(u_y - u_{\mathrm{CJ}}\right) - h_z \rho_z \left(u_z - u_{\mathrm{CJ}}\right) = \dot{M} q,$$

where the mass flow rate is

$$\dot{M} = \rho_y \left(u_y - u_{\mathrm{CJ}}\right) = \rho_z \left(u_z - u_{\mathrm{CJ}}\right).$$

energy conservation can therefore be simplified as

$$h_y - h_z = q.$$

Using the perfect-gas expression for enthalpy gives

$$\frac{1}{2}\left(\left(u_y - u_{\mathrm{CJ}}\right)^2 - \left(u_z - u_{\mathrm{CJ}}\right)^2\right) + \frac{p_y \gamma_y}{\left(\gamma_y - 1\right)\rho_y} - \frac{p_z \gamma_z}{\left(\gamma_z - 1\right)\rho_z} = q$$

which can be rewritten as

$$\frac{1}{2}\left(\frac{\left(\rho_y \left(u_y - u_{\mathrm{CJ}}\right)\right)^2}{\rho_y} - \frac{\left(\rho_z \left(u_z - u_{\mathrm{CJ}}\right)\right)^2}{\rho_z}\right) + \frac{p_y \gamma_y}{\left(\gamma_y - 1\right)\rho_y} - \frac{p_z \gamma_z}{\left(\gamma_z - 1\right)\rho_z} = q, \qquad \text{(A.1)}$$

or

$$\frac{1}{2}\left(\frac{\left(\rho_z\left(u_z-u_{\mathrm{CJ}}\right)\right)^2}{\rho_y}+\left(\frac{\left(\rho_y\left(u_y-u_{\mathrm{CJ}}\right)\right)^2}{\rho_y}-\frac{\left(\rho_z\left(u_z-u_{\mathrm{CJ}}\right)\right)^2}{\rho_y}\right)-\frac{\left(\rho_z\left(u_z-u_{\mathrm{CJ}}\right)\right)^2}{\rho_z}\right)$$
$$+\frac{p_y\gamma_y}{\left(\gamma_y-1\right)\rho_y}-\frac{p_z\gamma_z}{\left(\gamma_z-1\right)\rho_z}=q.$$

By applying momentum conservation, this can be written as

$$\frac{1}{2}\left(\frac{\rho_z\left(u_z-u_{\mathrm{CJ}}\right)^2}{\rho_y}-\frac{\rho_z\left(u_z-u_{\mathrm{CJ}}\right)^2}{\rho_z}+\frac{P_z-p_y}{\rho_y}\right)+\frac{p_y\gamma_y}{\left(\gamma_y-1\right)\rho_y}-\frac{p_z\gamma_z}{\left(\gamma_z-1\right)\rho_z}=q,$$

or

$$\frac{1}{2}\left(-\frac{\left(\rho_y\left(u_y-u_{\mathrm{CJ}}\right)\right)^2}{\rho_z}+\left(\frac{\left(\rho_y\left(u_y-u_{\mathrm{CJ}}\right)\right)^2}{\rho_z}-\frac{\left(\rho_z\left(u_z-u_{\mathrm{CJ}}\right)\right)^2}{\rho_z}\right)+\frac{\left(\rho_z\left(u_z-u_{\mathrm{CJ}}\right)\right)^2}{\rho_y}+\frac{P_z-p_y}{\rho_y}\right)$$
$$+\frac{p_y\gamma_y}{\left(\gamma_y-1\right)\rho_y}-\frac{p_z\gamma_z}{\left(\gamma_z-1\right)\rho_z}=q.$$

Applying momentum conservation once again gives

$$\frac{1}{2}\left(-\frac{\left(\rho_y\left(u_y-u_{\mathrm{CJ}}\right)\right)^2}{\rho_z}+\frac{\left(\rho_z\left(u_z-u_{\mathrm{CJ}}\right)\right)^2}{\rho_y}+\frac{P_z-p_y}{\rho_y}-\frac{P_y-p_z}{\rho_z}\right)+\frac{p_y\gamma_y}{\left(\gamma_y-1\right)\rho_y}-\frac{p_z\gamma_z}{\left(\gamma_z-1\right)\rho_z}=q,$$

and

$$\frac{1}{2}\left(-\frac{\rho_y\left(u_y-u_{\mathrm{CJ}}\right)^2}{\rho_z}+\frac{\rho_z\left(u_z-u_{\mathrm{CJ}}\right)^2}{\rho_y}+\left(P_z-P_y\right)\left(\frac{1}{\rho_y}+\frac{1}{\rho_z}\right)\right)+\frac{p_y\gamma_y}{\left(\gamma_y-1\right)\rho_y}-\frac{p_z\gamma_z}{\left(\gamma_z-1\right)\rho_z}=q.$$

Now, by applying mass conservation, this becomes

$$\frac{1}{2}\left(-\frac{\left(u_y-u_{\mathrm{CJ}}\right)^2\left(u_z-u_{\mathrm{CJ}}\right)}{u_y-u_{\mathrm{CJ}}}+\frac{\left(u_y-u_{\mathrm{CJ}}\right)\left(u_z-u_{\mathrm{CJ}}\right)^2}{u_z-u_{\mathrm{CJ}}}+\left(P_z-P_y\right)\left(\frac{1}{\rho_y}+\frac{1}{\rho_z}\right)\right)$$
$$+\frac{p_y\gamma_y}{\left(\gamma_y-1\right)\rho_y}-\frac{p_z\gamma_z}{\left(\gamma_z-1\right)\rho_z}=q,$$

and

$$\frac{1}{2}\left(\left(u_y-u_{\mathrm{CJ}}\right)\left(u_z-u_{\mathrm{CJ}}\right)-\left(u_y-u_{\mathrm{CJ}}\right)\left(u_z-u_{\mathrm{CJ}}\right)+\left(P_z-P_y\right)\left(\frac{1}{\rho_y}+\frac{1}{\rho_z}\right)\right)$$
$$+\frac{p_y\gamma_y}{\left(\gamma_y-1\right)\rho_y}-\frac{p_z\gamma_z}{\left(\gamma_z-1\right)\rho_z}=q,$$

and finally

$$\frac{p_y\gamma_y}{\left(\gamma_y-1\right)\rho_y}-\frac{1}{2}\left(p_y-p_z\right)\left(\frac{1}{\rho_y}+\frac{1}{\rho_z}\right)-\frac{p_z\gamma_z}{\left(\gamma_z-1\right)\rho_z}=q.$$

Thus, velocity has been eliminated from the expression. The mass conservation gives

$$\rho_y\left(u_y-u_{\mathrm{CJ}}\right)=\rho_z\left(u_z-u_{\mathrm{CJ}}\right).$$

Momentum conservation gives

$$\rho_y\left(u_y-u_{\mathrm{CJ}}\right)^2+p_y=\rho_z\left(u_z-u_{\mathrm{CJ}}\right)^2+p_z.$$

By combineing the expressions for mass and momentum conservation, one can write

$$\rho_y^2 \left(u_y - u_{\mathrm{CJ}}\right)^2 = \frac{p_y - p_z}{\frac{1}{\rho_z} - \frac{1}{\rho_y}}.$$

The CJ conditions is that

$$u_y - u_{\mathrm{CJ}} = -C_y = -\sqrt{\frac{p_y \gamma_y}{\rho_y}}.$$

Combining these together gives

$$p_y \gamma_y \rho_y = \frac{p_y - p_z}{\frac{1}{\rho_z} - \frac{1}{\rho_y}}.$$

Using this relation and the Hugoniot curve to find p_y and ρ_y in terms of p_z and ρ_z gives,

$$p_y \gamma_y \rho_y = \frac{p_y - p_z}{\frac{1}{\rho_z} - \frac{1}{\rho_y}}.$$

Finally, by making use of a variable change, $v_y = \frac{1}{\rho_y}$, $v_z = \frac{1}{\rho_z}$ and p_y can be expressed as:

$$\begin{aligned} p_y &= \frac{p_z}{\left(\frac{1}{\rho_z} - \frac{1}{\rho_y}\right)\left(\frac{1}{\frac{1}{\rho_z} - \frac{1}{\rho_y}} - \gamma_y \rho_y\right)} \\ &= \frac{p_z}{\left(v_z - v_y\right)\left(\frac{1}{v_z - v_y} - \frac{\gamma_y}{v_y}\right)} \\ &= \frac{p_z}{1 - \frac{\gamma_y (v_z - v_y)}{v_y}} \\ &= \frac{p_z}{(\gamma_y + 1) - \frac{v_z \gamma_y}{v_y}}. \end{aligned}$$

This can be used with equation A.1 to give

$$-\frac{1}{2}\left(v_y + v_z\right)\left(\frac{p_z v_y}{v_y\left(\gamma_y + 1\right) - v_z \gamma_y} - p_z\right) + \frac{\gamma_y \left(p_z v_y^2\right)}{\left(\gamma_y - 1\right)\left(v_y\left(\gamma_y + 1\right) - v_z \gamma_y\right)} - \frac{p_z v_z \gamma_z}{\gamma_z - 1} = q.$$

Isolating v_y leads to

$$\begin{aligned} &\frac{p_z v_y^2 \gamma_y}{\gamma_y - 1} - \frac{p_z \gamma_z v_z \left(v_y\left(\gamma_y + 1\right) - v_z \gamma_y\right)}{\gamma_z - 1} \\ &\frac{1}{2}\left(v_y + v_z\right)\left(-\left(p_z v_y - p_z\left(v_y\left(\gamma_y + 1\right) - v_z \gamma_y\right)\right)\right) = q\left(v_y\left(\gamma_y + 1\right) - v_z \gamma_y\right), \end{aligned}$$

and

$$\begin{aligned} &\frac{p_z v_y^2 \gamma_y}{\gamma_y - 1} - \frac{p_z v_y \gamma_z \left(v_z\left(\gamma_y + 1\right)\right)}{\gamma_z - 1} + \frac{p_z v_z^2 \gamma_y \gamma_z}{\gamma_z - 1} \\ &\frac{1}{2} v_y^2 \left(p_z\left(\gamma_y + 1\right)\right) - \frac{1}{2} v_y \left(p_z v_z \gamma_y\right) - \frac{1}{2} p_z v_y^2 - \frac{1}{2} v_y \left(p_z v_z\right) \\ &-\frac{1}{2} p_z v_z^2 \gamma_y + v_y + \left(\frac{1}{2} v_z \left(p_z\left(\gamma_y + 1\right)\right)\right) - v_y\left(q\left(\gamma_y + 1\right)\right) + q v_z \gamma_y = 0. \end{aligned}$$

This can be rearranged as:

$$\left[\frac{p_z\gamma_y}{\gamma_y-1}+\frac{1}{2}p_z\left(\gamma_y+1\right)-\frac{p_z}{2}\right]v_y^2+\left[\frac{p_zv_z^2\gamma_y\gamma_z}{\gamma_z-1}-\frac{1}{2}p_zv_z^2\gamma_y+qv_z\gamma_y\right]$$
$$-\left[\frac{1}{2}p_zv_z\gamma_y-\frac{1}{2}v_z\left(p_z\left(\gamma_y+1\right)\right)+\frac{p_z\gamma_z\left(v_z\left(\gamma_y+1\right)\right)}{\gamma_z-1}+\frac{p_zv_z}{2}+q\left(\gamma_y+1\right)\right]v_y=0.$$

and

$$v_y^2p_z\left(\frac{\gamma_y\left(\gamma_y+1\right)}{2\left(\gamma_y-1\right)}\right)-\left[\frac{p_zv_z\gamma_z}{\gamma_z-1}+q\right]\gamma_y+1v_y+\left[\frac{p_zv_z^2\gamma_y\left(\gamma_z+1\right)}{2\left(\gamma_z-1\right)}+qv_z\gamma_y\right]=0.$$

This is a second order polynomial of v_y. The root corresponding to a CJ-deflagration is

$$v_y=\frac{\left[\frac{p_zv_z\gamma_z}{\gamma_z-1}+q\right]\gamma_y+1+\sqrt{\left[\frac{p_zv_z\gamma_z}{\gamma_z-1}+q\right]^2\left(\gamma_y+1\right)^2-\frac{2p_z(\gamma_y(\gamma_y+1))}{\gamma_y-1}\left(\frac{p_zv_z^2\gamma_y(\gamma_z+1)}{2(\gamma_z-1)}+qv_z\gamma_y\right)}}{\frac{p_z(\gamma_y(\gamma_y+1))}{\gamma_y-1}}.$$

This is simplified as

$$v_y=\frac{\left[\frac{p_zv_z\gamma_z}{\gamma_z-1}+q\right]\gamma_y-1+\gamma_y-1\sqrt{\left[\frac{p_zv_z\gamma_z}{\gamma_z-1}+q\right]^2-\frac{2p_z\gamma_y^2}{(\gamma_y-1)(\gamma_y+1)}\left(\frac{p_zv_z^2(\gamma_z+1)}{2(\gamma_z-1)}+\mathrm{qv}_z\right)}}{p_z\gamma_y},$$

$$v_y=\frac{\left[\frac{p_zv_z\gamma_z}{\gamma_z-1}+q\right]\gamma_y-1+\left(\gamma_y-1\right)\sqrt{\frac{q(2p_zv_z\gamma_z)}{\gamma_z-1}-\frac{\mathrm{qv}_z\left(2p_z\gamma_y^2\right)}{\gamma_y^2-1}-\frac{p_zv_z^2(\gamma_z+1)\left(2p_z\gamma_y^2\right)}{\left(\gamma_y^2-1\right)(2(\gamma_z-1))}+\frac{p_z^2v_z^2\gamma_z^2}{(\gamma_z-1)^2}+q^2}}{p_z\gamma_y},$$

$$v_y=\left[\frac{q}{p_z\gamma_y}+\frac{v_z\gamma_z}{\gamma_y\left(\gamma_z-1\right)}\right]\gamma_y-1$$
$$+\left(\gamma_y-1\right)\sqrt{-\frac{2}{p_z\left(\gamma_y^2-1\right)}\left(\frac{p_zv_z^2\left(\gamma_z+1\right)}{2\left(\gamma_z-1\right)}+\mathrm{qv}_z\right)+\frac{2q\left(v_z\gamma_z\right)}{p_z\gamma_y^2\left(\gamma_z-1\right)}+\left(\frac{q}{p_z\gamma_y}\right)^2+\frac{v_z^2\gamma_z^2}{\gamma_y^2\left(\gamma_z-1\right)^2}},$$

$$v_y=\left[\frac{q}{p_z\gamma_y}+\frac{v_z\gamma_z}{\gamma_y\left(\gamma_z-1\right)}\right]\gamma_y-1$$
$$+\left(\gamma_y-1\right)\sqrt{\left(\frac{q}{p_z\gamma_y}\right)^2+\frac{\mathrm{qv}_z2\left(\frac{\gamma_z}{\gamma_y^2(\gamma_z-1)}-\frac{1}{\gamma_y^2-1}\right)}{p_z}+\left[\frac{\gamma_z^2}{\gamma_y^2\left(\gamma_z-1\right)^2}-\frac{\gamma_z+1}{\left(\gamma_y^2-1\right)\left(\gamma_z-1\right)}\right]v_z^2},$$

$$v_y=\left[\frac{q}{p_z\gamma_y}+\frac{v_z\gamma_z}{\gamma_y\left(\gamma_z-1\right)}\right]\gamma_y-1$$
$$+\left(\gamma_y-1\right)\sqrt{\left(\frac{q}{p_z\gamma_y}\right)^2+\frac{\mathrm{qv}_z2\left(\frac{\gamma_z}{\gamma_y^2(\gamma_z-1)}-\frac{1}{\gamma_y^2-1}\right)}{p_z}+\left[\frac{\left(\gamma_y^2-1\right)\gamma_z^2}{\left(\gamma_y^2\left(\gamma_y^2-1\right)\right)\left(\gamma_z-1\right)^2}-\frac{\gamma_y^2\left(\gamma_z^2-1\right)}{\left(\gamma_y^2-1\right)\left(\gamma_z-1\right)^2}\right]v_z^2},$$

$$v_y = \left[\frac{q}{p_z\gamma_y} + \frac{v_z\gamma_z}{\gamma_y\left(\gamma_z-1\right)}\right]\gamma_y - 1$$
$$+\left(\gamma_y-1\right)\sqrt{\left(\frac{q}{p_z\gamma_y}\right)^2 + \frac{\mathrm{qv}_z 2\left(\frac{\gamma_z}{\gamma_y^2(\gamma_z-1)} - \frac{1}{\gamma_y^2-1}\right)}{p_z} + \left[\frac{\left(\gamma_y^2-1\right)\gamma_z^2 - \gamma_y^2\left(\gamma_z^2-1\right)}{\left(\gamma_y^2\left(\gamma_y^2-1\right)\right)\left(\gamma_z-1\right)^2}\right]v_z^2},$$

$$v_y = v_z\left(\gamma_y-1\right)\left(\frac{q}{\gamma_y\left(p_z v_z\right)} + \frac{\gamma_z}{\gamma_y\left(\gamma_z-1\right)}\right)$$
$$+\left(\gamma_y-1\right)v_z\sqrt{\frac{\left(\frac{q}{p_z v_z}\right)^2}{\gamma_y^2} + \frac{q2\left(\frac{\gamma_z}{\gamma_y^2(\gamma_z-1)} - \frac{1}{\gamma_y^2-1}\right)}{p_z v_z} + \left[\frac{\gamma_y^2-\gamma_z^2}{\left(\gamma_y^2\left(\gamma_y^2-1\right)\right)\left(\gamma_z-1\right)^2}\right]}.$$

There are two cases of interest to be investigated, one with $\gamma_y = \gamma_z$ and one with $\gamma_y \neq \gamma_z$:
(1) If $\gamma_y = \gamma_z$,

$$\frac{\gamma v_y\left(v_z\left(\frac{p_z}{\left(v_z\left(v_z-v_y\right)\right)\left(\frac{1}{v_z-v_y}-\frac{\gamma}{v_y}\right)} - \frac{p_z}{v_y}\right)\right)}{\gamma-1} - \frac{1}{2}\left(v_y+v_z\right)\left(p_z\left(\frac{1}{\left(v_z-v_y\right)\left(\frac{1}{v_z-v_y}-\frac{\gamma}{v_y}\right)} - 1\right)\right) = q,$$

$$\frac{\gamma v_y\left(v_z\left(\frac{p_z v_y}{v_z\left(v_y-\gamma\left(v_z-v_y\right)\right)} - \frac{p_z}{v_y}\right)\right)}{\gamma-1} - \frac{p_z\left(v_y+v_z\right)\left(\gamma\left(v_z-v_y\right)\right)}{2\left(v_y-\gamma\left(v_z-v_y\right)\right)} = q,$$

$$\frac{\gamma\left(p_z v_y^2\right)}{\left(\gamma-1\right)\left((\gamma+1)v_y-\gamma \mathrm{v}_z\right)} - \frac{p_z\gamma\left(v_z^2-v_y^2\right)}{2\left((\gamma+1)v_y-\gamma \mathrm{v}_z\right)} = \frac{\gamma p_z v_z}{\gamma-1} + q,$$

$$\frac{\left(\gamma p_z\right)\left(\frac{v_y^2}{\gamma-1} + \frac{1}{2}\left(v_y^2-v_z^2\right)\right)}{(\gamma+1)v_y-\gamma \mathrm{v}_z} = \frac{\gamma p_z v_z}{\gamma-1} + q,$$

$$\frac{p_z\left(\gamma\left((\gamma+1)v_y^2-(\gamma-1)v_z^2\right)\right)}{2(\gamma-1)} = \left(\frac{\gamma p_z v_z}{\gamma-1}+q\right)\left((\gamma+1)v_y-\gamma \mathrm{v}_z\right),$$

$$\frac{v_y^2\left((\gamma(\gamma+1))p_z\right)}{2(\gamma-1)} - \frac{1}{2}p_z\gamma \mathrm{v}_z^2 = (\gamma+1)v_y\left(\frac{\gamma p_z v_z}{\gamma-1}+q\right) - \gamma \mathrm{v}_z\left(\frac{\gamma p_z v_z}{\gamma-1}+q\right),$$

$$-(\gamma+1)v_y\left(\frac{\gamma p_z v_z}{\gamma-1}+q\right) + \gamma \mathrm{v}_z\left(\frac{\gamma p_z v_z}{\gamma-1}+q\right) + \frac{v_y^2\left((\gamma(\gamma+1))p_z\right)}{2(\gamma-1)} - \frac{1}{2}p_z\gamma \mathrm{v}_z^2 = 0.$$

To here, v_y has been isolated successfully. Simplifying leads to,

$$v_y = \frac{(\gamma+1)\left((\gamma-1)q + v_z\gamma \mathrm{p}_z\right)}{(\gamma(\gamma+1))p_z} \pm \frac{\sqrt{(\gamma+1)^2\left(\gamma p_z v_z + (\gamma-1)q\right)^2 - 2(\gamma(\gamma+1))p_z\left(\gamma \mathrm{v}_z\left(\gamma p_z v_z + (\gamma-1)q\right) - \frac{1}{2}(\gamma-1)p_z\gamma \mathrm{v}_z^2\right)}}{(\gamma(\gamma+1))p_z}.$$

For the simplification gives

$$v_y = \frac{\left((\gamma+1)v_z\gamma \mathrm{p}_z \pm \sqrt{\left(\left(\gamma^2-1\right)q + (\gamma+1)v_z\gamma \mathrm{p}_z\right)^2 - 2\gamma^2 p_z^2 v_z^2\left(\frac{1}{2}(\gamma+1)^2 + \frac{(\gamma^2-1)q}{p_z v_z}\right)}\right) + \left(\gamma^2-1\right)q}{\gamma(\gamma+1)p_z},$$

$$v_y = \frac{\left(\gamma^2-1\right)q + (\gamma+1)v_z\gamma \mathrm{p}_z}{(\gamma(\gamma+1))p_z} \pm \frac{\sqrt{-2\gamma^2 p_z^2\left(v_z^2\left(\frac{1}{2}(\gamma+1)^2 + \frac{(\gamma^2-1)q}{p_z v_z}\right)\right) + (\gamma+1)^2\gamma^2 p_z^2 v_z^2 + \left(\gamma^2-1\right)^2 q^2 + 2\left(\gamma^2-1\right)((\gamma+1)q)v_z\gamma \mathrm{p}_z}}{(\gamma(\gamma+1))p_z},$$

$$v_y = \left(v_z \pm \frac{(\gamma-1)\sqrt{q^2 + \frac{(2\gamma)\mathrm{q}\mathrm{p}_z v_z}{\gamma^2-1}}}{\gamma \mathrm{p}_z}\right) + \frac{(\gamma-1)q}{\gamma \mathrm{p}_z},$$

$$v_y = \frac{((\gamma-1)q)\left(1 \pm \sqrt{\frac{(2\gamma)(p_z v_z)}{(\gamma^2-1)q} + 1}\right)}{\gamma \mathrm{p}_z} + v_z, \tag{A.2}$$

This used in the Hugoniot curve,

$$\frac{\gamma\left(p_y v_y - p_z v_z\right)}{\gamma-1} - \frac{1}{2}\left(p_y - p_z\right)\left(v_y + v_z\right) = q,$$

$$p_y\left(\frac{\gamma v_y}{\gamma-1} - \frac{1}{2}\left(v_y + v_z\right)\right) = p_z\left(\frac{\gamma v_z}{\gamma-1} - \frac{1}{2}\left(v_y + v_z\right)\right) + q,$$

which leads to

$$p_y = \frac{p_z\left(\frac{\gamma v_z}{\gamma-1} - \frac{1}{2}\left(v_y + v_z\right)\right) + q}{\frac{\gamma v_y}{\gamma-1} - \frac{1}{2}\left(v_y + v_z\right)}. \tag{A.3}$$

Using the sonic condition,

$$-\rho_y\sqrt{\frac{\gamma p_y}{\rho_y}} = \rho_z\left(u_z - u_{\mathrm{CJ}}\right),$$

$$u_{\mathrm{CJ}} = u_z + \frac{\sqrt{\gamma p_y \rho_y}}{\rho_z}, \tag{A.4}$$

One can obtain

$$u_y = u_{\mathrm{CJ}} - \sqrt{\frac{\gamma \mathrm{p}_y}{\rho_y}}.$$

Again, for the sonic condition,

$$u_y = u_z + \sqrt{\frac{\gamma \mathrm{p}_y}{\rho_y}} \left(\frac{\rho_y}{\rho_z} - 1 \right),$$

One can obtain

$$u_y = u_z + \sqrt{\frac{\gamma \mathrm{p}_y}{v_y}} \left(v_z - v_y \right). \tag{A.5}$$

Formulae A.2 to A.5 give the CJ-deflegration jump condition for equal γ conditions.
(2) If $\gamma_y \neq \gamma_z$, setting $Q = \frac{q}{p_z v_z}$ gives

$$\frac{v_y}{v_z} = \gamma_y - 1 \left(\left[\frac{Q}{\gamma_y} + \frac{\gamma_z}{\gamma_y \left(\gamma_z - 1 \right)} \right] + \sqrt{\frac{Q^2}{\gamma_y^2} + Q2 \left(\frac{\gamma_z}{\gamma_y^2 \left(\gamma_z - 1 \right)} - \frac{1}{\gamma_y^2 - 1} \right) + \left[\frac{\gamma_y^2 - \gamma_z^2}{\left(\gamma_y^2 \left(\gamma_y^2 - 1 \right) \right) \left(\gamma_z - 1 \right)^2} \right]} \right) = T. \tag{A.6}$$

Using the Hugoniot curves,

$$\frac{p_y \gamma_y}{\left(\gamma_y - 1 \right) \rho_y} - \frac{1}{2} \left(p_y - p_z \right) \left(\frac{1}{\rho_y} + \frac{1}{\rho_z} \right) - \frac{p_z \gamma_z}{\left(\gamma_z - 1 \right) \rho_z} = q,$$

$$p_y \left(\frac{v_y \left(\gamma_y + 1 \right)}{\gamma_y - 1} - v_z \right) = p_z \left(\frac{v_z \left(\gamma_z + 1 \right)}{\gamma_z - 1} - v_y \right) + 2q,$$

$$p_y = \frac{p_z \left(\frac{v_z (\gamma_z + 1)}{\gamma_z - 1} - T v_z \right) + 2q}{\frac{T v_z (\gamma_y + 1)}{\gamma_y - 1} - v_z},$$

One can write

$$\frac{p_y}{p_z} = \frac{2Q + \left[\frac{\gamma_z + 1}{\gamma_z - 1} - T \right]}{\frac{T(\gamma_y + 1)}{\gamma_y - 1} - 1} = W. \tag{A.7}$$

From the sonic condition,

$$-\rho_y \sqrt{\frac{p_y \gamma_y}{\rho_y}} = \rho_z \left(u_z - u_{\mathrm{CJ}} \right),$$

One can find

$$u_{\mathrm{CJ}} = \sqrt{\frac{W p_z v_z \gamma_y \gamma_z}{T \gamma_z}} + u_z,$$

$$u_{\mathrm{CJ}} = c_z \sqrt{\frac{W\gamma_y}{T\gamma_z}} + u_z,$$

$$\frac{u_{\mathrm{CJ}} - u_z}{c_z} = \sqrt{\frac{W\gamma_y}{T\gamma_z}} = U, \tag{A.8}$$

$$u_y = (v_z - v_y) \sqrt{\frac{p_y \gamma_y}{v_y}} + u_z,$$

$$u_y = (1 - T) \sqrt{\frac{W p_z v_z \gamma_y \gamma_z}{T\gamma_z}} + u_z,$$

$$u_y = (1 - T) c_z \sqrt{\frac{W\gamma_y}{T\gamma_z}} + u_z,$$

$$\frac{u_y - u_z}{c_z} = (1 - T) \sqrt{\frac{W\gamma_y}{T\gamma_z}} = V. \tag{A.9}$$

Formulae A.6 to A.9 give the CJ deflagration jump condition for non-equal γ.

Appendix B

Model of "N" Wave Dissipation Rate with Constant Wavelength and Amplitude

This Appendix provides a model of "N" wave decaying equations which are listed in Chapter 4. As Fig. B.1 shows, the sinusoidal forward facing waves would finally change to the "N" type of waves, because of its non-linear propagation effect. These "N" waves are each constructed by a leading shock wave and an expansion wave behind.

Unlike the steady shockwave, the strength of "N" wave will decay during the propagation. This is due to the expanding post-shock gas, which is characterized by a gradient of speed and other state variables, as illustrated in Fig. B.1. In this appendix, a model is constructed liking the post-shock expansion to the shock decay rate in order to obtain the attenuation rate of the N-wave shock train.

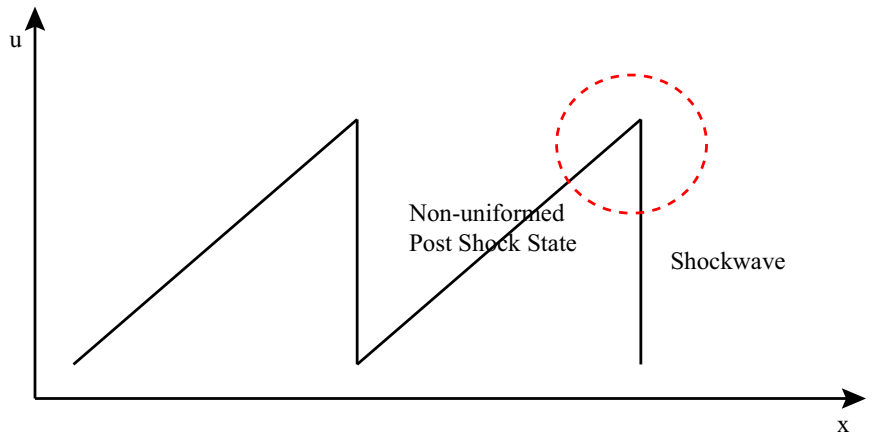

Figure B.1: A sketch of "N" wave.

B.1 Triangle-Shape Shock Wave Evolution

The evolution of each shock wave forming the train of N-waves can be obtained with the knowledge of the speed gradient behind each shock through the so-called shock change equations [15]. A derivation of these equations relating the shock speed, , its decay rate, and the gradient behind the shock follows.

B.1.1 Post Shock Solution

The Euler equations could be transformed to

$$\frac{\partial p}{\partial t} + u\frac{\partial p}{\partial x} + \rho c^2 \frac{\partial u}{\partial x} = 0, \tag{B.1}$$

and

$$\frac{\partial p}{\partial x} + \rho\frac{\partial u}{\partial t} + \rho u\frac{\partial u}{\partial x} = 0.$$

The second equation can be re-written as:

$$\frac{\partial u}{\partial t} + u\frac{\partial u}{\partial x} + \frac{\partial p}{\rho\partial x} = 0. \tag{B.2}$$

Then denote that the derivative of pressure along the x-t path dx=D dt, i.e., along the shock trajectory,

$$\left.\frac{dp}{dt}\right|_s = \frac{\partial p}{\partial t} + D\frac{\partial p}{\partial x}, \tag{B.3}$$

and further the derivative of particle velocity could be written as

$$\left.\frac{du}{dt}\right|_s = \frac{\partial u}{\partial t} + D\frac{\partial u}{\partial x}. \tag{B.4}$$

So the two above equations represent the property changes of the post-shock state. Put equations B.3 into B.1, then

$$\left.\frac{dp}{dt}\right|_s + (u - D)\frac{\partial p}{\partial x} + \rho c^2\frac{\partial u}{\partial x} = 0. \tag{B.5}$$

Put equation B.4 into B.2, then

$$\left.\frac{du}{dt}\right|_s + (u - D)\frac{\partial u}{\partial x} + \frac{\partial p}{\rho\partial x} = 0. \tag{B.6}$$

Combining the equation B.5 and B.6 to eliminate $\frac{\partial p}{\partial x}$, we have

$$\left.\frac{dp}{dt}\right|_s - \rho(u - D)\left.\frac{du}{dt}\right|_s - \rho\,(u - D)^2\,\frac{\partial u}{\partial x} + \rho c^2\frac{\partial u}{\partial x} = 0. \tag{B.7}$$

B.1.2 Shock Hugoniot Ratio

The equation B.7 is called shock change equation [15]. In this "N" wave problem, the post shock gradient $\frac{\partial u}{\partial x}$ can be modeled given the forcing frequency and relation amplitude of successive shocks in the N wave train. The post-shock pressure change $\left.\frac{dp}{dt}\right|_s$ and post-shock particle velocity change $\left.\frac{du}{dt}\right|_s$ are related through the shock jump equations:

$$\begin{aligned}\frac{u_b - u_a}{c_a} &= \frac{2(M^2-1)}{(\gamma+1)M} \\ \frac{v_b}{v_a} &= \frac{(\gamma-1)M^2+2}{(\gamma+1)M^2} \\ \frac{p_b}{p_a} &= \frac{2\gamma(M^2-1)}{\gamma+1} + 1,\end{aligned}$$

where the state a is the state ahead of the shock, and the state b is the post shock condition which need to be obtained. Differentiating the shock jump conditions, we obtain:

$$\begin{aligned}du_b &= \left[c_a\left(\frac{2}{(\gamma+1)} + \frac{2}{(\gamma+1)M_i^2}\right)\right]dM \\ dv_b &= -\left[v_a\left(\frac{4}{(\gamma+1)M_i^3}\right)\right]dM \\ dp_b &= p_a\frac{4\gamma M_i}{\gamma+1}dM,\end{aligned}$$

where M_i is the shock Mach Number. dM is the perturbation on leading shock. When we linearize the shock jump condition, the coefficients are constant for the certain shockwave these three constants could be measured. For post shock conditions, dM is redundant. It is better to only focus on the part that the post shock condition changes:

$$\frac{dp_b}{du_b} = \frac{p_a\frac{4\gamma M_i}{\gamma+1}}{c_a\left(\frac{2}{(\gamma+1)} + \frac{2}{(\gamma+1)M_i^2}\right)} = \Theta,$$

$$\frac{dp_b}{du_b} = \frac{2p_a\gamma M_i^3}{c_a(M_i^2+1)} = \Theta.$$

The Θ is a constant in a particular shockwave which provides the relation between the $\left.\frac{dp}{dt}\right|_s$ and $\left.\frac{du}{dt}\right|_s$.

B.1.3 Shock Changes Prediction

The Θ is constructed by the linearized shock strength and initial state. Using Θ one can eliminate the $\left.\frac{dp}{dt}\right|_s$ by $\Theta \left.\frac{du}{dt}\right|_s$, so:

$$\left[\Theta - \rho(u-D)\right] \left.\frac{du}{dt}\right|_s + \rho\left[c^2 - (u-D)^2\right] \frac{\partial u}{\partial x} = 0.$$

Finally it changes to:

$$\left.\frac{du}{dt}\right|_s = -\frac{\rho\left[c^2 - (u-D)^2\right]}{\Theta + \rho(u-D)} \frac{\partial u}{\partial x},$$

which means once we specify the ρ, u, D, Θ, c and $\frac{\partial u}{\partial x}$ in the post shock section, we can predict the changes of shock strength.

B.1.4 The Expression Non-shocked State

In this fluctuation problem the slope of the post shock velocity could be expressed by its initial fluctuation wavelength:

$$\frac{\partial u}{\partial x} \approx \frac{u}{L}.$$

Where L is the wavelength of fluctuation which has been assumed to be constant. Since

$$u = \frac{2c_0\left(M^2-1\right)}{(\gamma+1)M},$$

applying the shock change equation, one can have

$$\left.\frac{du}{dt}\right|_s = \frac{2c_0\left(M^2+1\right)}{(\gamma+1)M^2} \frac{dM}{dt}.$$

The shock change equation can be written as:

$$\frac{2c_0\left(M^2+1\right)}{(\gamma+1)M^2} \frac{dM}{dt} = -\frac{\rho\left[c^2 - (u-D)^2\right]}{\Theta + \rho(u-D)} \frac{\partial u}{\partial x}.$$

Next, the right hand side should be expressed by shock Mach number:

$$\frac{2c_0\left(M^2+1\right)}{(\gamma+1)M^2} \frac{dM}{dt} = -\frac{\rho c^2 + \rho_0 D\left(u-D\right)}{\Theta + \rho_0 D} \frac{\partial u}{\partial x}.$$

For the ideal gas,

$$\rho c^2 = \gamma p.$$

For the post shock pressure velocity,

$$p = p_0\left[\frac{2\gamma(M^2-1)}{\gamma+1} + 1\right],$$

$$u = c_0 \frac{2(M^2-1)}{(\gamma+1)M}.$$

Shock change equation becomes

$$\frac{2c_0\,(M^2+1)}{(\gamma+1)\,M^2}\frac{dM}{dt} = -\frac{\gamma p_0\left[\dfrac{2\gamma(M^2-1)}{\gamma+1}+1\right]+\rho_0 M c_0\left(c_0\dfrac{2(M^2-1)}{(\gamma+1)M}-Mc_0\right)}{\Theta+\rho_0 M c_0} c_0 \frac{2(M^2-1)}{(\gamma+1)ML}.$$

Rearrange it,

$$\frac{(M^2+1)}{M}\frac{dM}{dt} = -\frac{\gamma p_0\left[\dfrac{2\gamma(M^2-1)}{\gamma+1}+1\right]+M\rho_0 c_0^2\left(\dfrac{2(M^2-1)}{(\gamma+1)M}-M\right)}{\Theta+M\rho_0 c_0}\frac{(M^2-1)}{L}.$$

Express Θ by shock Mach number:

$$\frac{(M^2+1)}{M}\frac{dM}{dt} = -\frac{\gamma p_0\left[\dfrac{2\gamma(M^2-1)}{\gamma+1}+1\right]+M\rho_0 c_0^2\left(\dfrac{2(M^2-1)}{(\gamma+1)M}-M\right)}{\dfrac{2p_0\gamma M^3}{c_0(M^2+1)}+M\rho_0 c_0}\frac{(M^2-1)}{L}.$$

Rearrange it,

$$\frac{dM}{dt} = -\frac{p_0(2M^2\gamma^2-\gamma^2+\gamma)+\rho_0 c_0^2(M^2-2-\gamma M^2)}{2p_0\gamma M^2+\rho_0 c_0^2(M^2+1)}\frac{(M^2-1)}{\gamma+1}\frac{c_0}{L}.$$

Since $\rho_0 c_0^2 = \gamma p_0$,

$$\frac{dM}{dt} = -\frac{p_0(2M^2\gamma^2-\gamma^2+\gamma)+\gamma p_0(M^2-2-\gamma M^2)}{2p_0\gamma M^2+\gamma p_0(M^2+1)}\frac{(M^2-1)}{\gamma+1}\frac{c_0}{L}.$$

Rearrange it again,

$$\frac{dM}{dt} = -\frac{(2M^2\gamma^2-\gamma^2+\gamma)+\gamma(M^2-2-\gamma M^2)}{2\gamma M^2+\gamma(M^2+1)}\frac{(M^2-1)}{\gamma+1}\frac{c_0}{L},$$

$$\frac{dM}{dt} = -\frac{2M^2\gamma^2-\gamma^2+\gamma+M^2\gamma-2\gamma-M^2\gamma^2}{2\gamma M^2+\gamma(M^2+1)}\frac{(M^2-1)}{\gamma+1}\frac{c_0}{L},$$

$$\frac{dM}{dt} = -\frac{M^2\gamma-\gamma-1+M^2}{3M^2+1}\frac{(M^2-1)}{\gamma+1}\frac{c_0}{L},$$

where c_0/L is fluctuation frequency. The simplified expression is

$$\frac{dM}{dt} = -\frac{M^2\gamma-\gamma-1+M^2}{3M^2+1}\frac{(M^2-1)}{\gamma+1}f,$$

$$\frac{dM}{dt} = -\frac{(M^2-1)(\gamma+1)}{3M^2+1}\frac{(M^2-1)}{\gamma+1}f,$$

$$\frac{dM}{dt} = -\frac{(M+1)^2(\gamma+1)}{3M^2+1}\frac{(M-1)^2}{\gamma+1}f,$$

$$\frac{dM}{dt} = -\frac{(M+1)^2(M-1)^2}{3M^2+1}f. \tag{B.8}$$

The equation B.8 only use shock strength and fluctuation frequency to predict the change of the shock strength in an "N" wave. The initial shock strength could be calculated from the fluctuation amplitude.

B.1.5 Approximation at $M \to 1$

If the initial fluctuation amplitude is very small, the linear approximation could be make to further simplify the ODE B.8 such that it can be easily integrated. Set $\eta = M - 1$, then $M = \eta + 1$, $dM = d\eta$.When $M \to 1^+$, $\eta \to 0^+$. The equation B.8 can be approximated by

$$\frac{d\eta}{dt} = -\frac{4\eta^2}{4}f = -\eta^2 f.$$

We can integrate it:

$$\eta = \frac{1}{ft + C}.$$

When $t = 0$, $\eta = \eta_0$:

$$C = \frac{1}{\eta_0} - ft_0,$$

$$\eta = \frac{1}{f(t - t_0) + \dfrac{1}{\eta_0}},$$

$$M = \frac{1}{f(t - t_0) + \dfrac{1}{M_0 - 1}} + 1.$$

Appendix C

Model for Temperature Hotspots

This Appendix provides a physical model for the magnitude of the temperature hotspots generated by the perturbations driven by the oscillating piston, whose main predictions were given in Chapter 4. The model accounts for the interaction of the forward facing waves with the lead shock, which create entropy waves along the particle paths, which we label "hotspots". Figure C.1 sketches the mechanism of hotspots formation.

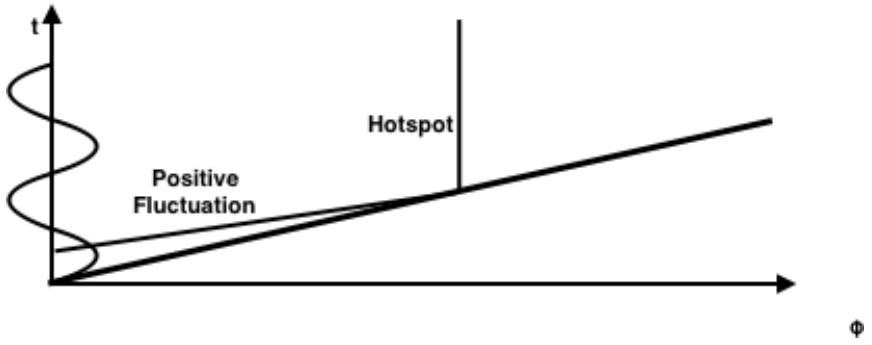

Figure C.1: The mechanism of hotspots formation

C.1 Non-Dimensionalization and Fluctuations Denoting With Acoustic Approach

In the shock induced ignition problems, the post shock state has been fluctuated and the fluctuation could be separated from each properties:

$$p = p_s + p_1$$
$$v = v_s + v_1$$
$$u = u_s + u_1.$$

where p_s, v_s and u_s are the constant post-shock state, and p_1, v_1 and u_1 are fluctuation components in pressure, specific volume and particle velocity. Now consider the description in a frame of reference moving with the constant post shock gas, which means the non-fluctuated post shock speed is zero:

$$u_s = 0.$$

Then we can quantify the velocity:

$$\begin{aligned} p &= p_s + p_1 \\ v &= v_s + v_1 \\ u &= 0 + u_1. \end{aligned}$$

C.1.1 Lagrangian Space Conservation Laws

In Lagrangian space, the three conservation laws could be written as

$$\begin{aligned} \frac{\partial v}{\partial t} - \frac{\partial u}{\partial \phi} &= 0 \\ \frac{\partial u}{\partial t} + \frac{\partial p}{\partial \phi} &= 0 \\ \frac{\partial}{\partial t}\left(\frac{pv}{\gamma - 1} + \frac{u^2}{2}\right) + \frac{\partial pu}{\partial \phi} &= 0. \end{aligned}$$

The first two equations for perturbation could be written as:

$$\begin{aligned} \frac{\partial v_1}{\partial t} - \frac{\partial u_1}{\partial \phi} &= 0 \\ \frac{\partial u_1}{\partial t} + \frac{\partial p_1}{\partial \phi} &= 0. \end{aligned}$$

The last equation for the perturbation could be written as:

$$v_s \frac{\partial}{\partial t}\left(\frac{p_1}{\gamma - 1}\right) + p_s \frac{\partial}{\partial t}\left(\frac{v_1}{\gamma - 1}\right) + u_s \frac{\partial u_1}{\partial t} + u_s \frac{\partial p_1}{\partial \phi} + p_s \frac{\partial u_1}{\partial \phi} = 0.$$

Because the non-perturbed initial velocity equals zero, then

$$v_s \frac{\partial}{\partial t}\left(\frac{p_1}{\gamma - 1}\right) + p_s \frac{\partial}{\partial t}\left(\frac{v_1}{\gamma - 1}\right) + p_s \frac{\partial u_1}{\partial \phi} = 0,$$

applying $\frac{\partial v_1}{\partial t} - \frac{\partial u_1}{\partial \phi} = 0$ one can have

$$v_s \frac{\partial}{\partial t}\left(\frac{p_1}{\gamma - 1}\right) + p_s \frac{\partial}{\partial t}\left(\frac{\gamma v_1}{\gamma - 1}\right) = 0.$$

In this case,

$$\frac{1}{p_s}\frac{\partial p_1}{\partial t} = -\frac{\gamma}{v_s}\frac{\partial v_1}{\partial t}$$

Here the conservation laws could be linearized and expressed by two equations.

$$\frac{v_s}{\gamma p_s}\frac{\partial p_1}{\partial t} + \frac{\partial u_1}{\partial \phi} = 0 \tag{C.1}$$

$$\frac{\partial u_1}{\partial t} + \frac{\partial p_1}{\partial \phi} = 0 \tag{C.2}$$

To solve the system, partial derivative the first equation with ϕ and the second equation with time, then:

$$\frac{\partial^2 p_1}{\partial t \partial \phi} + \frac{\gamma p_s \partial^2 u_1}{v_s \partial^2 \phi} = 0, \tag{C.3}$$

$$\frac{\partial^2 u_1}{\partial^2 t} + \frac{\partial^2 p_1}{\partial \phi \partial t} = 0. \tag{C.4}$$

(C.4)-(C.3) gives

$$\frac{\partial^2 u_1}{\partial^2 t} - \frac{\gamma p_s}{v_s}\frac{\partial^2 u_1}{\partial^2 \phi} = 0.$$

Define the Lagrangian wave speed of acoustic waves $c = \sqrt{\frac{\gamma p_s}{v_s}}$, the PDE is the standard wave equation:

$$\frac{\partial^2 u_1}{\partial^2 t} - c^2\frac{\partial^2 u_1}{\partial^2 \phi} = 0.$$

Separating the operator we solve the equation

$$\left(\frac{\partial}{\partial t} - c\frac{\partial}{\partial \phi}\right)\left(\frac{\partial}{\partial t} + c\frac{\partial}{\partial \phi}\right)u_1 = 0,$$

$$u_1 = f(\phi + ct) + g(\phi - ct).$$

This is the general solution for u_1 at post shock area.

C.1.2 Left Boundary Condition

Left boundary is where the fluctuation comes from and is modeled as a piston in this problem. Assume the left piston moving with the constant fluctuation amplitudes A and B and with a constant frequency $\frac{\omega}{2\pi}$:

$$u_1(0,t) = A\sin(\omega t) + B\cos(\omega t) = L(t).$$

That means the left boundary has been fixed by $L(t)$:

$$g(-ct) = L(t) - f(ct).$$

C.1.3 Right Boundary Condition

Right boundary is a moving shock. The right boundary start from left boundary and continuing move right towards with a constant speed D. When waves acting on the leading shockwaves, the shockwave will reflect the corespond wave to the left region. To handle the right boundary condition, one need to start from shock conditions:

$$\frac{u_b - u_a}{c_a} = \frac{2\left(M^2-1\right)}{\left(\gamma+1\right)M}\frac{v_b}{v_a} = \frac{\left(\gamma-1\right)M^2+2}{\left(\gamma+1\right)M^2}\frac{p_b}{p_a} = \frac{2\gamma\left(M^2-1\right)}{\gamma+1}+1,$$

where the state a is the non-shocked state with no perturbation, and the state b is the post shock condition which need to be obtained. Linearize the jump condition around the incident shock strength:

$$du_b = \left[c_a\left(\frac{2}{\left(\gamma+1\right)}+\frac{1}{\left(\gamma+1\right)M_i^2}\right)\right]dM dv_b = -\left[v_a\left(\frac{4}{\left(\gamma+1\right)M_i^3}\right)\right]dM dp_b = p_a\frac{4\gamma M_i}{\gamma+1}dM.$$

where M_i is the non-perturbed shock Mach Number. dM is the perturbation on leading shock. When we linearize the shock jump condition, the coefficients are constant for the certain shockwave these three constants could be measured. For post shock conditions, dM is redundant. It is better to only focus on the part that the post shock condition changes:

$$\frac{dp_b}{du_b} = \frac{p_a\dfrac{4\gamma M_i}{\gamma+1}}{c_a\left(\dfrac{2}{\left(\gamma+1\right)}+\dfrac{1}{\left(\gamma+1\right)M_i^2}\right)} = \Theta,$$

$$\frac{dp_b}{dv_b} = \frac{p_a\dfrac{4\gamma M_i}{\gamma+1}}{-v_a\left(\dfrac{4}{\left(\gamma+1\right)M_i^3}\right)} = \Gamma.$$

Put the shock conditions into post shock boundary conditions:

$$p_1 = \Theta u_1 p_1 = \Gamma v_1.$$

For the general solution,

$$\frac{\partial p_1}{\partial t} = -c^2\frac{\partial u_1}{\partial \phi}.$$

So at the right boundary,

$$\Theta\frac{\partial u_1}{\partial t} = -c^2\frac{\partial u_1}{\partial \phi}.$$

Substitute it by the general solution. The right boundary is always at the place $\phi = Dt$ where D is a known constant. The right boundary condition could be written as:

$$\Theta c f'\left(Dt+ct\right) - \Theta c g'\left(Dt-ct\right) = -c^2 f'\left(Dt+ct\right) - c^2 g'\left(Dt-ct\right),$$

$$f'\left(Dt+ct\right) = \frac{\Theta-c}{\Theta+c}g'\left(Dt-ct\right).$$

C.1.4 Combine the Two Boundary Conditions

Take the first derivative with t from the left boundary conditions:

$$g'(-t) = f'(t) - L'\left(\frac{t}{c}\right).$$

The second boundary condition could become

$$f'(t) = \frac{\Theta - c}{\Theta + c} g'\left(\frac{D - c}{D + c} t\right).$$

Then link the two relations together we have

$$g'(-t) = \frac{\Theta - c}{\Theta + c} g'\left(\frac{D - c}{D + c} t\right) - L'\left(\frac{t}{c}\right),$$

or

$$g'(t) = \frac{\Theta - c}{\Theta + c} g'\left(\frac{c - D}{c + D} t\right) - L'\left(-\frac{t}{c}\right).$$

The solution of such relation is an infinite series:

$$g'(t) = -\sum_{n=0}^{\infty} \left(\frac{\Theta - c}{\Theta + c}\right)^n L'\left[-\left(\frac{c - D}{c + D}\right)^n \frac{t}{c}\right],$$

$$f'(t) = -\sum_{n=1}^{\infty} \left(\frac{\Theta - c}{\Theta + c}\right)^n L'\left[\left(\frac{c - D}{c + D}\right)^n \frac{t}{c}\right],$$

where $g'(t)$ only make sense when $t < 0$, while $f'(t)$ only make sense when $t > 0$.

C.1.5 Mean Temperature

The mean temperature behind the lead shock is controlled by Leading shock strength:

$$dM = \frac{du_b}{c_a} \frac{1}{\frac{2}{(\gamma + 1)} + \frac{1}{(\gamma + 1) M_i^2}}.$$

From the ideal gas law,

$$RdT = vdp + pdv.$$

So the shock front temperature is

$$T_1 = \left(v_0 \Theta + \frac{p_0 \Theta}{\Gamma}\right) u_1.$$

The mean temperature at certain place could approximately be substituted by the moment that pressure fluctuation equals zero. The pressure evolution on the certain particle is

described by perfect gas law.
The initial condition for the certain particle is that:

$$T_1 = \left(v_0\Theta + \frac{p_0\Theta}{\Gamma} \right) u_1, \tag{C.5}$$

$$p_1 = \Theta u_1. \tag{C.6}$$

From perfect gas law we have,

$$Tp^{\frac{1-\gamma}{\gamma}} = C,$$

$$p^{\frac{1-\gamma}{\gamma}} dT + T\frac{1-\gamma}{\gamma} p^{\frac{1-2\gamma}{\gamma}} dP = 0,$$

$$dT + T\frac{1-\gamma}{\gamma} p^{-1} dP = 0. \tag{C.7}$$

Since the pressure drop by the fluctuation is $-p_1$, once the pressure recovered to the non-fluctuated pressure, the temperature will recover to the T_{1m}, which can be written as:

$$T_{1m} = \left(v_0\Theta + \frac{p_0\Theta}{\Gamma} \right) u_1 - \frac{T_0}{P_0}\frac{1-\gamma}{\gamma}\Theta u_1,$$

$$T_{1m} = \left(v_0\Theta + \frac{p_0\Theta}{\Gamma} - \frac{T_0}{P_0}\frac{1-\gamma}{\gamma}\Theta \right) u_1.$$

This equation is constructed by using C.5, C.6 and C.7.

Appendix D

Hydrogen-Oxygen Simulation Plots

This appendix provides the particle velocity, pressure and density plots for the simulations in Chapter 5.

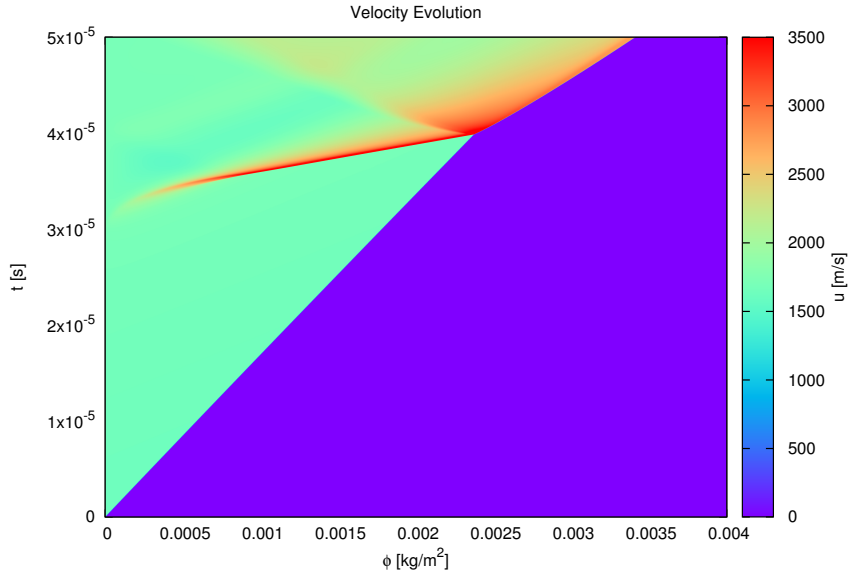

Figure D.1: Particle velocity profile of hydrogen fluctuating shock-induced ignition with a post shock temperature of 1100 K and piston oscillation frequency of 4.535 kHz, and amplitude of 5%.

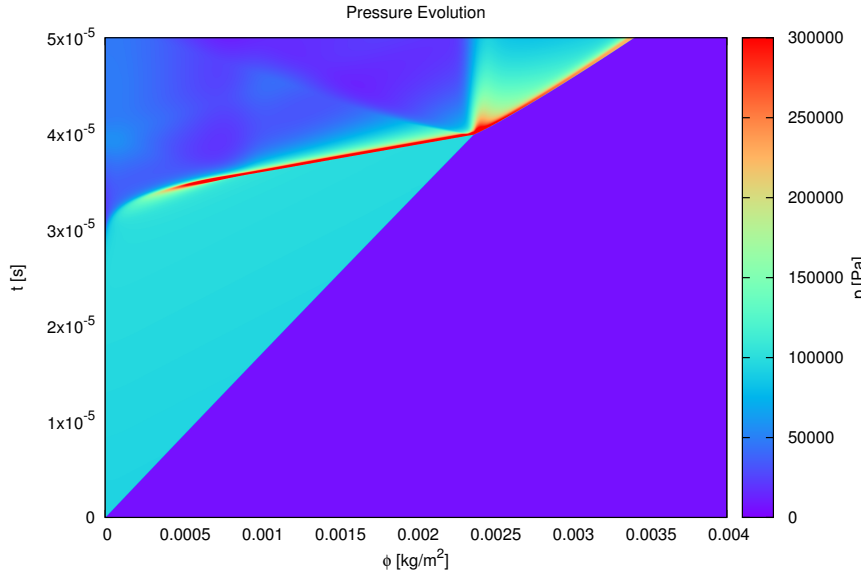

Figure D.2: Pressure profile of hydrogen fluctuating shock-induced ignition with a post shock temperature of 1100 K and piston oscillation frequency of 4.535 kHz, and amplitude of 5%.

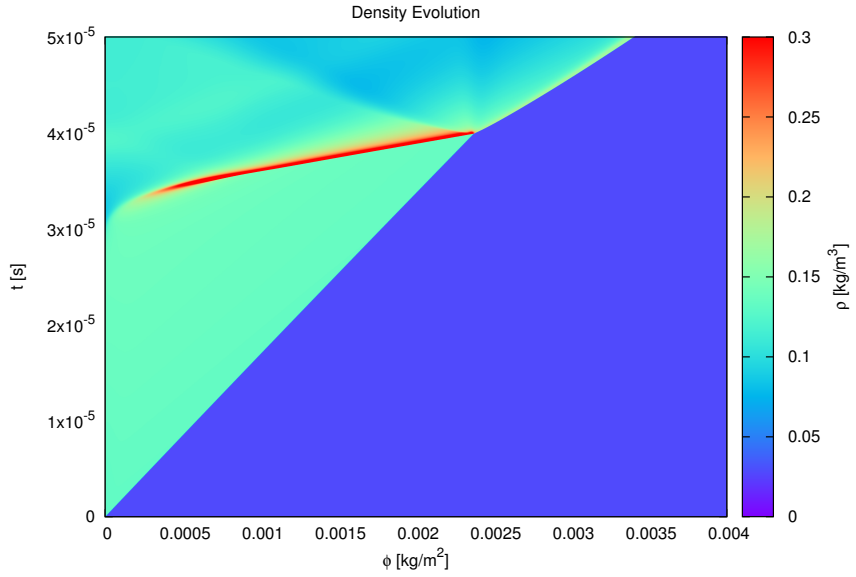

Figure D.3: Density profile of hydrogen fluctuating shock-induced ignition with a post shock temperature of 1100 K and piston oscillation frequency of 4.535 kHz, and amplitude of 5%.

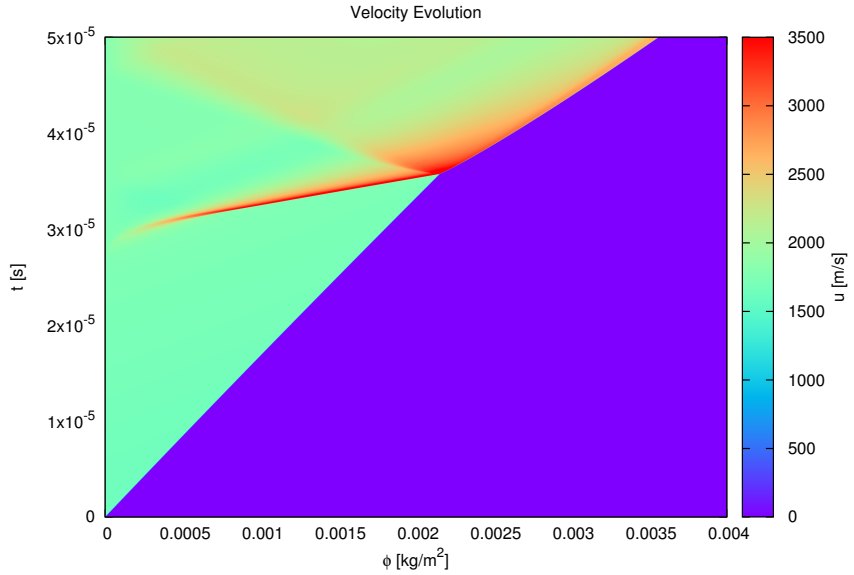

Figure D.4: Particle velocity profile of hydrogen fluctuating shock-induced ignition with a post shock temperature of 1100 K and piston oscillation frequency of 4.535 kHz, and amplitude of 10%.

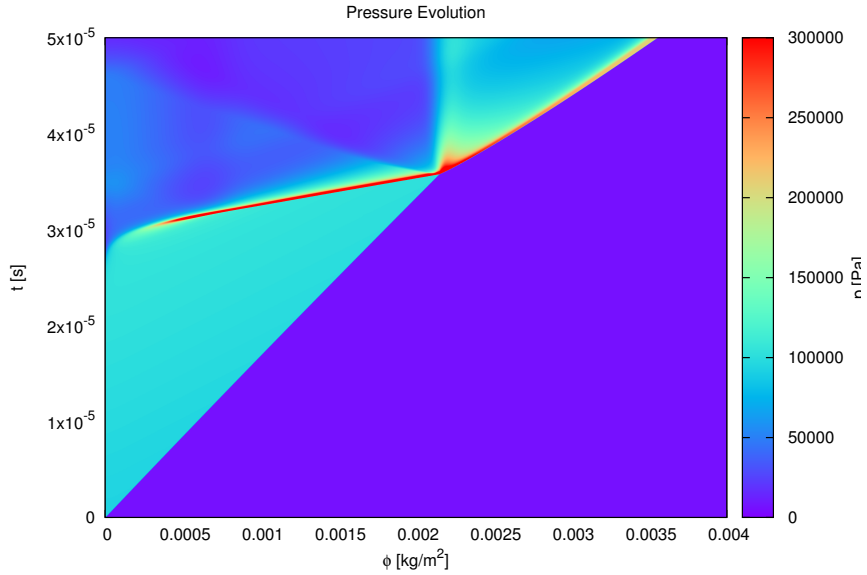

Figure D.5: Pressure profile of hydrogen fluctuating shock-induced ignition with a post shock temperature of 1100 K and piston oscillation frequency of 4.535 kHz, and amplitude of 10%.

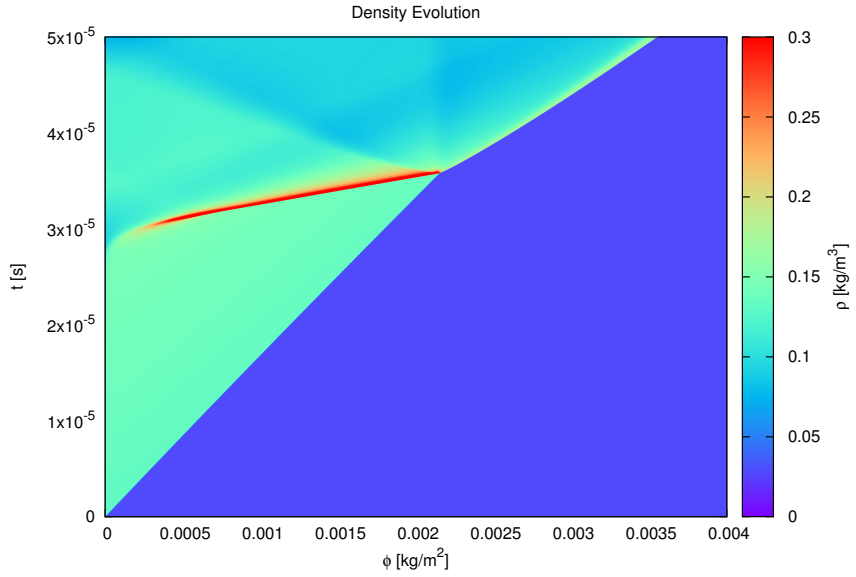

Figure D.6: Density profile of hydrogen fluctuating shock-induced ignition with a post shock temperature of 1100 K and piston oscillation frequency of 4.535 kHz, and amplitude of 10%.

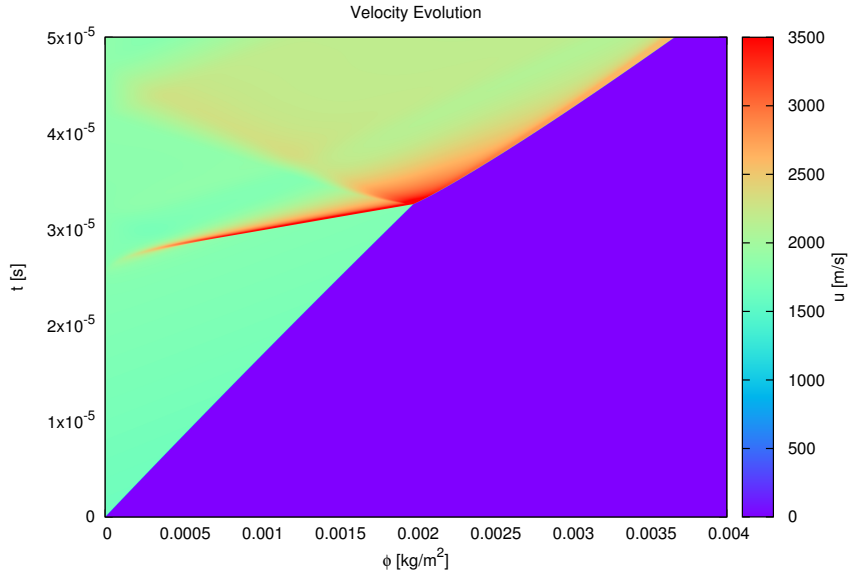

Figure D.7: Particle velocity profile of hydrogen fluctuating shock-induced ignition with a post shock temperature of 1100 K and piston oscillation frequency of 4.535 kHz, and amplitude of 15%.

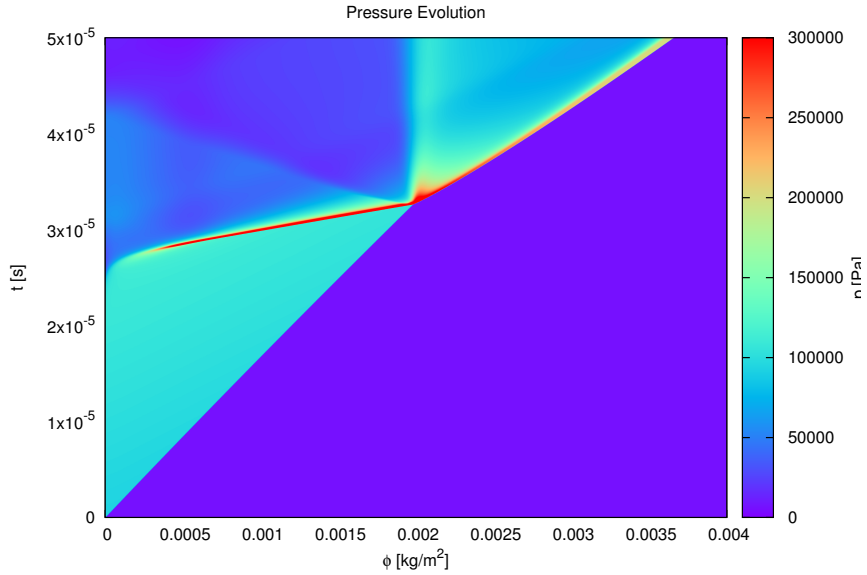

Figure D.8: Pressure profile of hydrogen fluctuating shock-induced ignition with a post shock temperature of 1100 K and piston oscillation frequency of 4.535 kHz, and amplitude of 15%.

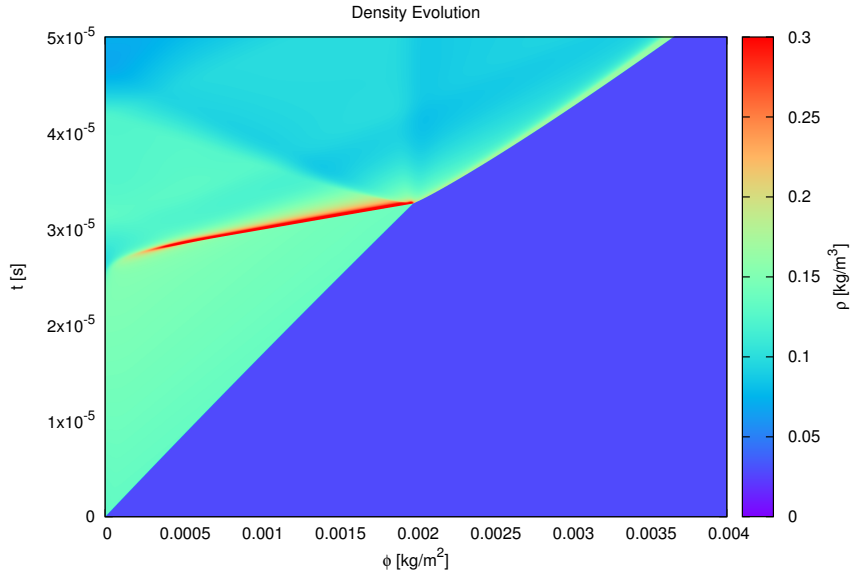

Figure D.9: Density profile of hydrogen fluctuating shock-induced ignition with a post shock temperature of 1100 K and piston oscillation frequency of 4.535 kHz, and amplitude of 15%.

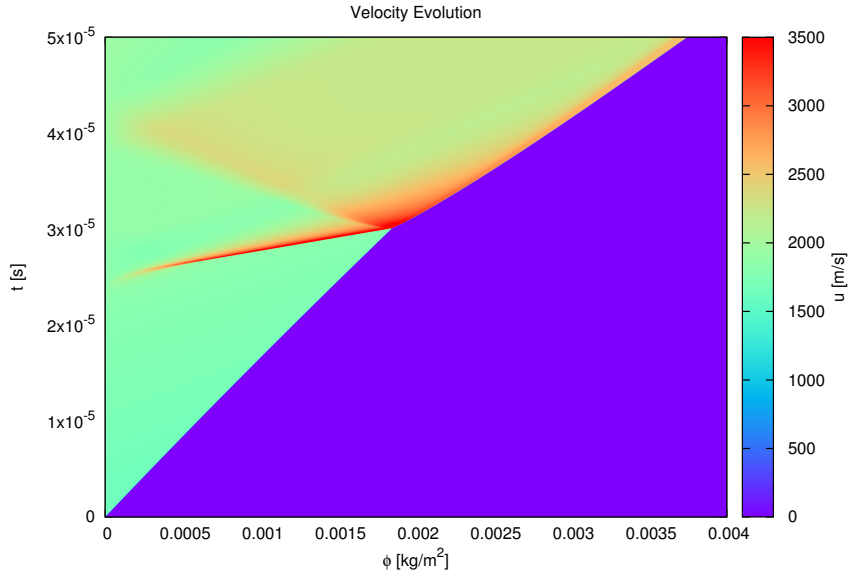

Figure D.10: Particle velocity profile of hydrogen fluctuating shock-induced ignition with a post shock temperature of 1100 K and piston oscillation frequency of 4.535 kHz, and amplitude of 20%.

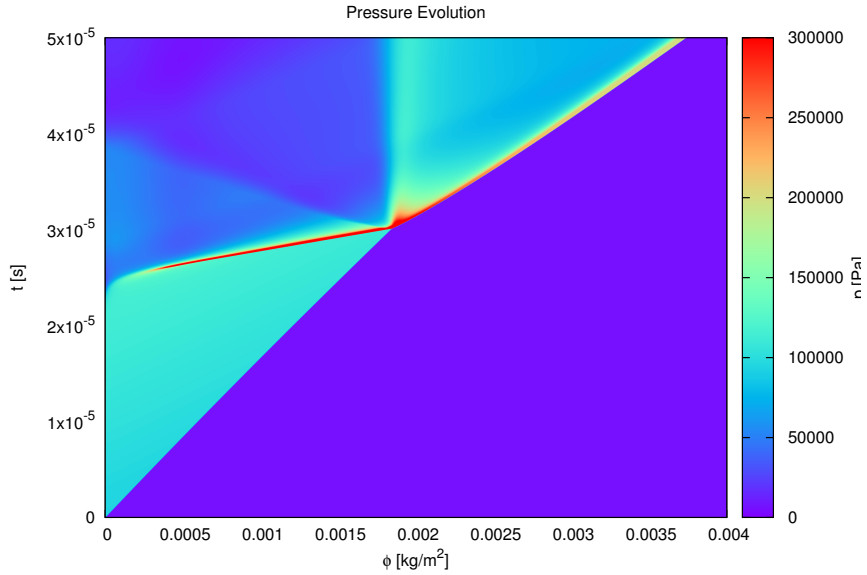

Figure D.11: Pressure profile of hydrogen fluctuating shock-induced ignition with a post shock temperature of 1100 K and piston oscillation frequency of 4.535 kHz, and amplitude of 20%.

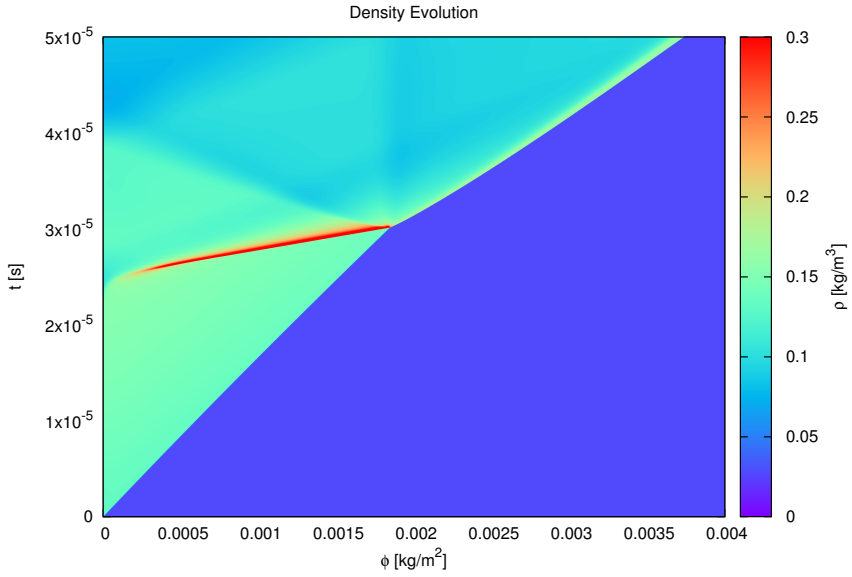

Figure D.12: Density profile of hydrogen fluctuating shock-induced ignition with a post shock temperature of 1100 K and piston oscillation frequency of 4.535 kHz, and amplitude of 20%.

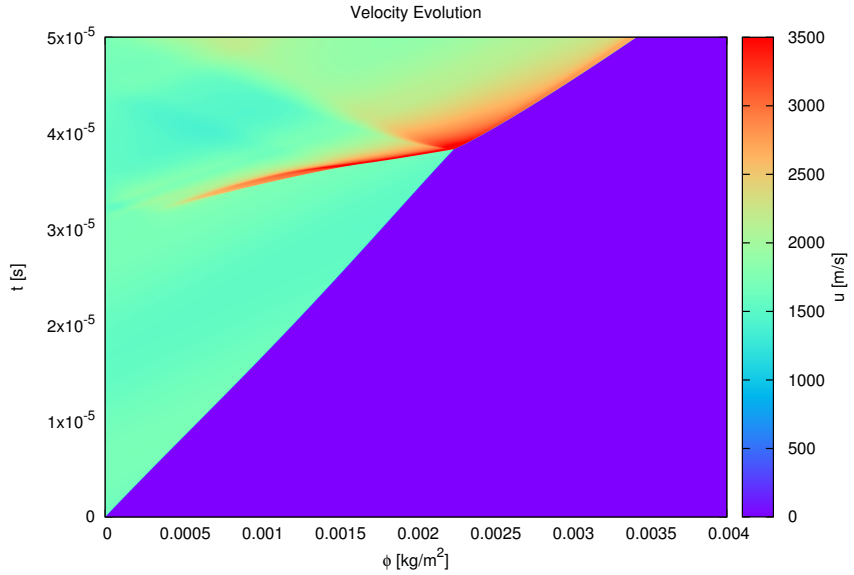

Figure D.13: Particle velocity profile of hydrogen fluctuating shock-induced ignition with a post shock temperature of 1100 K and piston oscillation frequency of 45.35 kHz, and amplitude of 5%.

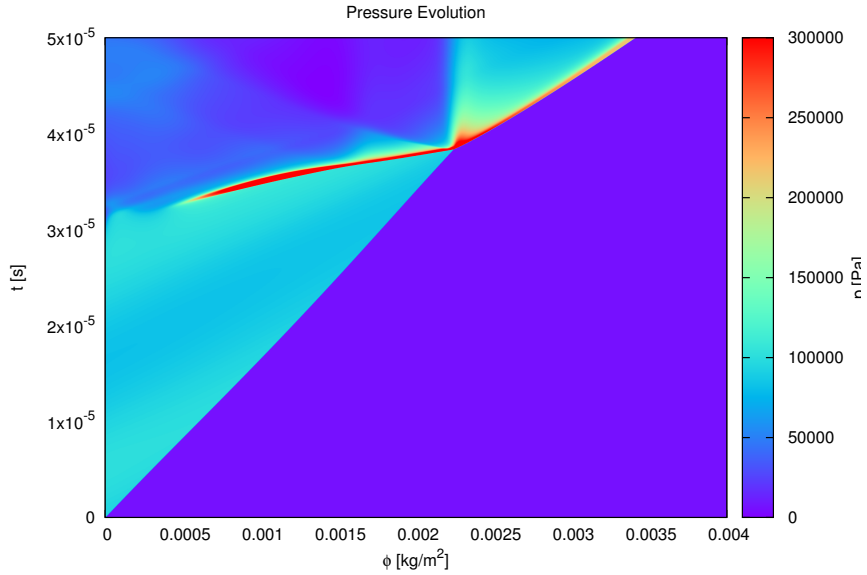

Figure D.14: Pressure profile of hydrogen fluctuating shock-induced ignition with a post shock temperature of 1100 K and piston oscillation frequency of 45.35 kHz, and amplitude of 5%.

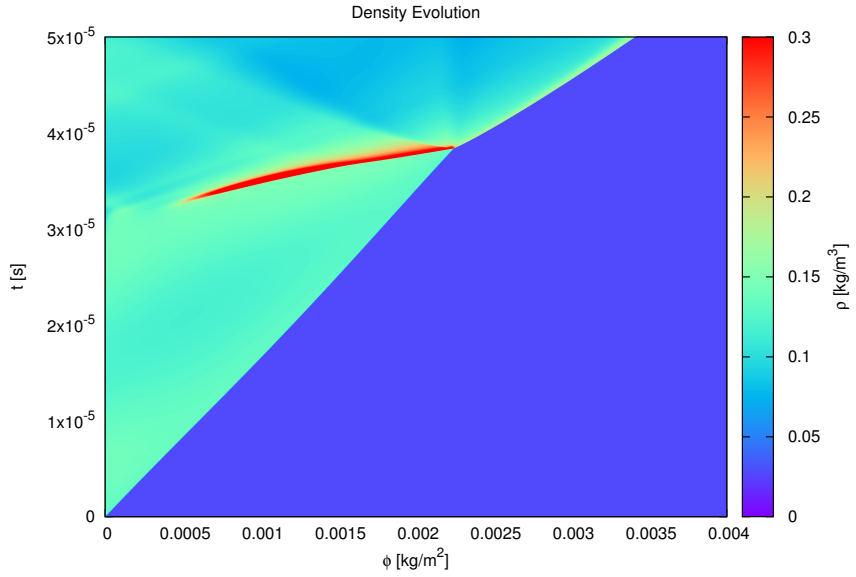

Figure D.15: Density profile of hydrogen fluctuating shock-induced ignition with a post shock temperature of 1100 K and piston oscillation frequency of 45.35 kHz, and amplitude of 5%.

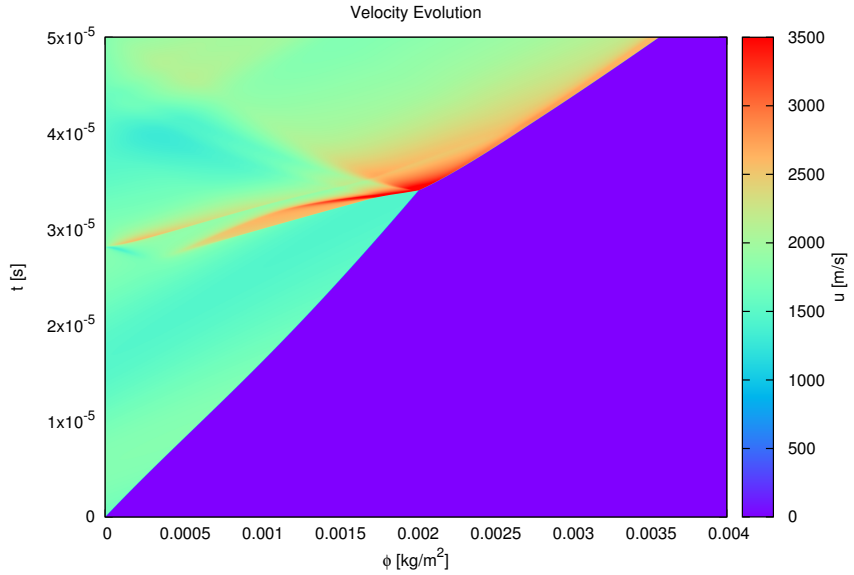

Figure D.16: Particle velocity profile of hydrogen fluctuating shock-induced ignition with a post shock temperature of 1100 K and piston oscillation frequency of 45.35 kHz, and amplitude of 10%.

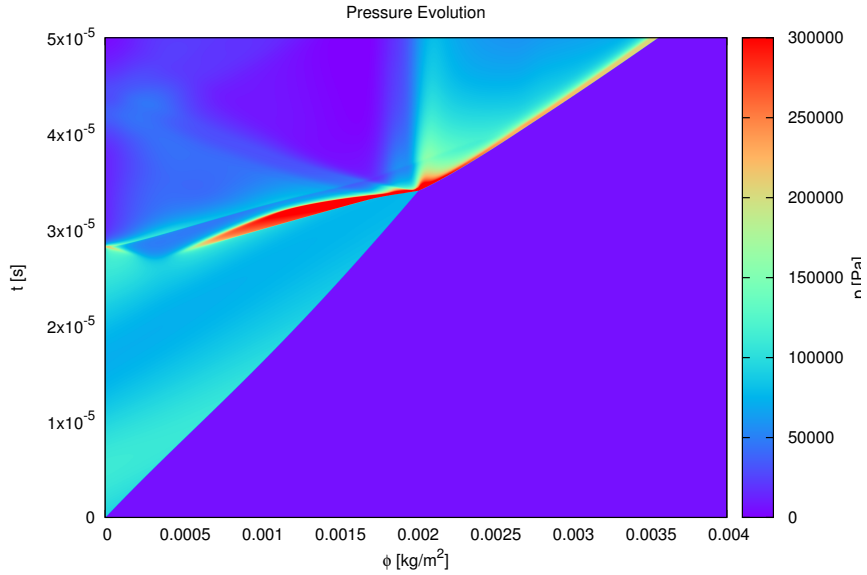

Figure D.17: Pressure profile of hydrogen fluctuating shock-induced ignition with a post shock temperature of 1100 K and piston oscillation frequency of 45.35 kHz, and amplitude of 10%.

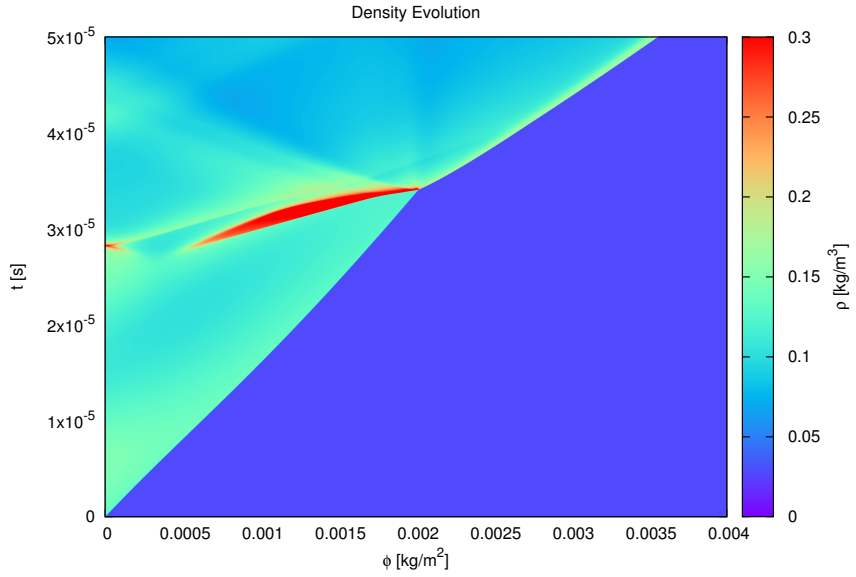

Figure D.18: Density profile of hydrogen fluctuating shock-induced ignition with a post shock temperature of 1100 K and piston oscillation frequency of 45.35 kHz, and amplitude of 10%.

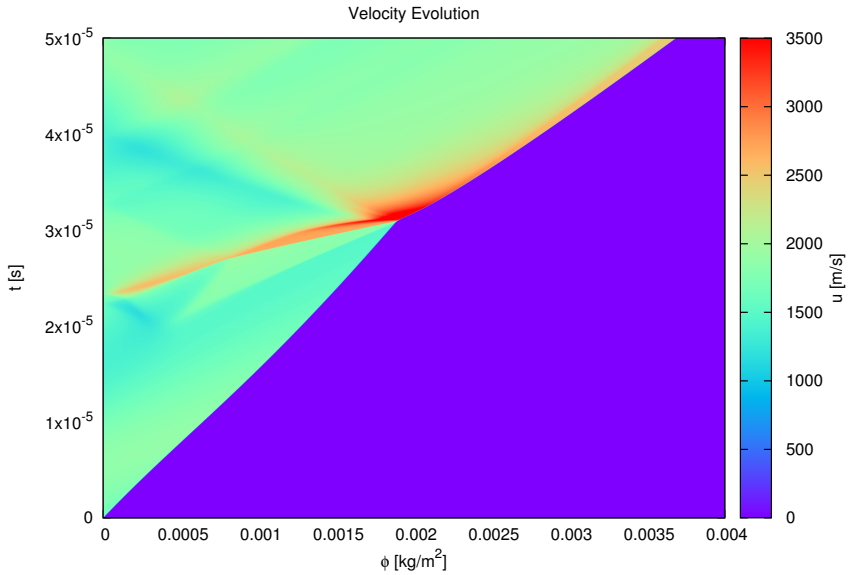

Figure D.19: Particle velocity profile of hydrogen fluctuating shock-induced ignition with a post shock temperature of 1100 K and piston oscillation frequency of 45.35 kHz, and amplitude of 15%.

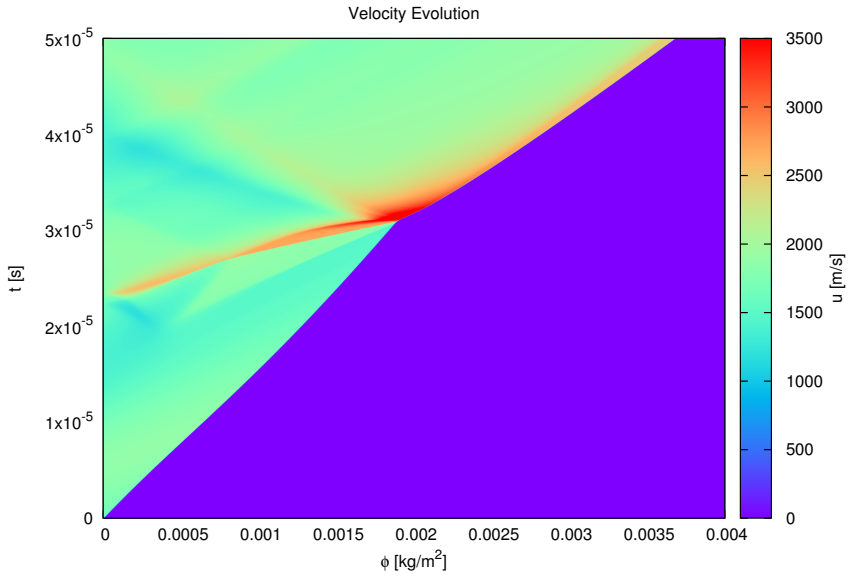

Figure D.20: Particle velocity profile of hydrogen fluctuating shock-induced ignition with a post shock temperature of 1100 K and piston oscillation frequency of 45.35 kHz, and amplitude of 15%.

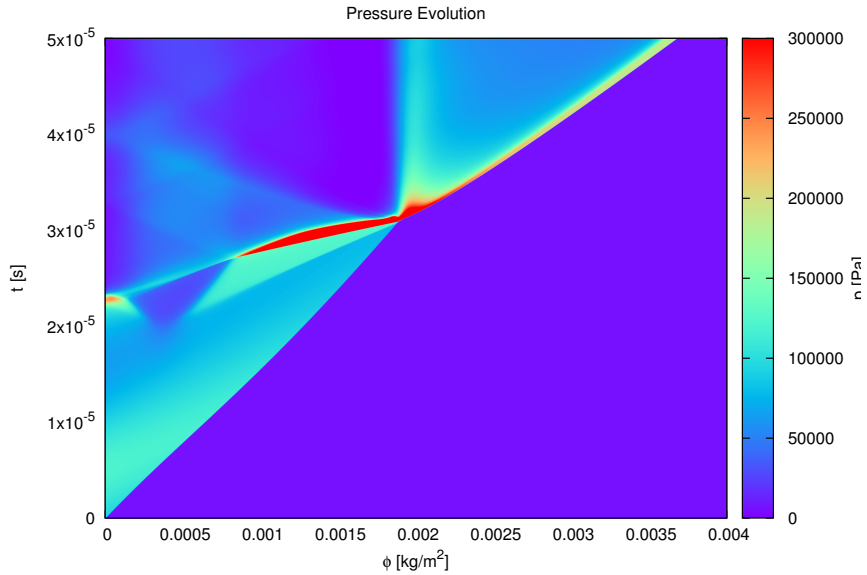

Figure D.21: Pressure profile of hydrogen fluctuating shock-induced ignition with a post shock temperature of 1100 K and piston oscillation frequency of 45.35 kHz, and amplitude of 15%.

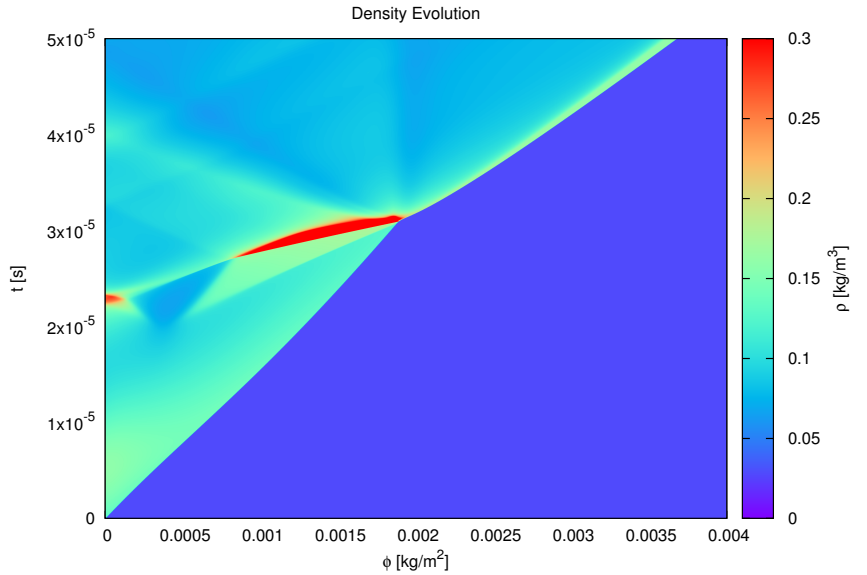

Figure D.22: Density profile of hydrogen fluctuating shock-induced ignition with a post shock temperature of 1100 K and piston oscillation frequency of 45.35 kHz, and amplitude of 15%.

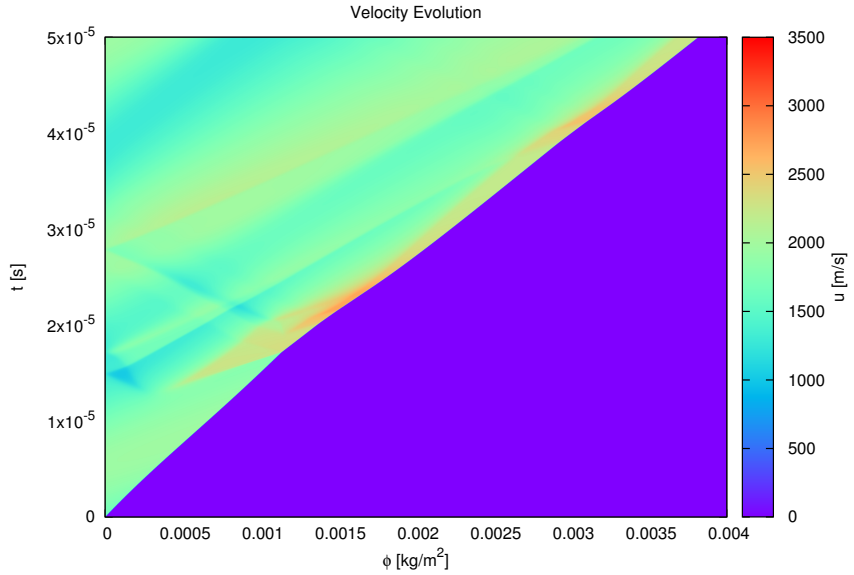

Figure D.23: Particle velocity profile of hydrogen fluctuating shock-induced ignition with a post shock temperature of 1100 K and piston oscillation frequency of 45.35 kHz, and amplitude of 20%.

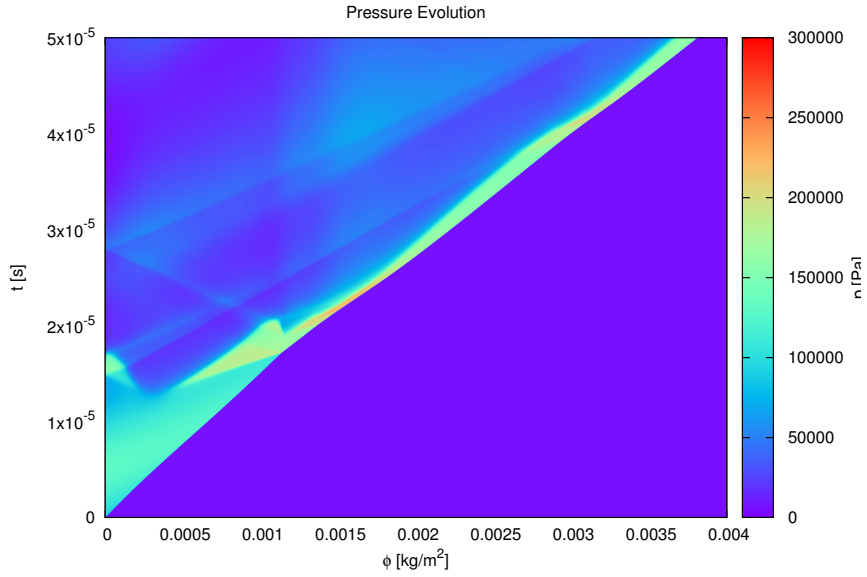

Figure D.24: Pressure profile of hydrogen fluctuating shock-induced ignition with a post shock temperature of 1100 K and piston oscillation frequency of 45.35 kHz, and amplitude of 20%.

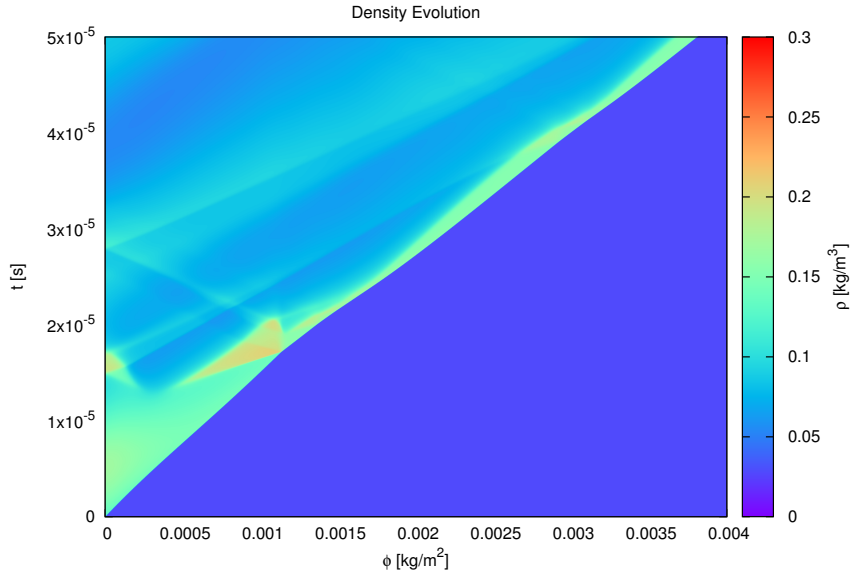

Figure D.25: Density profile of hydrogen fluctuating shock-induced ignition with a post shock temperature of 1100 K and piston oscillation frequency of 45.35 kHz, and amplitude of 20%.

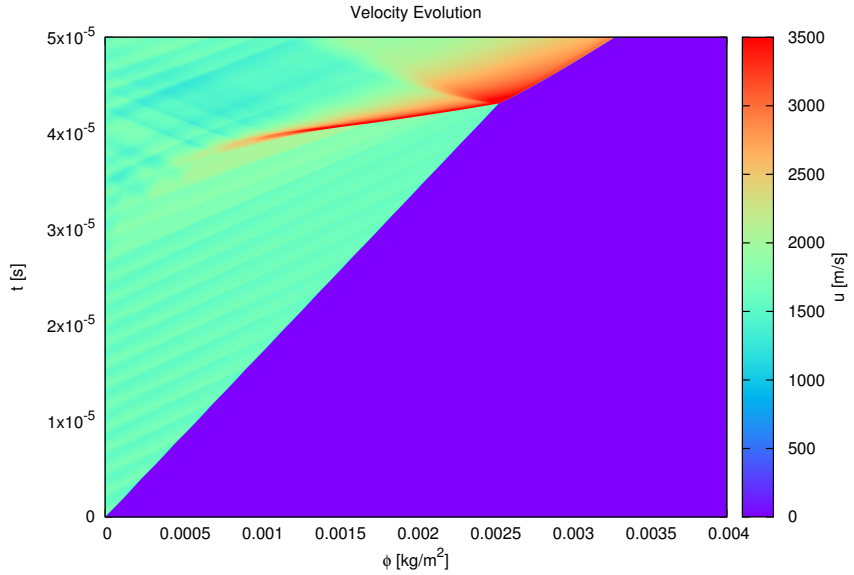

Figure D.26: Particle velocity profile of hydrogen fluctuating shock-induced ignition with a post shock temperature of 1100 K and piston oscillation frequency of 453.5 kHz, and amplitude of 5%.

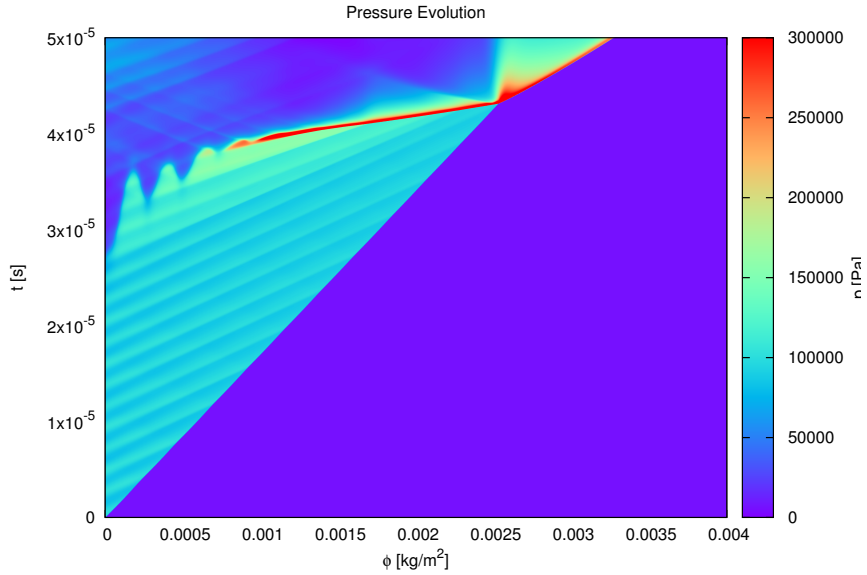

Figure D.27: Pressure profile of hydrogen fluctuating shock-induced ignition with a post shock temperature of 1100 K and piston oscillation frequency of 453.5 kHz, and amplitude of 5%.

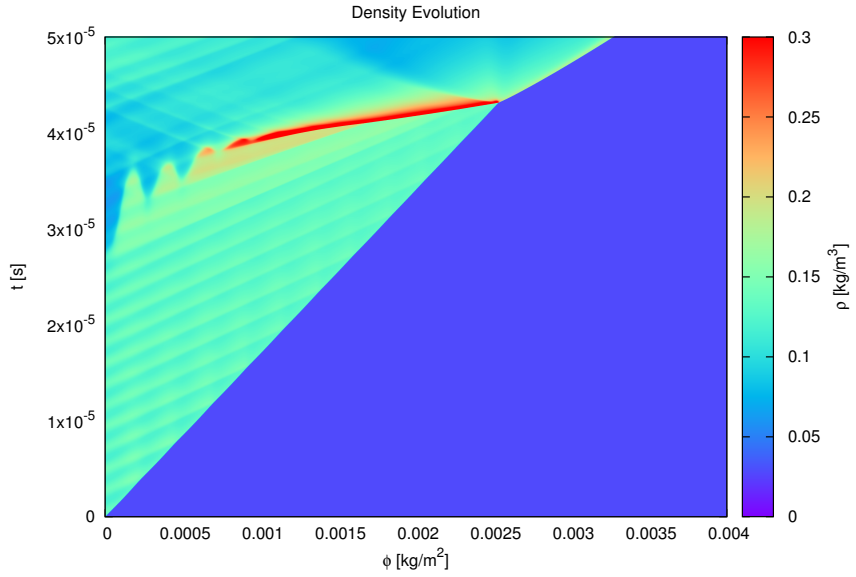

Figure D.28: Density profile of hydrogen fluctuating shock-induced ignition with a post shock temperature of 1100 K and piston oscillation frequency of 453.5 kHz, and amplitude of 5%.

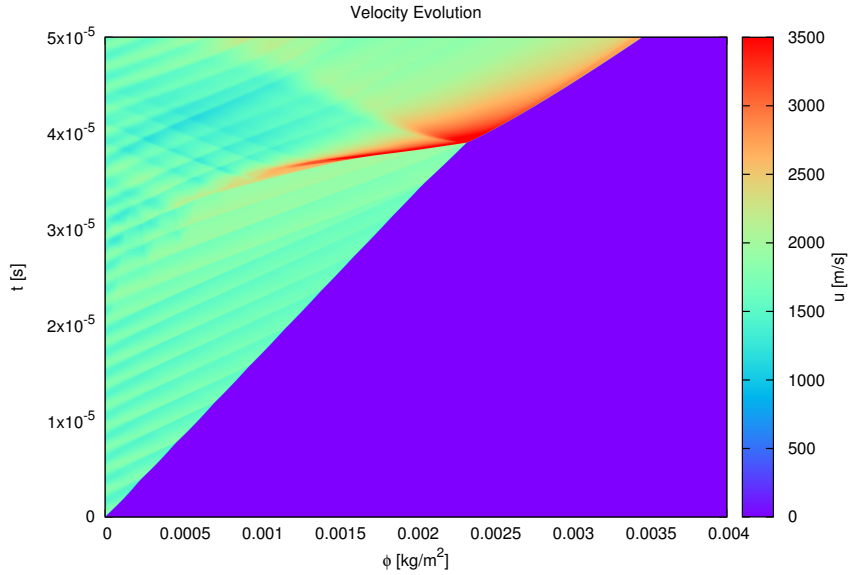

Figure D.29: Particle velocity profile of hydrogen fluctuating shock-induced ignition with a post shock temperature of 1100 K and piston oscillation frequency of 453.5 kHz, and amplitude of 10%.

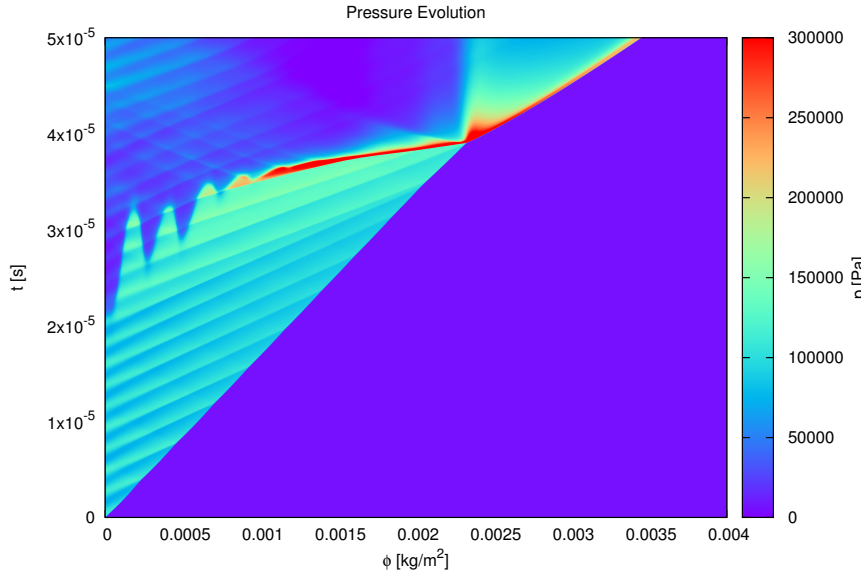

Figure D.30: Pressure profile of hydrogen fluctuating shock-induced ignition with a post shock temperature of 1100 K and piston oscillation frequency of 453.5 kHz, and amplitude of 10%.

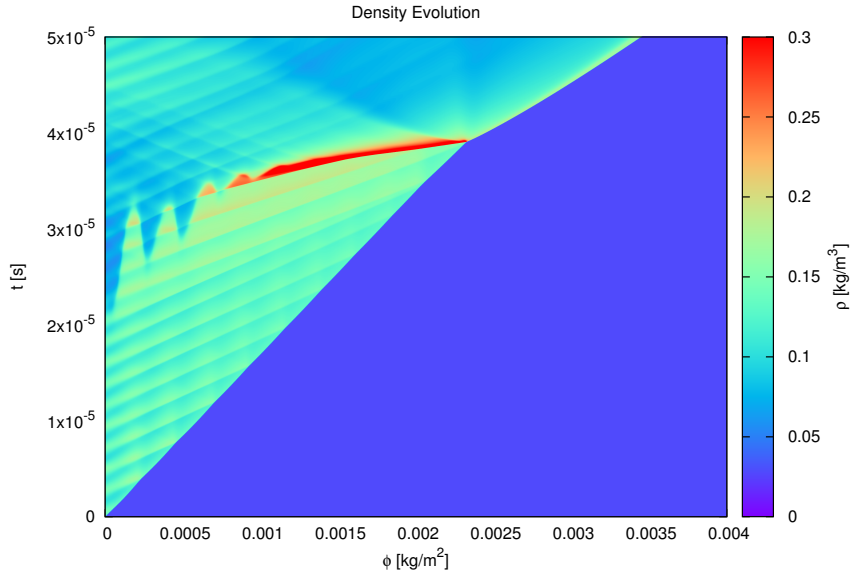

Figure D.31: Density profile of hydrogen fluctuating shock-induced ignition with a post shock temperature of 1100 K and piston oscillation frequency of 453.5 kHz, and amplitude of 10%.

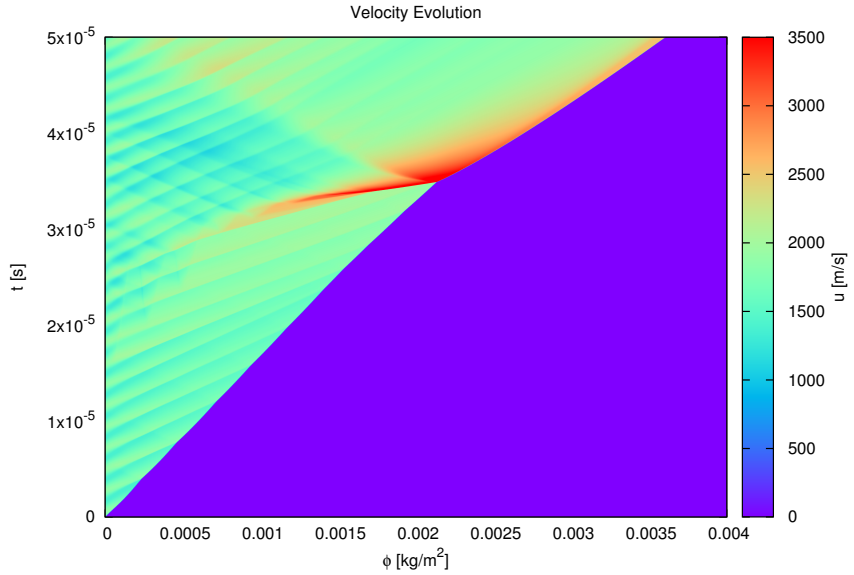

Figure D.32: Particle velocity profile of hydrogen fluctuating shock-induced ignition with a post shock temperature of 1100 K and piston oscillation frequency of 453.5 kHz, and amplitude of 15%.

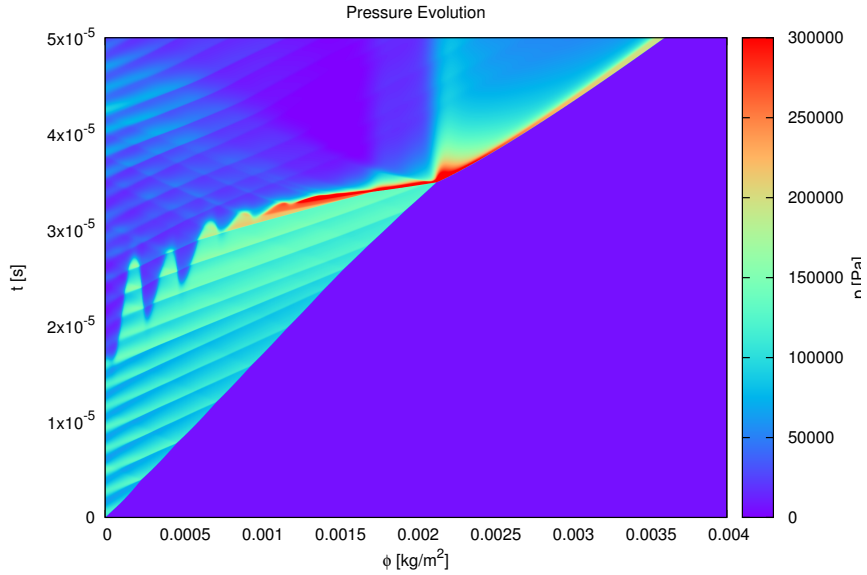

Figure D.33: Pressure profile of hydrogen fluctuating shock-induced ignition with a post shock temperature of 1100 K and piston oscillation frequency of 453.5 kHz, and amplitude of 15%.

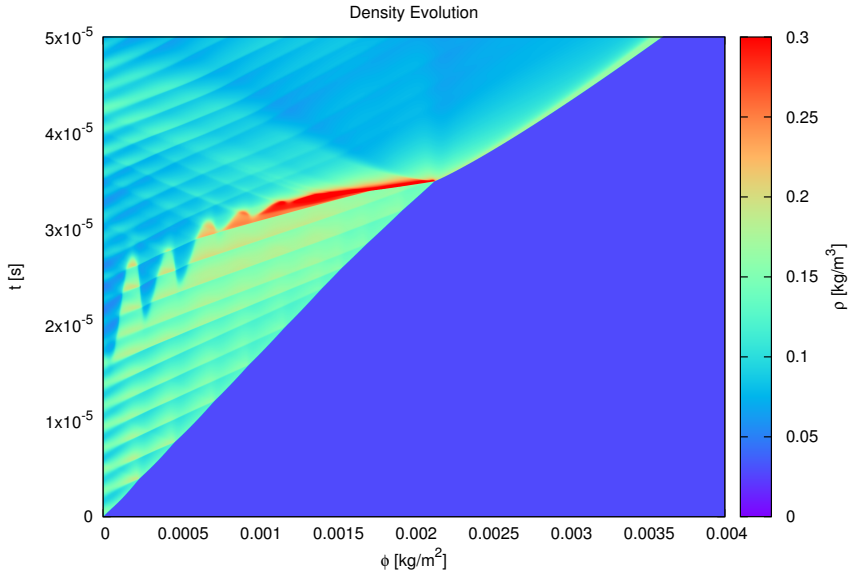

Figure D.34: Density profile of hydrogen fluctuating shock-induced ignition with a post shock temperature of 1100 K and piston oscillation frequency of 453.5 kHz, and amplitude of 15%.

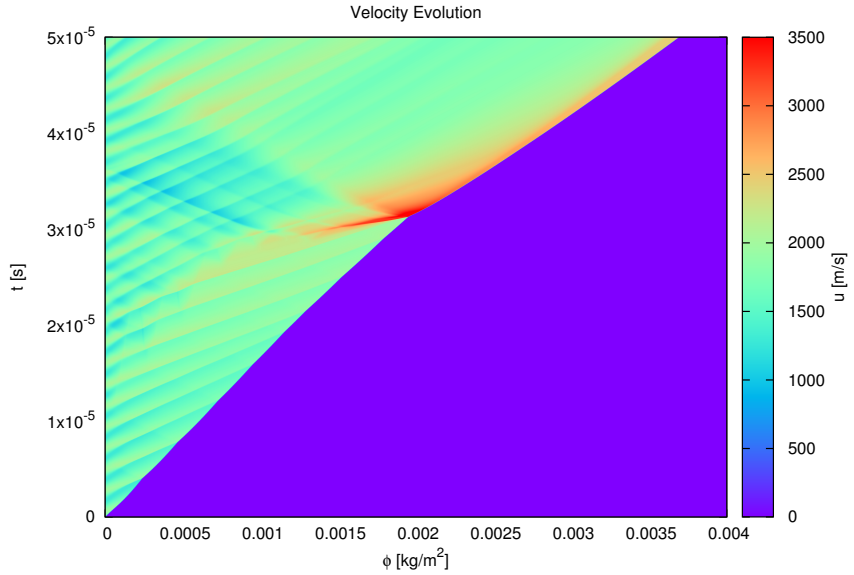

Figure D.35: Particle velocity profile of hydrogen fluctuating shock-induced ignition with a post shock temperature of 1100 K and piston oscillation frequency of 453.5 kHz, and amplitude of 20%.

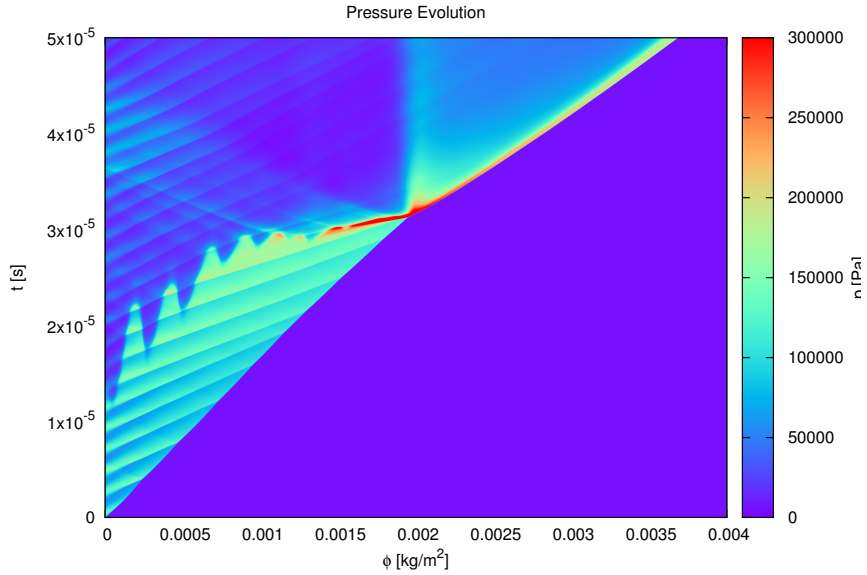

Figure D.36: Pressure profile of hydrogen fluctuating shock-induced ignition with a post shock temperature of 1100 K and piston oscillation frequency of 453.5 kHz, and amplitude of 20%.

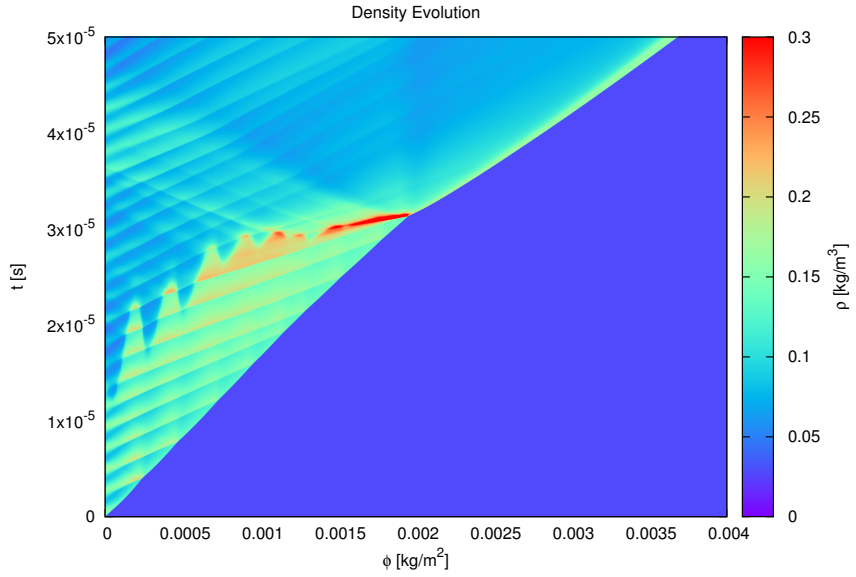

Figure D.37: Density profile of hydrogen fluctuating shock-induced ignition with a post shock temperature of 1100 K and piston oscillation frequency of 453.5 kHz, and amplitude of 20%.

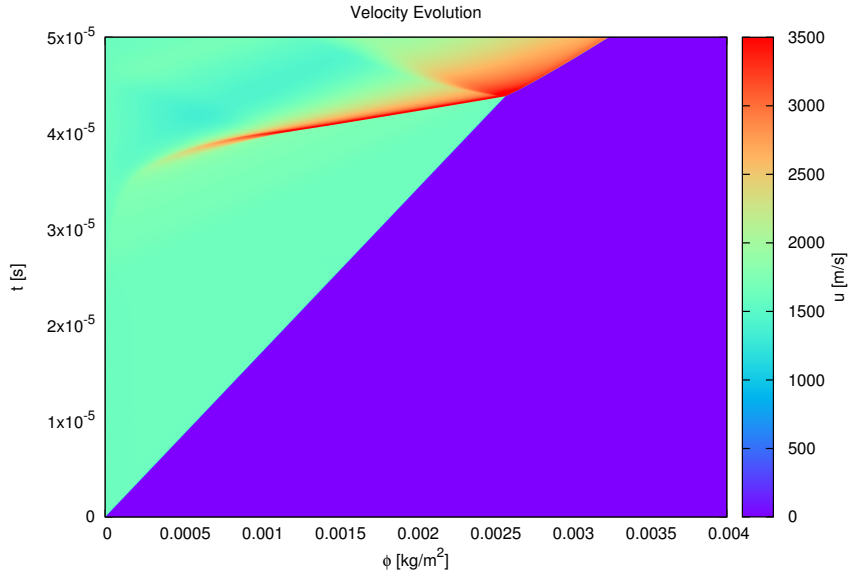

Figure D.38: Particle velocity profile of hydrogen fluctuating shock-induced ignition with a post shock temperature of 1100 K and piston oscillation frequency of 4535 kHz, and amplitude of 5%.

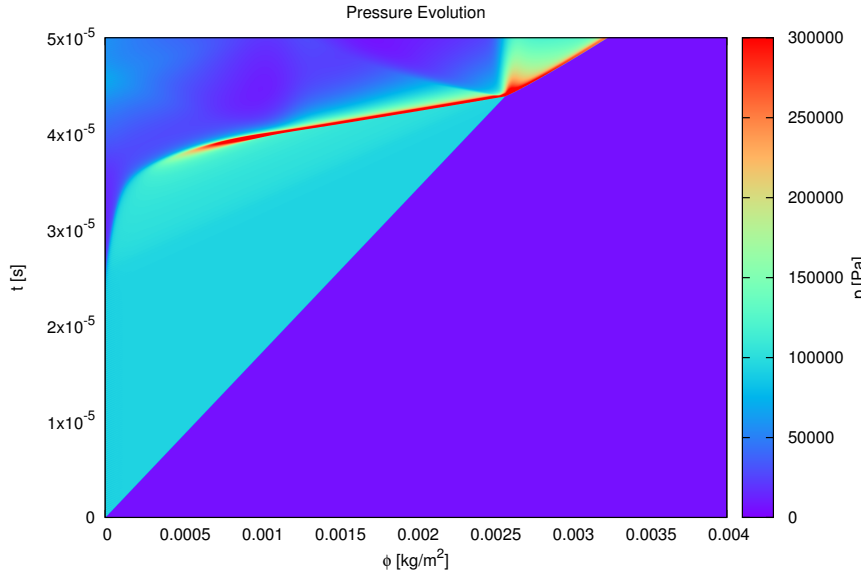

Figure D.39: Pressure profile of hydrogen fluctuating shock-induced ignition with a post shock temperature of 1100 K and piston oscillation frequency of 4535 kHz, and amplitude of 5%.

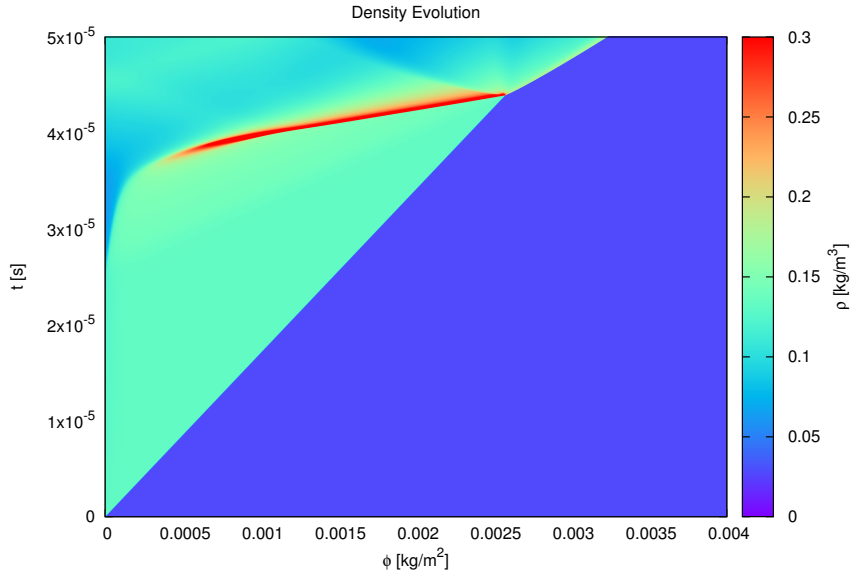

Figure D.40: Density profile of hydrogen fluctuating shock-induced ignition with a post shock temperature of 1100 K and piston oscillation frequency of 4535 kHz, and amplitude of 5%.

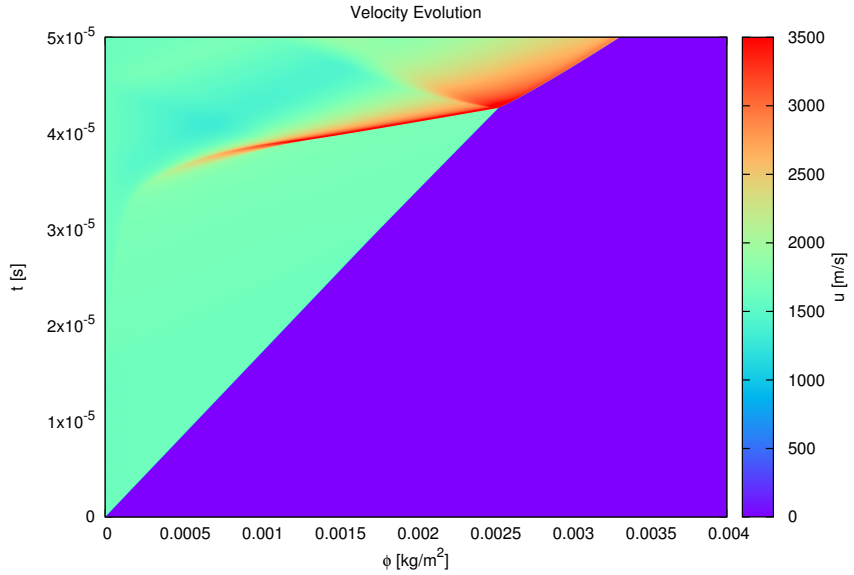

Figure D.41: Particle velocity profile of hydrogen fluctuating shock-induced ignition with a post shock temperature of 1100 K and piston oscillation frequency of 4535 kHz, and amplitude of 10%.

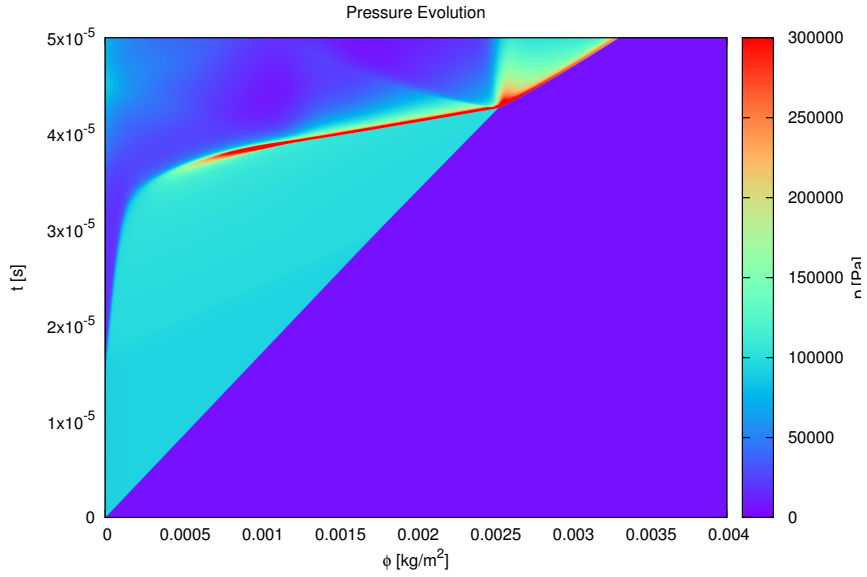

Figure D.42: Pressure profile of hydrogen fluctuating shock-induced ignition with a post shock temperature of 1100 K and piston oscillation frequency of 4535 kHz, and amplitude of 10%.

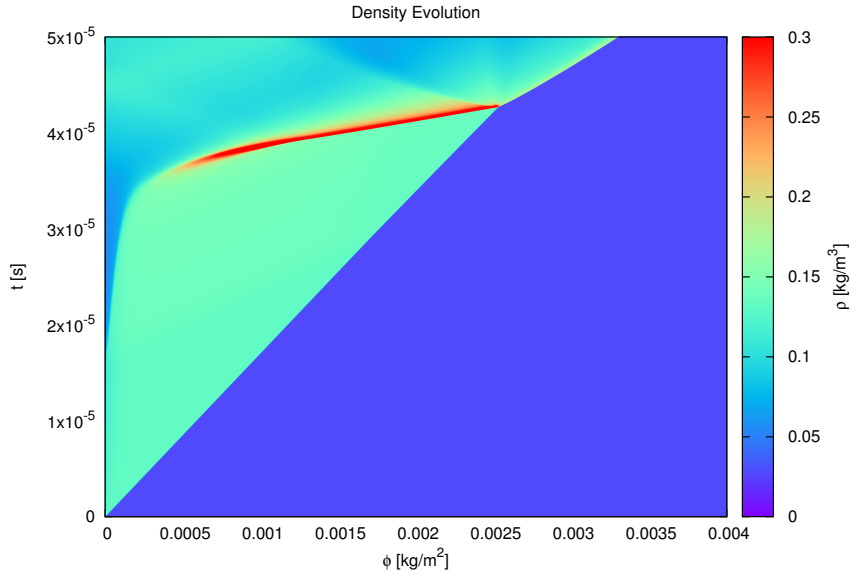

Figure D.43: Density profile of hydrogen fluctuating shock-induced ignition with a post shock temperature of 1100 K and piston oscillation frequency of 4535 kHz, and amplitude of 10%.

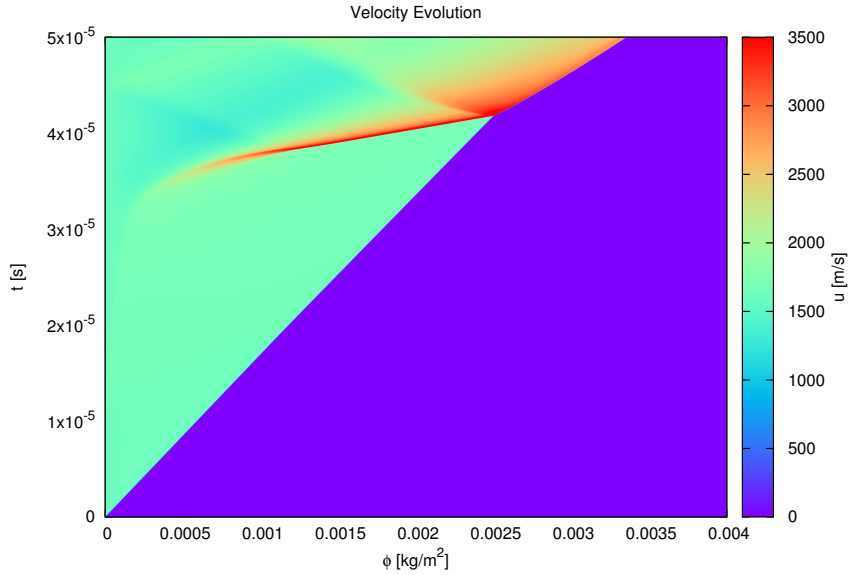

Figure D.44: Particle velocity profile of hydrogen fluctuating shock-induced ignition with a post shock temperature of 1100 K and piston oscillation frequency of 4535 kHz, and amplitude of 15%.

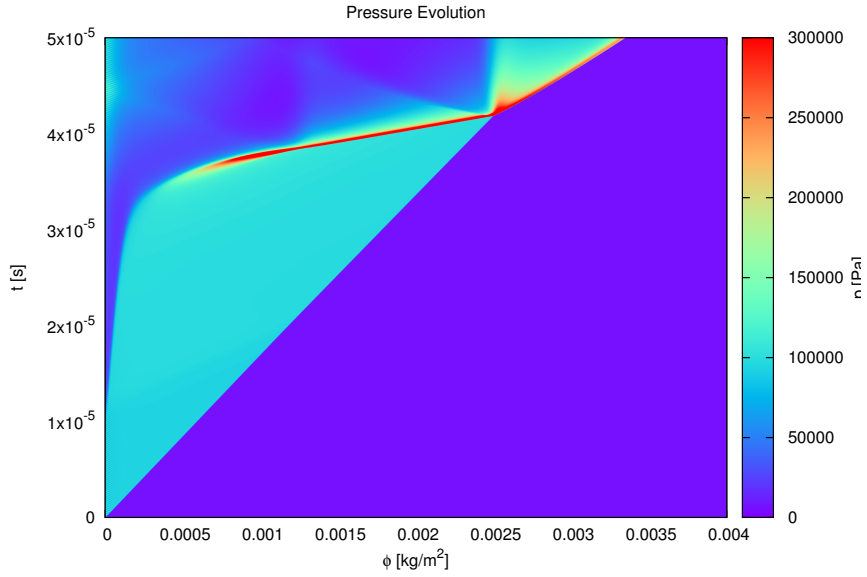

Figure D.45: Pressure profile of hydrogen fluctuating shock-induced ignition with a post shock temperature of 1100 K and piston oscillation frequency of 4535 kHz, and amplitude of 15%.

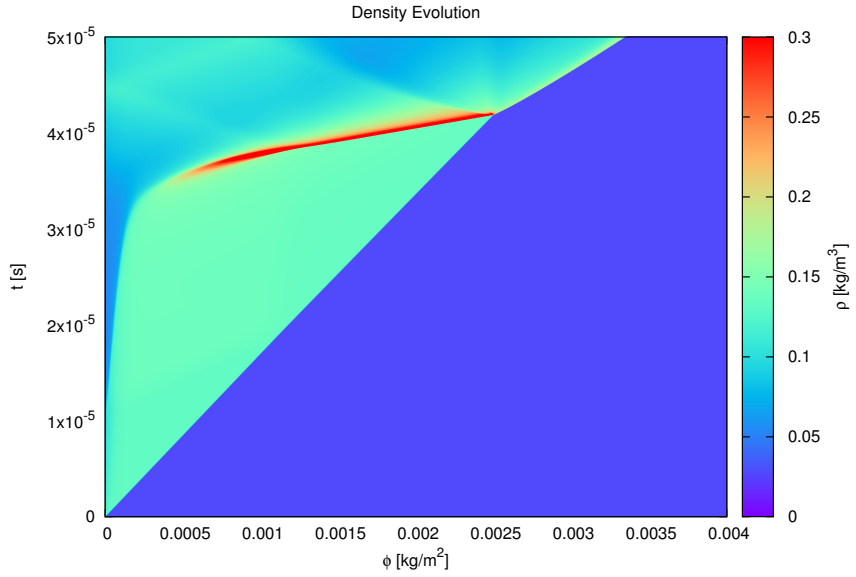

Figure D.46: Density profile of hydrogen fluctuating shock-induced ignition with a post shock temperature of 1100 K and piston oscillation frequency of 4535 kHz, and amplitude of 15%.

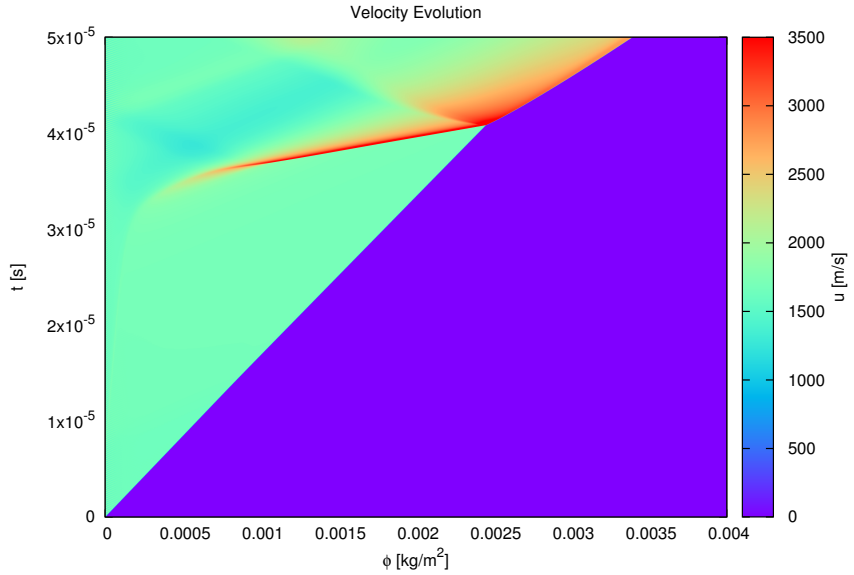

Figure D.47: Particle velocity profile of hydrogen fluctuating shock-induced ignition with a post shock temperature of 1100 K and piston oscillation frequency of 4535 kHz, and amplitude of 20%.

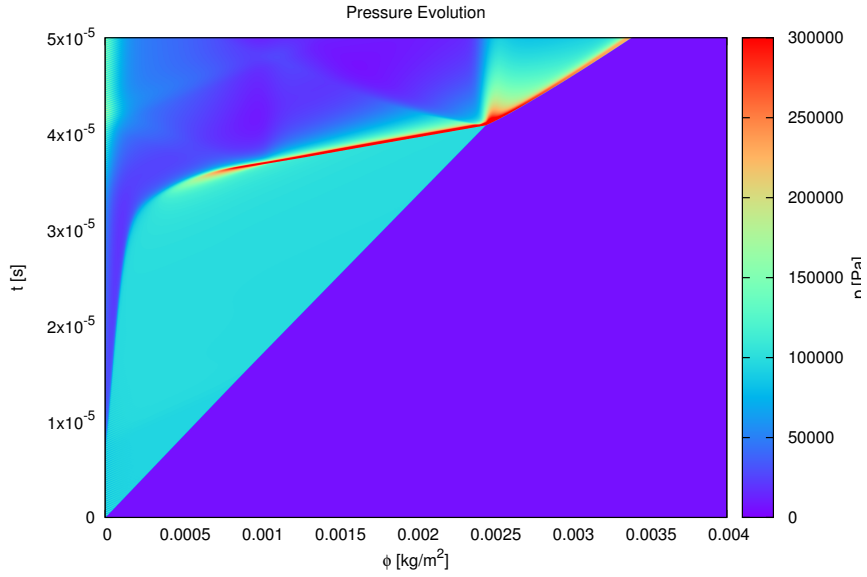

Figure D.48: Pressure profile of hydrogen fluctuating shock-induced ignition with a post shock temperature of 1100 K and piston oscillation frequency of 4535 kHz, and amplitude of 20%.

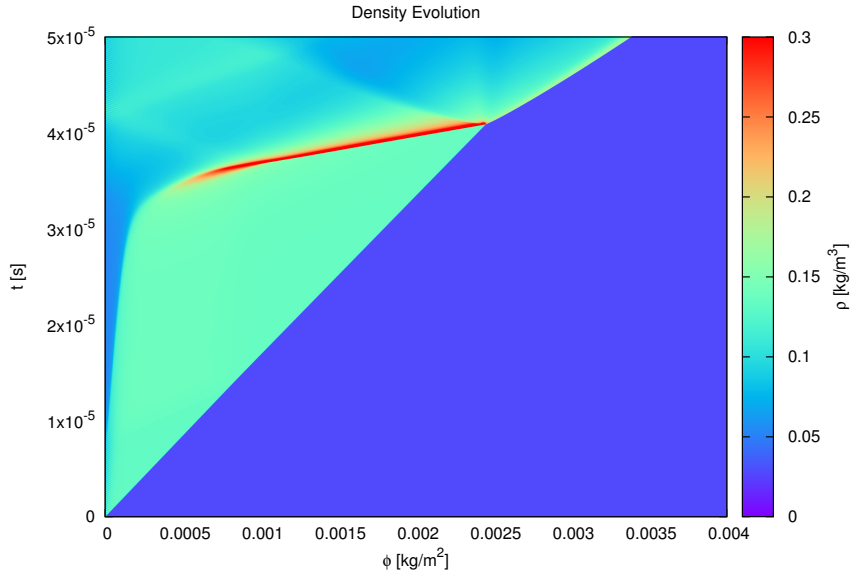

Figure D.49: Density profile of hydrogen fluctuating shock-induced ignition with a post shock temperature of 1100 K and piston oscillation frequency of 4535 kHz, and amplitude of 20%.

Appendix E

Ethylene-Oxygen Simulation Plots

This appendix provides the particle velocity, pressure and density plots for the simulations in Chapter 6.

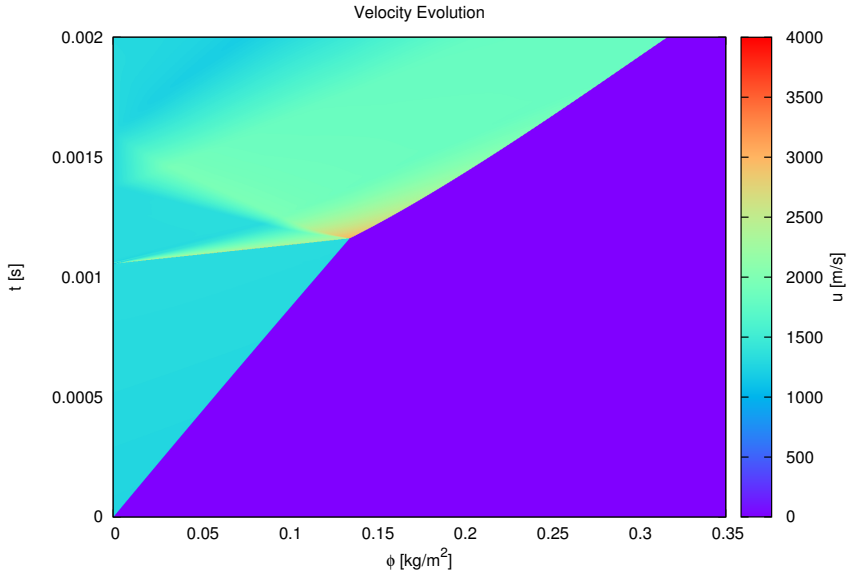

Figure E.1: Particle velocity profile of ethylene fluctuating shock-induced ignition with incident shock Mach number of 4.5, and piston oscillation frequency of 0.2 kHz, and amplitude of 5%.

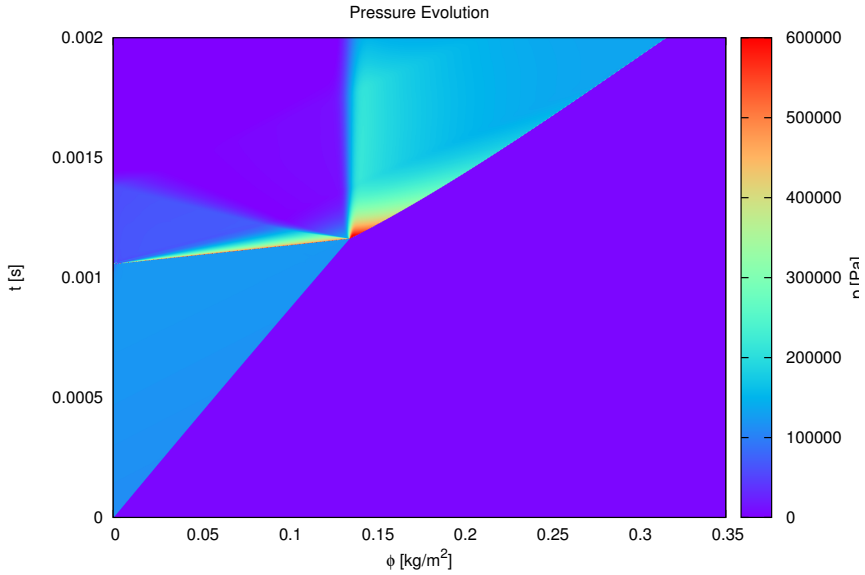

Figure E.2: Pressure profile of ethylene fluctuating shock-induced ignition with incident shock Mach number of 4.5, and piston oscillation frequency of 0.2 kHz, and amplitude of 5%.

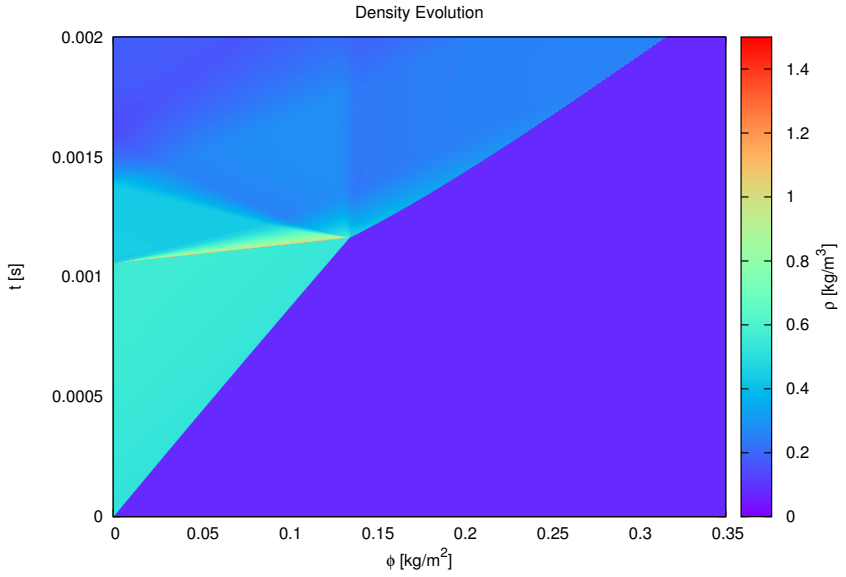

Figure E.3: Density profile of ethylene fluctuating shock-induced ignition with incident shock Mach number of 4.5, and piston oscillation frequency of 0.2 kHz, and amplitude of 5%.

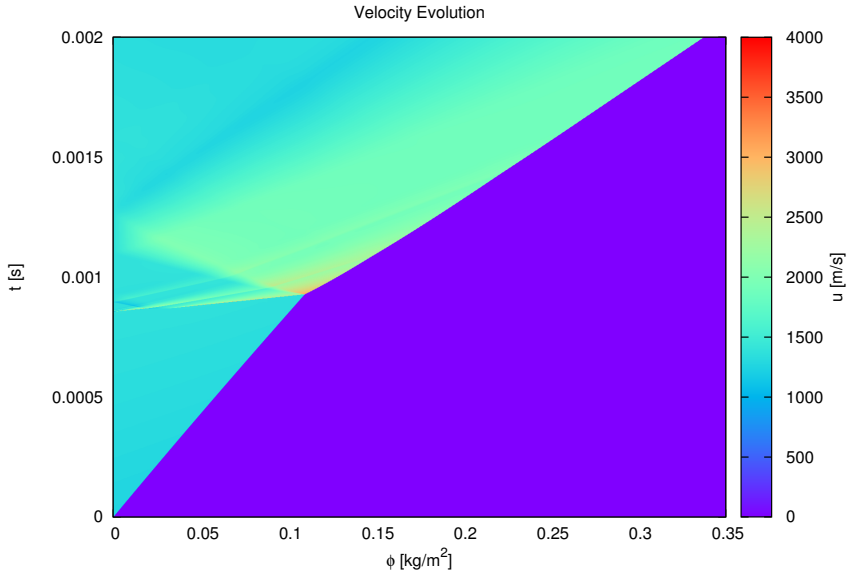

Figure E.4: Particle velocity profile of ethylene fluctuating shock-induced ignition with incident shock Mach number of 4.5, and piston oscillation frequency of 0.2 kHz, and amplitude of 10%.

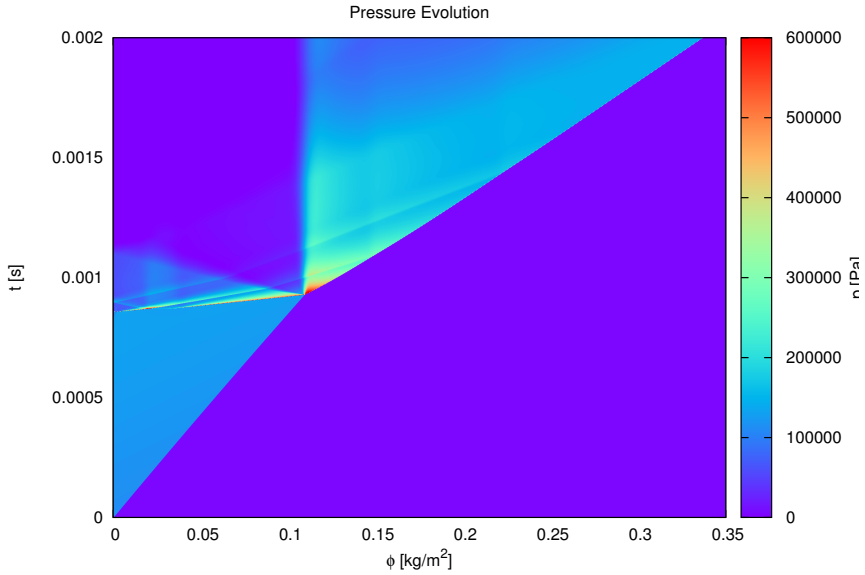

Figure E.5: Pressure profile of ethylene fluctuating shock-induced ignition with incident shock Mach number of 4.5, and piston oscillation frequency of 0.2 kHz, and amplitude of 10%.

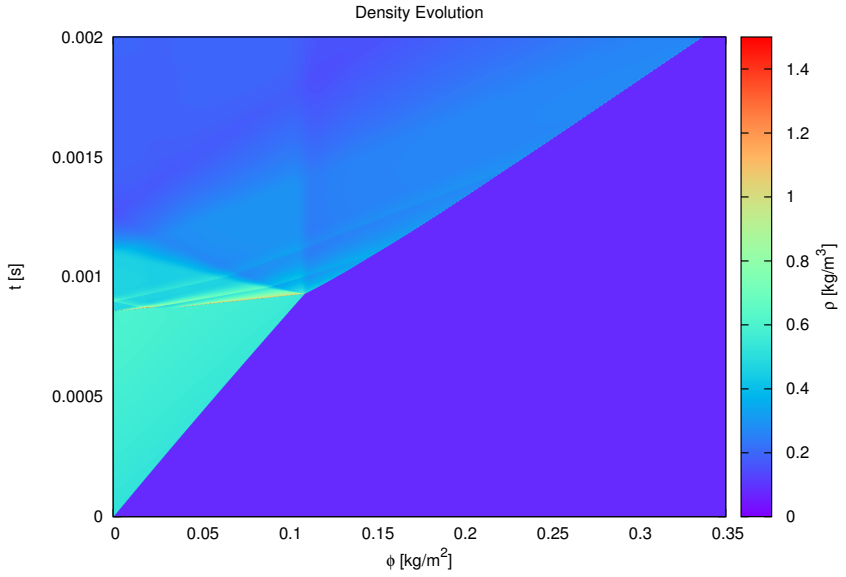

Figure E.6: Density profile of ethylene fluctuating shock-induced ignition with incident shock Mach number of 4.5, and piston oscillation frequency of 0.2 kHz, and amplitude of 10%.

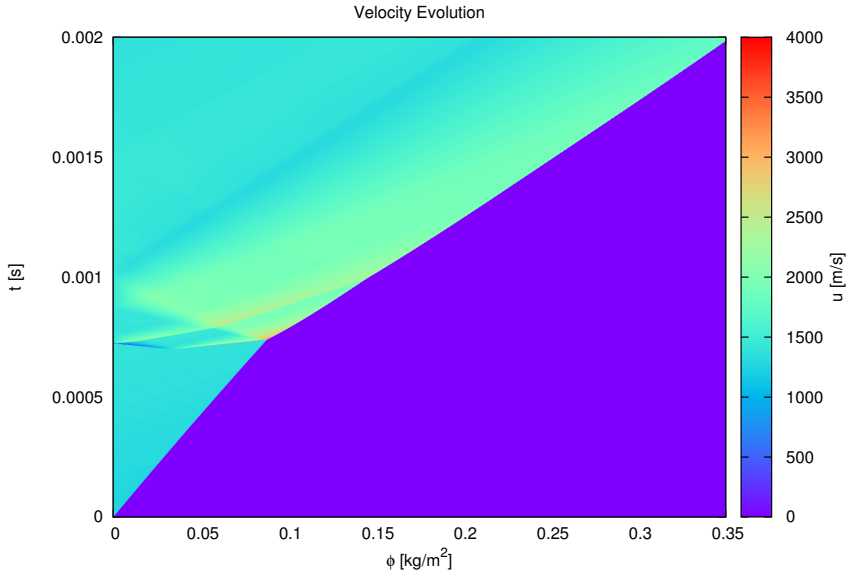

Figure E.7: Particle velocity profile of ethylene fluctuating shock-induced ignition with incident shock Mach number of 4.5, and piston oscillation frequency of 0.2 kHz, and amplitude of 15%.

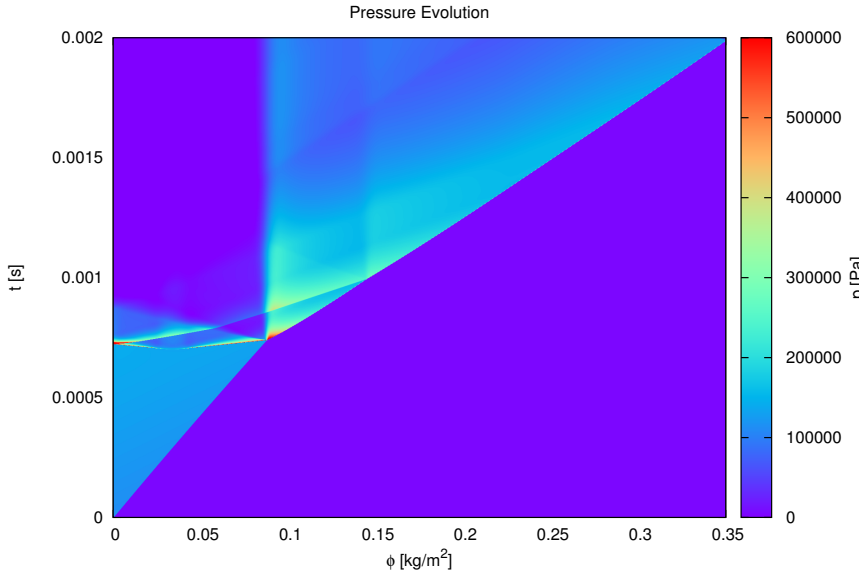

Figure E.8: Pressure profile of ethylene fluctuating shock-induced ignition with incident shock Mach number of 4.5, and piston oscillation frequency of 0.2 kHz, and amplitude of 15%.

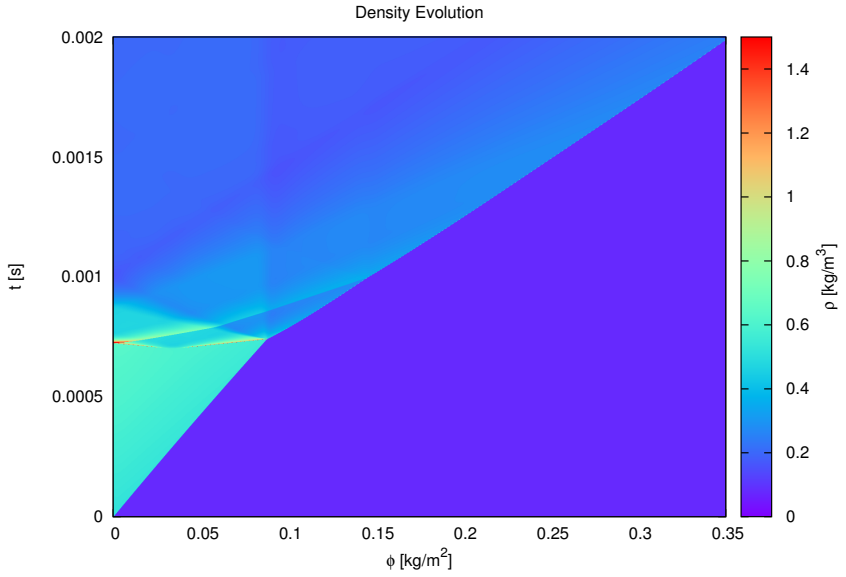

Figure E.9: Density profile of ethylene fluctuating shock-induced ignition with incident shock Mach number of 4.5, and piston oscillation frequency of 0.2 kHz, and amplitude of 15%.

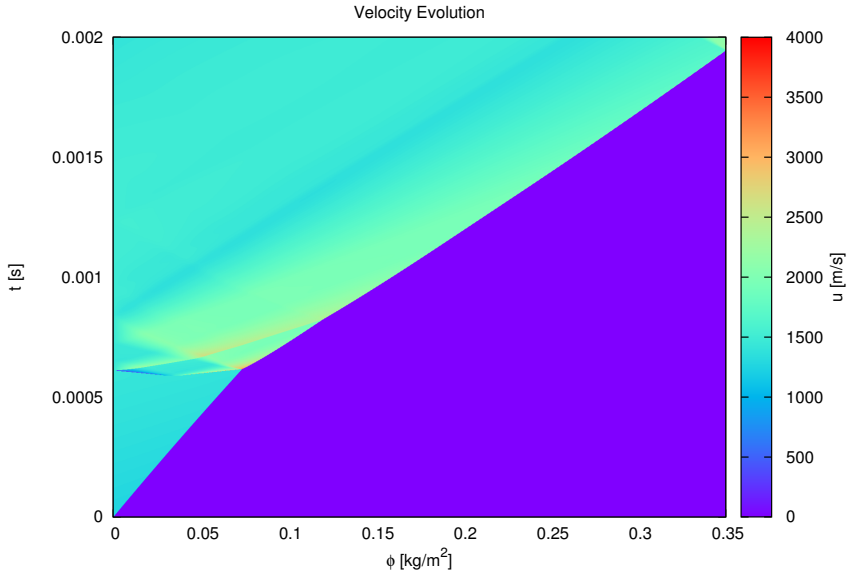

Figure E.10: Particle velocity profile of ethylene fluctuating shock-induced ignition with incident shock Mach number of 4.5, and piston oscillation frequency of 0.2 kHz, and amplitude of 20%.

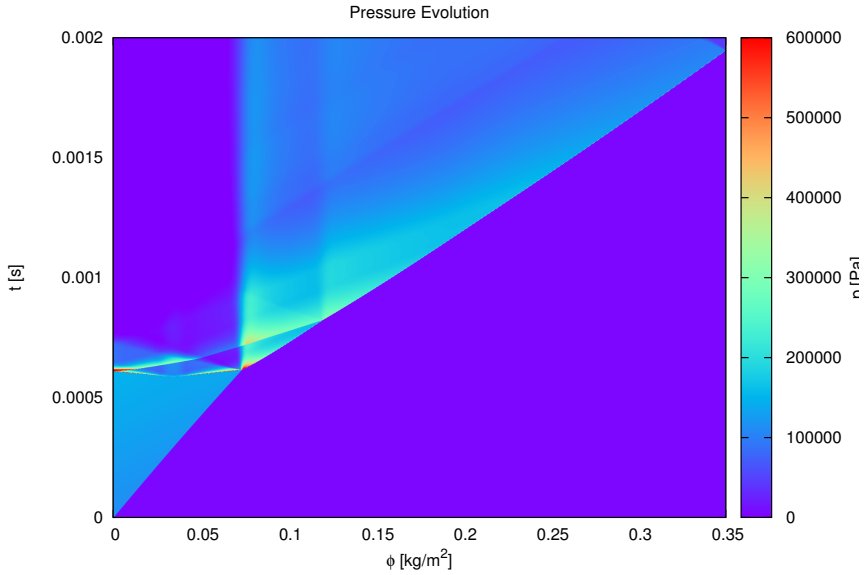

Figure E.11: Pressure profile of ethylene fluctuating shock-induced ignition with incident shock Mach number of 4.5, and piston oscillation frequency of 0.2 kHz, and amplitude of 20%.

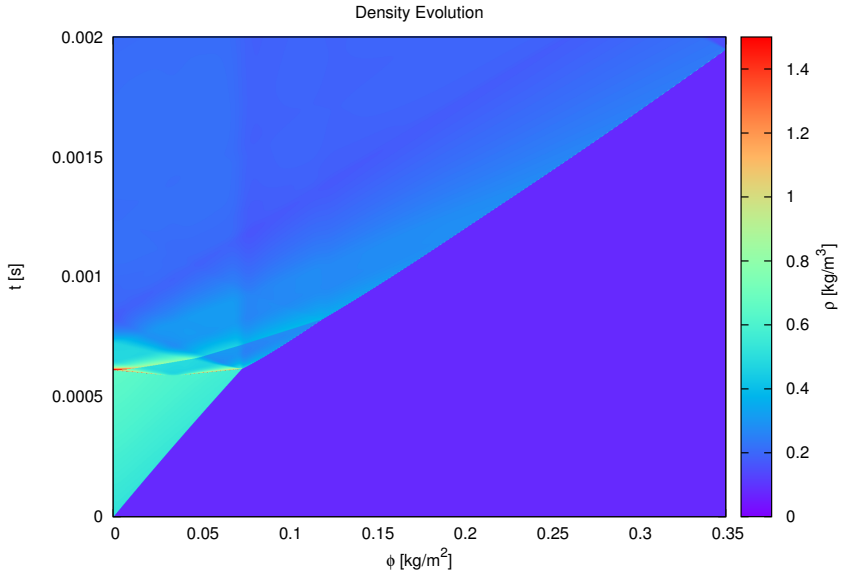

Figure E.12: Density profile of ethylene fluctuating shock-induced ignition with incident shock Mach number of 4.5, and piston oscillation frequency of 0.2 kHz, and amplitude of 20%.

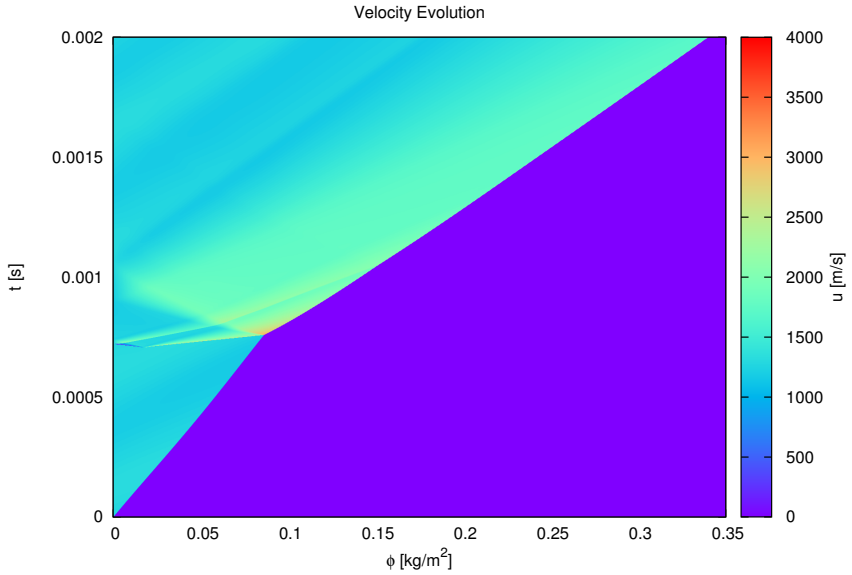

Figure E.13: Particle velocity profile of ethylene fluctuating shock-induced ignition with incident shock Mach number of 4.5, and piston oscillation frequency of 2.0 kHz, and amplitude of 5%.

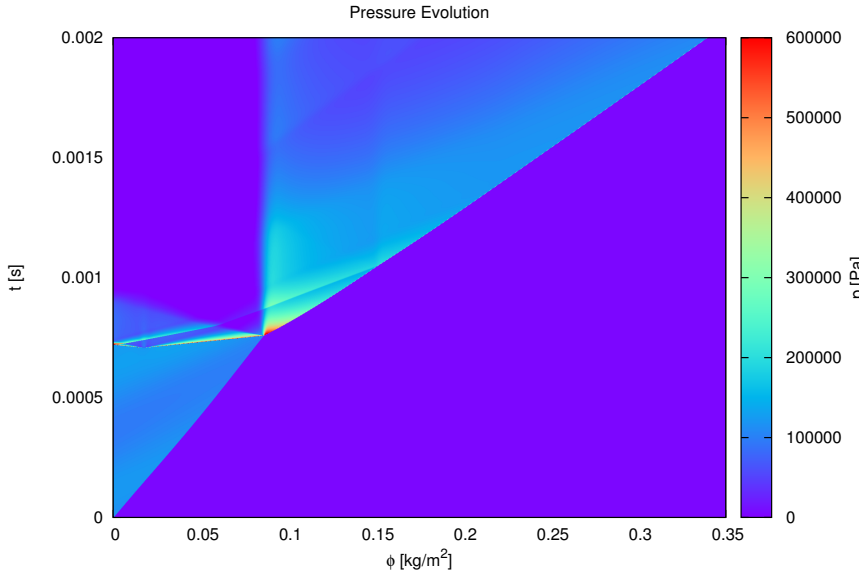

Figure E.14: Pressure profile of ethylene fluctuating shock-induced ignition with incident shock Mach number of 4.5, and piston oscillation frequency of 2.0 kHz, and amplitude of 5%.

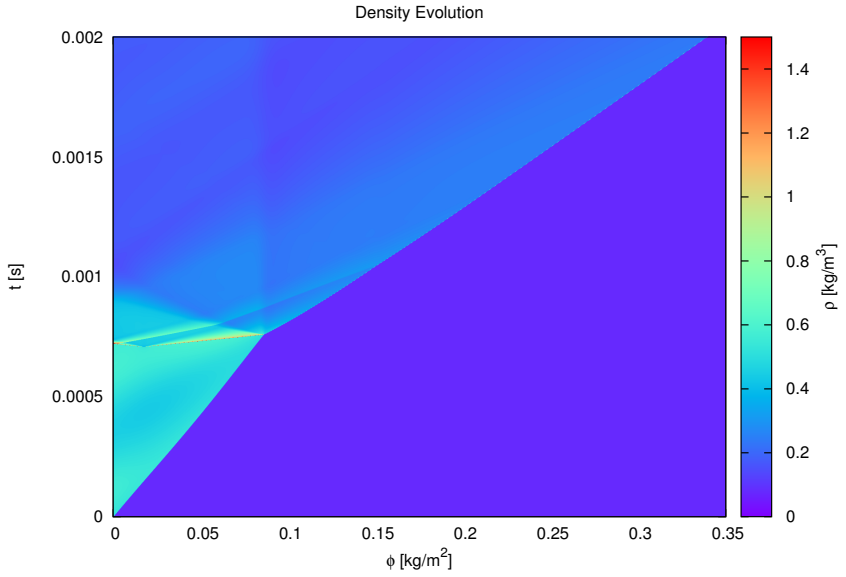

Figure E.15: Density profile of ethylene fluctuating shock-induced ignition with incident shock Mach number of 4.5, and piston oscillation frequency of 2.0 kHz, and amplitude of 5%.

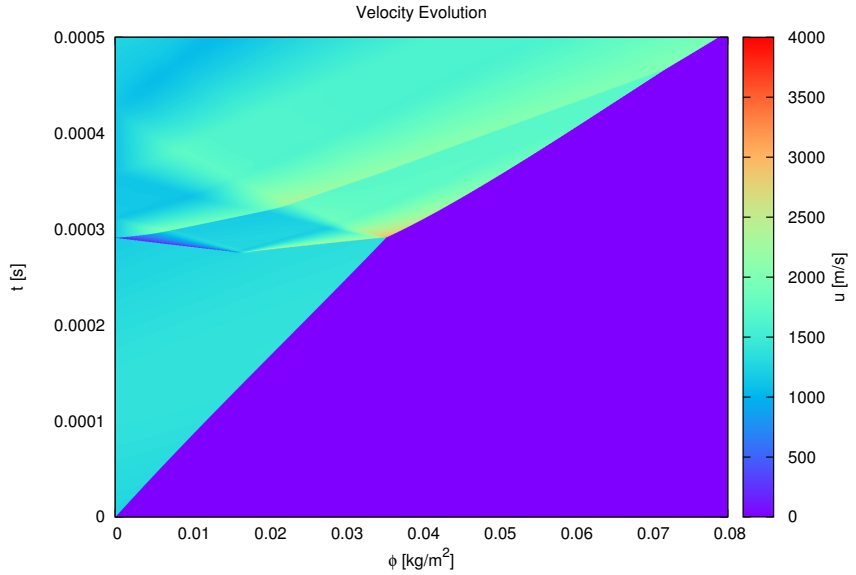

Figure E.16: Particle velocity profile of ethylene fluctuating shock-induced ignition with incident shock Mach number of 4.5, and piston oscillation frequency of 2.0 kHz, and amplitude of 10%.

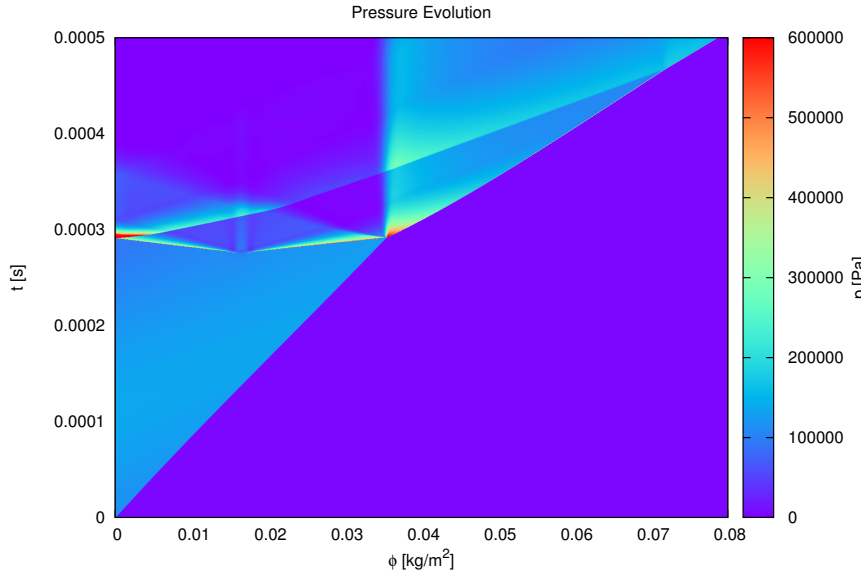

Figure E.17: Pressure profile of ethylene fluctuating shock-induced ignition with incident shock Mach number of 4.5, and piston oscillation frequency of 2.0 kHz, and amplitude of 10%.

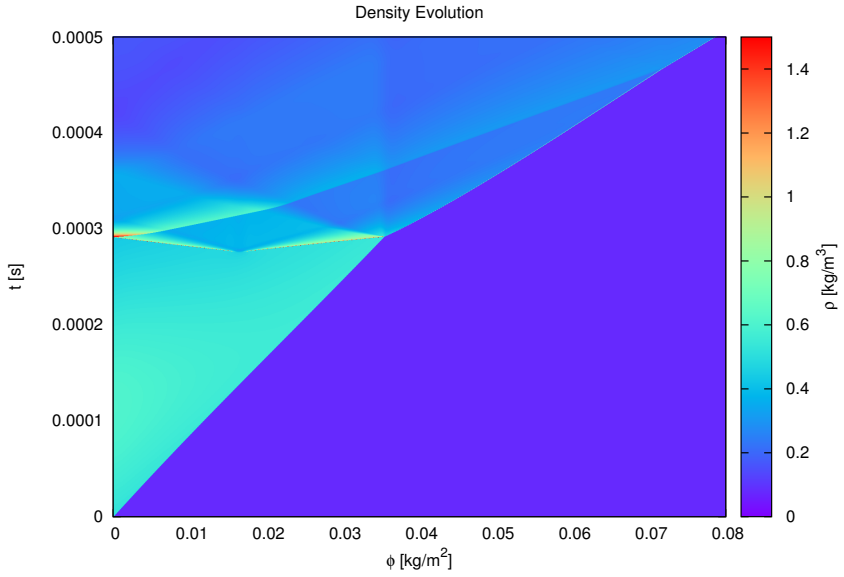

Figure E.18: Density profile of ethylene fluctuating shock-induced ignition with incident shock Mach number of 4.5, and piston oscillation frequency of 2.0 kHz, and amplitude of 10%.

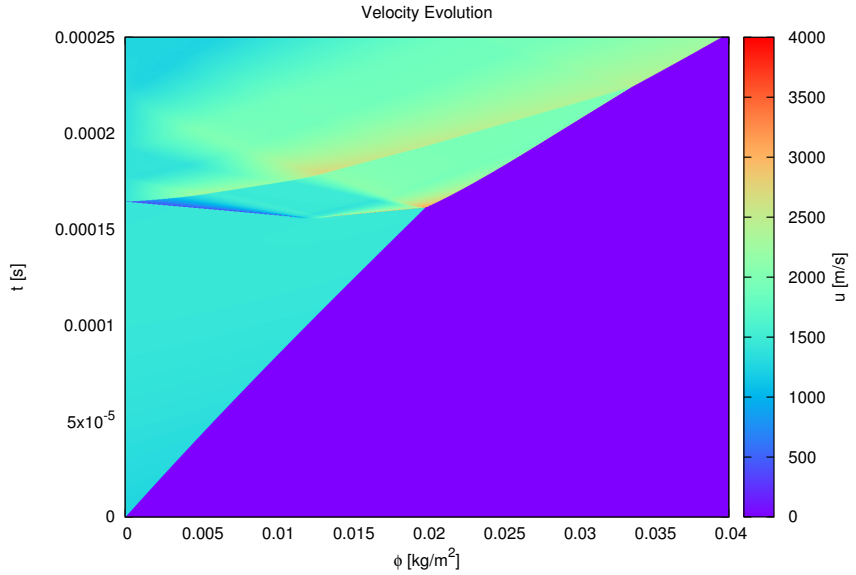

Figure E.19: Particle velocity profile of ethylene fluctuating shock-induced ignition with incident shock Mach number of 4.5, and piston oscillation frequency of 2.0 kHz, and amplitude of 15%.

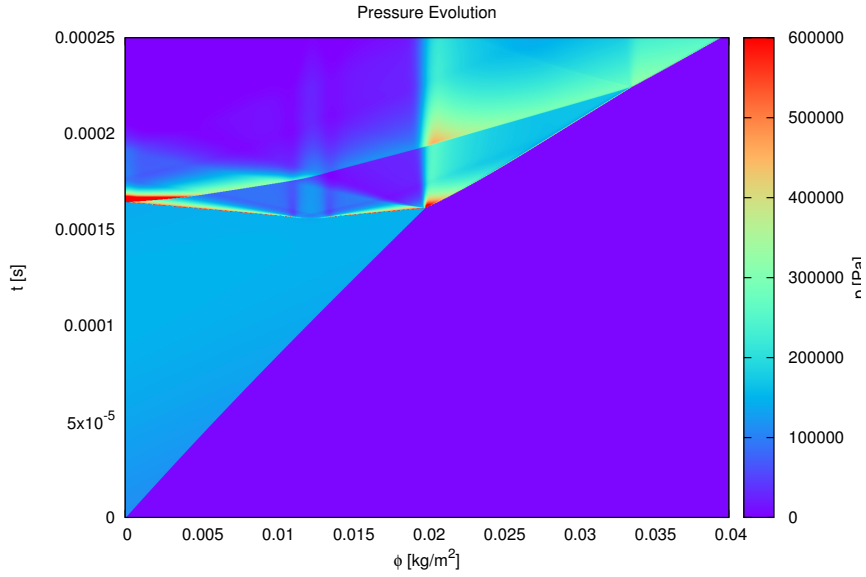

Figure E.20: Pressure profile of ethylene fluctuating shock-induced ignition with incident shock Mach number of 4.5, and piston oscillation frequency of 2.0 kHz, and amplitude of 15%.

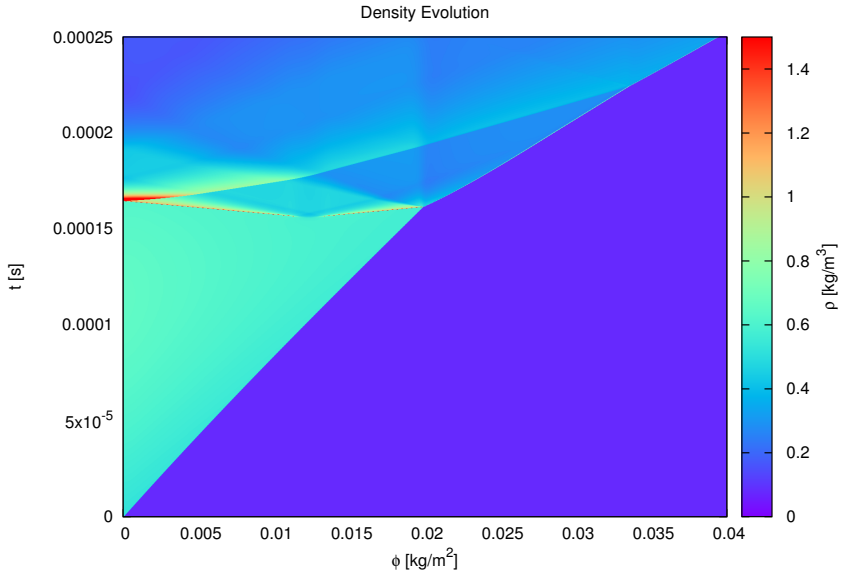

Figure E.21: Density profile of ethylene fluctuating shock-induced ignition with incident shock Mach number of 4.5, and piston oscillation frequency of 2.0 kHz, and amplitude of 15%.

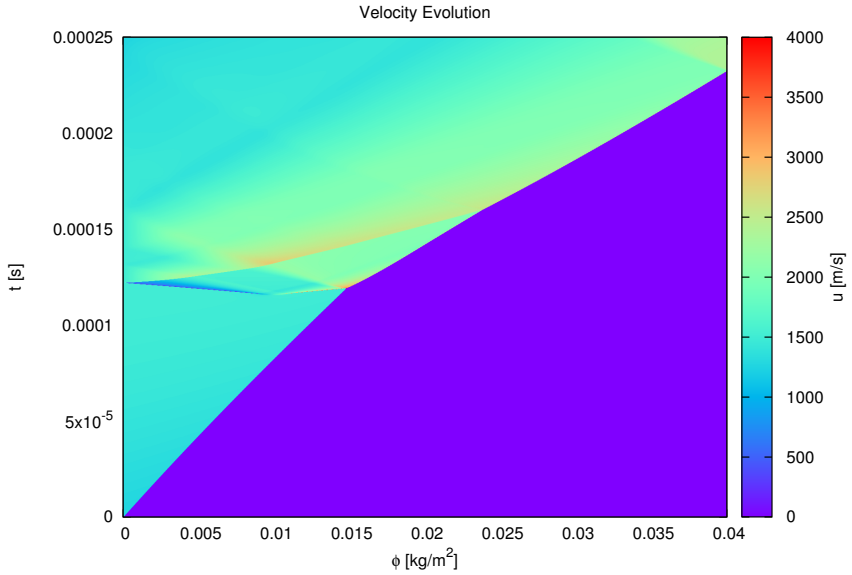

Figure E.22: Particle velocity profile of ethylene fluctuating shock-induced ignition with incident shock Mach number of 4.5, and piston oscillation frequency of 2.0 kHz, and amplitude of 20%.

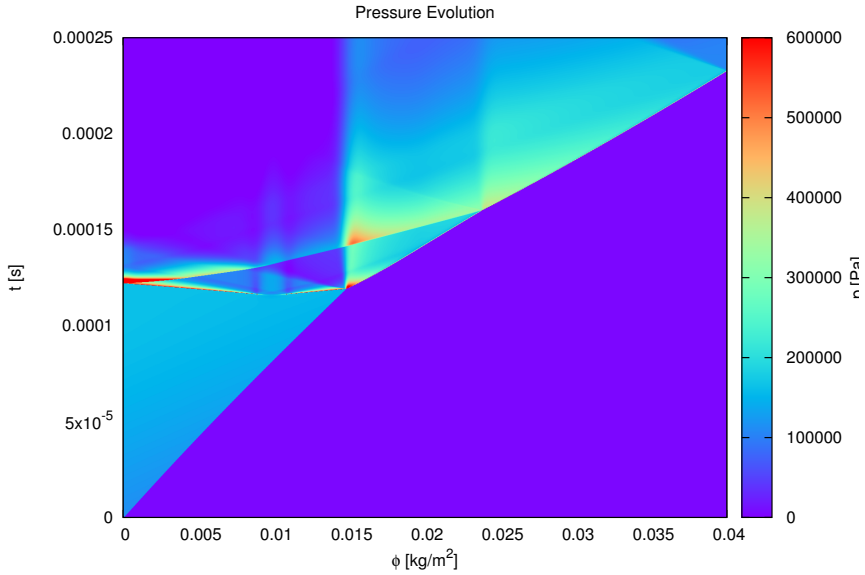

Figure E.23: Pressure profile of ethylene fluctuating shock-induced ignition with incident shock Mach number of 4.5, and piston oscillation frequency of 2.0 kHz, and amplitude of 20%.

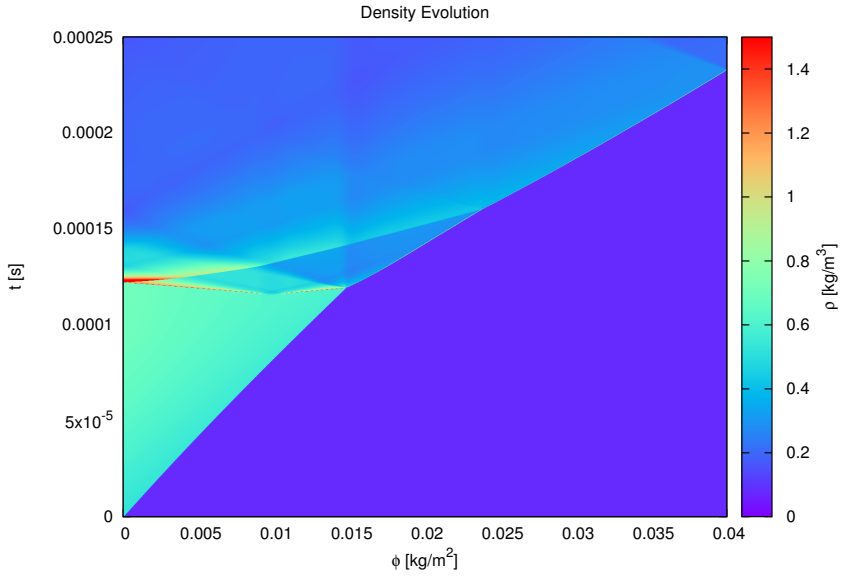

Figure E.24: Density profile of ethylene fluctuating shock-induced ignition with incident shock Mach number of 4.5, and piston oscillation frequency of 2.0 kHz, and amplitude of 20%.

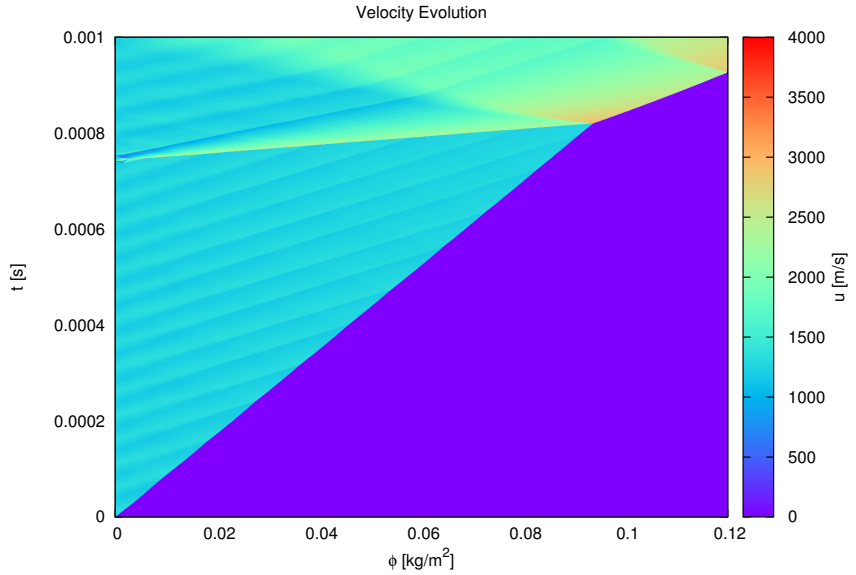

Figure E.25: Particle velocity profile of ethylene fluctuating shock-induced ignition with incident shock Mach number of 4.5, and piston oscillation frequency of 20 kHz, and amplitude of 5%.

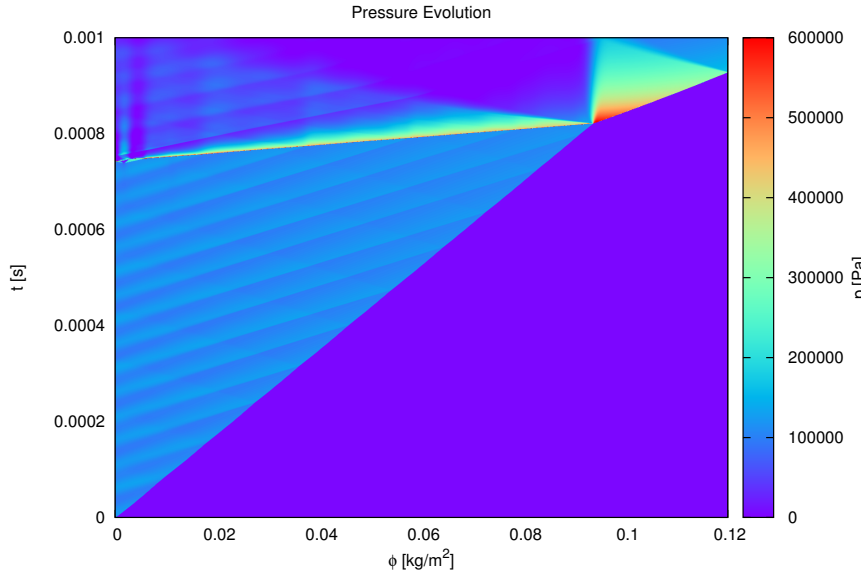

Figure E.26: Pressure profile of ethylene fluctuating shock-induced ignition with incident shock Mach number of 4.5, and piston oscillation frequency of 20 kHz, and amplitude of 5%.

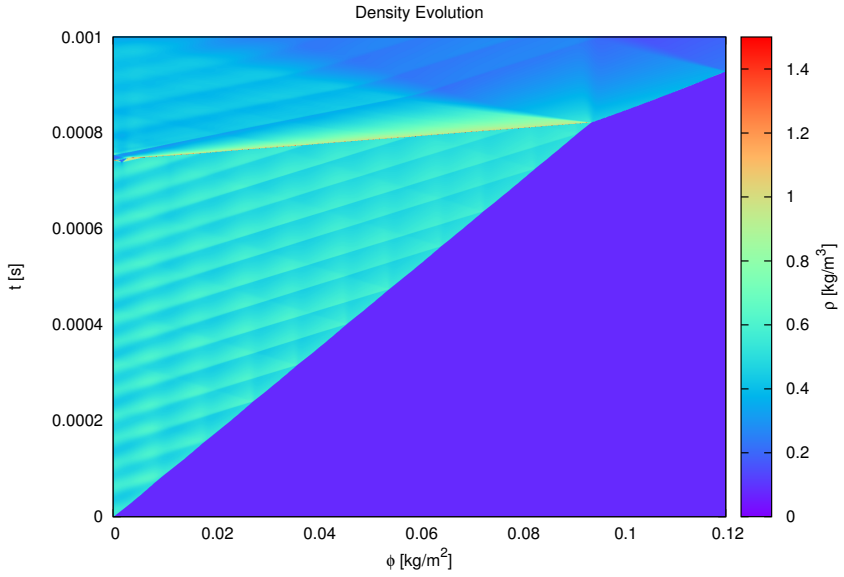

Figure E.27: Density profile of ethylene fluctuating shock-induced ignition with incident shock Mach number of 4.5, and piston oscillation frequency of 20 kHz, and amplitude of 5%.

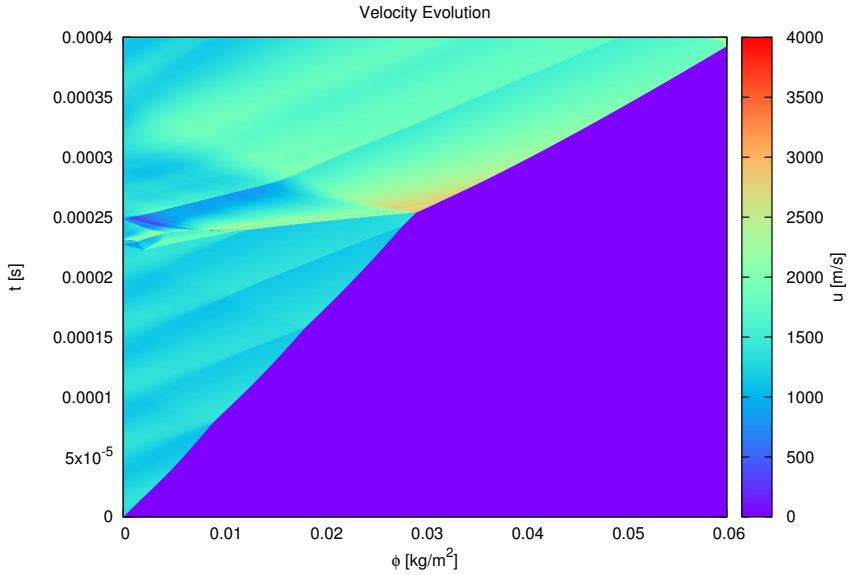

Figure E.28: Particle velocity profile of ethylene fluctuating shock-induced ignition with incident shock Mach number of 4.5, and piston oscillation frequency of 20 kHz, and amplitude of 10%.

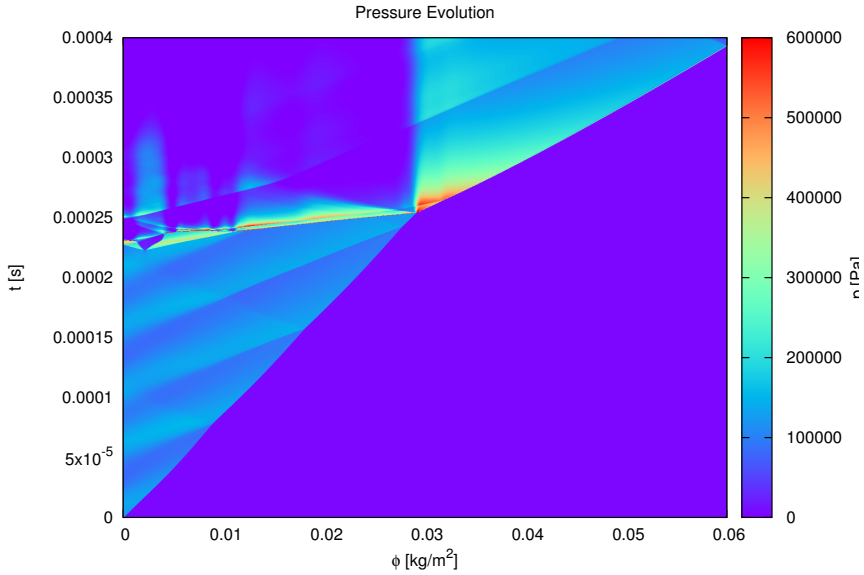

Figure E.29: Pressure profile of ethylene fluctuating shock-induced ignition with incident shock Mach number of 4.5, and piston oscillation frequency of 20 kHz, and amplitude of 10%.

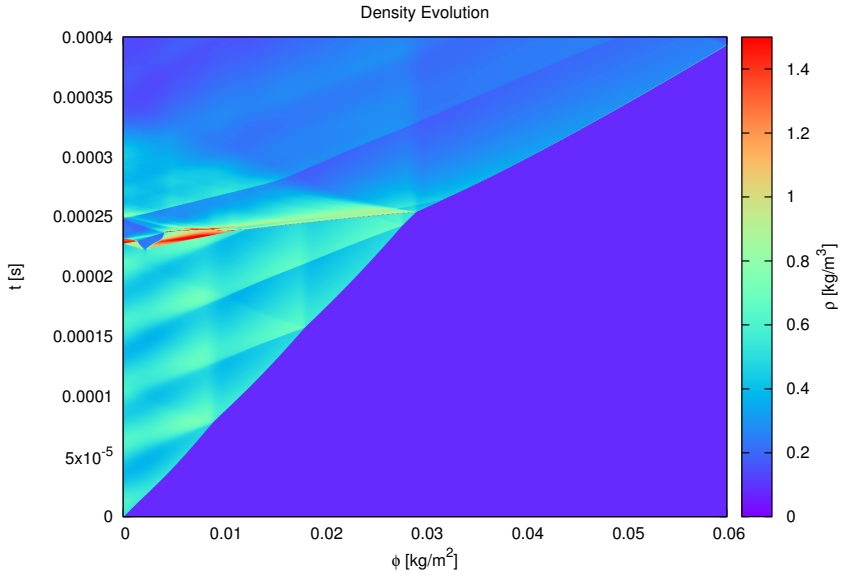

Figure E.30: Density profile of ethylene fluctuating shock-induced ignition with incident shock Mach number of 4.5, and piston oscillation frequency of 20 kHz, and amplitude of 10%.

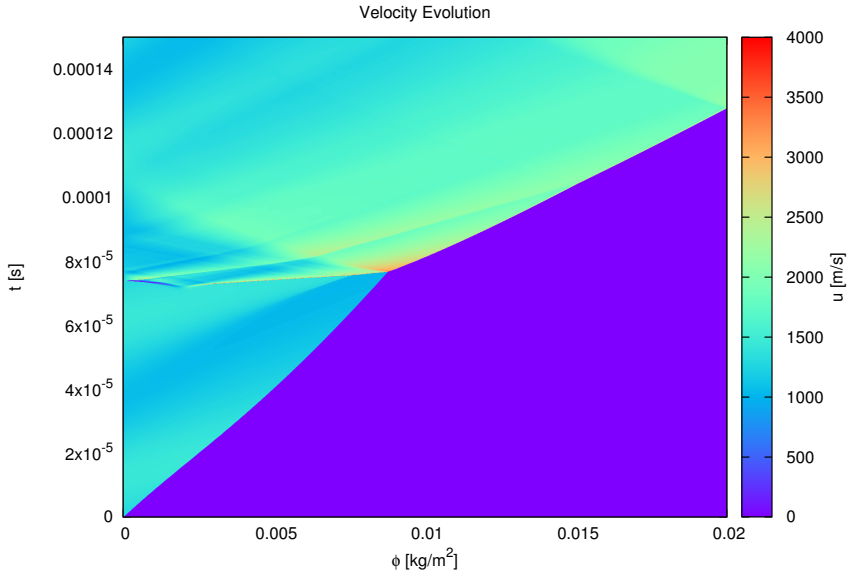

Figure E.31: Particle velocity profile of ethylene fluctuating shock-induced ignition with incident shock Mach number of 4.5, and piston oscillation frequency of 20 kHz, and amplitude of 15%.

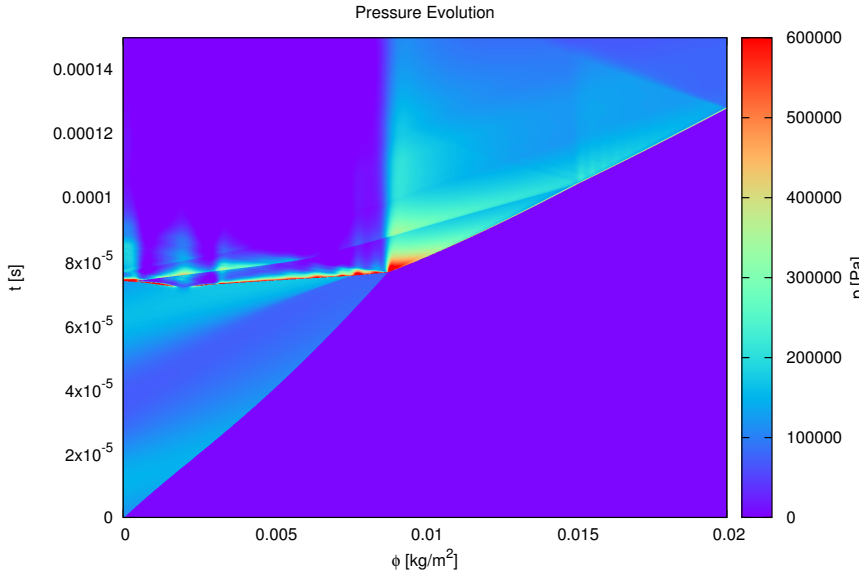

Figure E.32: Pressure profile of ethylene fluctuating shock-induced ignition with incident shock Mach number of 4.5, and piston oscillation frequency of 20 kHz, and amplitude of 15%.

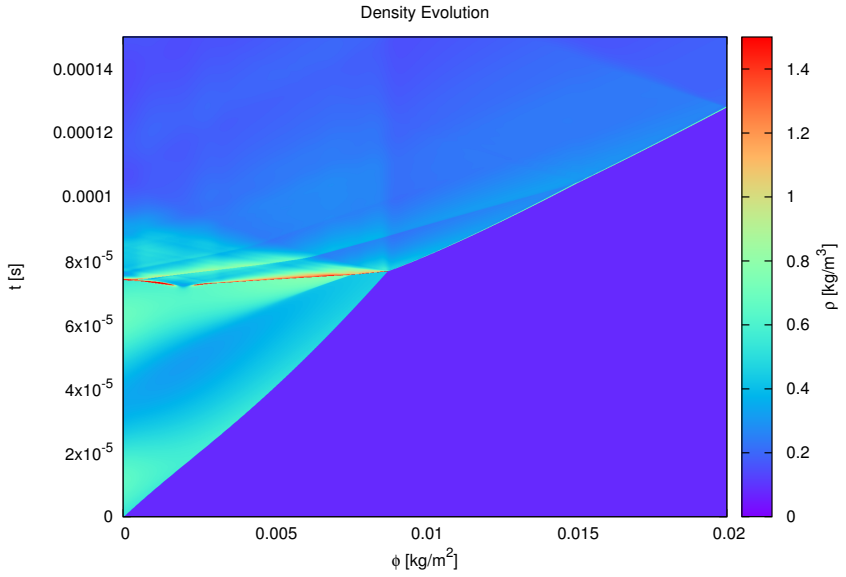

Figure E.33: Density profile of ethylene fluctuating shock-induced ignition with incident shock Mach number of 4.5, and piston oscillation frequency of 20 kHz, and amplitude of 15%.

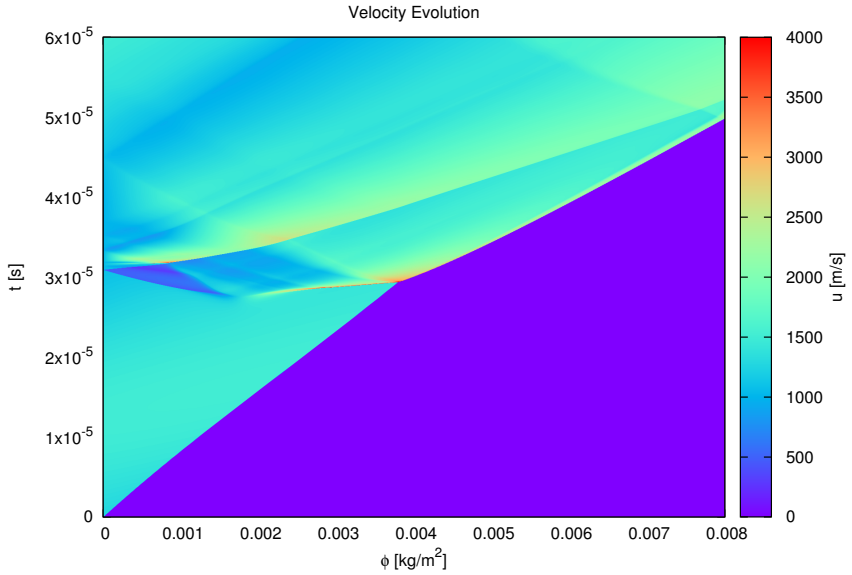

Figure E.34: Particle velocity profile of ethylene fluctuating shock-induced ignition with incident shock Mach number of 4.5, and piston oscillation frequency of 20 kHz, and amplitude of 20%.

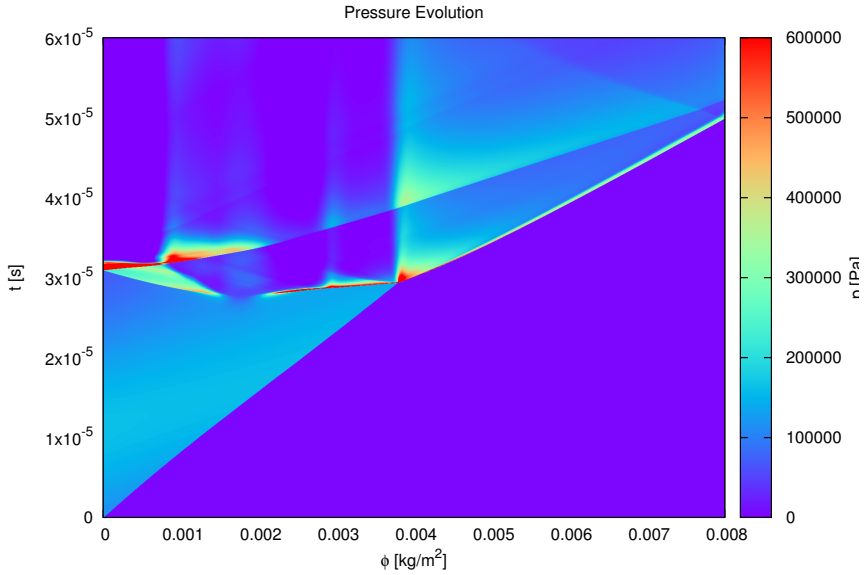

Figure E.35: Pressure profile of ethylene fluctuating shock-induced ignition with incident shock Mach number of 4.5, and piston oscillation frequency of 20 kHz, and amplitude of 20%.

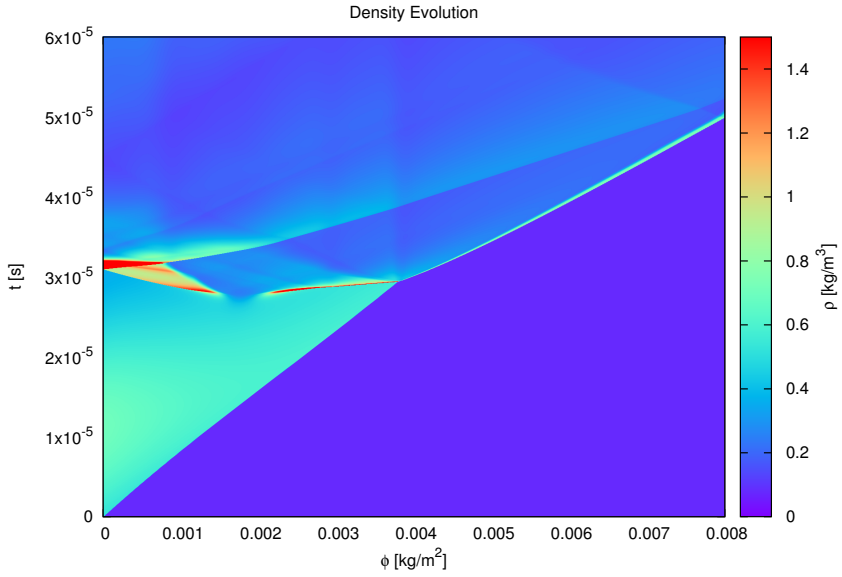

Figure E.36: Density profile of ethylene fluctuating shock-induced ignition with incident shock Mach number of 4.5, and piston oscillation frequency of 20 kHz, and amplitude of 20%.

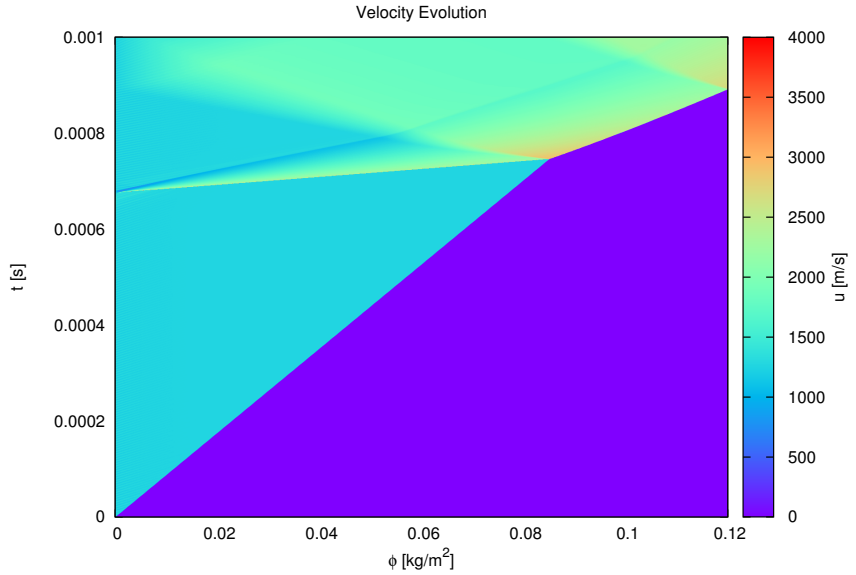

Figure E.37: Particle velocity profile of ethylene fluctuating shock-induced ignition with incident shock Mach number of 4.5, and piston oscillation frequency of 200 kHz, and amplitude of 5%.

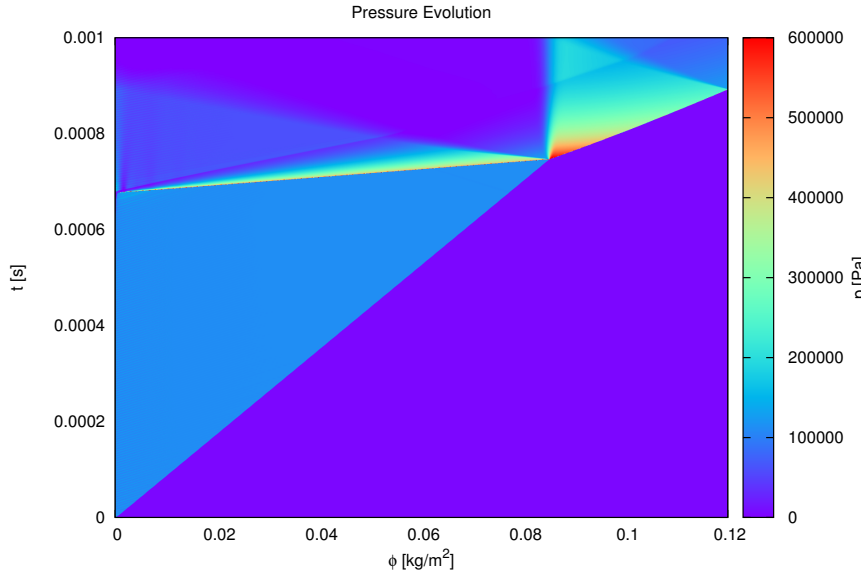

Figure E.38: Pressure profile of ethylene fluctuating shock-induced ignition with incident shock Mach number of 4.5, and piston oscillation frequency of 200 kHz, and amplitude of 5%.

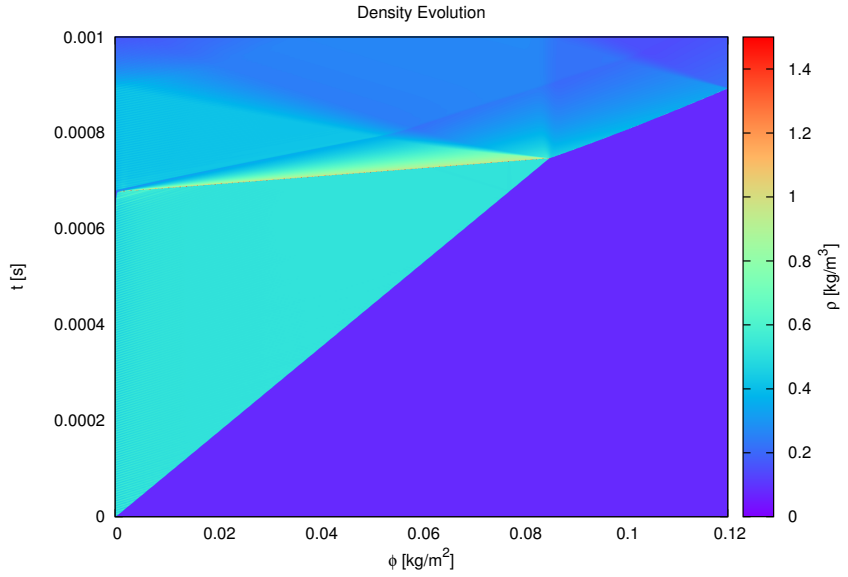

Figure E.39: Density profile of ethylene fluctuating shock-induced ignition with incident shock Mach number of 4.5, and piston oscillation frequency of 200 kHz, and amplitude of 5%.

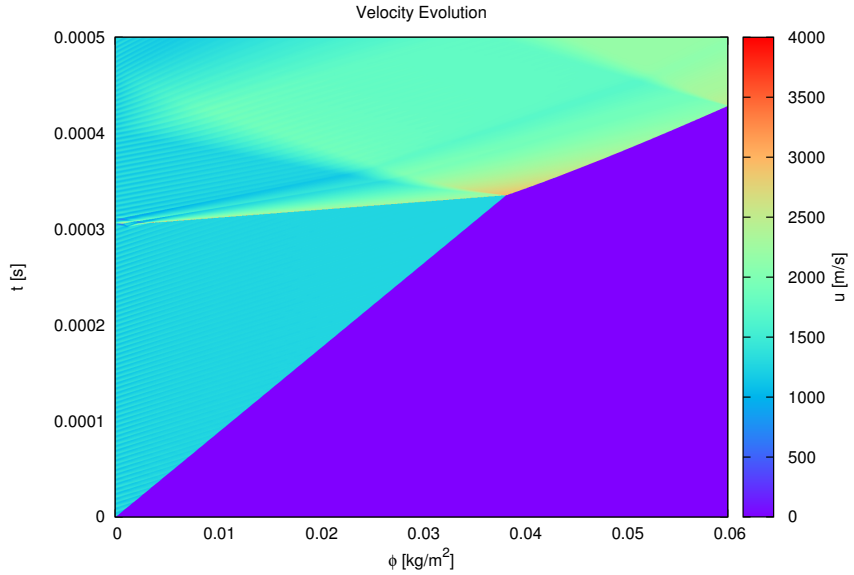

Figure E.40: Particle velocity profile of ethylene fluctuating shock-induced ignition with incident shock Mach number of 4.5, and piston oscillation frequency of 200 kHz, and amplitude of 10%.

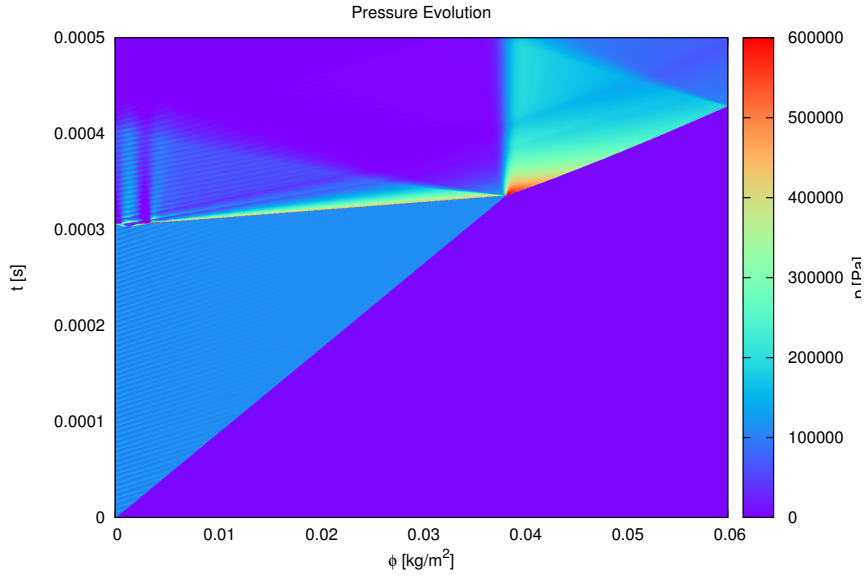

Figure E.41: Pressure profile of ethylene fluctuating shock-induced ignition with incident shock Mach number of 4.5, and piston oscillation frequency of 200 kHz, and amplitude of 10%.

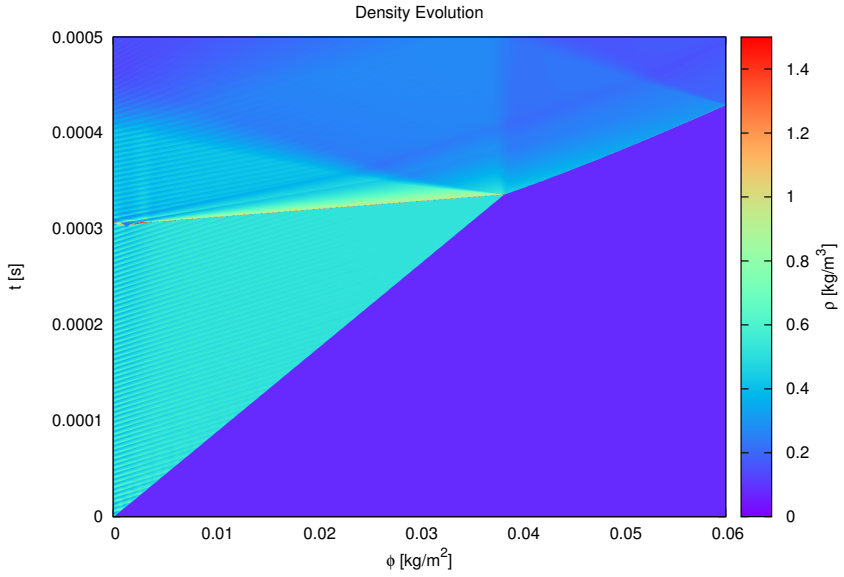

Figure E.42: Density profile of ethylene fluctuating shock-induced ignition with incident shock Mach number of 4.5, and piston oscillation frequency of 200 kHz, and amplitude of 10%.

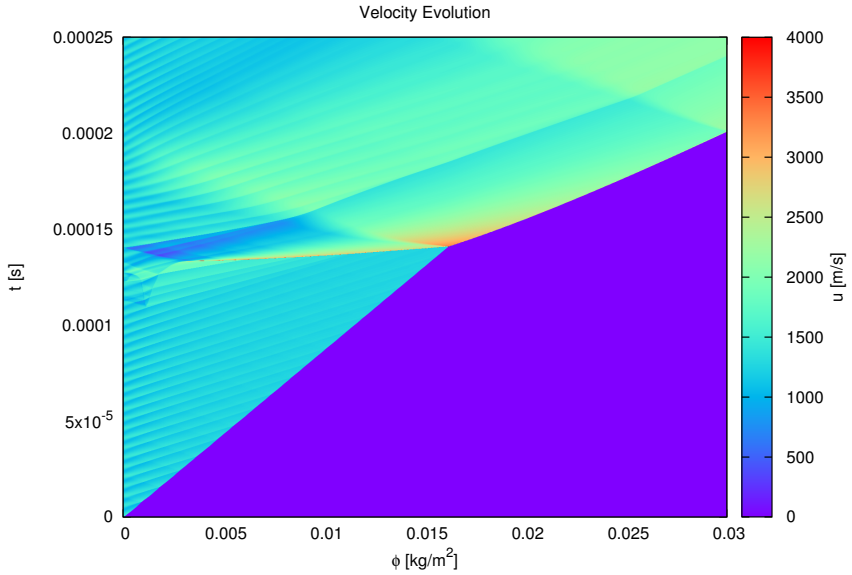

Figure E.43: Particle velocity profile of ethylene fluctuating shock-induced ignition with incident shock Mach number of 4.5, and piston oscillation frequency of 200 kHz, and amplitude of 15%.

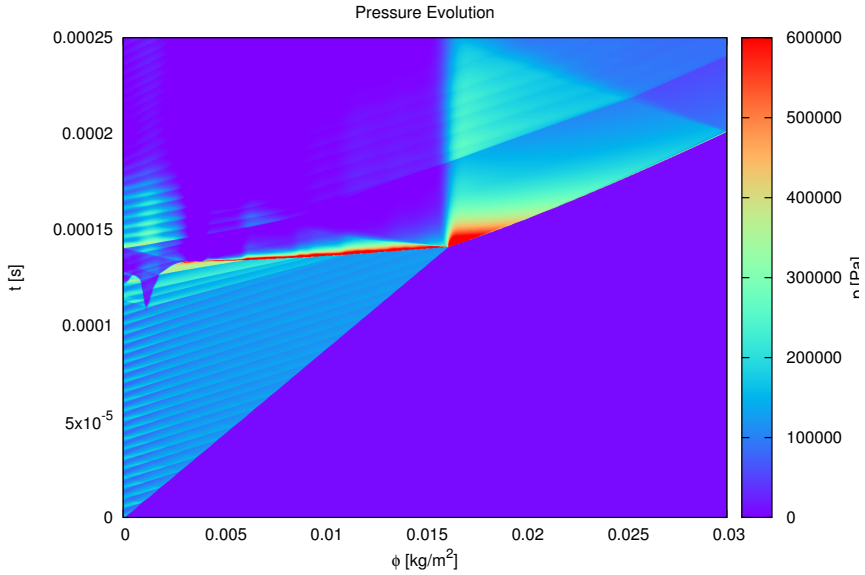

Figure E.44: Pressure profile of ethylene fluctuating shock-induced ignition with incident shock Mach number of 4.5, and piston oscillation frequency of 200 kHz, and amplitude of 15%.

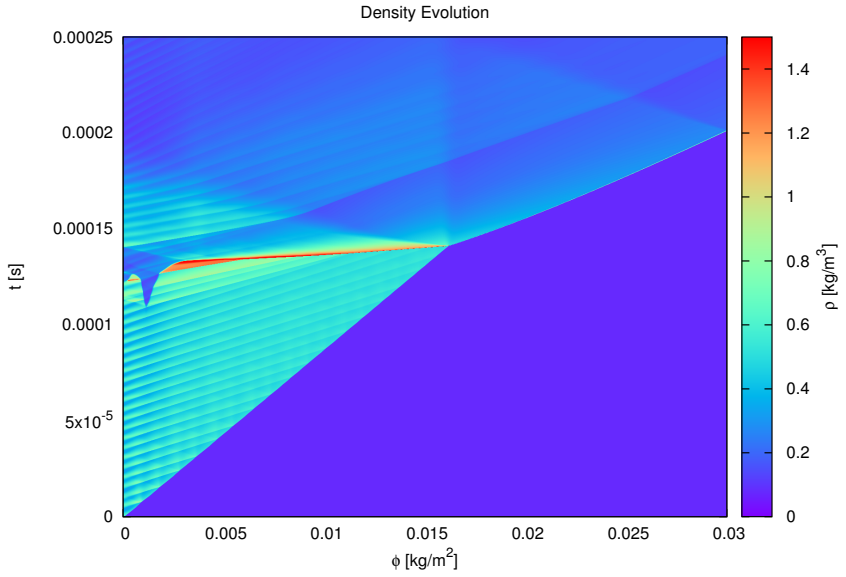

Figure E.45: Density profile of ethylene fluctuating shock-induced ignition with incident shock Mach number of 4.5, and piston oscillation frequency of 200 kHz, and amplitude of 15%.

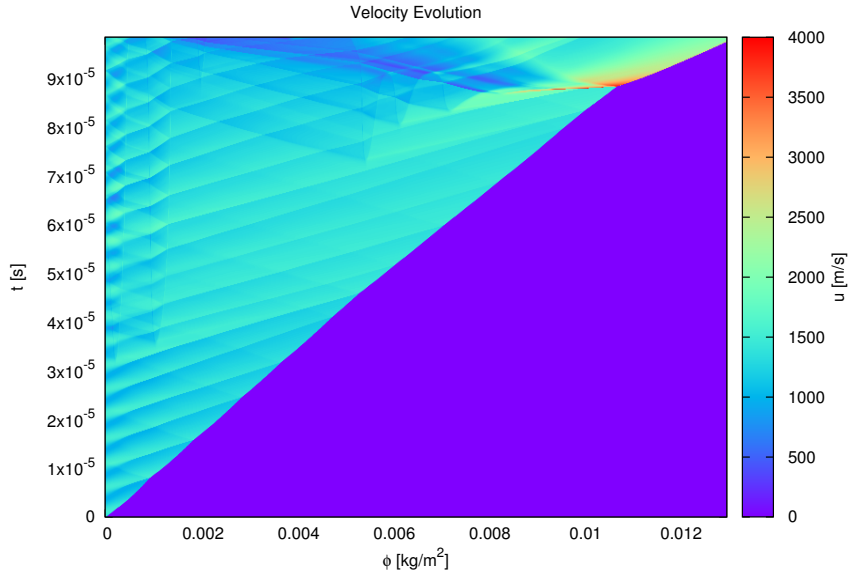

Figure E.46: Particle velocity profile of ethylene fluctuating shock-induced ignition with incident shock Mach number of 4.5, and piston oscillation frequency of 200 kHz, and amplitude of 20%.

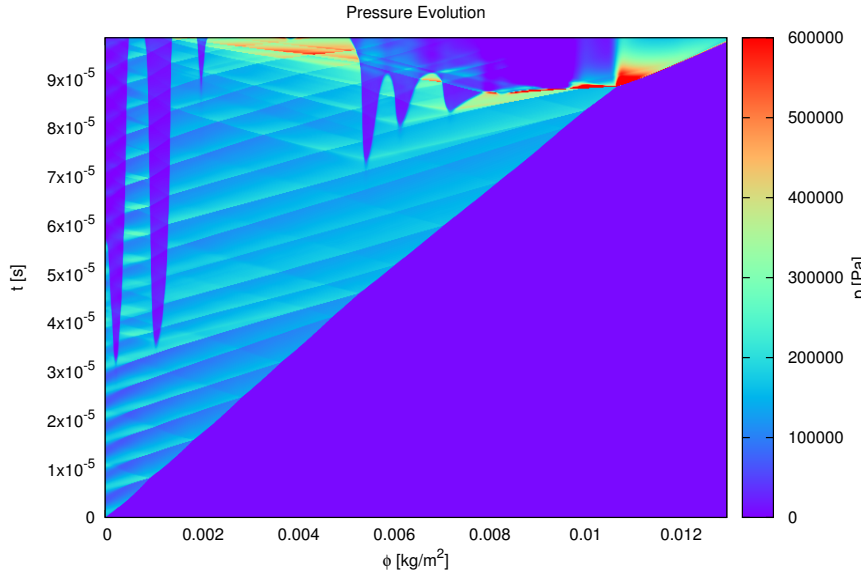

Figure E.47: Pressure profile of ethylene fluctuating shock-induced ignition with incident shock Mach number of 4.5, and piston oscillation frequency of 200 kHz, and amplitude of 20%.

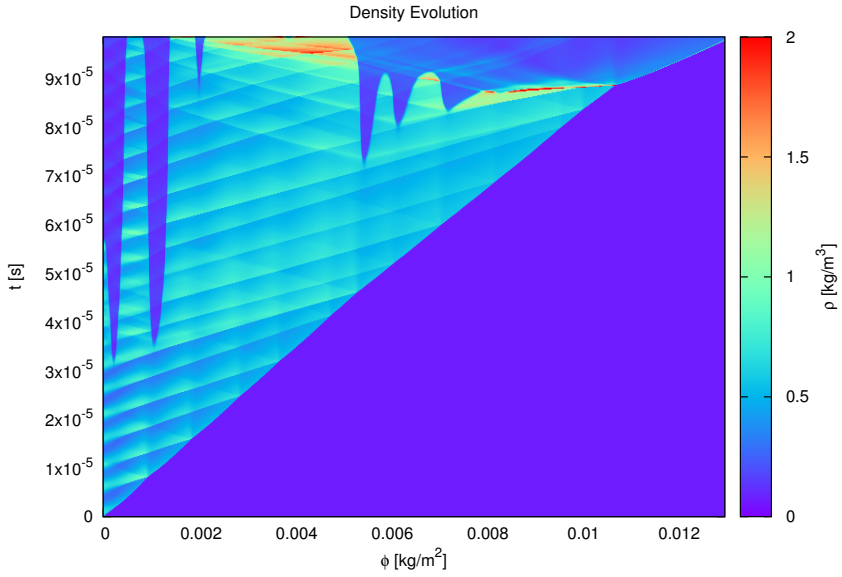

Figure E.48: Density profile of ethylene fluctuating shock-induced ignition with incident shock Mach number of 4.5, and piston oscillation frequency of 200 kHz, and amplitude of 20%.

Appendix F

Resolution Tests

This appendix provides the low-resolution results for all the simulations which have perturbation of 20% amplitude. The high-resolution results are in Chapter 5 and 6. The simulations with amplitude of 5%, 10% and 15% do not have corresponding low resolution results, because the highest amplitude cases have the most complicate patterns which need the best resolution.

F.1 Resolution Tests on Hydrogen-Oxygen Simulations

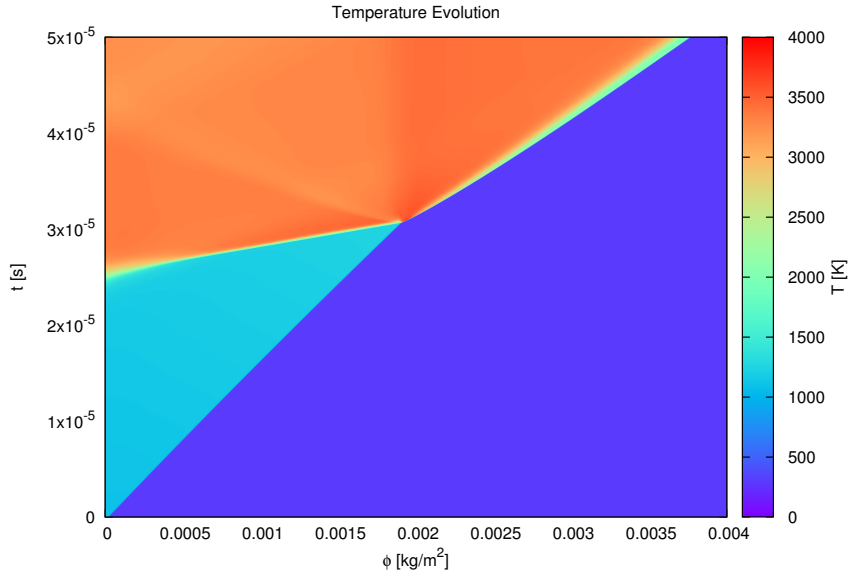

Figure F.1: Temperature profile of hydrogen fluctuating shock-induced ignition with a post shock temperature of 1100 K and piston oscillation frequency of 4.535 kHz, and amplitude of 20% with 1000 cells. (Normal simulation has 2000 cells).

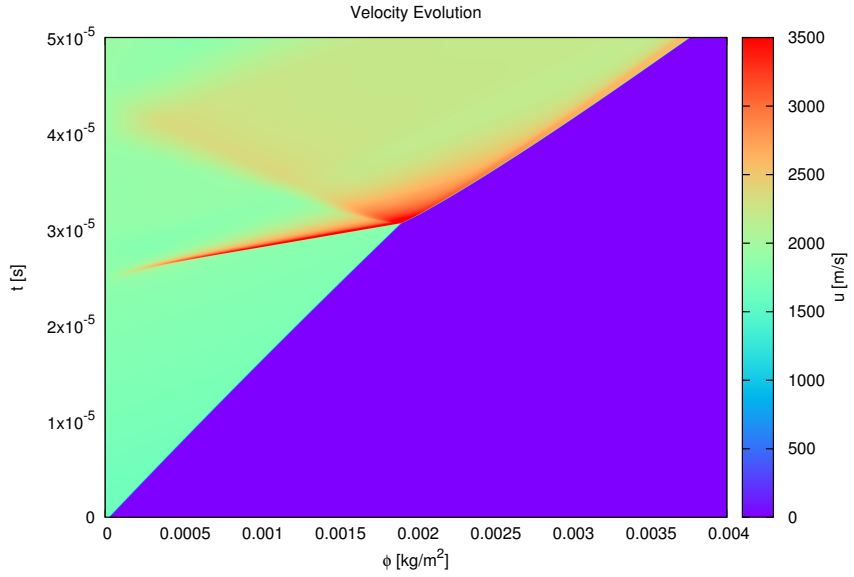

Figure F.2: Particle velocity profile of hydrogen fluctuating shock-induced ignition with a post shock temperature of 1100 K and piston oscillation frequency of 4.535 kHz, and amplitude of 20% with 1000 cells. (Normal simulation has 2000 cells).

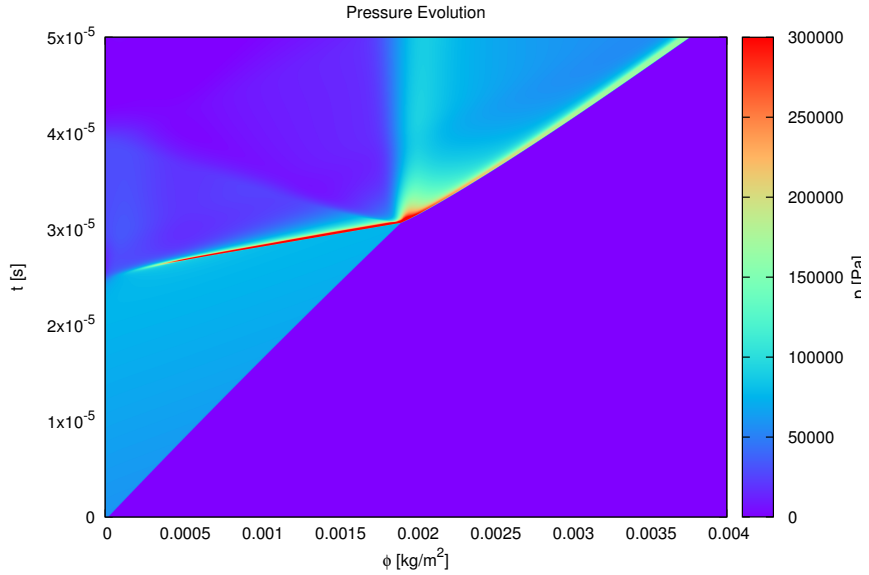

Figure F.3: Pressure profile of hydrogen fluctuating shock-induced ignition with a post shock temperature of 1100 K and piston oscillation frequency of 4.535 kHz, and amplitude of 20% with 1000 cells. (Normal simulation has 2000 cells).

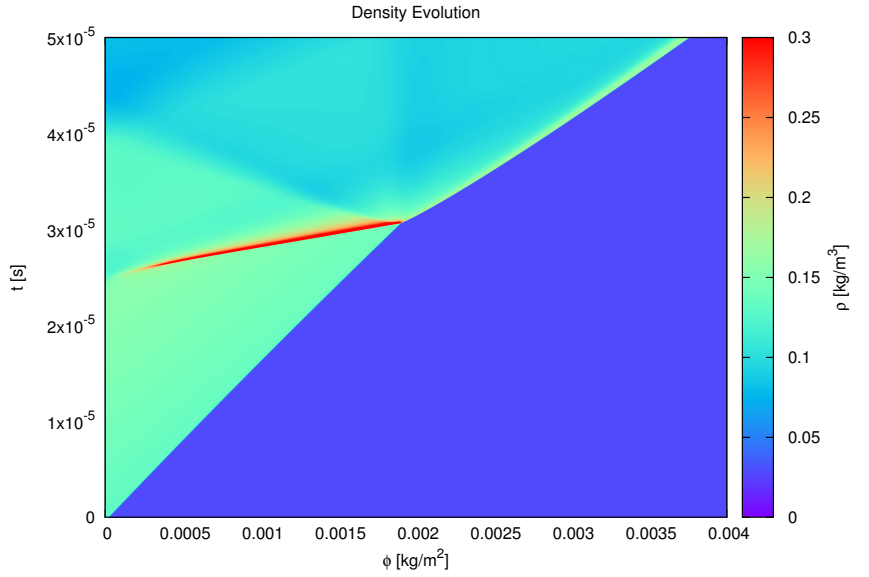

Figure F.4: Density profile of hydrogen fluctuating shock-induced ignition with a post shock temperature of 1100 K and piston oscillation frequency of 4.535 kHz, and amplitude of 20% with 1000 cells. (Normal simulation has 2000 cells).

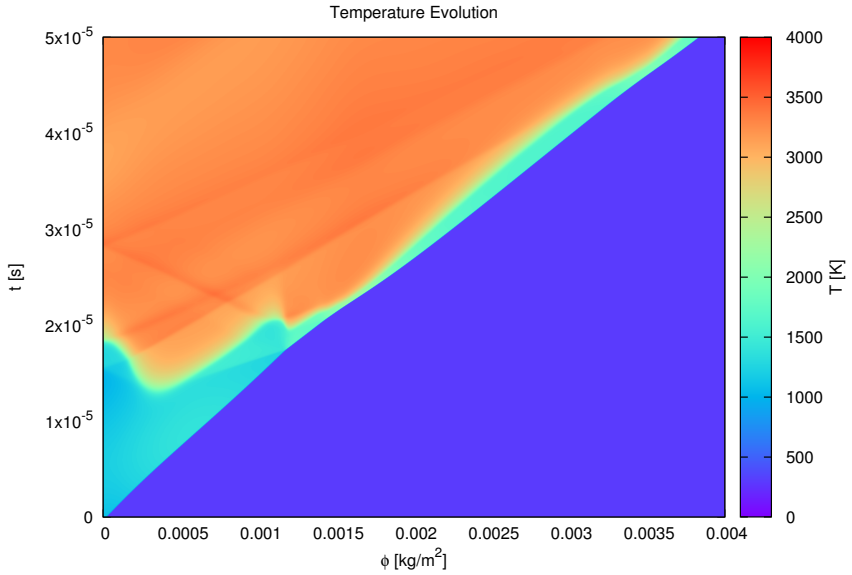

Figure F.5: Temperature profile of hydrogen fluctuating shock-induced ignition with a post shock temperature of 1100 K and piston oscillation frequency of 45.35 kHz, and amplitude of 20% with 1000 cells. (Normal simulation has 2000 cells).

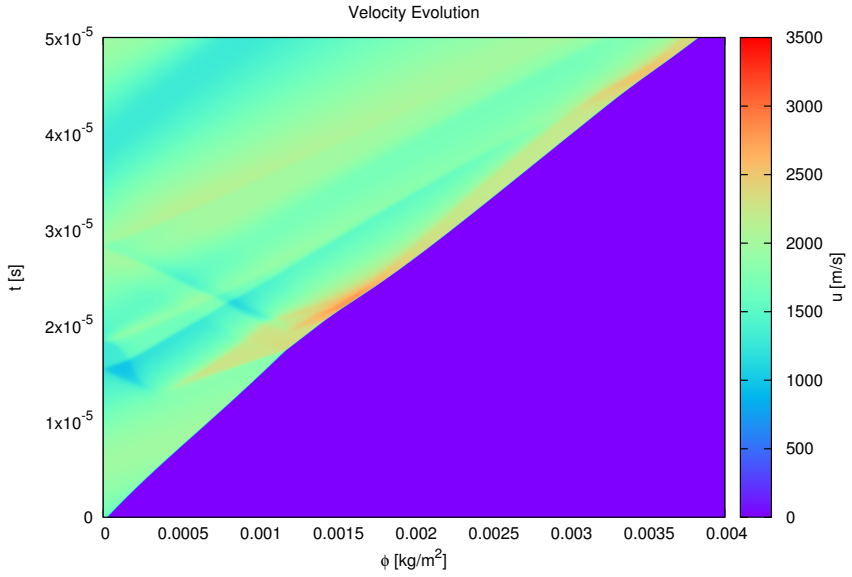

Figure F.6: Particle velocity profile of hydrogen fluctuating shock-induced ignition with a post shock temperature of 1100 K and piston oscillation frequency of 45.35 kHz, and amplitude of 20% with 1000 cells. (Normal simulation has 2000 cells).

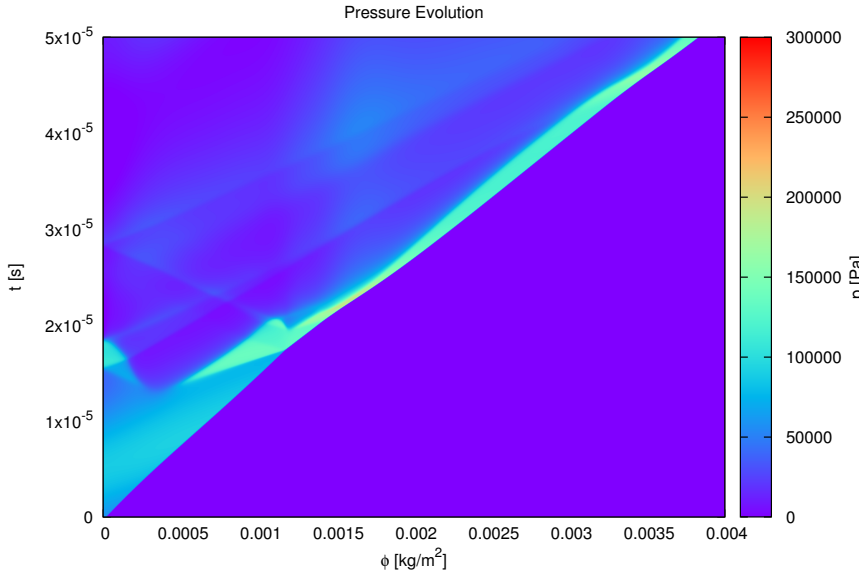

Figure F.7: Pressure profile of hydrogen fluctuating shock-induced ignition with a post shock temperature of 1100 K and piston oscillation frequency of 45.35 kHz, and amplitude of 20% with 1000 cells. (Normal simulation has 2000 cells).

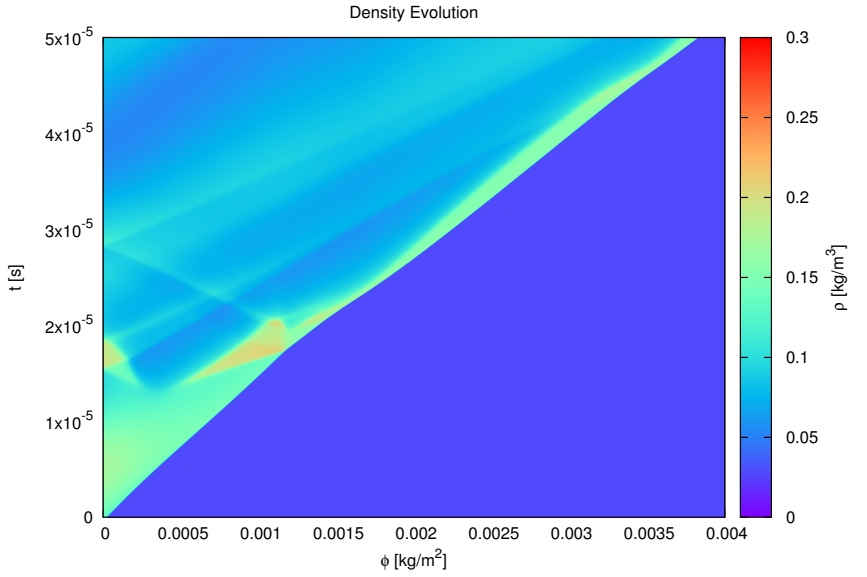

Figure F.8: Density profile of hydrogen fluctuating shock-induced ignition with a post shock temperature of 1100 K and piston oscillation frequency of 45.35 kHz, and amplitude of 20% with 1000 cells. (Normal simulation has 2000 cells).

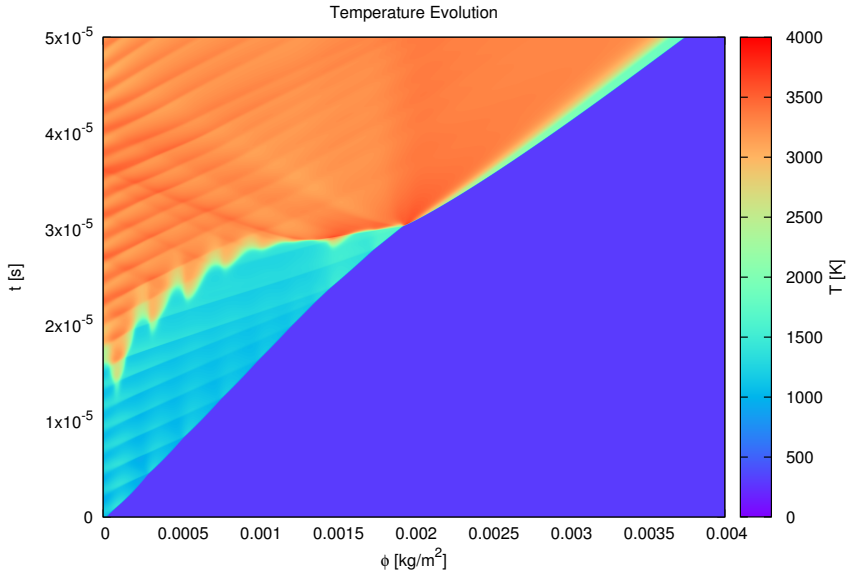

Figure F.9: Temperature profile of hydrogen fluctuating shock-induced ignition with a post shock temperature of 1100 K and piston oscillation frequency of 453.5 kHz, and amplitude of 20% with 1000 cells. (Normal simulation has 2000 cells).

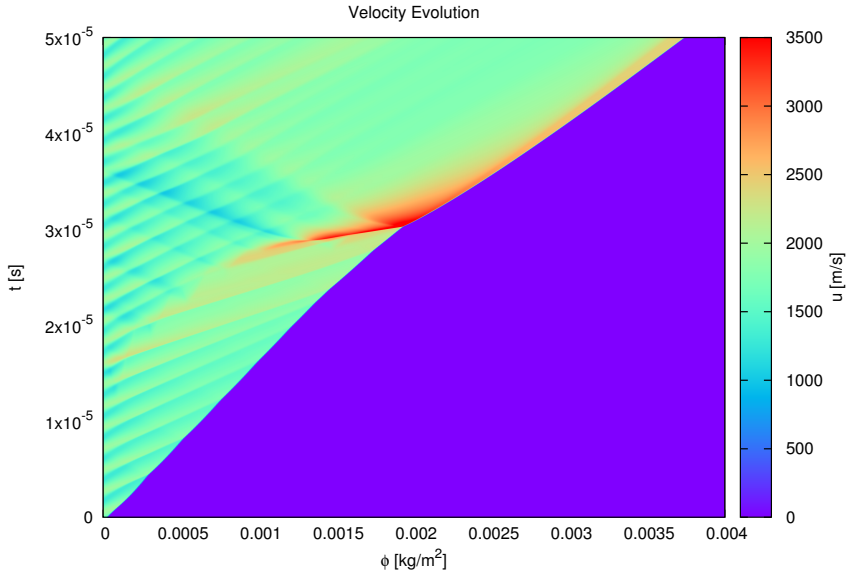

Figure F.10: Particle velocity profile of hydrogen fluctuating shock-induced ignition with a post shock temperature of 1100 K and piston oscillation frequency of 453.5 kHz, and amplitude of 20% with 1000 cells. (Normal simulation has 2000 cells).

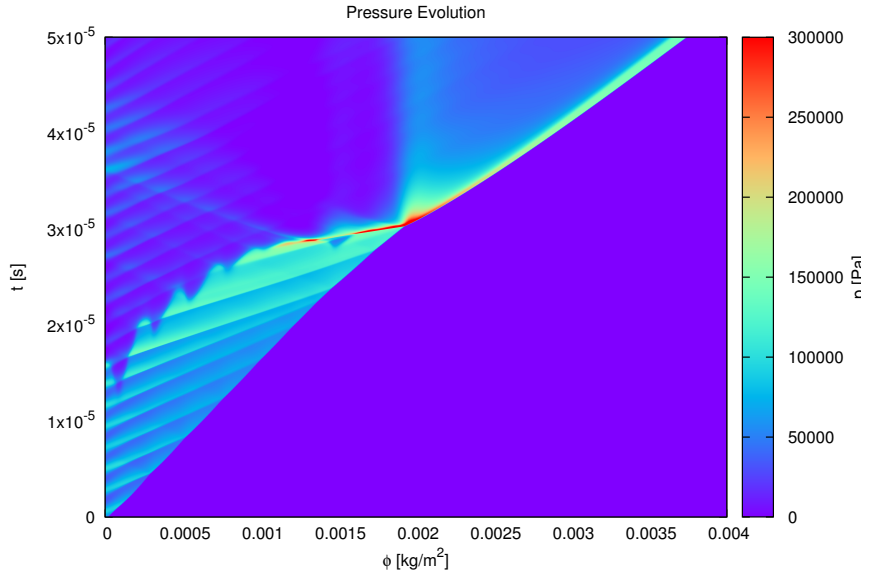

Figure F.11: Pressure profile of hydrogen fluctuating shock-induced ignition with a post shock temperature of 1100 K and piston oscillation frequency of 453.5 kHz, and amplitude of 20% with 1000 cells. (Normal simulation has 2000 cells).

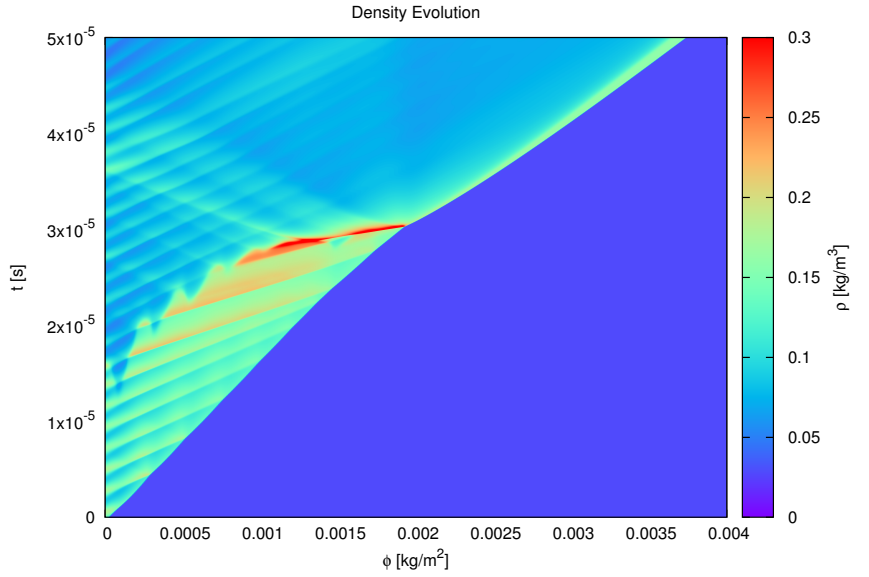

Figure F.12: Density profile of hydrogen fluctuating shock-induced ignition with a post shock temperature of 1100 K and piston oscillation frequency of 453.5 kHz, and amplitude of 20% with 1000 cells. (Normal simulation has 2000 cells).

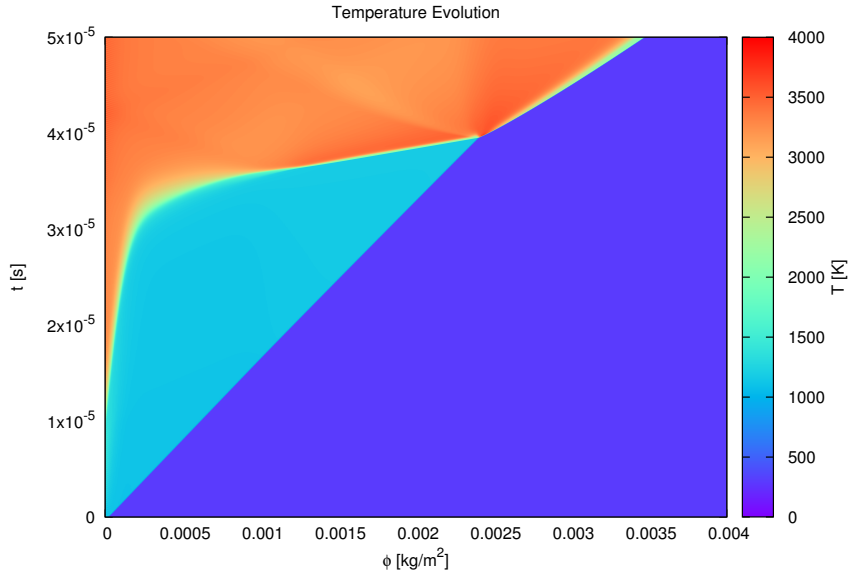

Figure F.13: Temperature profile of hydrogen fluctuating shock-induced ignition with a post shock temperature of 1100 K and piston oscillation frequency of 4535 kHz, and amplitude of 20% with 1000 cells. (Normal simulation has 2000 cells).

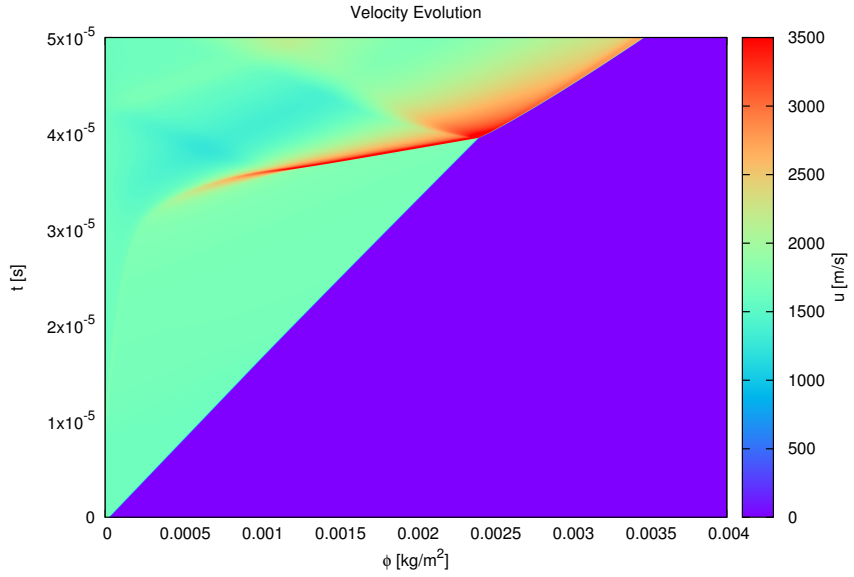

Figure F.14: Particle velocity profile of hydrogen fluctuating shock-induced ignition with a post shock temperature of 1100 K and piston oscillation frequency of 4535 kHz, and amplitude of 20% with 1000 cells. (Normal simulation has 2000 cells).

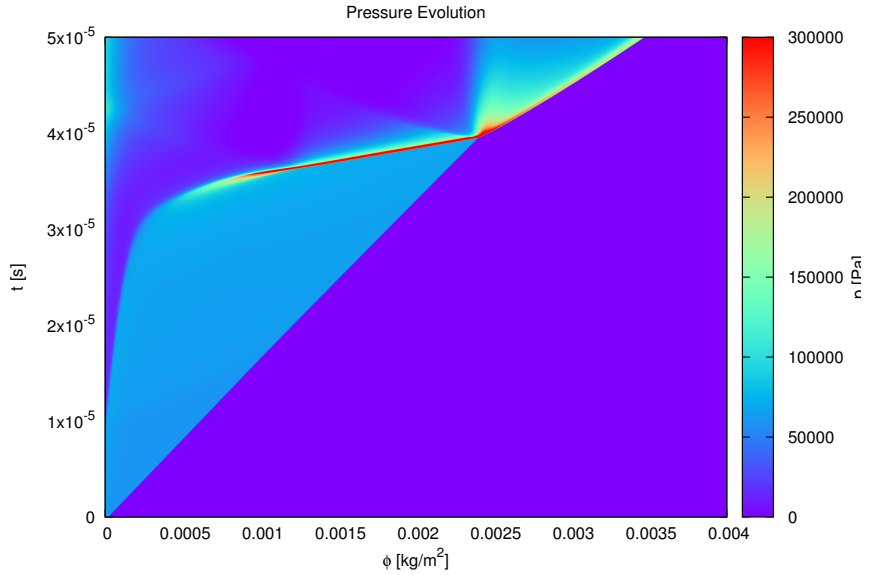

Figure F.15: Pressure profile of hydrogen fluctuating shock-induced ignition with a post shock temperature of 1100 K and piston oscillation frequency of 4535 kHz, and amplitude of 20% with 1000 cells. (Normal simulation has 2000 cells).

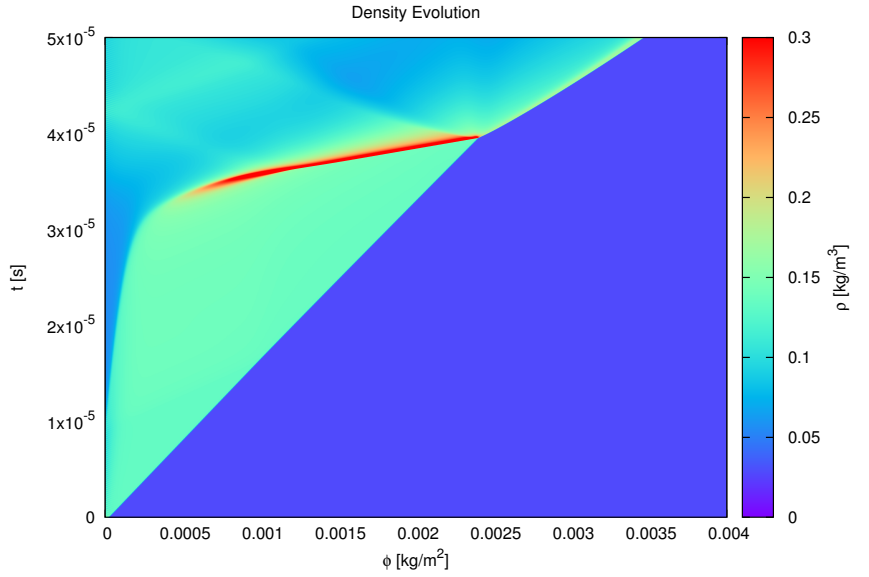

Figure F.16: Density profile of hydrogen fluctuating shock-induced ignition with a post shock temperature of 1100 K and piston oscillation frequency of 4535 kHz, and amplitude of 20% with 1000 cells. (Normal simulation has 2000 cells).

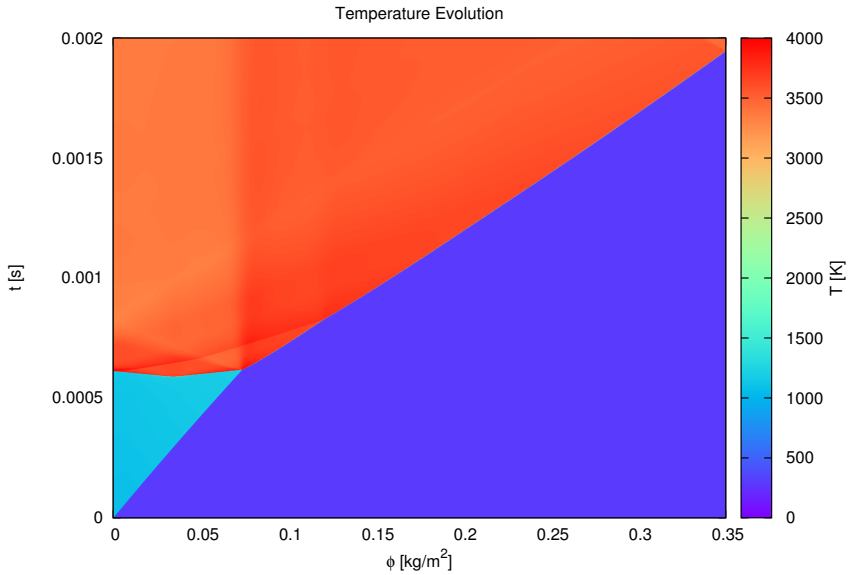

Figure F.17: Temperature profile of ethylene fluctuating shock-induced ignition with incident shock Mach number of 4.5, and piston oscillation frequency of 0.2 kHz, and amplitude of 20% with 1000 cells. (Normal simulation has 5000 cells).

F.2 Resolution Tests on Ethylene-Oxygen Simulations

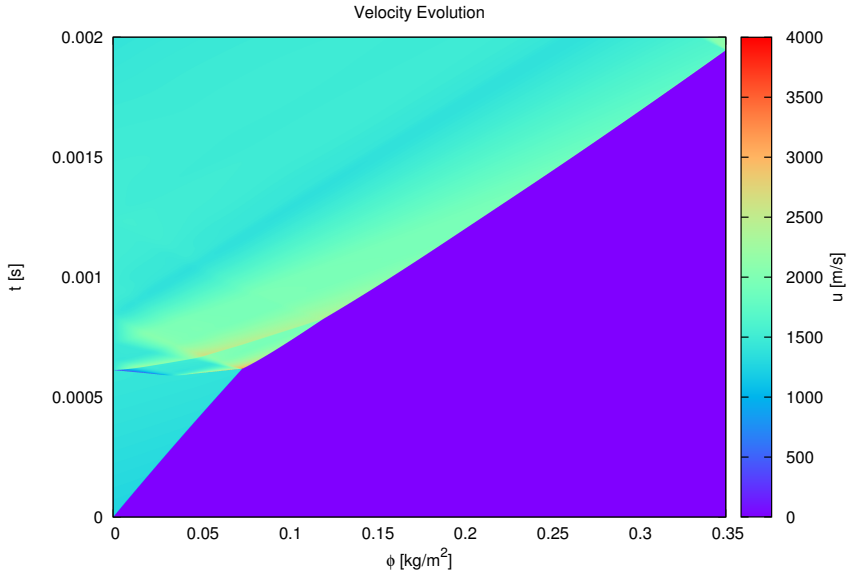

Figure F.18: Particle velocity profile of ethylene fluctuating shock-induced ignition with incident shock Mach number of 4.5, and piston oscillation frequency of 0.2 kHz, and amplitude of 20% with 1000 cells. (Normal simulation has 5000 cells).

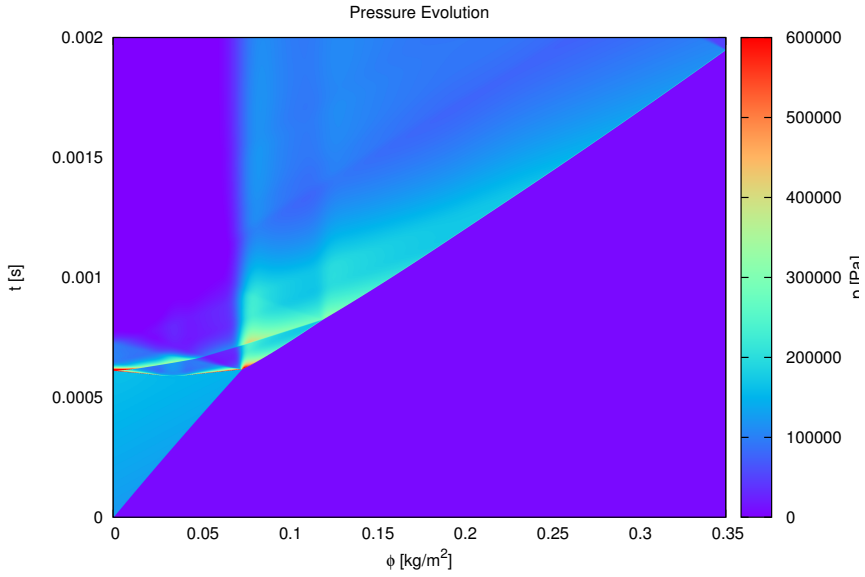

Figure F.19: Pressure profile of ethylene fluctuating shock-induced ignition with incident shock Mach number of 4.5, and piston oscillation frequency of 0.2 kHz, and amplitude of 20% with 1000 cells. (Normal simulation has 5000 cells).

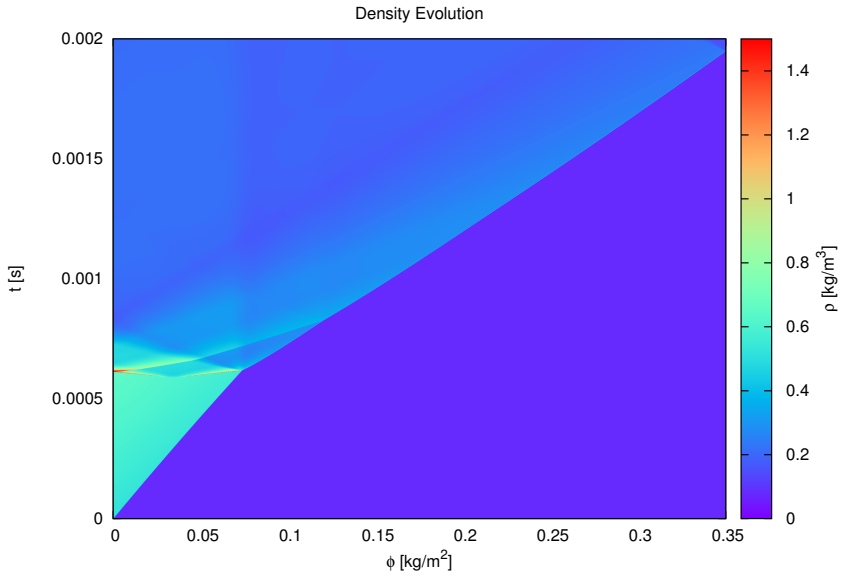

Figure F.20: Density profile of ethylene fluctuating shock-induced ignition with incident shock Mach number of 4.5, and piston oscillation frequency of 0.2 kHz, and amplitude of 20% with 1000 cells. (Normal simulation has 5000 cells).

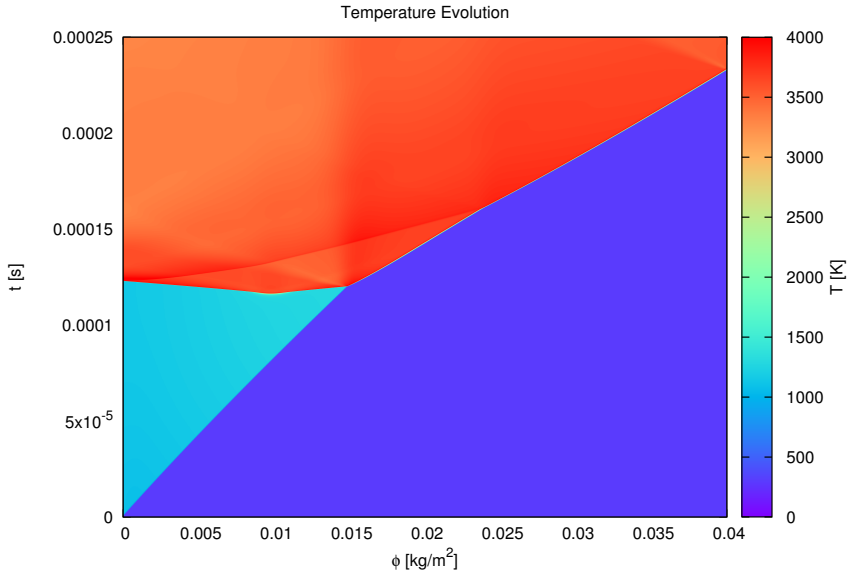

Figure F.21: Temperature profile of ethylene fluctuating shock-induced ignition with incident shock Mach number of 4.5, and piston oscillation frequency of 2.0 kHz, and amplitude of 20% with 1000 cells. (Normal simulation has 5000 cells).

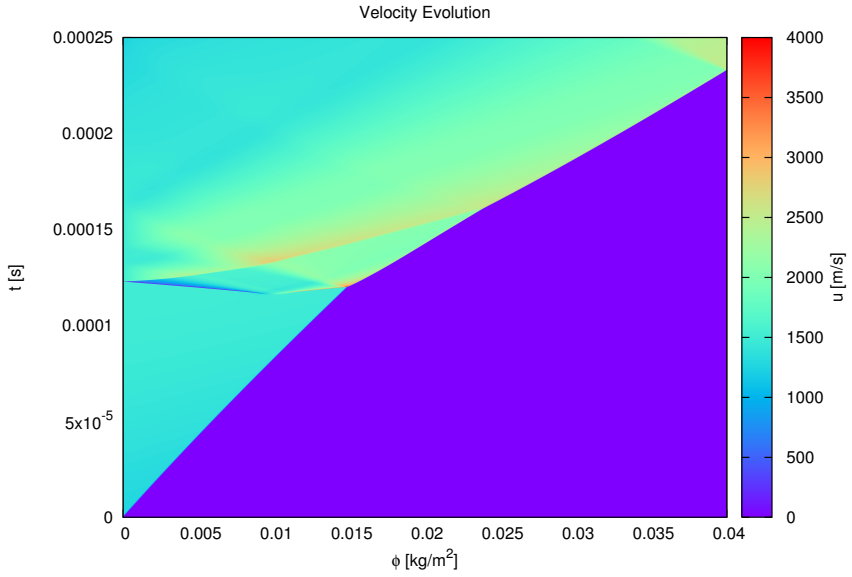

Figure F.22: Particle velocity profile of ethylene fluctuating shock-induced ignition with incident shock Mach number of 4.5, and piston oscillation frequency of 2.0 kHz, and amplitude of 20% with 1000 cells. (Normal simulation has 5000 cells).

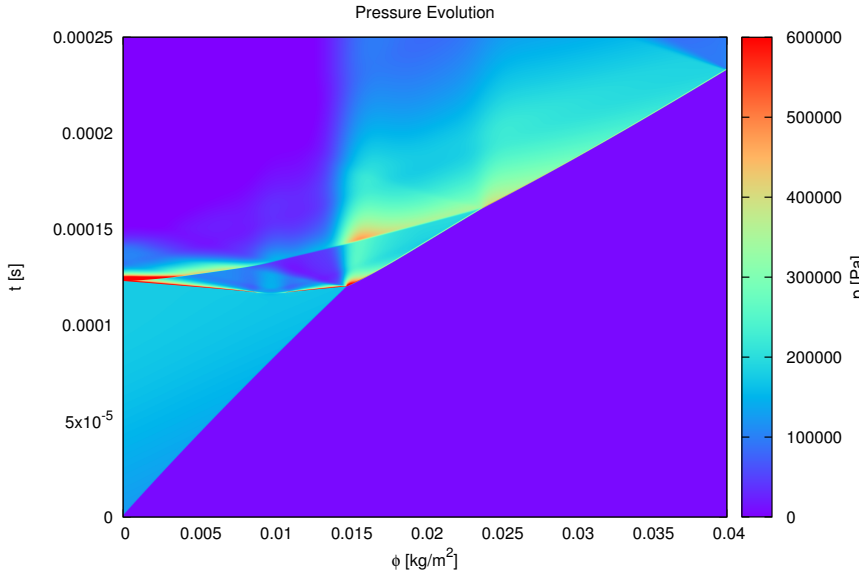

Figure F.23: Pressure profile of ethylene fluctuating shock-induced ignition with incident shock Mach number of 4.5, and piston oscillation frequency of 2.0 kHz, and amplitude of 20% with 1000 cells. (Normal simulation has 5000 cells).

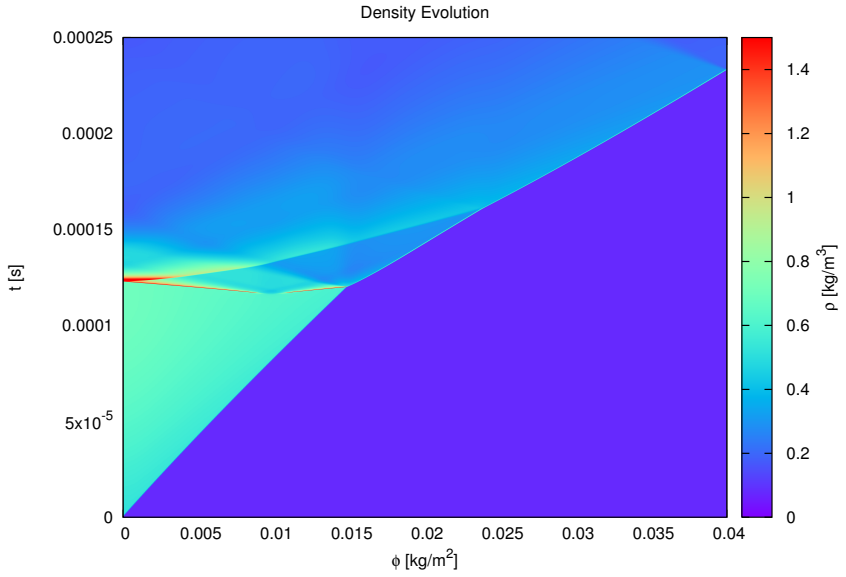

Figure F.24: Density profile of ethylene fluctuating shock-induced ignition with incident shock Mach number of 4.5, and piston oscillation frequency of 2.0 kHz, and amplitude of 20% with 1000 cells. (Normal simulation has 5000 cells).

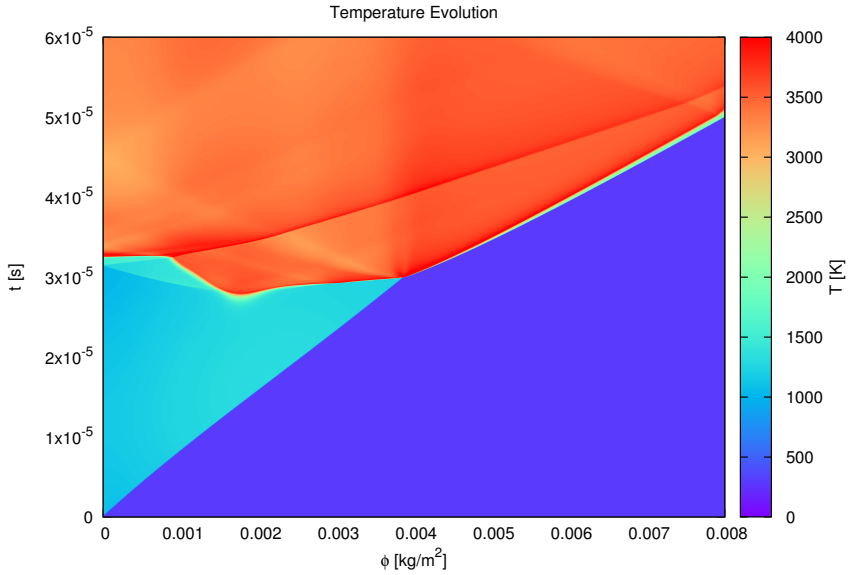

Figure F.25: Temperature profile of ethylene fluctuating shock-induced ignition with incident shock Mach number of 4.5, and piston oscillation frequency of 20 kHz, and amplitude of 20% with 1000 cells. (Normal simulation has 5000 cells).

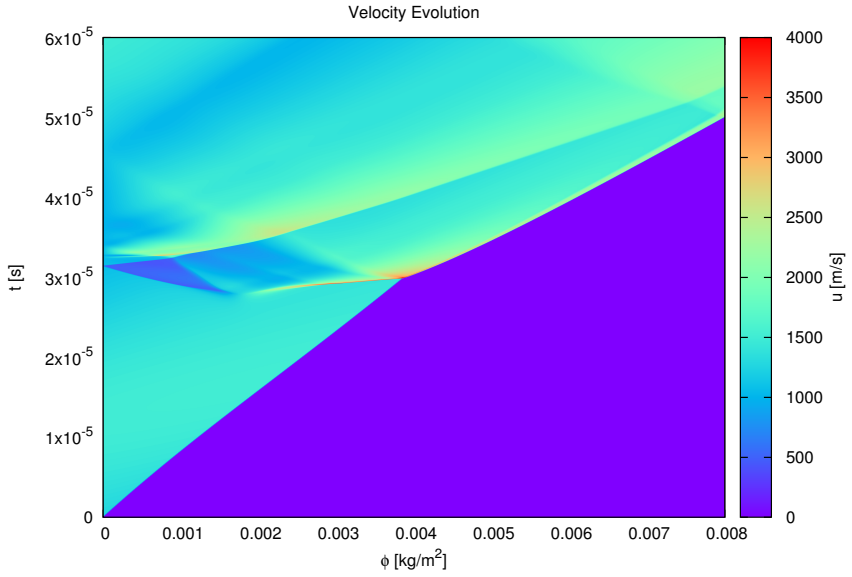

Figure F.26: Particle velocity profile of ethylene fluctuating shock-induced ignition with incident shock Mach number of 4.5, and piston oscillation frequency of 20 kHz, and amplitude of 20% with 1000 cells. (Normal simulation has 5000 cells).

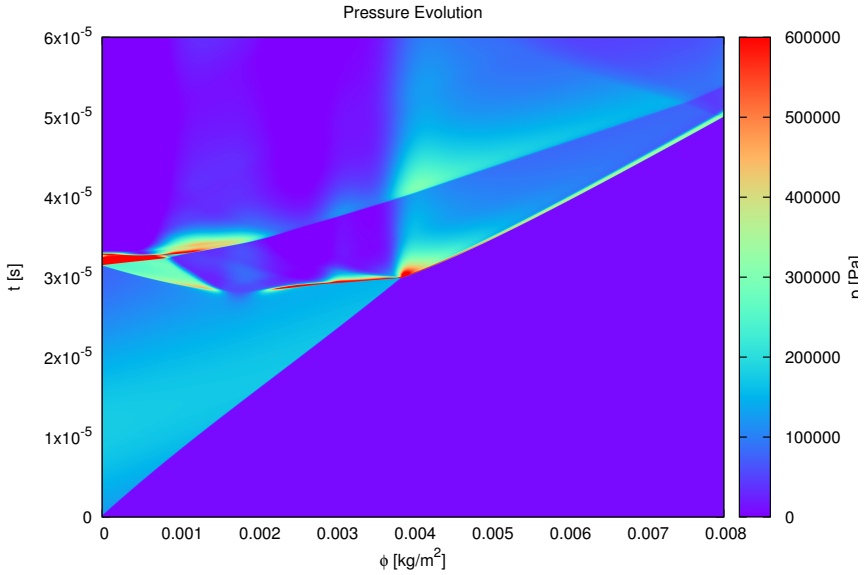

Figure F.27: Pressure profile of ethylene fluctuating shock-induced ignition with incident shock Mach number of 4.5, and piston oscillation frequency of 20 kHz, and amplitude of 20% with 1000 cells. (Normal simulation has 5000 cells).

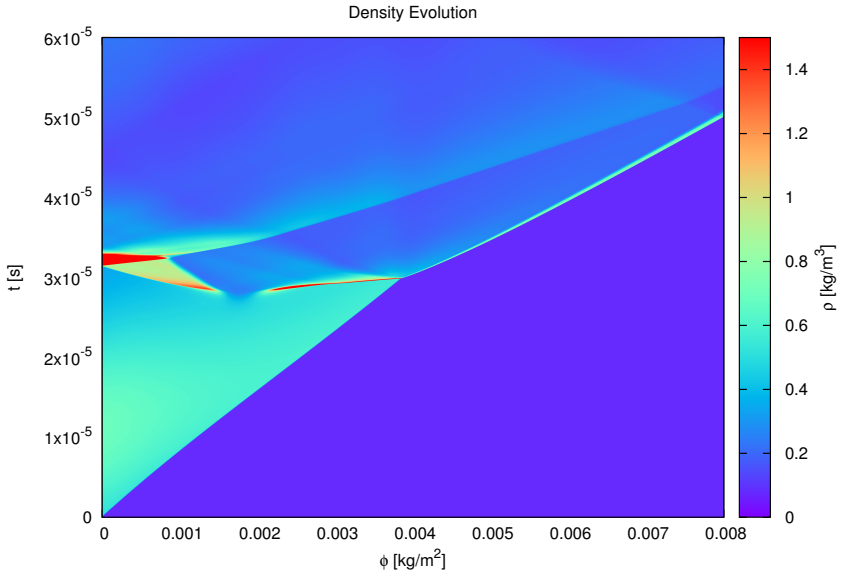

Figure F.28: Density profile of ethylene fluctuating shock-induced ignition with incident shock Mach number of 4.5, and piston oscillation frequency of 20 kHz, and amplitude of 20% with 1000 cells. (Normal simulation has 5000 cells).

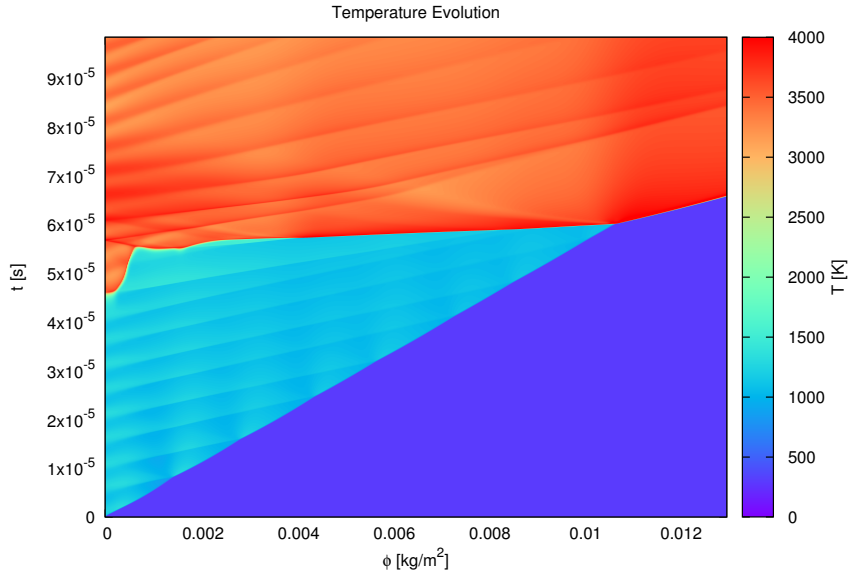

Figure F.29: Temperature profile of ethylene fluctuating shock-induced ignition with incident shock Mach number of 4.5, and piston oscillation frequency of 200 kHz, and amplitude of 20% with 1000 cells. (Normal simulation has 5000 cells).

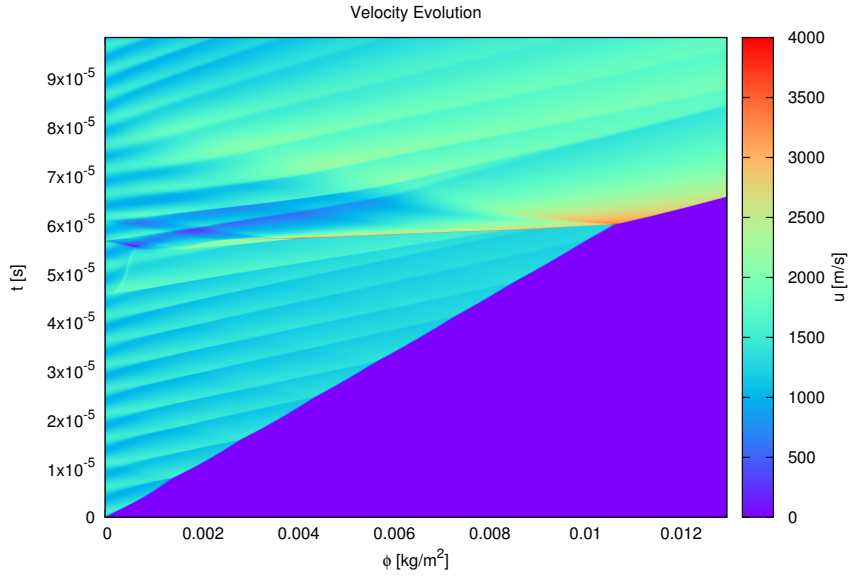

Figure F.30: Particle velocity profile of ethylene fluctuating shock-induced ignition with incident shock Mach number of 4.5, and piston oscillation frequency of 200 kHz, and amplitude of 20% with 1000 cells. (Normal simulation has 5000 cells).

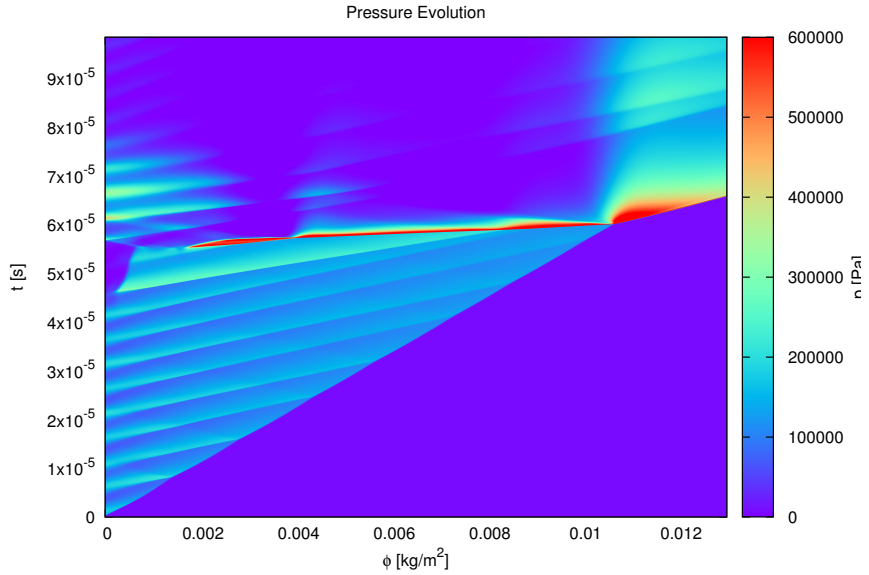

Figure F.31: Pressure profile of ethylene fluctuating shock-induced ignition with incident shock Mach number of 4.5, and piston oscillation frequency of 200 kHz, and amplitude of 20% with 1000 cells. (Normal simulation has 5000 cells).

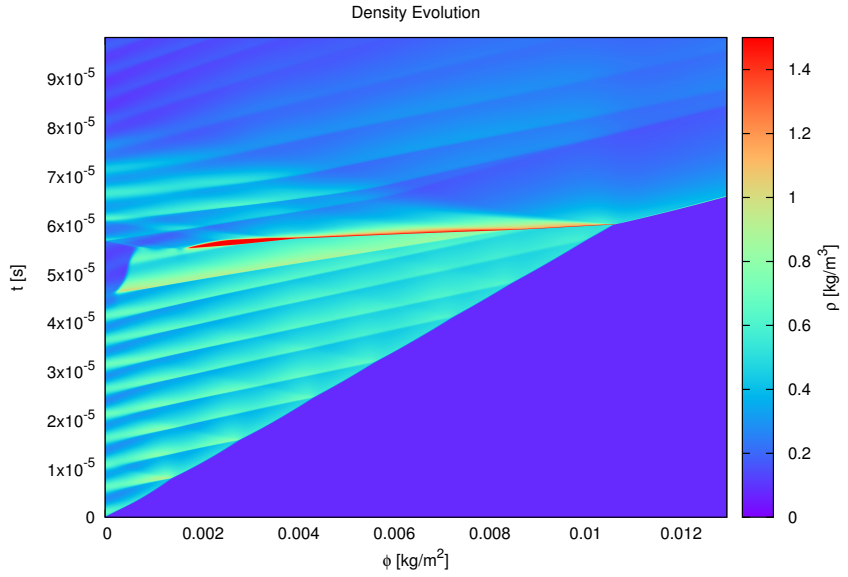

Figure F.32: Density profile of ethylene fluctuating shock-induced ignition with incident shock Mach number of 4.5, and piston oscillation frequency of 200 kHz, and amplitude of 20% with 1000 cells. (Normal simulation has 5000 cells).